Influence of Dynamic Ice Cover on River Hydraulics and Sediment Transport

by

Soheil Ghareh Aghaji Zare

Thesis submitted to the
Faculty of Graduate and Postdoctoral Studies
In partial fulfillment of the requirements
For the Ph.D. degree in
Civil Engineering

Department of Civil Engineering
Faculty of Engineering
University of Ottawa

Thesis committe following defence. From left to right: Prof. Jochen Lang (Defence Chairperson), Prof. Brian Morse (Laval University), Prof. Shawn Kenny (Carlton University), Prof. Colin Rennie (University of Ottawa, Thesis Supervisor), Soheil Ghareh Aghaji Zare, Prof. Ousmane Seidou (University of Ottawa- Thesis Co-supervisor), Prof. Majid Mohammadian (University of Ottawa), Prof. Andrew Cornett (University of Ottawa)- Photo courtesy of S. Ansari.

Abstract

Ice regime plays a significant role in River hydraulics and morphology in Northern hemisphere countries such as Canada. The formation, propagation and recession of ice cover introduce a dynamic boundary layer to the top of the stream. Ice cover affects the water velocity magnitude and distribution, water level and consequently conveyance capacity. A stable ice cover also tends to reduce bed shear and associated sediment transport, but bank scour and ice jamming events can increase sediment entrainment. These effects are even more intense during the ice cover break-up period when extreme conditions such as ice-jamming and release and mechanical ice cover break-up can locally accelerate the flow, and ice can mechanically scour the river bed and banks.

The presence of ice has some important implications for hydro-electrical power generation operations too. The ice cover changes the channel conveyance capacity (and therefore increases the flood risk), may increase sediment transport and causes scouring, and is likely to block water intakes and turbines. The rate of water release should, therefore, be adjusted in the presence of the ice cover to avoid unwanted consequences on the dam structure and equipments as well as on the downstream channel and the environment. Even though the influence of ice cover on rivers is widely recognized, large gaps still exist in our understanding of ice cover processes in rivers. Two main reasons for such a shortage are the difficulty and danger involved in collecting hydraulic and sediment transport data under ice cover, especially during the unstable periods of freeze-up and break-up. In the absence of sufficient data, the applicability of available formulae and theories on hydraulic processes in ice-covered rivers cannot be extensively tested and improved.

The purpose of this research mainly is

a) to perform a continuous, in-situ monitoring of water velocity profiles, sediment loads and ice-cover condition during several years through winter field campaigns at a section of the Lower Nelson River, Manitoba, Canada.The Lower Nelson River is a regulated river (Manitoba Hydro). It receives augmented flow from the Churchill River Diversion, and is subject to operation of many hydro-electricity facilities, one of which is currently under construction, while others are planned to be constructed in the future. Due to the geographical location of the study reach, it is covered by ice and experiences severe ice condition for several months during the year.

b) Analysis of the collected data in order to study the impact of ice cover on the hydraulic properties and sediment conveyance capacity at the study reach and

c) using the insight gained from the field data analysis to improve a river ice simulation model to apply in the study of Lower Nelson River ice regime. The selection of the Lower Nelson river is motivated by intention of Manitoba Hydro (MH) ,as the industrial partner in this research, to study the winter flow regime at the Lower Nelson River. Manitoba Hydro operates several dams on the Lower Nelson River and is considering more hydropower developments in the future.

This study is composed of six steps as are described in the following main steps.

Step 1: Selection of potential study sites and data collection techniques: The particular study site for this research is located immediately upstream of Jackfish Island, between Limestone generating station and Gillam Island in Lower Nelson River, Manitoba, Canada. River width at the study site location is about 1km. Water depth at the deployment site varies between 10-12 meters depending on both the time of year and the time of day due to hydropeaking fluctuations. Given the low accessibility to the field during winter time and considering the type of the required data, acoustic techniques were selected as the main approach for the field measurements. Two types of acoustic instruments, Acoustic Doppler Current Profiler (ADCP) and Shallow Water Ice Profiling Sonar (SWIPS) are selected for field investigations in this study. Both of them were planned to be deployed in the river for an extended period of time in order to record necessary data during the ice cover and open water periods.

Step 2: Data acquisition. After the site selection and defining the appropriate techniques, data acquisition has been started through a series of annual field measurement campaigns starting from winter 2012. Measured data mainly consist of water velocity and sediment suspension during various ice cover stages, including river ice break-up. The velocity profiles are analyzed to determine dynamic changes in boundary shear stress and hydraulic resistance and stresses in the flow during the both open water and ice cover periods.

Step 3: Data analysis and development/testing of roughness and sediment transport formulas. Several aspects of river-ice interactions are covered in the recorded data including ice cover condition and cover thickness variation, river hydraulic characteristics such as depth and velocity and finally information about the concentration of suspended particles. These data are analyzed to define the behavior of the ice cover and river during different ice stages. Ice effect on river conveyance capacity is also evaluated . The accuracy of common assumptions in composite roughness calculations in rivers is estimated and a new approach is developed and validated using the field observations and measurements. Ice cover influence on suspended sediment concentration is also studied as the other part of this research. Considering the type of the river sediment load (mostly bed load) available methods for sediment transport simulation are studied and applied for estimation of the sediment transport under ice cover condition. According to the results, the most suitable methods were planned to be a part of the river ice numerical simulation model, developed in this study. Turbulent characteristics in ice covered flows are also studied through two years of data recordings. Acoustic Doppler Current Profiler employed in this study is programmed for appropriate recording of the water velocity for this purpose. Results are analyzed and turbulent structures in the river are studied in this research as well.

Step 4: Testing of Hatch-MH's river ice simulation model. A numerical model has been selected in order to simulate the river ice process at the study site (LNR). ICESIM, a steady state, one-dimensional river ice process model originally developed in 1973 by Acres International Limited (now Hatch), is selected for this study.

ICESIM is originally developed in FORTRAN and is capable of predicting the progression and stabilization of river ice cover.

Step 5: Improvement of Hatch-MH's river ice simulation model: ICESIM model is converted to Matlab as the first step of the model improvements. A Graphical User Interface (GUI) is designed for the program which facilitates the assessment of model performance during the simulation leads to a more user-friendly model to operate. The new model, ICESIMAT is calibrated and evaluated based on the conducted field studies. Simulation capabilities of ICESIMAT are improved in the form of extended or additional subroutines to enhance its capabilities in the simulation of river ice processes and sediment transport. The current version of ICESIMAT is a steady state model, capable of simulating river ice , river hydrodynamic characteristics and sediment transport along the study reach. Though the model is restricted in the terms of the dimensions of the simulation (only one dimensional) its lower computational cost, permits a longer study reach to be simulated (in the scale of hundred kilometers instead of couple hundred meters in three dimensional simulation). ICESIM model is unable to simulate the break-up period which reduces the model capability in the simulation of the complete cycle of river ice. New subroutines are designed and added to extend the model capability to include simulation of ice processes during the ice cover break-up and finally to calculate the sediment transport under the ice cover.

Step 6: As the final step, the new subroutines are adjusted and linked to the main improved code, providing a new framework for dynamic ice cover simulation, more prepared for further future improvements both in terms of conceptual and programming aspects of the river ice modeling . The new Matlab basis of the code facilitates upgrading the model to include more complicated processes like river ice jam simulations.

As the general result of this thesis, we have a better understanding of hydraulics and sediment transport processes in ice covered rivers (direct and indirect measurements of river hydraulics characteristics), improved formulas for these processes (including more involving parameters) and a better version of the river ice simulation model (capable of simulating the complete river ice processes) for the contributors to this study in the industry.

Acknowledgements

To my life-coaches, my parents Mehri and Mahmoud: because I owe it all to you. Many Thanks!

My eternal cheerleader, my beloved wife, Farima: words can't explain how appreciative I am for all sacrifices you have made through our life.

I am grateful to my sisters, Sona and Solmaz, who have provided me with moral and emotional support in my life.

I also would like to express my sincere gratitude to my advisors Prof. Colin Rennie and Prof. Ousmane Seidou for the continuous support of my PhD study and related research, for their patience, motivation, and immense knowledge. Their guidance helped me in all the time of research and writing of this thesis.

Besides my advisors, I would like to thank my thesis evaluation committee: Prof. Jochen Lang, Prof. Brian Morse, Prof. Shawn Kenny, Prof. Andrew Cornett and Prof. Majid Mohammadian for their insightful comments and encouragements and also questions which incented me to widen my thinking of the research topic from various perspectives.

My interested, encouraging and always enthusiastic friends, Saber Ansari and Amir Gharavi: I miss our interesting and long-lasting chats.

My dear friend, Dr. Reza Feizi: he was always keen to know what I was doing and how I was proceeding.

With special mention to Dr. Habib Ahmari and Dr. Jarrod Malenchak at Manitoba Hydro. It was fantastic to have the opportunity to work in your collaboration at Lower Nelson River. What a cracking place to work!

I am also thankful to Mark Lapointe and Nathan Lambkin for their unfailing support and assistance through the field investigations of my PhD research.

And finally, last but by no means least, also to everyone in the Hydraulic Laboratory at the University of Ottawa. It was great sharing laboratory with all of you during last five years.

Thanks for all your encouragement!

Table of Contents

List of Tables

List of Figures

Abbreviations

n : Manning roughness coefficient

n_c : Composite manning roughness coefficient

n_i : Manning roughness coefficient for ice

n_b: Manning roughness coefficient for bed

R_i : Hydraulic radius of ice zone

R_b : Hydraulic radius of bed zone

R_c : Composite hydraulic radius

y_i, Y_i : Water depth in Ice zone, ice zone total depth

y_b, Y_b : Water depth in bed zone, bed zone total depth

y_t, Y_t : Depth through the water column, Total water depth

V_i : Average water velocity in ice zone

V_b : Average water velocity in bed zone

V_c : Average water velocity at the cross section

S_i : Energy grade line of the ice zone

S_b : Energy grade line of the bed zone

S_c : Cross section total energy grade line

F_D : Doppler Frequency

f_r : Received frequency

f : Emitted frequency

v : Relative frequency

C : Speed of sound

u,v,w : Water velocity components(streamwise, crosssectional, vertical)

α : Angle between relative velocity vector and axis of the ADCP transducer

v_x, v_y, v_z : Forward, transverse and vertical velocities

v_{b_i} , $i = 1 : 4$: ADCP beam velocities

v_{n_i} , $n = x, y, z$: Cartesian velocity components

φ : ADCP beam vertical deflection angle

λ : Wave length

ω : Angular frequency

k : Spatial wave number

p : Complex pressure

r : Distance

I : Average intensity

ρ : Water density

n_w : Wave number

a : Particle radius

p_s : Backscattered pressure

p_i : Incident pressure

f_∞ : Far filed form function

α_w : Signal attenuation by water

α_s : Signal attenuation by suspended sediment

ψ : Near field correction function

D_i : Directivity pattern of the transducer

P_s : Ensemble mean square pressure

M : Mass concentration of particles

T : Period

t : Time

T : Temperature

$\alpha_{s,visc}$: Viscous attenuation of sediment

$\alpha_{s,scat}$: Scattering attenuation of sediment

ζ_v : Viscous attenuation constant

ζ_s : Viscous scattering constant

E_L : Amplitude of returned sound

S_L : Source level

T_S : Target strength

T_L : Transmission loss

d_i : Ice draft

θ : SWIPS transducer tilt angle

β : Sound speed correction coefficient

D : Ice bottom distance to the SWIPS transducer

$C_{act.}$: Actual sound speed

$C_{nom.}$: Nominal sound speed

H : Water depth

P_{btm}: Measured bottom pressure

P_{atm}: Atmospheric pressure

T_{ice} : Ice thickness measured by SWIPS

V_f : Volumetric production of ice

$L_{0,}B_0$: Length and width of the open water area

C_0: Heat transfer coefficient

T_W: Water temperature

T_a: Air temperature

λ_i : Latent heat of fusion for ice

ρ_i : Ice density

h_j : Ice thickness

V_u : Water velocity under ice cover

P_j : Ice cover porosity

W_b: Border ice width

D_d: Degree-days of freezing

F_t : Hydrodynamic force of the flow on the ice cover leading edge

d_H : Water depth under the ice cover leading edge

γ_w : Specific weight of the water

S : Slope of the hydraulic grade line

A : Area

F_D : Hydraulic fractional drag force

F_w : Gravitational force of the ice cover

γ_i : Specific weight of ice

V_0 : Volume of ice cover

F_{wd} : Wind drag force on the cover

P_W: Wind force

F_C: Cohesion force of the ice cover to the river banks

C_c : Ice cover/ river bank cohesion magnitude

t_h : Cross sectional average ice thickness

L : Length

F_f : Friction force of the ice cover to the river banks

f_i : Stress in the ice cover

k_1 : Coefficient equal to the ratio of lateral to longitudinal stress in the ice cover

φ_i : Angle of friction of ice/bank interface

S_i : Total stress in the ice cover

W_i : Ice cover width

F_{ir} : Internal resistance of ice cover

k_2 : Rankin's passive coefficient

T_m : Ice cover temperature at bottom

T_s : Ice cover temperature at top

k_i : Thermal conductivity of ice cover

h_i : Static ice thickness

a : Empirical coefficient of Stefan's method

h_s : Snow cover thickness

k_s : Thermal conductivity of snow cover

H_a : Heat transfer coefficient of the cover (ice and snow cover)

D_t : Accumulative thawing degree-days

C_{wi} : Heat transfer coefficient from water to ice

C_{ia} : Heat transfer coefficient at ice- air interface

C_{sa} : Heat transfer coefficient at the snow-air interface

V_w : Average flow velocity

b : Ice cover decay rate

aT_a : Rate of ice cover melting on the cover top

τ_b : Boundary shear stress

u_* : Boundary shear velocity

S_f, S : Energy grade line slope

U^+ : Characteristic velocity

u : Time averaged velocity

z : Distance from bed

κ : Von-Karman constant≈ 0.4

K_s : Equivalent sand roughness

Y : Water depth in open water condition

U_m : Depth averaged velocity

$U_{max},\ V_{max}$: Maximum velocity

Q : Flow discharge

W_w : Cross section width

p : Ice cover percentage

H_l : Head loss in length

f_c : Darcy-Weisbach friction factor

R_n: Reynolds number

ϵ : Absolute roughness

$S.F$: Shape factor

P_i : Wetted perimeter of ice zone

P_b : Wetted perimeter of bed zone

S_c : Composite energy grade line slope

$S_i,\ S_{fi}$: Energy grade line slope in ice zone

$S_b,\ S_{fb}$: Energy grade line slope in bed zone

$\bar{U}_i$: Mean velocity in ice zone

$\bar{U}_b$: Mean velocity in bed zone

u_{*i} : Shear velocity at ice zone

u_{*b} : Shear velocity at bed zone

f_i : Darcy-Weisbach friction factor for ice zone

f_b : Darcy-Weisbach friction factor for bed zone

τ_i : Shear stress in ice zone

τ_b : Shear stress in bed zone

q : Inflow rate of water per unit width of the channel

q_s: Inflow rate of sediment per unit width of the channel

ν : Kinematic viscosity

d : Bed sediment diameter

σ_g : Geometric standard deviation

$g\Delta\rho$: Submerged unit weight

t_s : Bed layer thickness

θ : Shield's parameter

θ_c : Critical value for initial entrainment of bed sediment

η : Shield's parameter ratio to sediment incipient motion value

Re_b : Bed layer Reynolds number

Re_* : Particle Reynolds number

$c\,(z)$: Vertical concentration profiles

c_a : References concentration of the specific size of sediment

P_n : Rouse number

d_* : non-dimensional diameter

u_{*cr} : Critical bed shear velocity

ω_s : Sediment fall velocity

$S_v\,(z)$: Theoretical backscatter power per unit volume

e : Ratio of elasticity of the particles to water

g_d : Ratio of the particles density to the water

$c\,(z, d)$: Concentration of particles of diameter d at height z

$p(d)$: Probability density function of the grain size distribution by volume of the bed material

E : Recorded acoustic intensity in counts

Ψ : Acoustic instrument specific coefficient

$PdBW$: Acoustic transmit power

b_s : ADCP bin size

C_{obs} : Observed sediment concentration

$S_{v_{obs}}$: Observed backscatter strength

C_{th} :Theoretical sediment concentration

$S_{v_{th}}$: Theoretical backscatter strength

U_i : Instantaneous velocity component in the direction of x_i

$\bar{U}_i$: Mean velocity component in the direction of x_i

u_i : Velocity fluctuation component in the direction of x_i

P: Hydrostatic pressure (Navier-Stokes)

ρ_r : Reference density (Navier-Stokes)

υ : Kinematic viscosity (Navier-Stokes)

ν_t : Eddy viscosity (Boussinesq concept)

ϕ : Concentration or temperature (Conservation of concentration)

λ : Molecular diffusivity of ϕ (Conservation of concentration)

S_ϕ : Source of ϕ (Conservation of concentration)

δ_{ij} : Kronecker delta

Γ : Mass turbulent diffusivity

σ_t : Schmidt (mass transport) or Prandtl (heat transport) number

$\langle U \rangle$: Mean velocity magnitude at the depth y.

h : Flow surface elevation

C_f : Skin friction coefficient

δ_v : Near boundary length

u_t : Velocity scale

y^+ : Viscose length (Wall Unit)

Re_τ : Friction Reynolds number

ς : Velocity gradient

$U(x,t)$: Eulerian Velocity

$E(x,t)$: Turbulent kinetic energy (Mean flow)

$k(x,t)$: Turbulent kinetic energy

p : Instantaneous pressure term in the Navier-Stokes equation

$\mathcal{P}$: Production of turbulent kinetic energy

p' : Decomposed fluctuating pressure term based on Reynolds hypothesis

F'_G : Submerged weight of the particle

γ_s : Submerged specific weight of the sediment

C_1 : Form factor (Sediment transport)

D : Characteristic particle diameter

F_D : Drag force (Sediment transport)

C_D : Drag coefficient (Sediment transport)

A_x : Projected particle surface perpendicular to the flow (Sediment transport)

F_L : Lift force

C_L : Lift coefficient

F_s : Particle mobility parameter

Re^* : Particle Reynolds number

S_s : Specific gravity parameter

g_b : Mass unit transport rate

d_m : Representative particle size

γ'_s : Sediment submerged specific weight

ξ : Hiding factor in Einstein method

$\varkappa$: Characteristic grain size

φ_* : Non-dimensionalized transport rate

ψ_* : Flow intensity parameter

$\mho$: Particle fall velocity

m'_b: Bed load submerged mass per unit area

G_{gri} : Dimensionless fractional transport parameter

D_{gri} : Fractional dimensionless grain diameter

ϖ : Modified straining function

σ_ϕ : Arithmetic standard deviation of the surface size distribution

$\mho$: Particle fall velocity

M : ADCP rotation matrix

Chapter 1

Introduction

1.1 Background on River ice

Ice in rivers and lakes is a subject of attention of people living around them, who deal with it for their everyday life. The longer the presence of the phenomenon, the more detailed the description of its status. For instance, there are more than twenty words in Inuktitut dialects to describe ice and its condition, which is not surprising given the pivotal role of ice in the sustenance and survival of the Inuit (Johns and Kielsen Holm, 2009). Ice engineering as a science emerged in the 19th century as industrial life and growing economy demanded control of natural resources and prevention of disastrous events and associated casualties. Public construction projects were the preliminary fields of ice studies during the first half of the 19th century Ashton (1986) . Some reports regarding the drastic effects related to ice can be found from the 1870s, such as the letter written by Moberley, Factor of the Hudson's Bay Co. post at Fort McMurray (Moberley and Cameron (1929) cited in Beltaos (1983)): "... The winter of 1874-75 was a bitter one... on striking the turn of the stream at the post it blocked the river and drove the ice two miles up the Clearwater (a major tributary) in piles 40 to 50 feet high. In less than an hour the water rose 57 feet, flooding the whole flat and mowing down trees, some three feet in diameter, like grass..." River ice studies started to appear in scientific literature during the early years of the 20th century mainly by Altberg in Russia, Barnes in Canada and Devik in Norway (Ashton, 1986). Detailed studies about river ice engineering were published during the early thirties by Devik and followed by comprehensive publications during the seventies by Starosolszky (1970) and Michel (1971). Since then, the scope of river ice engineering has grown and its several aspects have been discussed in publications, manuals and books. This could be mainly due to the vast geographical range of river ice and its serious impediments on operation of water supplies and hydro-electric facilities as well as catastrophic flood events related to ice jam formation and release. For instance, Morse (2001) addressed a 40 day stop in St. Lawrence River commercial navigation due to an ice jam event in 1993. Such suspension in trade and navigation costs several million dollars and emphasizes the necessity for detailed studies and accurate research activities in river and lake ice engineering.

Besides the direct impacts, river ice affects human life in many other aspects by changing

Figure 1.1: Ice jam, Don River near Queen Street.1901 (City of Toronto Archives)

river ecology (water quality, flora and fauna), geomorphology (shore stability, navigation and transportation) and hydrology (river discharge and conveyance capacity) during winter.

The important socio-economic effects of river ice in northern countries, including Canada, has precipitated many important advances in river ice engineering and hydrology research, some of which can be summarized as follows:

I. Two professional peer-reviewed journals dealing with scientific and technical problems in cold regions; Journal of Cold Regions Science and Technology (since 1979) by Elsevier and Journal of Cold Regions Engineering (since 1987) by American Society of Civil Engineers (ASCE).

II. Two special journal issues have directly highlighted the topic; Hydrological Processes in 2002 and Canadian Journal of Civil Engineering in 2003.

III. River ice has been the subject of six special conferences; Canadian Committee on River Ice Processes and the Environment in 1999-2001-2003, International Association of Hydraulic Research (IAHR) in 2000-2002 and an IAHR international symposium on ice in 2014.

IV. The Committee on River Ice Processes and the Environment (CRIPE) has hosted biannual workshops on river ice related topics since 1980.

Figure 1.2: Intense river ice cover at Port Nelson bridge, beached and damaged dredge at left, Mouth of Nelson River, Hudson Bay, Manitoba, Canada

Even though many river ice phenomena have been studied quantitatively in recent years, some aspects, e.g. riparian flow, are still underestimated or ignored (Shen, 2003; Morse and Hicks, 2005). Finally it should be noted that our understanding about the phenomenon has burgeoned during recent years thanks to new advancements in computer technology and field investigation techniques. Some of the previously known aspects of river and lake ice science are now being clarified and more accurately understood, modeled and simulated in laboratories. This helps engineers to design more safely (social and environmental) and economically, which increases the reliability of future plans necessary for society to flourish in the cold regions of the world.

1.2 Thesis objective

1.2.1 Main objective

The main objective of this research is to improve our understanding of the impact of the ice cover on stream hydraulics, flow conveyance capacity and sediment transport. In order to achieve this goal, field investigations are preformed using non-interference hydraulic measurement techniques and results are compared to developed theories for the subject. Ice cover presence adds a level of complexity to the flow by adding a dynamic boundary layer to the top of the stream. Complications due to formation of this new boundary layer also challenge the application of experimental techniques mostly developed for open water condition. On the other hand, in-situ field investigations are required to determine the river behavior under the ice cover in order to understand the tremendous effects of ice cover on river hydraulics and morphodynamics. This is especially the case during some of the most dynamic stages of the river ice such as freeze-up and break-up periods when the ice cover condition drastically affects the flow characteristics. Even so, river ice effects are poorly studied mainly due to difficulties in obtaining reliable, consistent measurements because of the hazardous nature of the ice and river during the ice cover period. This raises the importance of implementation of new experimental techniques in ice covered rivers. New approaches for long-term continuous measurements are needed in order to autonomously monitor and record potential variations in flow due to various ice cover conditions. As the main objective, variation of flow characteristics and sediment transport are studied and analyzed during various stages of the ice cover period. Acoustic instruments are deployed for autonomous measurements during several winter field campaigns in Lower Nelson River, Northern Manitoba. Data acquired during the field investigations provide information to study ice cover behaviour in time and its influence on river hydraulics (mainly represented by profiles of water velocity) and sediment flux. The latter is achieved by estimation of concentration of suspended particles in flow based on backscatter intensity and flow discharge. Effects of different ice stages on river flow capacity and sediment transport then can be evaluated and possible impacts can be recognized.

1.2.2 Secondary objectives

Secondary objectives for this research include the following:

I. Study of dynamic ice cover effect on boundary shear stress in an ice covered river, which is important for sediment entrainment to the stream. Shear stress magnitudes vary in time mainly because of variation in river flow and boundary condition. Consequently, higher exerted shear force on river bed causes higher sediment initiation in to the flow. Larger shear stress on upper boundary, changes the under ice cover roughness which itself alters the flow in the river.

II. Estimation of hydraulic resistance to the flow in presence of the ice cover, including different ice stages. Introduction of upper boundary layer to the top of the stream increases the hydraulic resistance to the flow which causes the back water occurrence in the river. The process may happen almost during all river ice stages increasing the risk of upstream inundation.

III. Evaluation of available methods to calculate the total hydraulic resistance to the flow (i.e., composite roughness coefficient) during the ice cover period. Several methods are introduced in order to calculate the composite hydraulic resistance to the flow. The most common approaches for composite roughness estimation for engineering purposes are selected to be described and apply in this study. Models accuracy can be discussed and evaluated.

IV. Development of a novel and improved method to estimate the composite roughness coefficient for the ice cover period. According to the findings of the this research, a new method is introduced in order to increase the accuracy of hydraulic resistance estimation in ice covered rivers.

V. Estimation of potential effect of river ice formation on turbulence in covered streams. As previously described, formation of ice cover alters the hydraulic characteristics in the river which can vary the formation of macro micro turbulent structures. These variation can quit drastic specifically during the highly dynamic ice cover variations. Turbulence characteristics in ice covered flows are studied in this research and effects of ice cover formation and evolution on abovementioned features are evaluated in this thesis.

VI. Ice cover propagation and associated changes in river hydraulics are also simulated using the one dimensional numerical model ICESIM. Ice processes along the study reach is simulated to compare the simulation results to the calculated and observed values during the field investigations.

VII. Improvement of the existing river ice model called ICESIM to a new Matlab based dynamic numerical model (ICESIMAT). The improved model includes the ice cover simulation during the stage of break-up (cover decay, recession) and sediment transport. The model is calibrated and its performance in both ice and sediment terms are verified using the continuous field data. Interactive algorithm for sediment transport calculation is also added to the model to select the most appropriate method for calculation of sediment load at river cross section considering the bed material and distribution.

1.3 Novelty

Novelties of the current study include:

A unique data set on hydraulic processes under ice cover:

A long-term, continuous, comprehensive field investigation of river ice processes, river hydraulics and sediment transport was performed. For this purpose, acoustic instruments are deployed on the river bed throughout the winter to obtain continuous, yet accurate field data, which allows the quantitative estimation of the effects of dynamic ice cover on river flow and sediment transport. This is particularly important for dynamic stages of the ice cover such as the break-up period, for which accurate, long-term field data and therefore analysis were previously absent in the literature mainly due to experimental difficulties. In this study, a 1200 kHz Teledyne RD Instruments Acoustic Doppler Current Profiler (ADCP) and a 546 kHz Shallow Water Ice Profiling Sonar (SWIPS) were deployed simultaneously in a river, under an ice-cover to measure vertical profiles of streamwise velocity and ice cover conditions continuously for several months during three winter field campaigns. Acoustic measurements include all of the three main river ice stages (freeze-up, stabilization and break-up). Recorded data covered the freeze-up and ice cover formation, stable ice cover interactions with the flow and the complete period of river ice break-up from thermal decay to ice jam formation and removal. Open water period data are also included to provide a comparison between river behavior with and without the ice cover. The presence and effect of important river ice features, such as slush ice and ice jams, are also evaluated.

A better understanding of hydraulic and sediment transport under ice: Variation in suspended sediment concentration and effect of the ice cover stages on it are also studied according to the recorded acoustic data. To the best of our knowledge, this is the first of such comprehensive study. In addition, the applicability of several common sediment transport models are studied in an ice covered river and a new version of a numerical model is provided which is able to simulate the sediment transport for all ice cover conditions.

Improved formulas for composite roughness estimation: Composite hydraulic resistance in a cross section of an ice-covered river as well as the performance of the available methods for this purpose are studied as a part of this research. Available composite resistance equations yielded various results, motivating development of a new equation to describe the total hydraulic resistance during stable ice cover.A theoretical formulation for total composite resistance is developed based on field measurements for boundary roughness calculation. The proposed formulation is tested and demonstrated to provide accurate estimations of composite resistance amongst other available approaches.

Investigation into the ice cover effect on turbulence in ice covered streams The acoustic instrument employed in this study are specifically programmed to record river hydraulic characteristics through a specific setting in order to provide information for analysis of the turbulence in ice cover period. Water velocity is analyzed through the acoustic beams of the instrument and turbulence characteristics (Reynolds stress magnitudes and distribution) are calculated based on a technique relies on the along beam variance of the velocity measurements. to the best of our knowledge, the current study is the first of its kind to study and estimate the Reynold stress in an alluvial stream during the ice cover period using acoustic field measurements.

An improved river ice simulation model: ICESIM model improved in some aspects in order to simulate the river ice processes more comprehensively. Model is also upgraded to a new version (ICESIMAT) capable of simulation of sediment transport under the ice cover during several stages of the river ice including dynamic stages of the break-up when higher sediment load variation is observed based on field measurements.

1.4 Publications

Results of this study are published/under publication in some scholarly outlets and presented in international conferences and symposia and technical meetings. Scientific and technical findings of this study are basis of a book chapter in Experimental Hydraulics Handbook - Chapter "Complex Experiments". The author also published the results of the current study in two refereed journals (Journal of Hydraulic Engineering, American Society of Civil Engineering, Water Resources Research, American Geophysical Union (presented in sections 4.2 and 5.2) . Two more journal articles are also under preparation (at the time of manuscript submission) to be published in Journal of Cold Regions Science and Technology, Elsevier and Canadian Journal of Civil Engineering, Canadian Society of Civil Engineers, representing the research findings in ice effects on turbulence and numerical simulation of river ice processes in ice covered streams respectively (sections 5.3 and 5.4) .

Author also published some parts of the current study in several international conferences in the fields of river ice and river engineering namely workshops of the Committee on River Ice Processes and Environment (CRIPE) (two publications) , River Ice symposium of the International Association for Hydro-Environment Engineering and Research (IAHR)(two publications), International Conference of Fluvial Hydraulics and Canadian Hydrotechnical Conference. Results are also presented in two technical sessions hosted by American Geophysical Union.

Chapter 2

Literature review

2.1 River ice research institutes in Canada and around the world

Michel (1971, 1978) comprehensively described ice regime and ice mechanics in rivers and lakes for the first time. Since then, Canada has become a leader of research in this field and developed well organized committees and scientific societies in the field of river and lake ice engineering. The most established Canadian organizations involved in ice related research can be listed as:

I. Canadian Committee on River Ice Processes and the Environment (CRIPE).

II. National Research Council Canada (NRCC).

III. Canadian Geophysical Union (CGU).

These organizations have conducted excellent research in the field of river ice engineering individually or in collaboration with each other or other organizations. For instance, a monograph on river ice break-up was published in 2005 by CRIPE and the Canadian Society of Civil Engineers (CSCE). CRIPE has been organizing biannual river ice workshops and short courses since 1981. Beltaos (1995b) and Davar et al. (1998) addressed the key role of CRIPE in publication of comprehensive studies about river ice jams. In 2009, a special issue of the journal Cold Regions Science and Technology published selected papers of 14th river ice workshop hosted by CRIPE in June 2007. The NRCC is another leading Canadian organization in river ice research. NRCC's particular field of research has been ice forces on structures, but their attention has recently changed to offshore ice issues. Another famous organization dealing with river ice in North America is the Cold Region Research and Engineering Laboratory (CRREL) of the United States Army Corps of Engineers. Finally, river ice studies have been fostered at an international collaborative level through a series of conferences and symposiums hosted by IAHS (International Association for Hydrological Science), IAHR (International Association of Hydro-environment

Engineering and Research), the Permanent International Association of Navigation Congresses (PIANC), and Port and Ocean Engineering under Arctic Conditions Association (POAC).

2.2 Review of ice processes in rivers

River ice processes include three main stages: freeze-up, stabilization and consolidation, and break-up. Each of these primary stages includes different sub-stages and various ice features. These processes are the result of complex interactions between several meteorological, hydrologic, mechanical and thermal factors. The river ice process begins by formation of frazil ice in rivers and streams exposed to cold weather. The determining factor for ice formation in rivers is flow intensity. In areas with low current intensity such as along the channel margins or river banks, frazil crystals can form on the water surface. Due to lack of high turbulence and mixing, skim ice can form on the surface even when the water column temperature is still above the freezing point. This skim ice formation usually starts from the banks or margins by secondary nucleation, thickens thermally by further cooling and forms border ice. Border ice is usually the first ice that appears along the natural river margins and, if the hydroclimatic conditions permit, continues to spread out over the adjacent areas.

In more turbulent areas, frazil ice crystals agglomerate and grow and form frazil ice floes instead of forming skim ice. These frazil floes flow and/or entrain to the river bottom due to high mixing of the water column, where they can attach to exposed bed objects and form anchor ice. Anchor ice growth continues until buoyancy and drag forces overcome the bond of the ice to the bed material and lift and transport the underlying bed materials (including coarse sand, gravel, and even boulders). Large volumes of material can sometimes be transported, because under the correct set of ice growth conditions, anchor ice can form an extensive blanket on the river bed. Marcotte (1984) reported a 20 km^2 zone of the St. Lawrence River covered with a 1.5 m thick blanket of anchor ice, which formed 6 m long floating ice blocks after release.

On the other hand, the agglomeration process of frazil ice floes can continue. The buoyancy of flocculated frazil can overcome turbulent dispersion, causing the ice to flow at the water surface. Floating ice particles can be categorized as either frazil ice pans or slush ice depending on the mixing power of the river. Surface floes can stick together and accumulate on the existing border ice, which results in lateral growth of surface ice and partial or total coverage of the channel section. Once an ice cover is initiated, it progresses upstream by congestion of incoming floes and their accumulation on the cover edge. Forces acting on the ice cover dictate the cover thickness, as the ice cover evolves to balance the applied forces. In other words, forces like water and wind drag, and more importantly the weight of the cover, mechanically thicken it under a process called "shoving. Once the ice cover is stabilized, upstream progression of the ice cover can continue.

A consolidated ice cover will decay and break-up in spring due to both hydrothermal and hydro mechanical processes (Beltaos, 1995b) . Thermal break-up processes affect the ice

Figure 2.1: Ice cover formation upstream of Jackfish Island, Lower Nelson River- Ice floes and border ice formation are apparent

cover even before air temperature rises above the freezing point, when the snow cover begins to melt due to solar radiation and introduces a new heat source to the thermodynamic balance of the river system. Warmer freshet flows in spring can also contribute heat. This new heat source effectively weakens the ice cover stability, making it more vulnerable to applied mechanical forces. On the other hand, the spring freshet increases the discharge and can rapidly raise the water level which is the main reason for mechanical break-up. A break-up ice run has similar basic mechanisms as a freeze-up run, except it has greater potential to occur abruptly and includes higher probability of ice jam formation, especially in the early spring break-up period (Shen, 2010). Ice cover decay and collapse result in presence of open water areas as well as large floating ice particles. Floating ice chunks can accumulate, bond together when temperatures drop below freezing (e.g., during night) and accumulate in narrow, constricted parts of the river (e.g., areas with strong remaining border ice) and restrict the flow. This action can result in rapid local increase in water level (ice jams). Rapid release of ice jams can lead to catastrophic flooding, and, presumably, high bed shear stresses.

Ice cover processes are slightly different in steep upland versus lowland river basins (Turcotte et al., 2011; Turcotte and Morse, 2011), even though most of the formed ice features are common in both, the sequence of formation may vary. The river ice process was comprehensively described (Figure 2.2) and mathematically modeled by (Shen, 2003). Mathematical models include both analytical and numerical models according to all complex interactions between different river ice aspects such as hydrodynamic, thermal and mechanical processes. These models are useful tools to simulate ice cover processes and to predict some of the hazardous effects of ice cover such as floods and ice jam formations (Haresign, 2012; Lindenschmidt et al., 2011). Ice processes in rivers and lakes have been modeled using different new approaches like artificial intelligence as well (Zaier et al., 2010; Guo et al., 2012).

Associated phenomena can also affect the river ice process. River ice mechanical characteristics have been studied by some researchers, providing information for future numerical modeling of ice cover progression (Timco and Cornett, 1997; Hammar et al., 2002). The effect of snow cover river ice was discussed by Andres and Van der Vinne (1998, 2001). Formation of open water patches in stable ice cover was studied by (Zabilansky et al., 2002; Zabilansky, 2002) . The river ice process also comprehensively described in gravel rivers by Ettema and Kempema (2012). Ice cover progression has been found to have important effects on fish ecology and fishery industries Brown et al. (2011). River ice processes and associated extreme events have been studied using image processing and remote sensing techniques in order to provide accurate data, describing the process in natural streams. (Lindenschmidt et al., 2011; Van Der Sanden and Drouin, 2011; Emond et al., 2011; Kääb et al., 2013; Gauthier et al., 2015). Ice cover progression complicates flow in rivers by addition of a new boundary layer to the top of the stream. The upper boundary layer affects important flow characteristics such as velocity, pressure, shear stress on stream boundaries and hydraulic resistance to the flow (Stickler et al., 2010; Ghareh Aghaji Zare et al., 2014, 2015).

Climate change i.e. changes in any important meteorological flux, is found to have extremely significant effect on river ice process. Drastic changes in ice cover processes due to changing climate can be categorized in two major fields. First, variation in condition of the cover, and second, timing of ice stages occurrence (Morse and Hicks, 2005). The latter can aggravate the ice cover related hazardous phenomena such as formation and release of ice jams and complicate their prediction and mitigation. The former affects mainly the mechanical behavior of the cover; reduction in bearing capacity can jeopardize the transportation industry in regions that rely on ice roads. This is particularly important in some areas, like northern Canada, where ice roads and ice bridges provide the only ground access for civic or industrial purposes such as Canada's diamond mines (Kuryk, 2003; Morse and Hicks, 2005). Other potential river ice response to climate change are described by authors such as Beltaos (2002a), Beltaos (2002b), Beltaos et al. (2001), Beltaos and Roswell (2001), Prowse and Beltaos (2002), Prowse and Ferrick (2002),Kuryk (2003) , Brown and Duguay (2010) , Derksen et al. (2012), Shiklomanov and Lammers (2014).

2.2.1 Frazil ice

Frazil ice is the terminology for small, needle shape, randomly oriented ice particles measuring 1-4 mm in length and 1-100 μm in thickness that usually form in turbulent, slightly super cooled water (Kivisild, 1970). Water mixture due to turbulence cools the water body but prevents the formation of skim ice on top and leads to frazil generation through the whole water depth. Frazil ice generation occurs in a significant rate, as large as 10^{6}

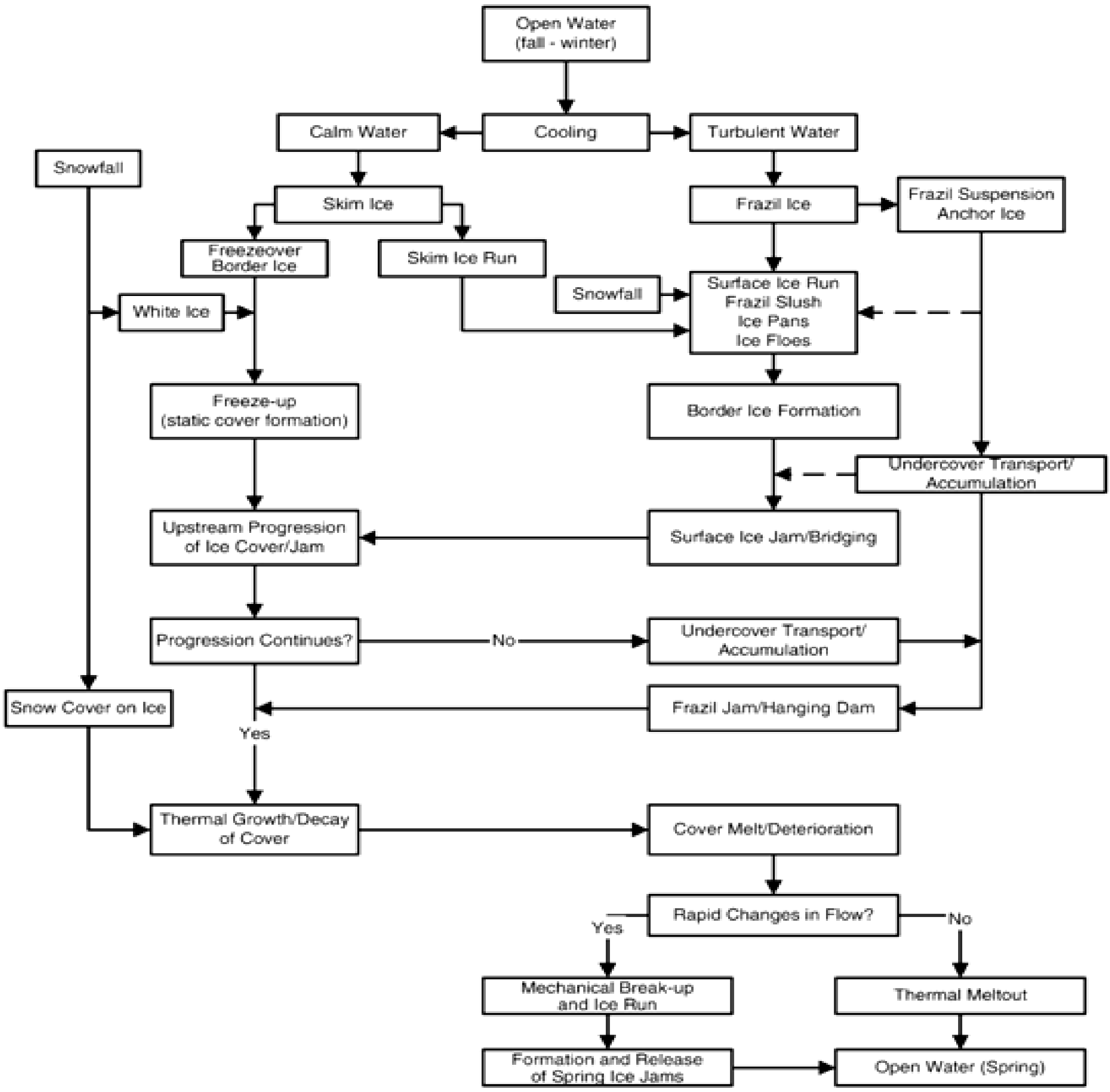

Figure 2.2: River ice processes described by Shen (2003)

m^3/day (Martin, 1981). Frazil ice may be generated through several mechanisms defined as homogenous, heterogeneous or secondary nucleation. Amongst them, the first two are extremely rare in natural streams due to their specific requirements which are not met in nature. Thus, secondary nucleation is the predominant process of frazil ice nucleation. Through this process, frazil ice nucleation occurs due to crystal collision with solid which generates numerous nuclei in water (Bauer and Martin, 1983; Ashton, 1986)

Frazil ice became a topic of continuous research during the 1990s (Hirayama et al., 1997) . Comprehensive laboratory studies on frazil ice evolution were performed using the counter

rotating flume performed at the University of Manitoba (Clark and Doering, 2002;

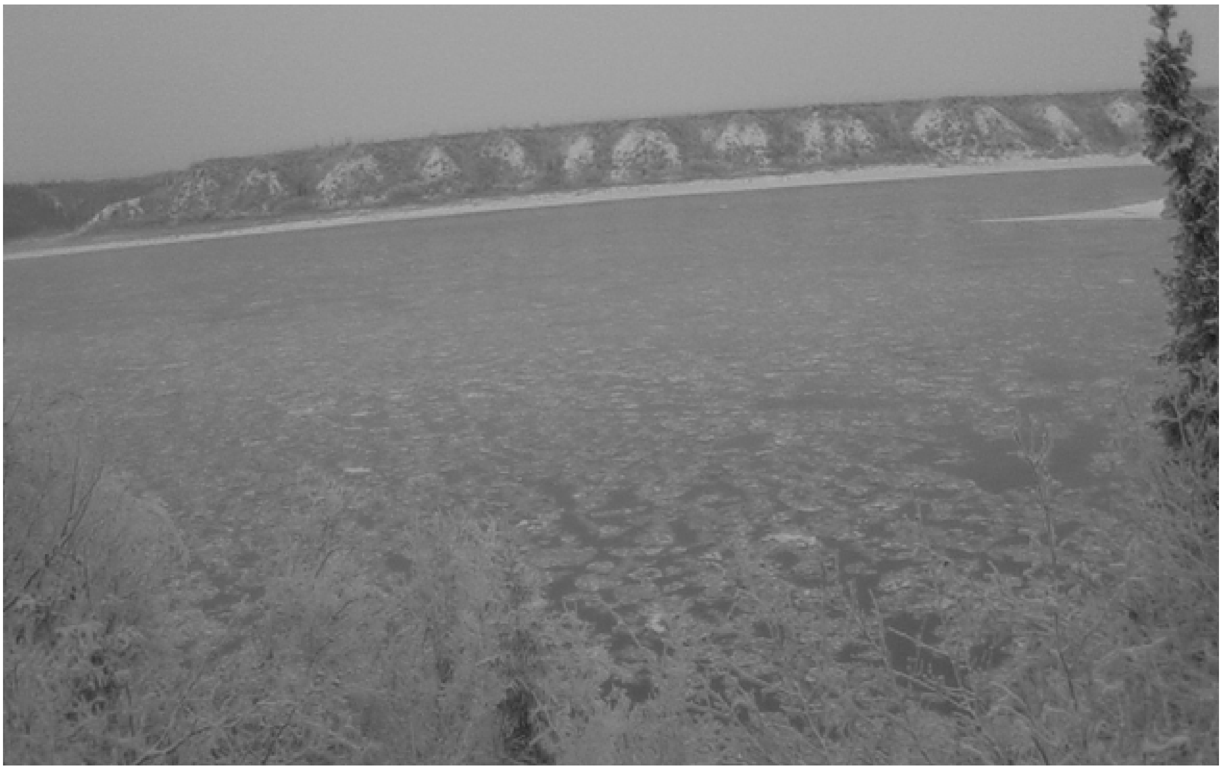

Figure 2.3: Frazil ice formation at Lower Nelson River, Northern Manitoba, December 2012, Temp.: -14 C

Doering and Morris, 2003; Ye and Doering, 2003). There have been field and laboratory studies about the frazil ice determination techniques and characteristics by ,Ke et al. (2000), Morse and Richard (2009),Ghobrial et al. (2012); Drucker et al. (2003),McFarlane et al. (1992). The super cooling process and frazil ice evolution has also been numerically modeled during the past years (Daly, 1984; Wang and Doering, 2005; Shen, 2010) .

Frazil ice effects on many engineering and environmental aspects have also been studied, including Brown et al. (2000) and White and Laible (2002) on fish habitat and river fauna, (Smedsrud, 1998; Sui et al., 2000) on sediment transport and morphology, (Asvall, 1998; Sui et al., 2008; Huokuna et al., 2009) on flooding events, (Morse and Quach, 2002; Gebre et al., 2013) on hydroelectric efficiency problems and water plumes and (Ettema et al., 2002; Morse et al., 2003; Smedsrud and Jenkins, 2004) on municipal water ways and intakes design.

2.2.2 Anchor Ice

The term "Anchor ice" or "Bottom ice" (Wigle, 1970) refers to ice protrusions in the form of delicate conglomerations of leaf like ice crystals (Mager et al., 2013) from the bottom of river or lake to the water body. Anchor ice grows by nucleation of ice crystals on bed materials (Michel and Ramseier, 1971), around submerged (Tsang, 1982) and moored objects or by accumulation of frazil ice particles (Carstens, 1966) mixed through the whole water body by sufficiently intense turbulence (Ashton, 1986) on river bed features. Anchor ice condition varies based on the formation and growth process (Piotrovich, 1956; Osterkamp and Gosink, 1983; Qu and Doering, 2007). Several possible scenarios for anchor ice formation and growth were explained by (Kerr et al., 1997) using comprehensive graphs and diagrams. Anchor ice formation and growth and its effect on hydraulic characteristics of the flow has been studied in laboratory (Doering et al., 2001; Kerr et al., 2002; Qu and Doering, 2007) or through field observations (Arden and Wigle, 1972; Parkinson et al., 1987; Marcotte and Robert, 1986; Yamazaki et al., 1996; Hirayama et al., 1997; Girling and Groeneveld, 1999; Malenchak et al., 2006; Stickler and Alfredsen, 2009; Jasek et al., 2010). Problems associated with anchor ice formation in hydro-electric facilities are addressed in some studies like Doering et al. (1999) and Gebre et al. (2013) .

2.2.3 Composite hydraulic resistance in ice covered rivers

Ice cover development forms an additional boundary layer on top of the river, and thereby affects water velocity magnitude and distribution, water stage and conveyance capacity. The influence of the ice cover changes in time as a function of the ice condition and time elapsed since cover stabilization. The presence of an ice cover can reduce conveyance capacity, which can cause serious problems such as reduction in water supply for hydroelectricity, rural and urban demands and finally imprecision in hydraulic measurements necessary to allocate water resources.

Amongst the important factors that determine a channels conveyance capacity, i.e., those are addressed in the Manning formula, hydraulic resistance to the flow in the form of Manning roughness (n) of a covered section is a factor that varies directly according to the condition of the ice cover . Ice cover presence also increases the hydraulic resistance to flow in streams in other ways such as decreasing hydraulic radius and cross sectional area, particularly when the underside of the cover includes large ice protrusions. Severe cover conditions have been observed to reduce the river discharge by up to 29% (Ohashi and Hamada, 1970; Pratte, 1979; Ashton, 1986). There has been continuous study on this subject since the early 1930's and several methods have been developed to estimate composite roughness in ice covered rivers. The credit for the first attempt to calculate the composite roughness belongs to Pavolovsky (1931) who tried to calculate composite roughness coefficient, n_c, as a balance between gravity force and boundary (bed and ice cover) shear forces along the channel (Nezhikhovskiy, 1964; Secil Uzuner, 1975).

Since then, several theories have been developed to estimate the composite roughness in ice covered rivers, most of which have employed assumptions for hydraulic radii, mean velocity magnitudes, and/or energy grade line slopes. Comprehensive reviews of available early methods and their main assumptions were provided by Secil Uzuner (1975) and Pratte (1979). Some of the earliest attempts made hydraulic radius assumptions. Pavolovsky (1931) assumed equal hydraulic radius for the bed and ice subsections as well as the total cross section. Lotter (1933) assumed constant hydraulic radius for the ice zone, i.e. R_i=const., and used Chezy's coefficient to develop an equation for composite roughness calculation (Lotter (1933) cited in Secil Uzuner (1975)). Later, Chow (1959) used Pavolovsky's method, but assumed total hydraulic radius as R_c=R_i+R_b (Chow (1959) cited in Secil Uzuner (1975)), where R_i , R_b, and R_c are the ice, bed and total composite hydraulic radii. More recently, researchers have assumed the hydraulic radii of the ice and bed zones equal to the subsection depth and hydraulic radius of the total cross section equals to half of the total depth (Larsen, 1969; Beltaos, 2011; Beltaos et al., 2012). If y_i=y_b then this method yields equal hydraulic radii for both subsections and the total cross section (Larsen, 1969). Another important series of assumptions are taken about the mean velocity magnitudes for subsections and the total cross section. Belkon (1938) assumed equal mean velocity for the subsections and the total cross section, i.e. v_c=v_i=v_b (Nezhikhovskiy, 1964; Secil Uzuner, 1975). Carey (1966), used the same assumption for his composite roughness calculation (Secil Uzuner, 1975). Another important assumption taken for composite roughness calculation is equal energy grade line for ice, bed and total cross section. This can be considered as the most common assumption, which has been taken or implicitly applied for composite roughness estimation since the late 1960s.

2.2.4 Break-up

Ice break-up is not necessarily a sudden event in rivers. Gradual rising in air and water temperature and water staging weaken the ice at its restraints. Released ice cover starts fragment and travel downstream in the form of ice runs. Weakening and fragmentation of the cover due to thermal decay and melting may occur in several locations along the reach. Spatiotemporal variation in break-up occurrence is a function of distribution of precipitation, snow melting due to higher solar radiation, ground water entrainment, river geomorphology and freshet water introduction at river subsidiary tributaries. Large scale climatic control and season of break-up are assessed in northern rivers and Canadian rivers in particular considering its geographical variations (Janowicz, 2010; Weyhenmeyer et al., 2011; Bieniek et al., 2011).

In one example case study, significant amount of water are being released during the break-up period at Mackenzie River. Up to 27% of the flow, which normally occurs during the open water condition, calculated to be stored into hydraulic and ice-growth storage in rivers during a 60 days period (Prowse and Carter, 2002) Water released from this storage during the spring snow melt accounted to be 15% - 19% of spring freshet volume.

Even though the break-up process can mainly be summarized into two distinct stages of initial lifting and final break-up (Donchenko, 1972; Parkinson, 1982), all river dynamical, kinematical and mechanical characteristics are involved in the start and progression of break-up (Ashton, 1986). Break-up can occur through intermittent processes including melting and decay, fragmentation, ice retreat and reconsolidation. Ice jams can occur in the last step of this sequence in rivers. The break-up finalizes with complete ice cover release. Dynamicity of river ice break-up has been studied by Jasek (1999, 2003), Khan et al. (2000) and Beltaos and Roswell (2001).

The sequence of events during the break-up period usually follows the process described by Donchenko (1972):

I. Water staging causes ice cover cracks along the shores of the river.

II. Fragmentation of the released cover into floating ice floes.

III. Conveyance of the broken cover and piling of ice pieces at stronger existing ice edges, or in open water at narrower sections, through the process called "showing".

IV. Ice cover's retreat toward downstream .

It is notable that the two last steps of the process are not restricted to the break-up period. During the freeze-up period, ice cover also thickens mechanically by the shoving process. Water level fluctuation can be considered as the main triggering factor of the mechanical break-up process. Many studies showed the importance of ratio of water surface fluctuation to ice thickness (Donchenko, 1972), break-up period surge passage (Billfalk, 1982) and the ratio of ice thickness to the stream width (Beltaos, 1983) in fragmentation and mechanical break-up of the cover. Fragmented ice particles are susceptible to higher attrition, particularly in smaller streams (Ashton, 1986) and melting (Parkinson, 1982). In one case, Calkins et al. (1982) calculated the volume of an ice jam to be only 10% of the volume of upstream fragmented ice cover. Kowalczyk and Hicks (2003) , studied dynamic water surges during the break-up period and provided a detailed documentation on peak speed and peak magnitude attenuation of these surges (Morse and Hicks, 2005). Severity of such a floods has also been studied with respect to the variation of air temperature by Prowse and Brown (2010) . Prowse and Culp (2003), Prowse and Brown (2010) and Engström et al. (2011) reported aspects of break-up on river ecology such as effects on biotic and abiotic factors, temperature gradient, riparian and aquatic vegetation communities found along the river and ice covered lotic systems which are less mobile and susceptible to damage.

2.2.5 River ice jams

The International Association of Hydro-environment Engineering and Research (IAHR) defined river ice jams as stationary accumulations of fragmented ice or frazil which block the flow in the stream . Several processes are involved in formation of ice jams in rivers including meteorological, hydraulic and geomorphic factors (Calkins et al., 1982; Tatinclaux and Gogus, 1983; Beltaos, 1995b, 2008b; Rădoane et al., 2010). According to the IAHR definition, ice jams can be classified according to the main processes and time of formation, and the location and condition of the cover. Regarding the nature of the ice jam, several factors dictate the severity of the phenomenon, including river hydraulics and morphology, physical characteristics of the jam and thermal condition of the jam's location. A review of river ice jam types and characteristics with respect to their main formation processes and season is presented in Tables 2.1and2.2 .

An important concpet in river ice jam studies is the definition of two type of jams known as "narrow" and "wide" ice jams (Pariset et al., 1966). The narrow ice jam formation is controlled by the river hydraulic condition as well as ice floes physical characteristics. ice cover internal forces are transferred to the river banks prior to any mechanical thickening. the narrow ice jams's propagation toward upstream is called "frontal progression"(Michel,

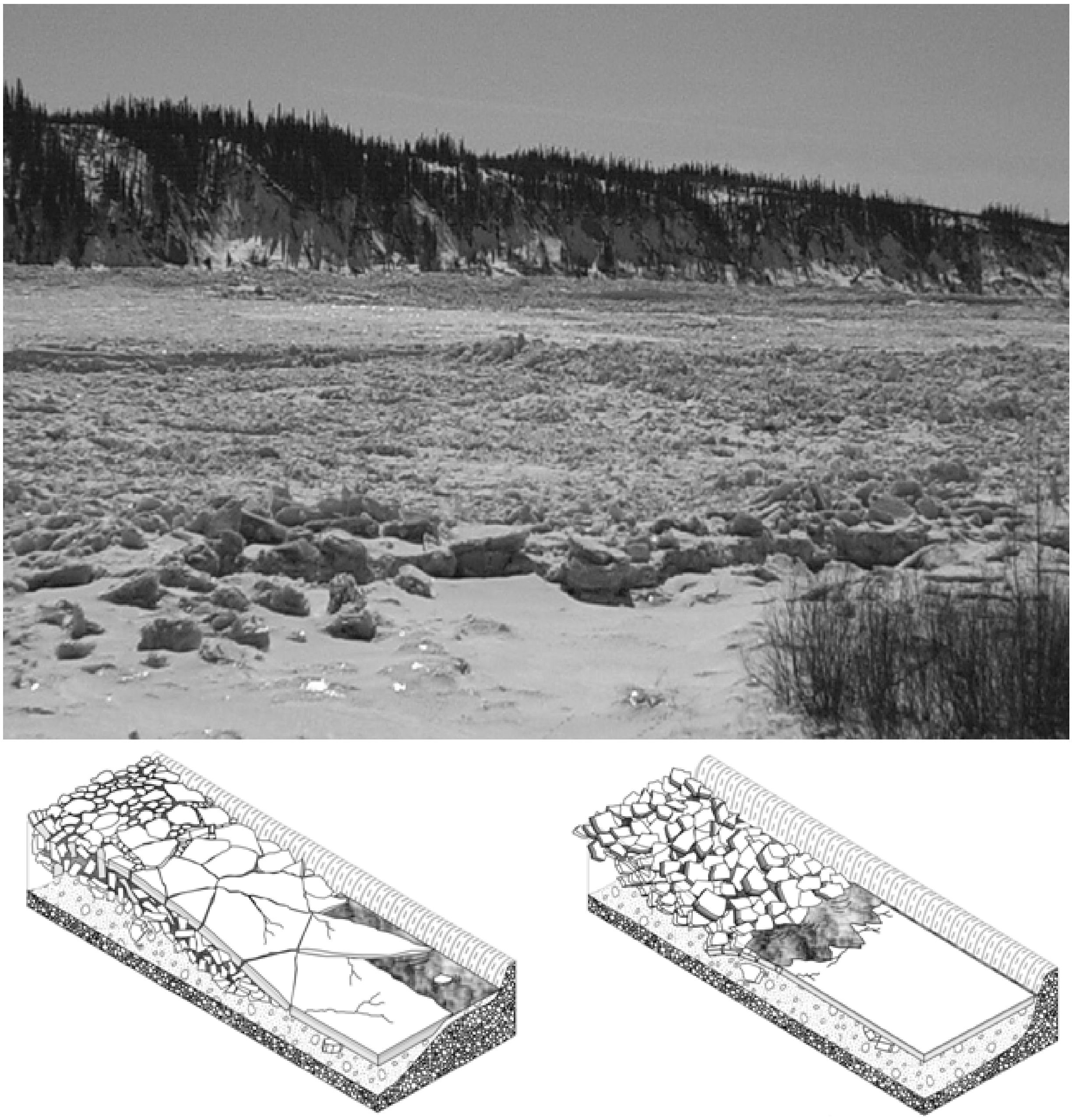

Figure 2.4: (Top) Ice cover break-up at Nelson River, Mid April, 2012, Temp.: 5.5 C. (Bottom) Two types of river break-up (Jasek, 2002): (left) sheet and (right) rubble.

1978). However, in wide ice jams, river geometry in terms of river width also contributes in the ice jam formation and thickness and wide jams generally develop through a dynamic sequence of progression/mechanical thickening(shoving) procedure Beltaos (1995a). According to the jam classes, it is reasonable to conclude that ice jams formed during break-up have greater flooding potential due to weaker internal structure, rougher under surface, and higher and rapidly increasing discharge during the break-up period (Davar et al., 1998; Beltaos and Burrell, 2010). The location and timing of a jam and its main formation process, more simply, "Where/When" and "How?" are the main questions in ice jam studies. Such studies can mainly be categorized as laboratory experiments (Zufelt and Ettema, 2000; Healy and Hicks, 2000; She et al., 2009; Beltaos and Carter, 2009; Beltaos et al., 2012) and numerical simulation (Beltaos, 1995a; Beltaos et al., 2003b; Lu et al., 1999; Beltaos and Burrell, 2003, 2010; Shen and Liu, 2003; Carson et al., 2003; Zufelt, 2005; Beltaos et al., 2012; Lindenschmidt et al., 2011, 2012; Beltaos and Tang). Several related aspects have been studied, including ice jam effects on water temperature (Beltaos and Burrell, 2006), flooding (Beltaos, 2000), release waves (She et al., 2009; Hutchison and Hicks, 2007) and climate change effect on ice jam formation, in an attempt to assess parameters that may affect the frequency and intensity of the ice jams (Beltaos and Roswell, 2001; Beltaos, 2002b, 2003; Beltaos and Burrell, 2006; Beltaos, 2012; Prowse et al., 2002; Goulding et al., 2009).

The formation mechanics of ice jams are sufficiently obscure that ice jam forecasting and simulation are extremely difficult. Hence, most of the simulation and prediction techniques and models are based on the empirical or semi-empirical methods. Consequently, guidelines for prediction of timing and location of jams are generally unavailable. Even though some general information about triggering and resisting factors (flow discharge and thermal budget; thickness and preceding freeze-up water level) and favorable geomorphological features (river bends, constrictions and shallows and areas of sudden slope and reducing velocity) are available, the forecasting procedure relies on experience and familiarity with local conditions (Beltaos, 1995a; Davar et al., 1998). This inability to predict timing and location of ice jams has social and economic consequences. For instance, dozens of homes were force to be evacuated on April, 2011 in north Winnipeg after a Red River ice jam shifted location. Due to the severe impacts of ice jams on safety and economy, several studies have been performed in order to understand the frequency of ice jam occurrence in rivers (Tuthill et al., 2003) and their main thermal or mechanical inducements (Guo, 2002; Beltaos et al., 2003a). The difficulty in predicting ice jam time and location aggravates our poor understanding of the phenomenon by reducing the chance for scientific documentation. Since forecasting ability is still limited, regardless of additional safety and logistic restrictions, it is almost impossible to be at the jam location prior to its occurrence to document it and record data (Morse and Hicks, 2005).

Beltaos (2001, 2008b) presented a study on hydraulic roughness estimation of ice jams within an equilibrium reach that connects shorter upstream and downstream transition reaches. Along this separating reach, almost uniform thickness of the jam and consequently uniform flow occurs (Uzuner and Kennedy, 1976).

River ice jam models can be categorized into equilibrium or non-equilibrium river ice jam models. Equilibrium models are based on the formation of equilibrium ice jam while the non-equilibrium models rely on longitudinal configuration of a steady-state, wide ice jams regardless of equilibrium condition of the jam. Amongst the available numerical models for river ice jam, the most well-known are as follows:

Equilibrium models:

I. ***ICEJAM*** by G. Flato and R.gerard (1986, 1988), University of Alberta.

Table 2.1: Different ice jams types based on the main formation process, (IAHR, 1986; Belatos, 1995)

	Congestion and non-submergence	Submergence and transport	Submergence and deposition	Shoving/Collapse
Configuration	Single layer of ice floes and pans, initiated at constrictions or at transverse obstacles	Arriving ice floes or pans are under turned and transported by the flow under the cover. They start to deposit and accumulate at low velocity areas until the velocity increases to a "critical" velocity and start to erode the underside of the cover.	The same as the previous stage, but under turned ice floes start to deposited immediately downstream of the existing ice edge, accumulation layer is thicker than the individual ice floes.	A surface jam or narrow jam starts to collapse due to increase of the external exerted forces relative to jam strength (internal friction and cohesion), thickening progresses until makes the jam able to resist against applied forces
Hydraulic and channel condition	Low velocity, less than 0.5 to 0.7 m/s	High velocity at ice edge, more than 1 m/s. Low velocity at deposition area. Accumulation occurs typically at river sections with unusual depth where it fills the cavity and follows bed topography.	Moderate flow velocity, sufficient enough to submerged but not to transport the ice floes	Internal friction of ice jam is generated by vertical internal stresses caused by buoyancy. External forces are proportional to the river width. Wider ice jams, formed in wider streams are more likely to collapse.
Season of occurrence	Mostly freeze-up. Acts as an important factor in ice cover formation. They are rare during the break-up period	Freeze-up	Mostly freeze-up	Mostly break-up
Common term	Surface jam	Hanging dam	Narrow channel jam	Wide channel jam

Figure 2.5: Ice jam remnants at Lower Nelson River, up to 4 meters tall, August 2013, photo by author

II. ***RIVJAM*** by Beltaos and Wong (1986a, 1991), Beltaos (1993, 2003), National Water Research Institute.

Non-equilibrium models:

I. ***ICETHK*** by Tuthill et al., (1998) ,uses the HEC-2 backwater model (US Army Corps of Engineers).

II. ***JAMSIM*** by Judge et. al., (1997) which is a modified version of ICESIM model (3.2.1 Introduction to ICESIM).

Some other methods for ice jam prediction at river confluences (Ettema et al., 1999b; McDonald et al., 2002) and water stage simulation during ice jam (Grover et al., 1999) have also been developed and tested. All ice jam prediction methods were reviewed comprehensively by White (2003) until that time. New approaches and techniques have also been

Table 2.2: Seasons of ice jam formation and jam characteristics (Beltaos, 1995)

	Freeze-up	Break-up
Weather condition	Forms in low air temperature. May exhibit cohesion and even shear strength due to formation of solid ice layer on top	Forms with positive or slightly negative air temperature. Cohesion seems to be negligible relative to internal friction.
Flow condition	Forms with relatively steady flow and ice discharge	May form with intensely unsteady flow and ice discharge
Amenability to release	Unlikely to release. Usually freezes in place and may cause locally thick ice cover	Release eventually, unless cold weather resumes and freezes in place. Sudden release may cause release surges attended by violent ice runs.

applied in river ice jam studies like application of neural networks (Massie et al., 2002) or data modeling (Daly, 2002) and satellite imagery and remote sensing (Gauthier et al., 2001; Robichaud and Hicks, 2001; Jasek, 2003; Tracy and Daly, 2003; Weber et al., 2003).

Ice jam release is associated with a release of the water stored in the backwater region upstream of the jam which travels downstream in the of wave. The wave formed in the ice jam release process is usually called *"jave"* (Beltaos, 2007, 2008b). Ice runs created by the javes in rivers during the break-up period can be classified in "impeded" or "unimpeded" ice runs (Jasek, 2003). During the impeded ice runs, the ice movement is restricted by an obstacle downstream and hence significant amount of energy is dissipated through the friction between ice pieces or ice and river banks.However, in unimpeded ice runs, ice accumulation upstream of a ice free zone mobilize and with higher water velocities compared to the impeded ice run Turcotte et al. (2011).

2.3 River ice and morphological effects

River ice effects on geomorphology are mostly high-lighted during break-up when ice is able to cause drastic erosional and depositional features. As a key research in this field, Prowse and Culp (2003) studied the relation of river ice and geomorphology. Before them, Milburn and Prowse (2002) and Milburn and Krishnappan (2002) discussed cohesive sediment transport under ice cover and its effect on the transport rate . Hicks (1993) demonstrated the river ice effect as a principal element in an anastomosing river system . Sui et al. (2000) studied sediment dynamics in a frazil jammed reach.

Zabilansky et al. (2002) used Time Domain Reflectometry (TDR) technology to study the effect of ice cover on bed scour at three study sites: Missouri River in eastern Montana, Mississippi River and White River, Vermont. They found that the rate of erosion or deposition of bed material depends on the variation of inflow discharge at the time of ice cover formation. Hains and Zabilansky (2004) also studied the effects of river ice on scour and sediment transport at bridge piers. Finally, it is notable that Ettema is one of the most active researchers in this field. He stated:The extent to which alluvial channels respond to ice-cover formation, presence, and break-up is not well understood. Some responses are well known and observed...other responses are known in concept, but are not well documented. Some potential responses are barely recognized... (Ettema, 2002). Variation in sediment flux is one of the alluvial channel responses to river ice and is one of the most important aspects of river mechanics, determining channel morphology and reservoir sedimentation.

The sediment transport process consists of three main components: initiation of motion, transfer and deposition, all of which are determined by the local flow strength and sediment properties. Channel morphology dictates the spatial variation of flow strength and sediment properties, and thus potential scouring zones. As a simplified description, sediments are eroded from scour zones where flow is converging and are deposited in locations where flow is diverging. Ice cover presence complicates this process by adding an upper boundary to the river, which is often as rough as the lower boundary and temporarily changes the river sediment transport capacity compared to free surface streams. Consequently, sediment transport tends to decrease under a floating ice cover due to reduced bed shear (Sayre and Song, 1979; Ettema et al., 2000). Conversely, an ice cover and/or ice jam can locally constrict the flow and thereby causes local scour (Neill, 1976; Sui et al., 2006), which can locally increase sediment transport (Sui et al., 2000) . Furthermore, local flow concentration by river ice has been observed to cause direct geomorphic effects including thalweg shifting and cut-off of meander loops (Ettema and Zabilansky, 2004). During spring ice break-up, increased freshet flow combined with flow surges (Jasek, 2003) due to temporary ice damming results in increased bed shear and sediment transport, and break-up flows can be the dominant channel forming flow (Beltaos, 2007) . However, as mentioned, this critical process remains poorly studied largely because of difficulty and danger of accessing rivers during spring break-up condition. Heaving of ice on river banks can also scour the river bank (Smith, 1979; Doyle, 1988) which can both remove sediment from the bank and inhibit growth of woody vegetation and thereby decrease bank strength which ultimately result in a wider channel (Smith, 1979; Hey and Thorne, 1986) . It appears that only Prowse (1993) , Milburn and Prowse (2002) , and (Beltaos and Prowse, 2001) have reported sediment transport measurements during ice break-up. Notably, Prowse and Milburn described a field campaign on the Liard River, Northwest Territories, in which physical suspended sediment samples were collected from a helicopter during break-up. They observed a 30-fold increase in suspended sediment concentration during break-up.

2.4 Mathematical modeling of river ice processes

Research demands of river ice were first addressed comprehensively by American Society of Civil Engineers (ASCE) about forty years ago (ASCE 1974). Several aspects have been studied since then and the progress is still continuing. Mathematical modeling, due to its financial advantages in simulation and prediction of river behavior, has received high attention (Ashton, 1986; Wuebben, 1988b; Shen, 2010). Such models have been used for large river engineering projects. Mathematical modeling provides necessary information for all four stages of design (preliminary, pre-feasibility, feasibility, detailed design) before commencement of the site construction (Beltaos, 1995b).

Mathematical models can be categorized as component and comprehensive models. The component models theoretically or conceptually study total or part of the river ice processes (Shen, 2010). Comprehensive models, on the other hand, use developed modeling knowledge and understanding from component models to illustrate and simulate the overall river ice process (Shen, 2010).

Several approaches have been taken in numerical modeling of river ice process to simulate various aspects of river ice including solution of Reynolds-averaged Navier-Stokes equations (Yoon et al., 1996; Beltaos et al., 2012) , depth averaged continuity and momentum (Svensson et al., 1989) , Eulerian and Lagrangian finite element method (Lu et al., 1999; Shen, 2002, 2010) , equilibrium ice-jam theories (Lal and Shen, 1991) , probability distribution of vertical fluctuating velocity (Ye and Doering, 2003) , state-space model using Kalman filter (Daly, 2002), neural network application(Tao et al., 2008) , turbulence simulation(Wang and Doering, 2005) , solution of Ordinary Differential Equations derived from balance of internal and external forces on the cover (ODE)(Beltaos and Burrell, 2010) , implication of implicit finite-difference scheme for ice processes simulation using applied stresses on the cover (Lindenschmidt et al., 2012) , large-scale coupled hydrologic and hydraulic modeling (Biancamaria et al., 2009) , application of freezing- degree hours (Bisaillon and Bergeron, 2009) and thermodynamic modeling (Greene and Outcalt, 1985) . Beside the application of available river hydraulic and hydro-dynamic models like HEC-RAS to study the river ice processes (Daly and Vuyovich, 2003) , several specifically designed models have been introduced for river ice simulation. Amongst all mathematical and numerical models, the most common and well-developed models for river ice simulation are as follows:

I. **SIMGLACE** (Rousseau et.al, 1983; Petryk,1995, Beltaos, 1995)

The one-dimensional, steady state model SIMGLACE, was originally conceived in 1977. It has been applied for river ice studies at the diversion of the East Main River in to the La Grande River by James Bay Energy Corporation, ice regime in Peace River by British Columbia Hydro, and for simulation of ice condition in hydroelectric plants by Hyrdo-Quebec. Model input data are river bathymetry and hydraulic roughness, ice mechanical and physical characteristics, time series of upstream water temperature, meteorological condition and water discharge. The model uses four criteria of frontal progression (narrow jam formation), shoving (wide jam formation), border ice simulation and calculation of under ice erosion for cover simulation process.

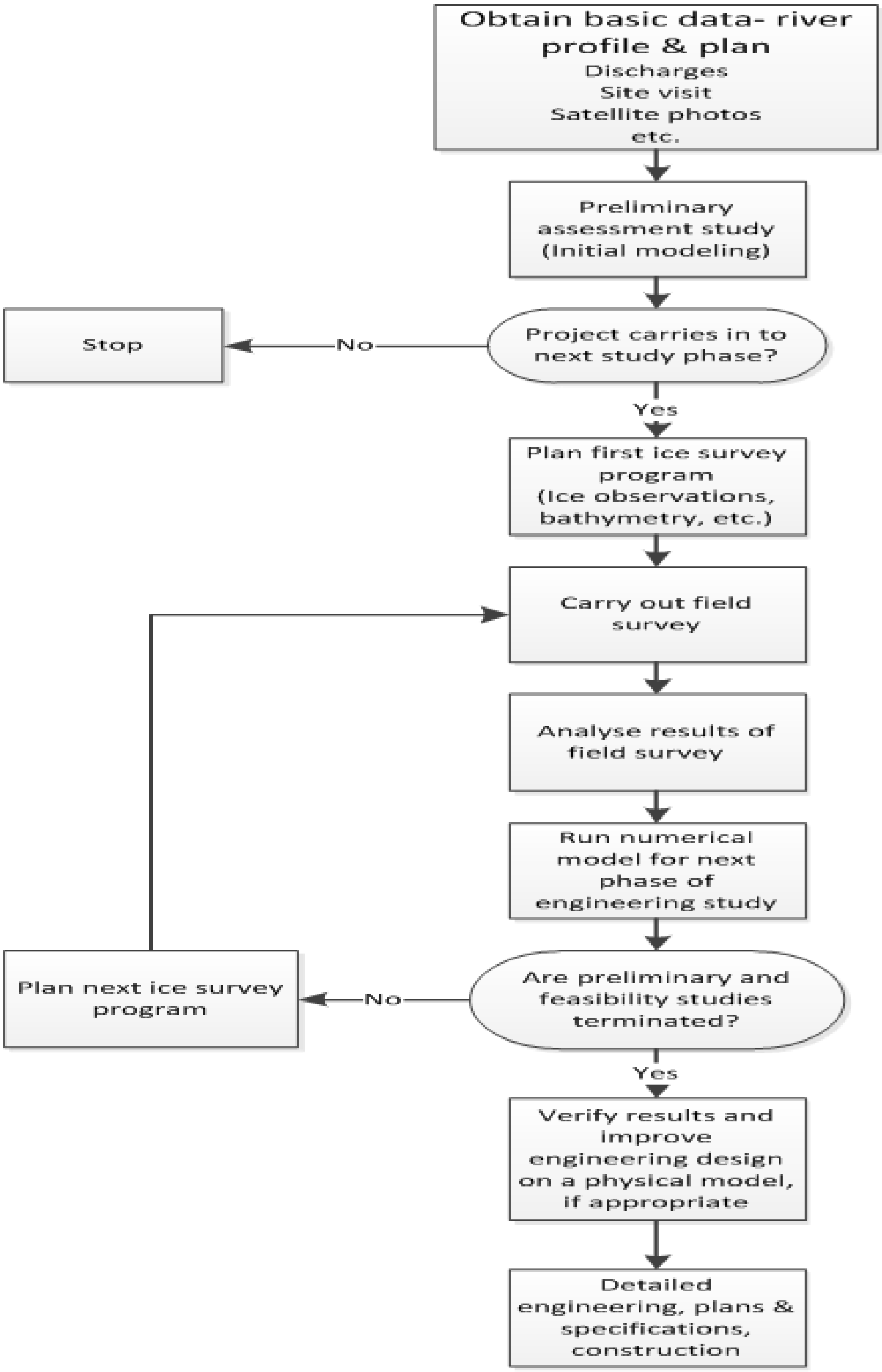

Figure 2.6: Numerical modeling in river development projects (after Beltaos, 1995)

Model outputs are mean velocity, water level, ice cover thickness, ice generation and transport, all as functions of time and distance from downstream. Reports by Rousseau et.al.,(1983) and Petryk et al. (1980) discussed detailed documentation and limitations of the model respectively. SIMGLACE calculates heat loss using heat sources or via the heat transfer coefficient. When water temperature drops to 0 C, frazil ice generation rate is calculated using the latent heat of fusion and porosity of frazil ice, i.e., 0.5-0.65 (Beltaos et al., 1981). Under ice erosion is calculated based on a limiting velocity according to the Meyer-Peter sediment transport equation (Pariset and Hauser, 1961).

Ice cover decay is estimated either by friction generated heat and heat transfer between water and air through the ice cover.

II. **LaSalle Hydraulics Laboratory Model** (Pariset and Hausser, 1961; LaSalle Hydraulics Laboratory, 1988; Beltaos, 1995)

This model was developed based on the Pariset and Hausser studies in the late fifties for the old Quebec Hydro Commission. Lasalle hydraulic laboratory developed the calculation process based on the accumulation of ice floes at river obstructions and forming the cover. The ice cover equilibrium assumption is applied in this model for ice cover formation and progression, which means the model assumes that sufficient supply of ice is generated to form the equilibrium ice cover. Ice thickness is calculated using the narrow and wide jam criteria, and water surface elevation is determined by simple back water calculations.

III. **ICEROUTE Model** (Beltaos, 1995)

ICEROUTE was developed by Crippen Acres Engineering for Manitoba Hydro in order to simulate the formation of hanging ice dams. Hanging ice dam formation causes water staging upstream of the dam, which results in variation in downstream flow discharge. The model routes the water level in the formed "reservoir" in order to determine the changes in flow, stage and storage during the winter period. Thus, the logic of the program can be illustrated in two parts: 1) Reach description and reservoir routing which divides the reach into segments, each represented as a reservoir, to calculate the storage behind it, and 2) Ice processes which calculate the ice generation and accumulation. Frazil ice generation is calculated using an empirical relation between heat loss and mean daily temperature. The ice cover initiates by formation of border ice and then followed by the ice cover progression (narrow jam) or by deposition of generated frazil ice under the existing cover (hanging dam). Hanging dam formation is controlled by a maximum deposition velocity criterion. The model is different from other methods in that it employs a steady-state assumption. Therefore it cannot be considered as generally valid, particularly in highly dynamic wave propagation situations since it uses simple flood routing techniques. However, moderate unsteadiness is expected to be reasonably simulated by the model.

IV. **RICE/RICEN Model** (Lal and Shen, 1991; Beltaos, 1995; Shen et. al., 1995; Shen, 2010)

RICE was developed as a one-dimensional river ice simulation model, capable of simulation of unsteady flow conditions for ice covered streams. Flow is calculated from the equations of momentum and continuity. The equations are solved by application of a four point implicit finite difference scheme. Model development started in early eighties at Clarkson University by Shen and his collaborators and has been under several developments since then. RICE includes several components for river ice process simulation mainly:

- Hydraulic computations
- Distribution of water temperature and frazil ice concentration
- Border ice and ice cover formation
- Ice floe accumulation and under cover transportation
- Ice cover thermal growth and decay
- Ice cover stability under the effect of hydrodynamic forces

The model calculates water temperature variation using a one dimensional conservation equation which includes net heat loss and neglects longitudinal dispersion. Frazil ice generation is calculated through the same equation when the temperature drops below zero(Matousek, 1984a,b) . Generated frazil ice rate is adjusted after considering additional sources and sinks representing ice volume deposited at or eroded from the existing cover for ice cover progression. An Eulerian-Lagrangian scheme is applied in RICE to solve the conservation equation. Ice discharge is calculated through two layers of surface and suspension and the model considers mass continuity and exchange between both layers. Deposition of the ice is simulated using a conservation equation that depends on the ice concentration in suspension. RICE has been improved during its application in several rivers like St. Lawrence, Ohio, Upper Niagara River and Lower Yellow River (Shen et al., 1991; Shen and Wang, 1993; Wang et al., 1996) . RICEN, a later version of RICE, was improved by a series of additions and modifications such as adjusting the undercover transport criterion (critical velocity to transport capacity), addition of an anchor ice simulation module, influence of wind, consideration of artificial ice breaking, and inclusion of super cooling condition in the water temperature formulation. The model later was improved to DYNARICE, a coupled Eulerian-Lagrangian model using a finite element scheme to simulate river hydrodynamics and a Lagrangian discrete -parcel method for ice dynamic calculation (Lu et al., 1999; Shen, 2002; Morse and Hicks, 2005). An extended two dimensional form of many of formulations in RICE/RICEN have been employed in the later commercial model CRISSP2D (Comprehensive River Ice Simulation System Program) (Liu et al., 2006; Bijeljanin, 2013; Malenchak et al., 2011).

V. **RHIVER Model** (Marcotte, 1984; Hausser et. al., 1985; Beltaos, 1995)

This model was developed by the Hydraulic department of Hydro-Quebec (1984) and revised and operated by LaSalle Hydraulic Laboratory (1985). RHIVER was the first model capable of simulation of anchor ice formation and identification of various types of ice that form on the water surface. The model does not follow any algorithm for river ice simulation but it is based on evaluation of thermal exchange during typical time steps. In general, water temperature drops below freezing point through the heat loss process and then the model calculates the frazil ice generation, anchor ice formation and re-adjustment of water temperature for latent heat release in subsequent.

VI. **Finnish River Ice Model- JJT** (Huokuna, 1990; Belatos, 1995)

The one dimensional, unsteady model JJT is capable of simulating ice cover process components including the water temperature and its longitudinal distribution, frazil ice generation, border ice formation, thermal growth, thickening and propagation and finally thermal decay of the cover during the break-up. Unsteady flow equations are solved and discharge and water stage at each cross section are calculated using a weighted four-point implicit scheme. Time and location of ice bridging and ice cover initiation is also considered in this model. A simple assumption is taken for this purpose, i.e., bridging occurs when the total amount of ice is sufficient to fill the width of the river at a particular cross section. Juxtaposition or under turning of the ice floes is controlled by the maximum possible Froude number. A submergence criterion is also applied for determination of surface or thickened jam formation, even though the stability of the jam is not checked in the model.

VII. **ICESIM/ICEDYN** (Simson and Carson, 1977; Petryk, 1995; Beltaos, 1995)

ICESIM was originally developed by Acres International Limited (now Hatch Ltd.) in the late 1960s and is a one dimensional, steady state program capable of simulation of various aspects of river ice processes in discrete time steps. Model outputs include river ice and river hydraulic characteristics along the river profile. A dynamic extension of the model, called ICEDYN has been developed which considers the dynamic variations of flow in regulated rivers during the winter period. ICESIM improvement is one of the objectives of this study and the model is elaborated in part 3.2.1

VIII. **RIVER 1D** (Andrishak and Hicks, 2008; She et. al., 2008)

River 1D was developed by the University of Alberta and is a hydraulic flood routing model. This model uses the characteristics-dissipative-Galerkin finite element method to solve the St.Venant equations in rectangular channels (Hicks, 1991; Hicks and Steffler, 1992). The current version of the model is capable of simulation of water temperature, frazil ice (suspended and surface), solid ice cover, ice front location and ice jam dynamic but not the anchor and border ice growth (Andrishak and Hicks, 2008). Internal resistance and a strain rate relationship of moving ice accumulation is calculated in the model using the one-seventh power law formulation(She et al., 2009).

IX. **RIVER 2D Ice Model** (Wojtowicz et. al., 2010;University of Alberta)

The University of Alberta developed River 2D, a depth averaged finite element hydrodynamic model, which models the river ice formation processes in a purely Eulerian frame (Wojtowicz et al., 2009). Ice thickness and ice roughness height at every node in the computational domain can be calculated for a known geometry. The model is still under validation and it is limited to open water and winter ice cover condition (Wojtowicz, 2010).

X. **MIKE-ICE** (Theriault et. al., 2010)

The model is an enhanced module of Danish Hydraulic Institute MIKE 11 and is an unsteady model to simulate river ice processes including water temperature simulation, frazil ice generation, juxtaposition, formation of hanging ice dam, border ice and static ice cover thickness estimation. The model is capable of simulating the ice regime in rivers and effects of water and temperature variations on ice condition and winter flow(Thériault et al., 2010).

All discussed models are developed to simulate river ice processes (progression-stabilization and break-up/Ice jams) and river hydraulics. Variation in river morphology, specifically during the dynamic stages of ice cover such as break-up, is tremendous and important and was subject to some more or less comprehensive studies (Ettema, 1999b; Ettema et al., 2000; Ettema, 2002; Ettema and Daly, 2004; Ettema and Kempema, 2012; Ghareh Aghaji Zare et al., 2013, 2014). However, dynamic interactions between the ice cover condition and sediment transport is missing amongst the available models. According to the abilities of the available models, sediment transport simulation would be a post-processing calculation using the modeled river hydraulic characteristics. Sediment transport simulation model should be used for this purpose which increases the processing cost/time due to restarting all calibration-validation processes.

The main focus of this research is to study the river ice cover on river hydraulics and consequently sediment transport under the ice cover. Following the field studies, a numerical river ice model (ICESIM) will be improved in order to add the sediment transport simulation capability under the ice cover. The model also will be ameliorate to include the all river ice cover stages (freeze-up-stabilization-break-up).

2.5 Hydraulic characteristics of ice covered rivers

2.5.1 Velocity distribution

Lu and Lueck (1999) applied the acoustic techniques to measure the velocity profiles in a tidal channel and discussed the principles of measurement in the application of broad band Acoustic Doppler Current Profiles. They also defined the data analysis and processing procedures in the application of such an instrument for velocity profiling in a turbulent environment. They emphasized the importance of the horizontal homogeneity to the derivation of the mean velocity vector in ADCP measurements and tested this assumption using two set of tests discussed in their research.

Healy et al. (2002) studied the unsteady velocity profiles under a floating cover using both Acoustic Doppler Velocimeter as well as Prandtl tubes (differential pressure tubes) and compared the performance of both techniques. After an appropriate digital filtering, they considered the measurements of Prandtl tubes as the representation of mean velocity variations of unsteady velocity profiles under the floating cover. Their observation also suggested that the behavior of unsteady velocity profiles is analogous to those under the open water condition. They also found that the technique called the *two-point method* for estimation of mean velocity is applicable for unsteady flow under the floating cover.

Kostaschuk et al. (2005) applied the ADCP for velocity and sediment transport measurements in rivers and addressed the advantageous and disadvantageous of the acoustic techniques for the task. They concluded that the main advantageous of the acoustic techniques to the other methods in velocity and suspended sediment studies are being non-intrusive, its capability to perform distanced measurements, and the consistency of the recordings in water depth which provides an understanding of the spatial variation of the measurements. They also pointed the ADCP disability for near boundary measurements as the most serious limitation of the technique for flow hydrometery.

Nystrom et al. (2007) assessed the ADCP capabilities for estimation of velocity profiles and Reynolds stress distribution using the both 3 beam and 4 beam ADCPs in an experimental flume. In the low turbulence areas, they assessed that the ADCP performance in the measurement of mean velocity profiles to be accurate away from the flume boundaries. However, in the high turbulence area, the associated errors with velocity measurements are assessed to be fairly large. Importantly, they found the measurements of the turbulence intensity based on four beam measurement of velocity to be more accurate and recommended the approach for shear velocity calculation. They also noted the flow inhomogeneity to be the biggest source of uncertainty in the estimation of Reynolds stress using ADCPs.

Sui et al. (2010) studied the velocity profiles and distribution under different ice cover conditions (smooth to rough) using direct laboratory measurement. They found that regardless of the boundary condition (smooth or rough) the relative velocity profile is almost similar but the location of the maximum velocity may vary from %60 of the depth from the bed to %70 of the depth from the ice for smooth and rough boundary conditions respectively.

Jasek et al. (2010) discussed the variation of velocity profiles in the ice cover period at Peace River, Alberta, Canada based on acoustic measurements. They also described their observations through the formation and release of the anchor ice at the study site. They also described some potential solutions for improvement of the ADCP measurements during the freeze-up period.

2.5.2 Turbulence and mixing

Lu and Lueck (1999) applied a broad band ADCP to study the flow in a tidal channel. Assuming a relation between the Reynolds stress and turbulent kinetic energy, they applied the variance technique to quantify turbulence characteristics in their study. The approach and formulation they provided necessitate the assumption of statistical homogeneity of the turbulent velocity fluctuation over the horizontal space covered by the of the ADCP . Since they used the beam velocity fluctuations, the ADCP should be rigidly mounted in order to avoid data contamination due to instrument motion. They also studied the statistical uncertainties in estimation of Reynolds stress and turbulent kinetic energy. Results of their analysis confirmed that the Doppler noise does not bring any bias to the Reynolds stress estimations if the opposing beams experience an identical Doppler noise.

Turbulence characteristics in tidal channels are studied by Lu and Lueck (1999). They used a broad band ADCP and a moored microstructure instrument (TAMI) to study the profiles of stress, turbulent kinetic energy (TKE), production and dissipation rate of TKE, eddy viscosity as well as mixing length in a tidal channel about 30 m depth. They used a combination of Reynolds stress and mean shear to estimate the TKE production rate. In their study, they confirmed the accuracy of Reynolds stress estimations through the broad band ADCP measurements. They also introduced an analysis to overcome the concerns about the underestimation of Reynolds stress due to the vertical averaging process in ADCP measurements. Their analysis showed that the spatial averaging reduces the estimated stress less than 5%. Results also demonstrated that the variation in Reynolds stress in depth in tidal channels corresponds to the vertical structure of the mean shear. The unsteady tidal variation is observed to be well represented in the streamwise component of the stress. However, the cross sectional component is only observed during the ebb when the high secondary circulation was taking place. Logarithmic velocity profile proved to exist during all the study period between 20% to 70% of the total depth. A higher rate of turbulent kinetic energy observed near the bed but events of higher production rate are also observed above the logarithmic layer. In general, it is found that the turbulent kinetic energy changes more with time rather than the depth.

Lu and Lueck (1999) found in their study that despite the good match between the mean velocity profiles to the logarithmic velocity distribution, the Reynolds stress is not constant through the log layer. The discrepancy in 2.5 fold is found in their analysis which is also consistent with findings of Johnson et al. (1994) which addressed the discrepancy factor of 3 between the bottom stresses obtained from log-layer fitting and that derived from dissipation estimate using collected data. Lu et al. (2000) speculated that the form drag causes the discrepancy between the near bottom Reynolds stress and bottom stress obtained from logarithmic velocity distribution fitting.

Sukhodolov et al. (1999) studied the turbulent structures in a straight reach of an ice covered, sand bed river using an Acoustic Doppler Velocimeter (ADV). They analyzed the statistical properties of three dimensional turbulent structures (bursting process i.e. ejection and sweep motions) based on the analysis of conditionally averaged velocity patterns. They concluded the non-uniformity of the spatial flow structure is due to non-uniform cross sectional ice cover presence. The spatial scale of the sweep motion is evaluated to be 0.7-0.8 times of the river depth while the scale for the ejection motion estimated to span over the whole water depth. They also addressed the low frequency variation of the streamwise velocity with the spatial scale of two to four times of the river depth.

Stacey et al. (1999) developed a technique based on the along beam variances of the velocity measurements for resolving the flow turbulent quantities. A broad band ADCP is deployed in an unstratified stream and the recorded velocity data are analyzed through their study. They compared the results of their analysis to the theory and concluded that the calculation of Reynolds stress in their study is unbiased by Doppler noise. However, they found that the estimation of turbulent kinetic energy is biased by an amount proportional to the Doppler noise. The analysis of mixing length scale based on Reynolds stress and mean shear both are found to be distributed parabolically in their study.

Tilston et al. (2009) developed a fully three-dimensional scheme for analysis of the coherent turbulent structures in river bends solving the Reynolds tensor and octant analysis. They investigated the motion orientation of the turbulent structure in their study. Results showed that the ejections and sweeps have more cross sectional orientation rather than the streamwise through the bend i.e. inner bank ejections and outer bank sweeps. They concluded that the orientation of turbulent structures in river bends is controlled by the vertical gradient of the cross-stream velocity component.

Robert and Tran (2012) performed a laboratory investigation to study the mean and turbulent flow fields in an ice covered gravel bed channel using Acoustic Doppler Velocimeter (ADV). They studied detailed profile measurements of Reynolds stresses and addressed the high negative Reynolds stresses indicating high turbulence levels in the vicinity of the ice cover. Results also showed the turbulent structures are considerably influenced by the ice cover presence and the roughness of the underside of the cover. Significant differences are revealed between the values of turbulent kinetic energy and Reynolds stress in open water and ice covered condition. Findings of the study showed that both values are greater in the near bed region when the flow is in covered mode.

McKay et al. (2013) applied the acoustic techniques to study the turbulence and mixing processes in a flooding coastal river during a minor flood prior to the establishment of tidally dominated flow. Study results showed that the river stayed well mixed through the flood and Reynolds stress and vertical eddy viscosity followed the classic pattern of open channel flows. Eddies length scale estimated to be on par with river bed.

Demers et al. (2013) studied the macroturbulent coherent structures in ice covered rivers using a downward looking pulse coherent ADCP. They applied the Anselin (1975) algorithm for detection of Local Indication of Spatial Associations (LISA) in order to analyze the coherent structures in the flow based on the identification of the presence of positive and negative autocorrelations in local flow phenomena. They have found in their study that the presence of the ice cover decreases the average length scale of macroturbulent coherent structures (MCS) from 2.5 and 1.8 of the flow depth to 0.4 of the depth for streamwise and vertical axes.

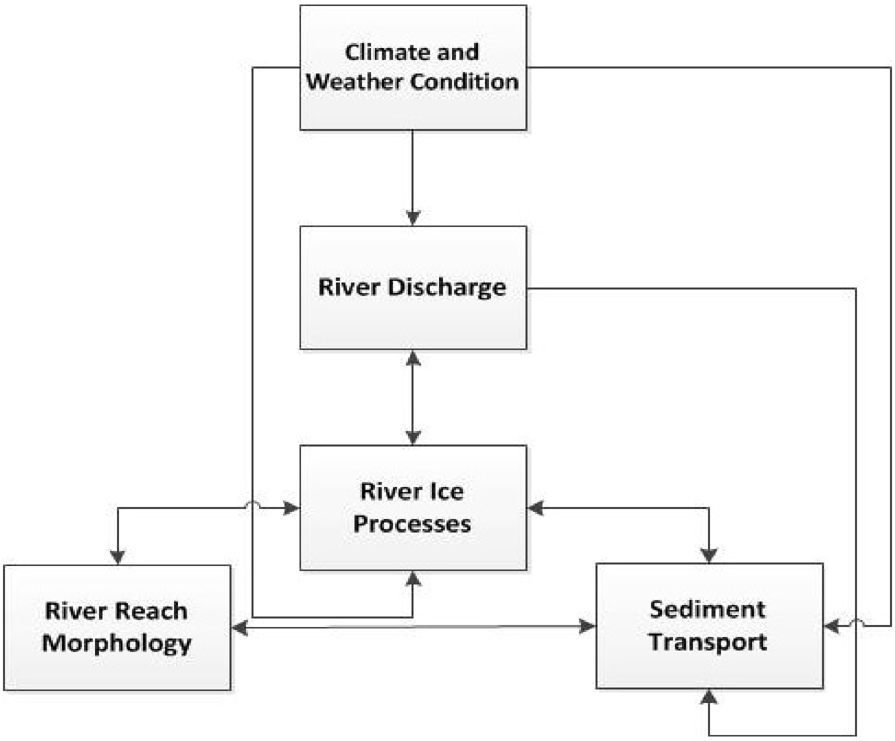

Figure 2.7: Interconnection between affecting parameters on river sedimentation (after Turcotte et al. (2011))

2.6 Sediment transport in ice covered rivers

River ice processes are well known to affect the river hydraulics and morphology. River ice effects on sediment transport consist of several aspects of riverine sedimentation processes including effects on potential sediment sources along the stream as well as the sediment transport capacity.

Rather than affecting the sediment availability and transport capacity, ice processes alter the river morphology physically through the processes such as eroding the stream banks, lifting and dragging of the river bed and bank material, and conveying the sediment particles trapped or stuck into the ice floes. Such a transport mechanism which usually is called rafting (Turcotte et al., 2011) introduces another specific form of sediment load different than the common bed and suspended sediment loads.

However, winter flow regime contributes to the stream sediment flux in many other ways causing the sediment particles to be initiated in to the stream and conveyed in a significantly lower threshold. Ice cover condition is known to control the intensity and scale of the sediment transport in ice covered rivers (Turcotte et al., 2011).

River ice processes and their interconnections with other processes controlling the stream sedimentation are represented as a global framework in figure 2.7.

2.6.1 Winter hydrodynamic and thermodynamic regimes and stream sedimentation

Cold temperatures in winter are associated with variation in river hydrodynamic and thermodynamic processes. These effects differ the flow regime in open and ice covered conditions significantly in several aspects most of which are capable of changing the sediment flux during the winter. Turcotte et al. (2011) presented an excellent review covering most of these effects in detail. A brief description of involving parameters is addressed as follows in this study.

Winter thermal effects on sedimentation

Cooling of water temperature changes the fluid properties and consequently the flow characteristics. In addition to the flow characteristics, sediment transport is partially related to the fluid properties as well, hence, variation in fluid properties, even though if it is small or local, can change the sediment initiation to the flow. Variation in water density in the range of normal (20°C) to freezing temperatures, is relatively small; however, kinematic viscosity experiences more drastic variations within this range. Reduction of water temperature is associated with the increase of kinematic viscosity and consequently the increase of the drag force on the bed material (Ettema et al., 2000; Ettema and Zabilansky, 2004; Ettema and Daly, 2004). The temporal scale of variation in kinematic viscosity is not clearly distinctive but spatially it is recognized to be applied all along the affected reach from upstream to downstream (Turcotte et al., 2011). Water cooling contributes to the formation of frazil ice particles through the processes described in sections 2.2.1. Frazil ice formation is reported to reduce the concentration of fine suspended particles in the water (Barnes (1928); Altberg (1936); Kempema et al. (1993). However, due to the nature of frazil ice formation (heterogenic nucleation), the rafted particles are still being transported but in on infinitesimal scale.

Effect of thermal cycle on stability of the stream banks

River banks are one of the most important sources of sediment availability in natural streams. The annual thermal cycle is found to affect this source in a fairly high degree by affecting the stability of the stream banks (Gatto, 1995).

In a general sense, thermal cycle influences the sediment supply to the stream by altering the river bank stability mainly through (Turcotte and Morse, 2011):

1. Affecting the soil internal stability and reducing the critical shear stress which leads to river bank failure.

2. Affecting the ground flow net form or into the river banks which changes the hydraulic gradient.

3. Contributing in to the exposure of bank materials to the environmental eroding elements such as the wind, flow and mechanical ice abrasion.

The climatic condition at the exposed area is another key factor in the thermal effects on bank stability. Whereas, in very cold, dry regions, winter freezing increases the bank stability by stabilizing the bank material and therefore, decreases the bank liability to the local erosive elements, in milder climates the thermal cycle of freeze-thaw occurs more frequently, destabilizing the river banks and makes them prone to failure or erosion (Gatto, 1995; Zabilansky et al., 2002; Turcotte et al., 2011). In conclusion, the annual thermal cycle increases the sediment supply to the flow in general. This process is more intensified prior to the break-up period.

Border Ice effect on sediment transport

Border ice forms at slow flowing areas mainly along the river banks. The border ice formation starts from the banks and the ice cover spans laterally through the river cross section as it grows. In relatively shallow areas, like near the stream banks, formation and thickening of the border ice bring the ice cover in contact with the considerable amount of bank and bed materials. Border ice formation locks the bed and bank material into the ice body, makes them potential to be carried if the border ice detaches from its location. Border ice effects on sediment dynamic can be summarized as (Turcotte and Morse, 2011):

- Increasing the bank and bed material stability during the winter when the border ice is grown and stable.
- Movement of bed and bank materials. Border ice movement and detachment from the banks due to the fluctuations in water surface elevation results in the bank and bed material scavenging through a process called Plucking (Wuebben, 1995; Ettema, 2008).
- Conveyance of the sediment material with a range from washload size (Turcotte et al., 2011) to pieces of the banks (Gatto, 1995) when the ice is detached.

Stable ice cover

Formation of the stable ice cover changes the river hydraulics and influences the sediment conveyance capacity. Water velocity is expected to be lower due to the addition of a new boundary on the top of the stream. The rough interface between the under ice surface and the water body causes an increase in the water level which is accompanied with a slower velocity. For a similarly rough top and bottom boundaries, up to 30% increase in water surface elevation is expected (Beltaos et al., 1993).

Slower velocity is associated with lower shear stresses on the bed and undersurface of the ice. Shear stress can be assumed to be distributed linearly from the maximum velocity location (lower than the water surface) to the boundaries (Larsen, 1973; Lau, 1982; Milburn and Prowse, 1998; Sayre and Song, 1979; Shen and Harden, 1978). Stable ice cover is also believed to decrease the vertical diffusivity and longitudinal dispersion (Beltaos et al., 1993, 1994). Therefore, diminishing effect of the stable ice cover on the sediment transport is interpreted in the literature. This is consistent with the findings of this study (as will be shown in section 5.4) excluding the break-up period (will be discussed later either in this section and section 5.1.4).

Stable ice cover is found to be effective on the channel bed forms. Due to the lower shear stress applied on the river boundaries, the bed load transport rate is expected to be reduced during the stable ice cover period. Yalin and Selim (1992) showed the independence of the ripple geometry from the flow depth but demonstrated that the dune wave length and height are dependent on the flow depth. Dune steepness is also found to be affected by flow intensity and relative particle size. Studies of Lau and Krishnappan (1985) and Smith and Ettema (1995) also confirmed Yalin's findings for the stable ice cover period.

Laboratory experiments showed the sediment transport rate tends to be lower during the stable ice cover period by 25% to 95% (Ettema et al., 1999a; Lau and Krishnappan, 1985; Sayre and Song, 1979; Smith and Ettema, 1995; Wuebben, 1986, 1988a). The wide range of reduction coefficient in literature, as Turcotte et al. (2011) explained, is related to the inconsistencies in the channel characteristics, tested hydraulic condition, sediment size distribution, nature and roughness of the model representing the ice cover and water temperature between the laboratory models.

The results of the current thesis (to be shown later) confirms that the ice cover stabilization reduces the sediment transport rate.

Analyzing the scales of the stable ice cover effects in both temporal and spatial viewpoints (Turcotte et al., 2011) reveals that the time scale of the stable ice cover effect rarely corresponds to the ice cover season. Instead, at least in mild rivers, frequent mid-winter break-ups potentially interrupt this scale. Spatial influence of the stable ice cover is restricted to the extent of the back water effect from upstream and ice cover edge at the downstream. Abovementioned upstream and downstream boundaries of the spatial effectiveness of stable ice cover may span over the entire reach in mild rivers whereas it is limited to the flat reaches in steep rivers (Turcotte et al., 2011).

Effect of anchor ice formation and release on sediment initiation and transport

Anchor ice forms due to the nature of frazil particles and their tendency to accumulate on the objects exposed to the flow stream. Though frazil ice is positively buoyant, it can be distributed through the water depth due to the flow turbulence, reaching very deep objects in the flow. The process of anchor ice formation is described in section 2.2.2 more in details.

Anchor ice effects on sediment transport can be analyzed from several aspects. First, anchor ice formation on the river bed covers the bed material from being in contact with the flow and therefore, initially can reduce the sediment initiation. This process concludes in decreasing the sediment transport rate (Kerr et al., 2002; Hirayama et al., 1997).

On the other hand, the formation of large scaled anchor ice can affect the flow hydraulics, makes the material more prone to be mobilized (Turcotte et al., 2011; Stickler et al., 2010; Stickler and Alfredsen, 2009). Furthermore, a sudden release of such obstacles causes the mid-winter ice cover breaking and flooding (Tesaker, 1996).

The main effect of anchor ice on sediment transport can be addressed during the release of the large pieces of the anchor ice. In such a condition, anchor ice can act as a mechanical factor for bed material mobilization i.e. initiation and transport (Reimnitz et al., 1990; Arden and Wigle, 1972; Chacho et al., 1986; Kempema et al., 1993; Osterkamp and Gosink, 1983). If the detached anchor ice becomes a part of the stable ice cover, materials locked in to the ice during the formation process may stay suspended for longer periods until the cover breaks up (Turcotte et al., 2011).

The concentration of sediment trapped in the ice texture can be significant. Applying the density balance evaluation Kempema et al. (1986) estimated a concentration up to 122 kg/m^3 of sediment in released anchor ice. Trapped sediment particles in anchor ice can vary in terms of size as well. Pebble concentration of 0.2 kg - 0.5 kg is observed and reported in frazil ice jam which can be associated with the anchor ice release from bed and its consequent merge into the jam (Sui et al., 2000). Bed materials with considerably large sizes are also reported to be carried by the released anchor ice, sometimes up to boulders as heavy as 30 kg (Prowse, 2001; Kempema and Ettema, 2011; Larsen and Billfalk, 1978; Martin, 1981).

Conclusively, the effect of anchor ice on sediment transport can be summarized as the effect on the mobilization of a range of material sizes and deposit them in various random locations according to the status of the released anchor ice pieces. Spatially, anchor ice effect is restricted to the steep river basins in general. Temporal scale of the effects mainly governed by the weather condition and can span from hours to several weeks (Turcotte et al., 2011).

Hanging ice dams and sediment transport

Hanging ice dams form usually in the confluence of steep and mild river beds. In such a location, higher water velocity prevents the incoming ice floes to be deposited at the leading edge. Instead, they under turn and start to accumulate under the existing cover at the cross sections with lower velocity . Hanging ice dam formation is well described in section 2.2. Hanging ice dam presence can alter the flow at the cross section where it forms and consequently changes the flow hydraulics. So, local effect on the bed formation and sediment transport rate is expected to be limited to the location of the hanging ice dam. Reduction in flow area up to 40% due to the hanging ice dam formation is reported in literature (Alford et al., 1987; Ashton, 1986; Beltaos et al., 1981; Sui et al., 2000, 2008).

Hanging ice dam can form over very long distances along the rivers. Michel and Drouin (1981) reported a hanging ice dam formation over 16 km of La Grande River containing 56 million m^3 of ice thickening to the river bed.

Due to the potential severity of the hanging ice dam, it can locally affect the bed forms or alternatively create scour holes on the river bed. Furthermore, repetitive aggradation

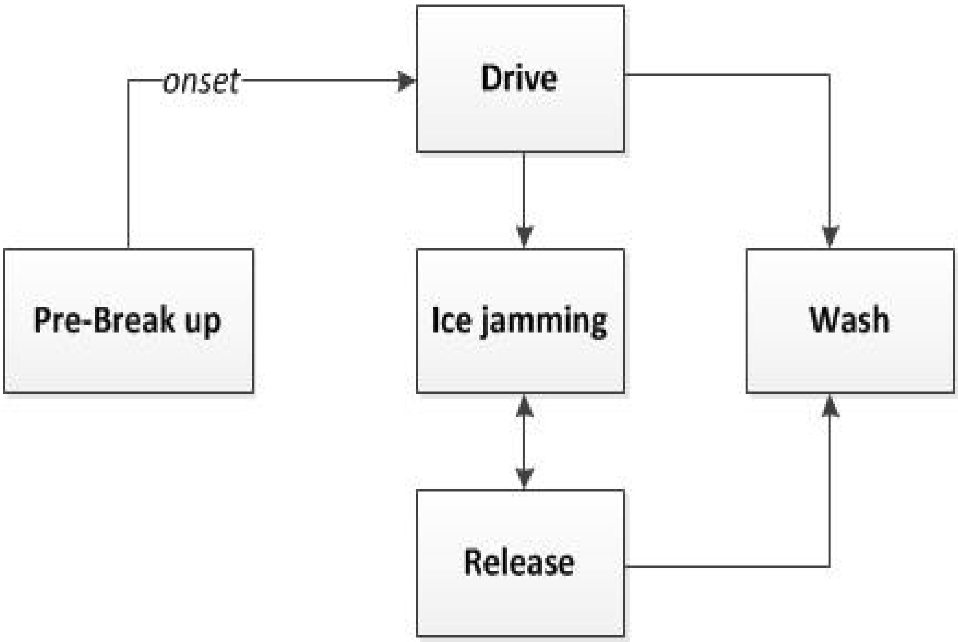

Figure 2.8: Schematic description of river ice break-up sequence in rivers, (after Desplanque and Bray (1986) and Beltaos (2008b)

and degradation of hanging ice dam material can affect the sediment in ice covered rivers (Sui et al., 2000).

It is notable that the clear effect of hanging ice dam formation on river bed formations is still yet to be clearly identified (G. Allard, 2009; Sui et al., 2008, 2010). However, in general sense, it is fairly precise to expect the local increase in sediment transport capacity under an aggrading hanging ice dam.

Sediment transport during the river ice break-up

Ice cover break-up occurs in rivers through several distinctively different stages each of them consisting of their own specific ice and hydraulic condition. Thus, the effect of each step on river sedimentation is potentially different from the rest. River ice break-up period and its all sub-periods are well described and discussed by Beltaos (2008a) and are represented in Figure 2.8 .

As described in section 2.2.4, break-up starts with an increase in air temperature. So, thermal processes are amongst the first to get involve and trigger the break-up process. Increase in air temperature accompanied by the introduction of warmer freshet water to the river system, thins and deteriorates the ice cover through a process called decay (Turcotte et al., 2011; Beltaos, 2008a; Prowse and Demuth, 1993). This initial phase of break-up usually is called pre-break-up. Though the effect of pre-break-up period on sediment transport evaluated to be limited (Turcotte et al., 2011), it can be summarized as: first, melting of the existing ice cover (sometime extensively up to 65 mm/day to 80 mm/day (Calkins, 1984; Prowse and Marsh, 1989) which causes the release of the ice

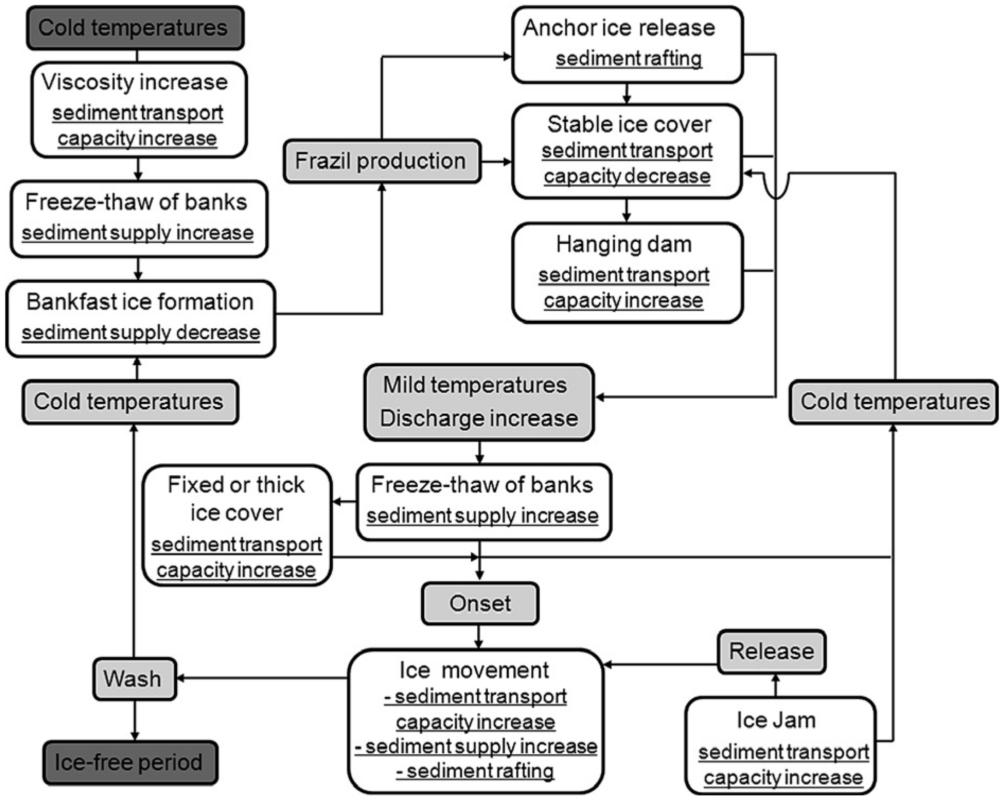

Figure 2.9: River ice processes and their effect on sediment transport rate (Turcotte et al., 2011)

trapped sediment into the stream (Turcotte et al., 2011). Second, variation in ice cover roughness during this period which is concluded to be the result of formation of randomly patterned, ice ripples under the cover (G.D. Ashton, 1972; Michel, 1971; Sayre and Song, 1979; Beltaos, 2008b; Turcotte and Morse, 2011). This process causes the maximum water velocity location to occur deeper and results in turbulence in the upper part of the flow depth (near to the ice cover) to increase. This conclusion is consistent with the findings of this study as well (will be shown later). Higher resistance to the flow during this stage, reduces the water velocity but meanwhile increases the turbulence in the water and presumably (still needed to be quantified) increases the river conveyance capacity for suspended sediments (results will be discussed in section 5.4). Other researchers such as Turcotte and Morse (2011) and Beltaos (2016) also reported such an observation in suspended sediment concentration.

The increase in discharge due to the reasons discussed above increases the hydraulic force on the ice cover. Eventually, if the force balance on the cover exceeds the cover resistance, ice cover starts to mobilize. This happens when the break-up *onset phase* starts (Beltaos, 1984). Ice cover starts to move in pieces, creating a dynamic stage of break-up also known as the *drive phase* (Turcotte et al., 2011).

The ice cover detachment from the river banks and its movement towards downstream during the thermal break-up process introduces a new source of sediment to the stream. First, floating ice cover which is in contact with the river banks and bed in the shallow parts, abrades the boundaries mechanically. This is even more severe in narrower cross sections. On the other hand, through the melting of the cover, as discussed before, potential sediment load in the ice will be introduced (whether in the form of sediment draft or suspended load) into the flow, temporarily increasing the sediment transport rate in the reach.

The mechanical break-up is also found to increase the sediment transport (Milburn and Prowse, 1996) mainly due to the higher rate of ice motion which is derived from the higher water discharge and velocity. This phenomenon increases the border ice detachment and ice floe discharge. Higher hydrodynamic forces on the mobilized ice pieces act like a mechanical abrading agent on the river bed and banks and increase the sediment entrainment to the flow. Furthermore, higher water turbulence due to higher velocity increases the sediment initiation from destabilized boundary material. Higher suspended sediment concentration is observed in field investigations through the current study as well as previous researches, confirms a peak in suspended material concentration. This material are interpreted to be originated from the re-mobilized winter deposits at upstream reaches (Milburn and Prowse, 1996, 2002; Turcotte et al., 2011; Ghareh Aghaji Zare et al., 2014).

Ice floes which are formed during the drive phase of the break-up may start to accumulate at narrower/shallower cross sections and form the ice jam. Ice jams previously are described in section 2.2.5.

The effect of Ice jam formation on sediment transport generally is described as effects on sediment erosion/deposition or even effects on the elevations (rising) of the river banks at zones affected by back water (Prowse and Culp, 2003; Ettema and Daly, 2004; Moore and Landrigan, 1999). On the other hand, backwater effect is potential to influence the river morphology, as will be discussed in section 2.3 , by increasing the erosion through the processes such as meander cut-off or river bank overtopping (Ettema and Daly, 2004).

Local scouring is expected to take place at the jam toe location where higher water velocities occur due to the reduction in cross section area (Mercer, 1968; Neill, 1976; Newbury, 1968; Newbury et al., 1984; Smith and Pearce, 2002; Tietze, 1961; USACE, 2005; Wuebben, 1988a).

Flow deflection in all directions (lateral and vertical) is reported due to the formation of ice jams in rivers (Wuebben, 1988a; USACE, 2005) which may cause the morphological variations such as thalweg shifting in ice jam affected reaches. Water diverted toward the river banks can potentially increase the bank erosion (Church, 1977; Hodel, 1986; Turcotte et al., 2011).

During the major river discharge losses, the floating ice jam may locally and temporarily come in to contact with the river bed. This process is called *grounding* (Beltaos and Wong, 1986; Beltaos, 1995a; Turcotte and Morse, 2011). Ice pieces which contact the bed are capable of mechanical abrading of bed material in significant quantities. On the other hand, during such a condition, the water passes the ice blockage through the several grooves formed in the ice jam. Higher water velocity in these grooves hydraulically improves the sediment transport rate by removing the river armor layer and exposing the underside materials to the flow.

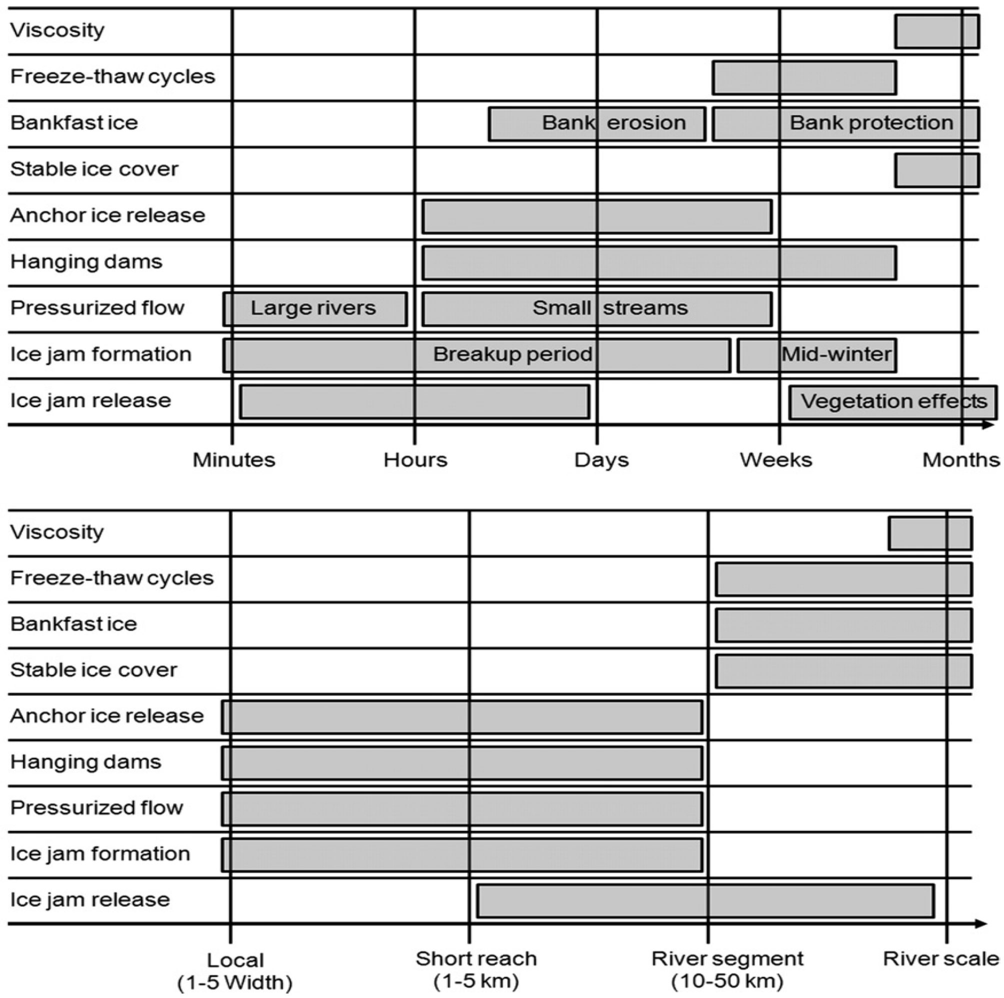

Figure 2.10: time scale (top) and space scale (bottom) of ice cover effects on sediment transport in ice affected rivers (Turcotte and Morse, 2011)

Ice jam effects on sediment transport are fairly limited in both temporal and spatial viewpoints. The effects are often temporally restricted to the time period required for the river cross section to be adopted to the new hydraulic condition through the boundary modifications. Ice jam effects spatially are defined to be effects on some limited cross sections (Turcotte and Morse, 2011).

Influence of ice jam release on river sedimentation can be generally described as a significant increase in bed and bank scour, specifically when the ice run includes large angular ice blocks (Beltaos, 2009; Collinson, 1971; T.J. Day, 1976; Mercer and Cooper, 1977; King and Martini, 1984; Prowse, 2001; Smith, 1979; Wuebben, 1988a; Ettema, 2008). Major ice runs are also found to increase the erosion of soft rocks(Bird, 1976; Danilov, 1972; Dionne et al., 1974).

On the other hand, higher water surface elevations, either during the jam induced backwater or the *jave* (jam release induced waves) passing period, may increase the bank instability and failure which introduces a major sediment source to the flow during the break-up period (Prowse and Culp, 2003; Code, 1973; Marusenko, 1956; Prowse, 2001).

High bank and bed abrasion are expected to take place during the impeded ice runs whereas the higher sediment transport rates potentially occur during the unimpeded ice runs (Turcotte et al., 2011).

The consequence of ice jam formation and release on sediment transport can be summarized as the increase in sediment transport due to ice rafting, increase in sediment supply due to mechanical abrading of the river bed and banks and finally increase in the total sediment conveyance capacity due to higher water velocities and turbulence (Turcotte et al., 2011).

Regarding the temporal and spatial scales of the ice jam influence on sediment transport, it is possible to relate both scales together. According to the nature of the ice jam release, the time scale may be restricted to some hours with spatial scale of single cross section of the river which is influenced by the ice jam, or for a sequence of ice jam formation and release, the time scale can extend for many weeks affecting the entire river reach (Turcotte et al., 2011).

The last remnants of the stages of the ice jam/ice runs are cleared during the *wash phase* which can be considered as the last stage of the break-up period. During the wash phase, the weakened bank and bed material, as well as jam deposited sediments, are washed and ice drafted suspended materials are released to the flow (Turcotte et al., 2011). In general, the effect of river ice on sediment transport decreases in time until it is completely removed (Beltaos, 1997).

In conclusion, the break-up period can be considered as the most dynamic stage of the river ice with the most drastic effects on the sediment transport. It can be the representation of the peak of annual sediment transport event specifically when it is associated with major ice jam formation and release (Ettema, 2002, 2008; Ettema and Daly, 2004). Up to 75% of the annual sediment flux may occur during the break-up in some northern rivers (Walker, 1970). Hence, it can be finalized that the sediment discharge relationships derived for open water condition, majorly underestimate the sediment load during the break-up period (Milburn and Prowse, 1996, 2002). Sediment initiation and transport parameters are at their highest during the break-up period causing a high rate of sediment supply and maintaining a high sediment conveyance capacity (Turcotte et al., 2011).

After all, it can be concluded that the effect of river ice on sediment transport is compound and complicated. In the ice affected rivers, the sediment transport processes are possible to commence in a considerably lower threshold of velocity and discharge through the rafting process. The freeze-up period also amy potentially increase the sediment transport by changing the fluid characteristics. Sequential freeze-thaw processes can affect the bank stability, increasing the chance of bank failure, providing a significant sediment availability source through the rest of the dynamic ice stages during the winter. River ice break-up period, as the most dynamic stage of ice cover processes, drastically increases the sediment transport capacity and rate during the winter. Mobilized ice blocks, prone to mechanically abrade the river bed and banks, increase the sediment transport by removing the bed armoring and exposing the bed material to the flow. This process leads to heavier bed materials movement. Ice jam formation generally reduces the water velocity and causes the sediment deposition to some degree. However, back water effect associated with the ice jam formation, destabilize the river boundaries upstream of the jam location. If the jam thickness increases or if the jam toe grounds, some mechanical effects are also expected to take place during the jamming process. The most important effect of break-up on sediment transport is during the ice jam removal which is accompanied by the fast flowing vertical surges moving downstream. Javes, increase the sediment transport and are responsible to the some of the most drastic alterations to the river sedimentation and morphology. In general, the effects of ice processes on sediment transport is evaluated to be significant. Therefore, more attention should be drawn to the winter period effects on sedimentation regimes in the northern rivers which are prone to be affected by severe ice processes through the winter period.

Chapter 3

Theory

3.1 Introduction to Acoustic techniques in river ice engineering and river hydraulic

Acoustic techniques are implemented in this research for river hydraulics and sediment transport studies. Autonomously recording acoustic instruments including a 1200 kHz RD Instruments Acoustic Doppler Current Profiler (ADCP) and 546 kHz ASL Shallow Water Ice Profiling Sonar (SWIPS) were deployed facing up from the river bottom in the thalweg just upstream of Jackfish Island, Lower Nelson River throughout several field campaigns since winter 2011. The main advantage of using acoustic methods in long-term velocity profile measurement for this case is that velocity sampling volumes are displaced from the instrument, thus are not disturbed by presence of the instrument. Furthermore, unlike traditional current meters, no moving parts are employed, which is important for long-term deployment under ice.

3.1.1 Acoustic techniques in Velocimetry

Acoustic instruments measure velocity based on the Doppler effect. Utilization of the Doppler effect in river velocity measurement is based on two main assumptions: **1.** There are suspended particles in the water that will backscatter the sound and **2.** These particles are traveling at the same speed as the water. Both of these assumptions are reasonable in natural streams and are particularly true in the homogenous suspension layer in rivers. The homogenous layer covers almost 90% of the water depth; the lower 10% is represented by the bed load layer. According to the deployment mount dimensions and ADCP blank distance (refer to 4.1.2), acoustic measurements of this study profile mainly the suspension layer where both mentioned assumptions are valid.

The *Doppler effect* is the variation of observed sound pitch caused by the relative motion of the sound source. A common example is variation in the pitch of a passing ambulance siren; it has higher pitch as it approaches and lower pitch when it recedes. The same logic is valid for an immobile sound source but moving object. Consequently, perceived sound by the object is different from the emitted sound, being higher pitch if the object moves toward the source and lower if it moves away.

Change in sound frequency due to Doppler effect can be presented as:

$$F_d = f_r - f \tag{3.1}$$

where f_r is the received frequency and f is the emitted sound frequency. The Doppler effect and the relative velocity can be represented as:

$$F_d = \frac{fv}{c} \tag{3.2}$$

Where v is the relative velocity between the source and the moving object and c is the speed of sound which is almost 1500 m/s in fresh water at 20° C. Using this concept Acoustic Doppler Current Profilers calculate the spatial average of the three principal water velocity components (u, v, w) in uniformly divided segments called "bins". ADCPs have three or four beams (four beams in this study) each beam works in monostatic configuration independently; which means the same beam emits acoustic pulses and receives back scattered sound. Transducers are orthogonal to each other (90° for four beam ADCPS) around a circle and angled from the vertical axis from 15° to 30° depending on the ADCP (C. D. Rennie, UOttawa River Hydraulic lectures). Doppler shift for backscattered sound is doubled since it occurs twice; once when the sound travels to the moving object and the other when it comes back to the source, thus Doppler shift would be $\frac{2fvnu}{c}$.

Doppler shift occurs only when the source and the object are in radial motion. Angular motion which changes the direction not the distance between source and the object does not cause any Doppler shift. Therefore, the ADCP measures the velocity component parallel

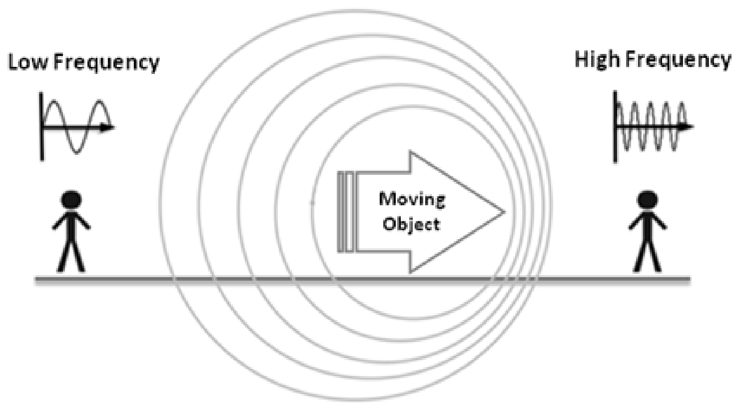

Figure 3.1: Doppler shift in moving object sound

to the acoustic beam. Limiting the Doppler shift to the radial component, 3.2 can be written as:

$$F_d = \frac{2f\ v\ cos\alpha}{c} \tag{3.3}$$

Where α is the angle between the relative velocity vector and the axis of the transducer (Instruments, 1996) .

3.1.2 The principle of operation of BroadBand ADCP -RD Instruments

ADCPs used in this study are categorized as BroadBand ADCPs (previously patented by RD Instruments). In this approach, Doppler processing is accomplished by simultaneously receiving echoes from two or more pulses (Brumley et al., 1991). Briefly, the BroadBand system emits complex pulses that include individual pulse pairs and measures the velocity using changes of backscattered signal in time (time dilation) rather than the frequency. Depending on the radial motion of the object (here the scatterer particle), change in travel time occurs which is called propagation delay. The BroadBand ADCPs use time lag in pulses (propagation delay) within the complex pulse to determine the phase. Long propagation delay makes it impossible to distinguish phases of n and n+360 degrees and phase ambiguity occurs. The phase ambiguity can be avoided by keeping the lag between consecutive pulses small but lower accuracy is associated with this approach. In fact, more precise measurements are obtained with long time lags. In order to overcome the phase ambiguity problem, the phase shift or propagation delay is extracted by computing the autocorrelation between coded individual pulse pairs within the complex pulse. The validity of this approach is dependant upon the assumption of correlation between different echoes from the coded pulse(Instruments, 1996).

3.1.3 Calculation of the three components of the velocity

Since only one velocity is possible to calculate from each beam, beam velocities need to be combined using trigonometry to determine three components of velocity in Cartesian coordinates *(x, y, z)*. Therefore, a minimum of three beams is required to yield three velocity components. On the other hand, due to the beam angle from the vertical axis, it is not possible for multiple beams to measure the same point in space for a given range bin, thus the conversion to Cartesian coordinates requires the assumption of homogenous velocity field in the horizontal direction. ADCPs with four beams calculate the vertical velocity twice using each pair of beams. This gives the ability of "error velocity" calculation. The error velocity value is an indication of violation of the horizontal homogeneity assumption of the velocity field.

Beam configuration for RD Instruments ADCPs is shown in Figure 3.2. This configuration of ADCP transducer is called *Janos* configuration, which is named after the roman

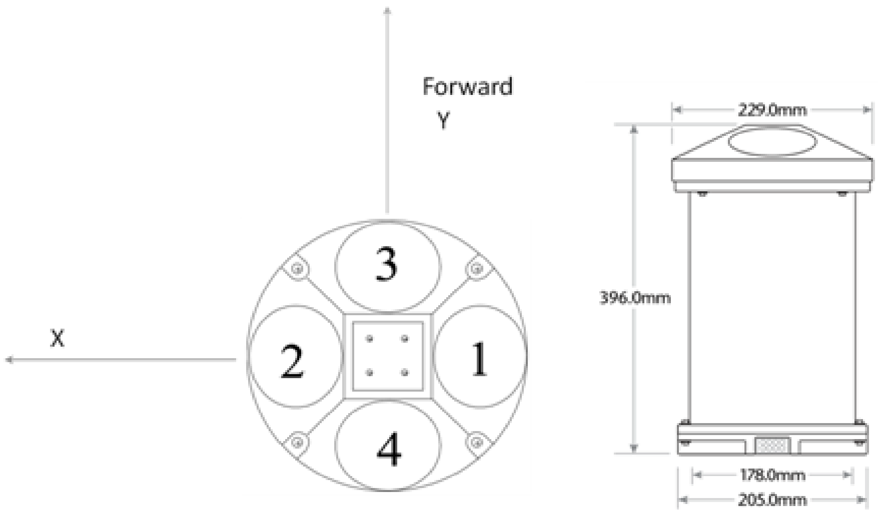

Figure 3.2: RDI ADCP beam configuration and dimensions (RD Instruments, 2011)

god who looks both forward and backward at the same time (Instruments, 1996). In this configuration, directions of beam three and two show the positive x and y directions. For upward looking ADCP mode, such as applied in this study, ADCP coordinate system follows the right hand rule for positive z direction. Assuming homogenous velocity field in all beams, forward (v_x), transverse (v_y) and vertical (v_z) velocities can be calculated as follows(Theriault, 1986) (Rennie, Uottawa lectures):

$$v_x = \frac{v_{b1} - v_{b2}}{2\sin(\theta)} \tag{3.4a}$$

$$v_y = \frac{v_{b4} - v_{b3}}{2\sin(\theta)} \tag{3.4b}$$

$$v_z = \frac{v_{b1} + v_{b2} + v_{b3} + v_{b4}}{4\cos(\theta)} \tag{3.4c}$$

$$v_e = \frac{v_{b1} + v_{b2} - v_{b3} - v_{b4}}{2\sqrt{2}\sin(\theta)} \tag{3.4d}$$

So, velocity for each beam can be calculated as:

$$v_{b1} = v_z sin\theta + v_z cos\theta + v_e \frac{\sqrt{2}}{2} sin\theta \tag{3.5a}$$

$$v_{b2} = v_x sin\theta - v_x sin\theta + v_e \frac{\sqrt{2}}{2} sin\theta \tag{3.5b}$$

$$v_{b3} = -v_y sin\theta + v_z cos\theta - v_e \frac{\sqrt{2}}{2} sin\theta \tag{3.5c}$$

$$v_{b4} = v_y sin\theta + v_z cos\theta - v_e \frac{\sqrt{2}}{2} sin\theta \tag{3.5d}$$

Where v_{ni} values are Cartesian velocity components at each beam and θ is the beam vertical deflection angle.

As seen in Equations 3.4a to 3.5d, an advantage of four beam systems is their better performance in condition of violation of homogenous velocity field assumption. Specifically, the horizontal velocity component is contaminated by only vertical velocity components, which are usually small, if the assumption of homogeneity became violated. Even though beam deflection is necessary to measure the horizontal velocity, the lower beam deflection angles, the more accurate are the measurements in the condition of violation of homogenous field assumption since the beams do not spread as far apart.

Received sound backscatter is being sampled in order to measure the velocity in discreet acoustic volumes (bins) along the beam axis. This process is called "range gating" in which backscatter sound is divided in to increments of equal duration , typically equal to the length emitted pulse. Each increment corresponds to a backscatter from a specific location along the beam axis. The distance of each of these locations i.e. bins can be calculated based on the speed of sound. Duration of receive window, determines the size of each bin but it is typically set equal to the duration of acoustic pulse. (C.D. Rennie, UOttawa lectures).

3.1.4 Signal strength analysis

Sound propagation

Sound propagates in the form of density oscillations including a sequence of crests and troughs at constant speed (c) in a homogenous medium. The number of passing crests at an observation point per unit time is called *frequency(f)* of the wave which is in Hertz (Hz). The *period* ($\mathcal{T}$) of the wave is the time between two adjacent crests and can be shown as: f^{-1} .The *wave length* (λ) is the length the wave travels in $\mathcal{T}$. So, sound speed can be represented as .c=$\lambda/\mathcal{T} = f\lambda$ Position of the passing wave can be represented within a wave cycle by an angle between 0 and 2π and is called *phase*. Another form of frequency can be addressed by absorbing the 2π into the frequency equation which results in to definition of *angular frequency* in form of .$\omega = 2\pi f = 2\pi/\mathcal{T}$(radians/sec.). *Spatial wave number* can be calculated as $k = 2\pi/\lambda$ which is in (radians/m).

In a homogenous medium, complex pressure (p) and particle velocity (u) at time t and distance r from a spherical source (having pressure p^*at distance r^*) an be presented as (Clay and Medwin, 1977):

$$p\,(r,t) = \frac{p^* r^*}{r}\, e^{i(\omega t - kr)} \tag{3.6}$$

$$u\left(r,t\right)=\frac{p^{*}r^{*}}{r\rho C}\left(1+\frac{1}{ikr}\right)e^{i(\omega t-kr)} \tag{3.7}$$

The average power passing through the unit area which is an average intensity of the wave can be calculated as:

$$I=\frac{p^{*2}r^{*2}}{r^{2}\rho C}=\frac{\left|p\right|^{2}}{\rho C} \tag{3.8}$$

Equation 3.8 shows the importance of the pressure amplitude in intensity of anacoustic wave.

Sound scattering

A portion of each emitted pulse is received back by the transducer and is used for Doppler shift effect calculation. The majority of the sound bounces on particles and scatters away from the transducer or is absorbed by the fluid medium. Sound scattering and attenuation depends on the physical characteristics of the scatterer particles and medium as well as the incident frequency. Due to the combination of involved parameters in this process, a non-dimensional wave number (n_w) is often used to express the sound scattering and attenuation. The non-dimensional wave number is described as a result of sound (represented by wave number, k) and particle characteristic (represented by particle radius, a) and can be illustrated as:

$$n_w = k\ .a \tag{3.9}$$

The value of $n_w$defines the regime of sound scattering and different physical processes involved in the scattering or attenuation of the emitted sound. Wave numbers higher than one represent the geometric regime while wave number values less than one indicate the Rayleigh regime. Suspended material at the study site is evaluated to be mainly clay and silt, with low amounts of very fine sand (Moore et al., 2014) . Thus, considering the ADCP's frequency, 1200 KHz, the non-dimensional wave number for suspended particles for the study site is calculated to be 0.005-0.05, which means acoustic studies performed in the Rayleigh frequency regime predominantly.

Backscattered pressure of a plane wave from a single homogenous particle of radius a, at distance r, at time t in water can be illustrated as (Sheng and Hay, 1988) :

$$p_s = \ p_i\ \frac{f_\infty a}{2r}\ e^{(\alpha_w r)}e^{i(kr-\omega t)} \tag{3.10}$$

Where p_i is the incident pressure amplitude, f_∞ is the far field form function, α_w is the signal attenuation by water. Far field form function illustrates the scattering characteristics of the particle.

Considering the measurements of this research were performed in a range less than the distance to the far field (far field distance is calculated as 25 m in this research), using equation 3.6 and considering transducer geometry, equation 3.10 can be modified for near field calculation as (Sheng and Hay, 1988):

$$p_i = \frac{p^* r^*}{\psi r} D_i e^{-\alpha_w r} \tag{3.11}$$

Where ψ is the near field correction function and D_i is the directivity pattern of the transducer. Refer to Clay and Medwin (1977) , Moore et al. (2013) for more derivation details.

Combination of equations 3.10 and 3.11 results in an equation for calculation of the amplitude of the pressure that is detected by the transducer as backscatter from a spherical particle (Moore et al., 2013):

$$p_d = \frac{p^* r^* f_\infty \ a}{2\psi r^2} D_i^{\ 2} \ e^{(-2\alpha_w r)} \tag{3.12}$$

Equation 3.12 accounts for transducer's directivity in the calculation of reception and attenuation of the backscattered sound.

For particles with a range of probability number size distribution (particles with more than one grain size) $n(a)$, the ensemble mean square pressure for scattering from a suspension of particles is the result of integration over the size distribution and parameter of interest :$\int_0^\infty n\,(a)\,da$ .The equation can be presented as (Sheng and Hay, 1988; Moore et al., 2013) :

$$P_s = \frac{3 \ M p^{*2} r^{*2}}{16\pi \rho_s} \frac{\int_0^\infty |f_\infty|^{\,2} a^2 n\,(a)\,da}{\int_0^\infty a^3 n\,(a)\,da} \int_V \frac{D_i^{\ 4}}{r^2} \ e^{(-4\alpha r)} dV \tag{3.13}$$

Where P_s is the ensemble mean square pressure for scattering from a large number of particles, M is the mass concentration of particles, $\alpha = \ \alpha_w + \alpha_s$ is the sum of the attenuation due to water body and suspended sediment and dV is the detected volume.

Multiple scattering effects, which occur at concentrations more than 1% by volume (Ma et. al., 1984), is not the case in this study since the maximum concentration encountered in the study site (0.55 kg/m^3, (Moore, 2012)) was significantly lower than the threshold value for multiple scattering (26.5 kg/m^3).

Sound attenuation

Sound attenuation is the description for the partial reduction in amplitude of the acoustic waves which is not due to geometrical spreading (Clay and Medwin, 1977). Signal amplitude decreases while it travels through the water (or any medium that sound spreads in) by acoustic energy transformation to heat due to viscosity of the medium.

Freshwater attenuation (m^{-1}) can be expressed as a function of the sound frequency and water temperature as (Fisher and Simmons, 1977):

$$\alpha_w = (55.9 - 2.37T + 4.77 \times 10^{-2}T^2 - 3.48 \times 10^{-4}T^3)10^{-15}f^2 \tag{3.14}$$

Where T is the water temperature in Celsius and f is the sound frequency in Hz.

Sound attenuation due to sediment suspension consists of two separate attenuations both linearly related to mass concentration of suspended sediment and thus should be averaged over the number size distribution (Moore, 2012):

$$\alpha_s = \alpha_{s,\ visc} + \alpha_{s,\ scat} = M\zeta_v + M\zeta_s \tag{3.15}$$

Where $\alpha_{s,\ visc}$ and $\alpha_{s,\ scat}$ are viscous and scattering attenuations averaged over the number size distribution and ζ_v and ζ_s are viscous and scattering attenuation constants. Refer to Thorne and Meral (2008) , and Moore et al. (2013) for more detailed information.

Considering the information presented above, suspended sediment concentration in a river can be estimated using the backscattered signal strength. Strength of backscattered signal is particularly important in distinguishing the medium phase change which can be interpreted as water-air or water-ice transition interfaces. Different sound propagation through each of these media causes variation in echo intensity level which is based on both range and reflectivity of the target. Since SWIPS does not employ Doppler processing to calculate velocities, optimized pulse processing based on backscatter intensity through the water column is the main logic to define the floating objects in the water. Thus, based on the amplitude of reflected sound received by the transducer, suspended and/or floating objects are detectable and distinguishable using the sonar equation.

Sonar equation

The amplitude of returned sound, , E_L can be calculated using the sonar equation as follows (Urick, 1948) :

$$E_L = S_L - 2 \times T_L + T_S \tag{3.16}$$

S_L is the strength of transmitted signal (source level), is T_S the target strength which means the reflectivity of scattering objects in water and T_L s the transmission loss. All terms are values relative to reference value in dB.

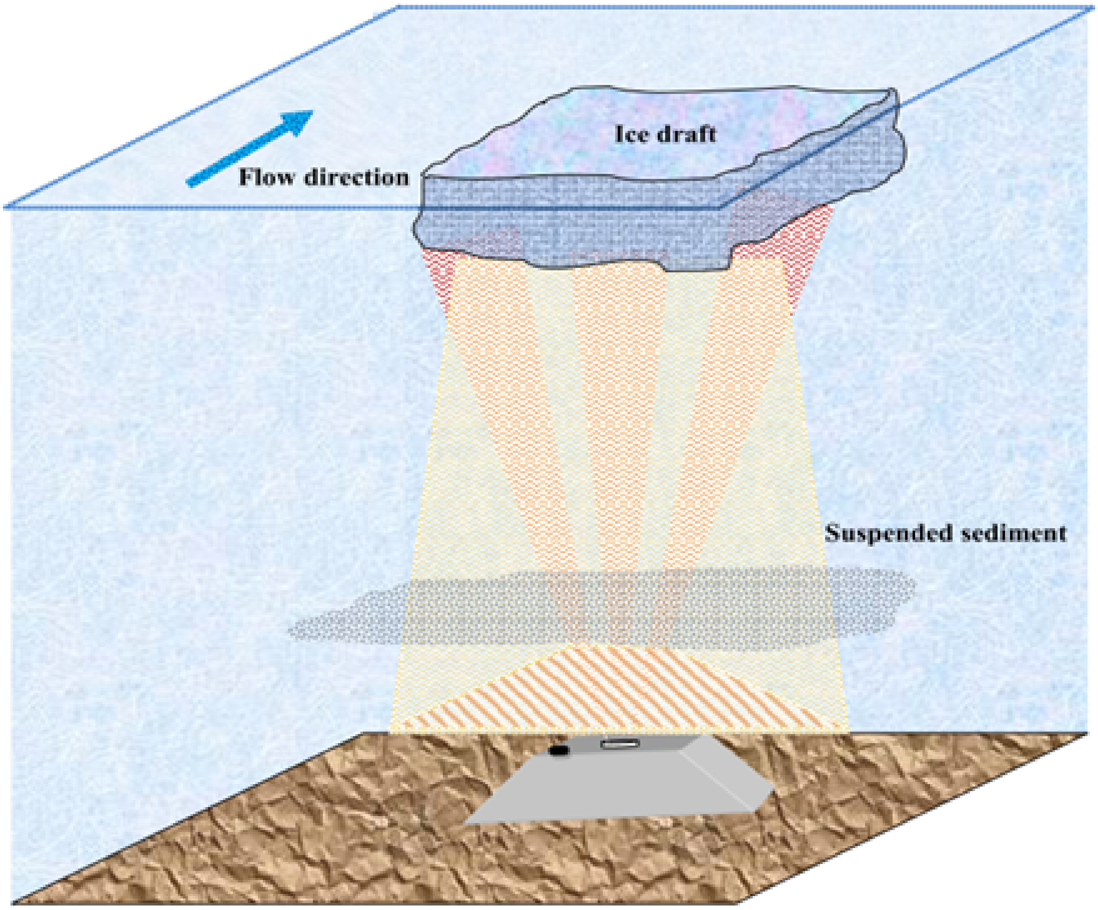

Figure 3.3: Schematic representation of acoustic sound pulse emitted from the ADCP and scattered back from suspended sediments and undersurface of the ice cover

The transmission loss term, , T_L includes two main sub-terms as follows (Urick, 1967):

$$T_L = 20 \; + \alpha \; r \tag{3.17}$$

The first term describes the geometrical spreading of a sound pulse propagating in the water column over the range (r) to the target. The second term accounts for signal attenuation in dB per meter, which varies as described with sound frequency, water temperature and salinity, and particle characteristics such as density, concentration, and grain size(Robert, 1983).

3.1.5 Ice thickness calculation

Ice Profiling Sonar (IPS) was introduced for polar ocean studies in 1990 (Melling et al., 1995) and has been improved through several generations since then.

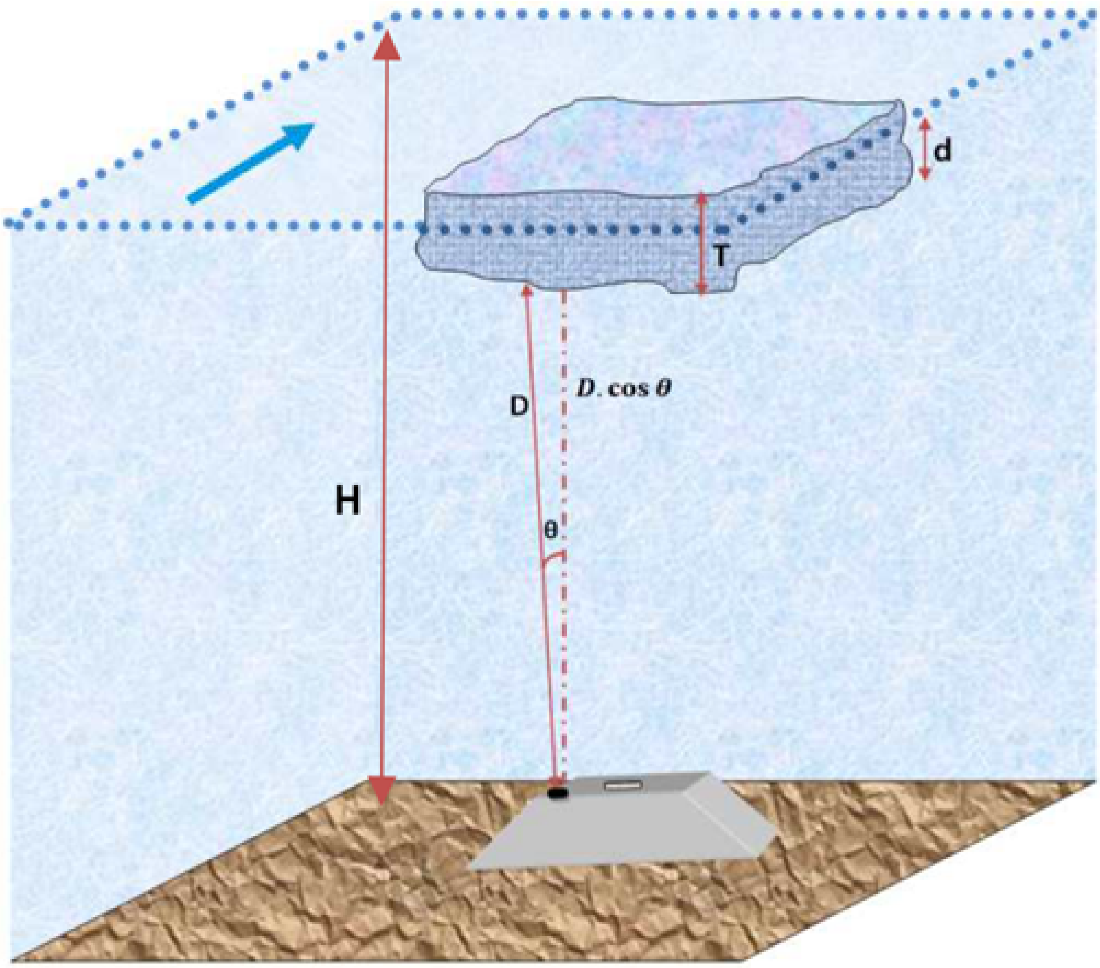

Figure 3.4: Representation of ice draft calculation using SWIPS data

The Shallow Water version of the Ice Profiling Sonar (SWIPS) implemented in this research was first introduced in 2004 for the Peace River ice monitoring program (Jasek et al., 2005). Marko and Fissel (2005) used SWIPS for monitoring the sea ice thickness and growth. Later in 2006,Marko et al. (2006) presented a review 18 th international symposium on ice about advances in ice and water profiling technology by the time. SWIPS also is utilized for detection of suspended and surface ice runs (Jasek and Marko, 2007; Marko and Jasek, 2010b), frazil ice measurements (Ghobrial et al., 2009), estimation of frazil ice size and distribution (Marko and Jasek, 2009), frazil ice evolution and river freeze-up monitoring(Ghobrial et al., 2010; Marko and Jasek, 2010a; Maxwell et al.; Ghobrial et al., 2013; Marko et al., 2015), evaluation of river ice models (Jasek et al., 2011) and zooplankton activities in the river (Jasek et al., 2013).

SWIPS can be deployed under the ice surface in depth range of 2-20 meters, sending sound pulses to the water column above the transducer and receiving the backscattered echoes in monostatic mode. SWIPS transducer generates a signal voltage of received backscatter, amplifies it to account for the signal strength losses, and digitizes it through an analog-to-digital (A/D) convertor. Resulting digitized voltage is interpreted as the amplitude of the returned sound. Depending on the digitization rate (64 kHz or 40 kHz) time resolution of the instrument varies from 16 μs to 25 μs. The maximum space resolution of 1 cm is attainable by the instrument (Buermans et al., 2010) .

Ice thickness can be calculated according to the data measured by SWIPS in a time series format of river ice draft. Ice draft, d, can be calculated as the difference between the simultaneous water level and elevation of the bottom of the ice, which is found from the peak in the vertical profile of back scatter intensity (3.4). Measured acoustic range to the underside of the cover is corrected for transducer tilt (θ).

$$d = H - \beta.D\ cos\theta \tag{3.18}$$

Where is β the correction for sound speed:

$$\beta = \frac{C_{act.}}{C_{nom.}} \tag{3.19}$$

Where $C_{nom}$is the nominal sound speed ($\approx$ 1500 m/s) and C_{act} is the actual sound speed that should be determined using empirical methods.

Water depth, H, can be determined using the measured bottom pressure P_{btm} , which should be adjusted according to the atmospheric pressure P_{atm}, measured at a nearby weather station, is ρ water density:

$$H = \frac{P_{btm} - P_{atm}}{\rho.g} \tag{3.20}$$

For relatively flat ice, ice thickness can be calculated using the buoyancy equation as follows:

$$T_{ice} = d.\ \frac{\rho_{water}}{\rho_{ice}} \tag{3.21}$$

3.1.6 Turbulence in alluvial streams

Turbulence is the highly unsteady eddying motion containing a wide range of eddy sizes and spectrum of fluctuations. The size of eddies and width of the spectrum are governed by the Reynolds number (Rodi, 1993).

The eddy in the flow is also determined by the boundary condition (for large eddies) and viscose forces (for smaller size eddies).

The kinetic energy is transferred from the mean motion of the flow through the spectrum of the eddy sizes, from large to small ones where the viscous forces dissipate the energy in the form of heat. This process is called *energy cascade* Rodi (1993). The large scale motion determines the rate of energy that is being dissipated through the eddies in the flow while the viscosity only determines the scale of the dissipation.

The direction of the mean flow and the direction imposed on the large scale turbulent motions are often identical which causes this motion to be highly anisotropic. It means that it varies spatially in both intensity and the length scale of the fluctuations. In wider fluctuation spectrums (i.e. high Reynolds stress values), the directional sensitivity diminishes and the small scale dissipative motion becomes isotropic. The concept of isotropic small scale motion versus the anisotropic large scale ones is called *local isotropy* (Rodi, 1993).

Mean flow equations

Mean flow quantities and distribution are governed by the mass, momentum conservation laws as well as the thermal energy or species concentration conservation (Rodi, 1993). These equations can be described in tensor notation as follows:

$$\frac{\partial U_i}{\partial x_i} = 0 \tag{3.22}$$

In the equation 3.22 (continuity equation), U_i is the instantaneous velocity component in the direction of x_i.

$$\frac{\partial U_i}{\partial t} + U_j \frac{\partial U_i}{\partial x_j} = -\frac{1}{\rho_r}\frac{\partial P}{\partial x_i} + \upsilon \frac{\partial^2 U_i}{\partial x_i \partial x_j} + g_i \frac{\rho - \rho_r}{\rho_r} \tag{3.23}$$

Equation 3.23 is called the *Navier -Stokes equation* which describes the conservation of momentum within the fluid medium. In this equation, P is the hydrostatic pressure, ρ_r is the reference density and υ is the kinematic viscosity. Applying the *Boussinesq approximation*, the variable density in equation 3.23 can be represented in the form of buoyancy (the last right term of the Navier-stokes equation).

$$\frac{\partial \phi}{\partial t} + U_i \frac{\partial \phi}{\partial x_i} = \lambda \frac{\partial^2 \phi}{\partial x_i \partial x_j} + S_\phi \tag{3.24}$$

Equation 3.24 describes the conservation of concentration . In the equation 3.24 the term ϕ stands either for the concentration or temperature and S_ϕ is the source term of the parameter. Here, λ is representing the molecular diffusivity of ϕ.

Combination of the equations presented through 3.22 to 3.24 with an equation relating the local ρ to the local temperature or concentration, forms a set of equations to describe the details of the turbulent motion.

$$U_i = \bar{U}_i + u_i \ , \ P = \bar{P}_i + p \tag{3.25}$$

Here, the mean terms can be presented as (Rodi, 1993):

$$\bar{U}_i, \bar{P}_i = \frac{1}{t_2 - t_1} \int_{t_1}^{t_2} \bar{U}_i, \bar{P}_i \ dt \tag{3.26}$$

replacing the mean terms by their representation in the form of equation 3.25 , the governing equation can be rewritten as:

Continuity:

$$\frac{\partial U_i}{\partial x_i} = 0 \tag{3.27a}$$

Momentum:

$$\frac{\partial U_i}{\partial t} + U_j \frac{\partial U_i}{\partial x_j} = -\frac{1}{\rho_r}\frac{\partial P}{\partial x_i} + \frac{\partial}{\partial x_i}\left(\upsilon \frac{\partial U_i}{\partial x_j} - \bar{u_i u_j}\right) + g_i \frac{\rho - \rho_r}{\rho_r} \tag{3.27b}$$

Temperature/ Concentration:

$$\frac{\partial \phi}{\partial t} + U_i \frac{\partial \phi}{\partial x_i} = \frac{\partial}{\partial x_i}\left(\lambda \frac{\partial \phi}{\partial x_i} - \bar{u_i \phi}\right) + S_\phi \tag{3.27c}$$

Equations above are exact nonlinear equations governing the mean flow quantities. However, unknown correlations between some parameters are introduced during the averaging process. Multiplication of ρ into these correlations physically defines the rate of momentum or heat transfer due to the fluctuating motion (i.e. turbulence).

The momentum transfer, $-\rho \bar{u_i u_j}$, has a stress effect on the fluid body and thus is called *Reynolds stress*. The term $\bar{u_i \phi}$ represents the heat or mass flux (whichever ϕ stands for) due to the turbulent motion. It should be noted that the laminar terms of $\upsilon \frac{\partial U_i}{\partial x_i}$ and $\lambda \frac{\partial \phi}{\partial x_i}$ are relatively small compared to the other described turbulent terms and therefore are often negligible (Rodi, 1993).

Determination of the turbulence correlation ($\bar{u_i u_j}$,$\bar{u_i \phi}$) is a key parameter in order to solve the equations for the mean flow quantities (equations 3.27a to 3.27c). Derivation of exact equations to solve the turbulence correlation leads to the introduction of even higher turbulence correlations which make the final solution unachievable through this approach. Hence, the turbulence in the flow should be modeled through an approximation of the correlations with the lower order or mean flow quantities (Rodi, 1993).

According to the nature of the simulated flow, calculation of turbulence correlation may or may not be important in the solution of momentum equation. However, since the temperature or concentration terms on the left-hand side of the equation (3.27c) are not governed by pressure or buoyancy gradient (such as it is in momentum equation), the turbulent heat flux term is always important to estimate in order to calculate the realistic distribution of the flux.

Concepts of turbulence in open channel flows

The main and most commonly used concept in turbulent flow studies in open channels is the *Boussinesqs eddy-viscosity* concept. Boussinesq (1877) assumed that the turbulent stresses are proportional to the mean velocity gradient. This is similar to the viscous stresses in laminar flow. However, in Boussinesqs eddy viscosity concept, the molecular viscosity (υ) which is the fluid property, is replaced by the eddy viscosity (υ_t) coefficient which spatially varies due to the turbulence state in different locations along the stream.

Boussinesqs eddy-viscosity concept can be presented as follows:

$$-\bar{u_i u_j} = \nu_t \left(\frac{dU_i}{dx_j} + \frac{dU_j}{dx_i} \right) - \frac{2}{3} k \delta_{ij} \tag{3.28}$$

Introduction of *Kronecker delta* term ,$\delta_{ij} = 1(i = j), \delta_{ij} = 0(i \neq j)$, into the equation above, makes the concept to be applicable for normal stress estimation. Normal stresses calculated from the equation above are conceptually positive values and their summary is equal to the twice of the energy of the fluctuation motion. This parameter is also known as *turbulent kinetic energy*:

$$k = \frac{1}{2} \left(\bar{u_1}^2 + \bar{u_2}^2 + \bar{u_3}^2 \right) \tag{3.29}$$

The normal stresses are scalar quantities and hence, the summary of them i.e. turbulent kinetic energy is a scalar parameter as well.

Even though eliminating the turbulent stresses in the momentum equation by using the eddy viscosity concept, introduces the kinetic energy into the momentum equation, it can be absorbed by the pressure gradient term. Therefore, only the eddy-viscosity is needed to be estimated (Rodi, 1993).

According to the analogy of the turbulent motion in Boussinesqs eddy-viscosity concept to the Stokes viscosity law for laminar flows (molecular motion), it is possible to conclude that the υ_t is proportional to the scale of the velocity which characterizes the fluctuation $\langle u_i u_j \rangle = \hat{V}$ and the length of the motion i.e. mixing length (Prandtl, 1925).

$$\nu_t \propto \hat{V} L \tag{3.30}$$

The scalar entity of the eddy-viscosity necessitates assuming that the υ_t is isotropic. Since such an assumption is a simplified presentation of the reality, spatially varying eddy-viscosity distribution sometimes is needed to be considered in the momentum equation for more complex flow situations like large water bodies. The other important concept in the analysis of turbulence in open channels is the *eddy-diffusivity* concept. Through this concept it is assumed that the mass transport is related to the gradient of the transport quantity as follows:

$$-\bar{u_i \varphi} = \Gamma \frac{\partial \phi}{\partial x_i} \tag{3.31}$$

In the equation above, Γ is the mass turbulent diffusivity. It is suggested that the turbulent diffusivity is closely related to the turbulent viscosity, υ_t (Rodi, 1993):

$$\Gamma = \frac{\nu_t}{\sigma_t} \tag{3.32}$$

In which the σ_t is called *Schmidt* (mass transport) or *Prandtl* (heat transport) number. Even though the buoyancy and the streamline curvature can affect the value of σ_t, experiments show that its variation is infinitesimal across the flow and hence, it is assumed to be constant in many schemes of turbulent flow analysis (Rodi, 1993).

As it is discussed above, the turbulent viscosity is proportional to the mean fluctuating velocity ($\hat{V}$) and a length scale which is called "*mixing length*" l_m (Prandtl, 1925):

$$\hat{V} = l_m \left| \frac{\partial U}{\partial y} \right| \tag{3.33}$$

in which the $\left|\frac{\partial U}{\partial y}\right|$ represents the mean velocity gradient. Based on what discussed in equation 3.30, the turbulent viscosity can be presented as:

$$\upsilon_t = {l_m}^2 \left| \frac{\partial U}{\partial y} \right| \tag{3.34}$$

The above relation defines the *Prandtls mixing length* hypothesis which relates the turbulent viscosity to the mean velocity gradient.

Theoretical concepts of turbulence in ice covered streams

Flow in open channels is bounded by the side and bed boundaries. During the ice cover period, another top boundary is being added to the flow. Such a condition turns the flow to an internal wall flow. In both mentioned conditions, the mean velocity component is almost or completely parallel to the upper and lower boundaries. The behaviour of near wall flow is very similar in both open and ice covered conditions though the magnitude and location of maximum and mean velocity/velocities might be different. Therefore, the turbulent flow characteristics can be described well by the wall flow theories in general.

Flow in a fully developed, ice covered channel (where the flow can be considered uniform in the streamwise direction), is statistically stationary and statistically one-dimensional, with velocity statistics varying only in flow depth (hypothetical y direction in this analysis) (Pope, 2000).

Reynolds hypothesis separates the instantaneous variable values in to mean and fluctuating components. Here, the flow condition can be described by the well-known Reynolds number described as:

$$Re = h\frac{\bar{U}}{\nu} \tag{3.35}$$

In which, h is the flow surface elevation and $\bar{U}$ is the bulk velocity defined by:

$$\bar{U} = \frac{2}{h} \int_0^{\frac{h}{2}} \langle U \rangle \, dy$$

Where the term $\langle U \rangle$ is the mean velocity magnitude at the depth y.

Flows with Reynolds number less than 1350 are laminar while for Reynolds numbers more than 1800, the flow can be considered as fully turbulent. Any flow with a Reynolds number between this range is in the transitional mode, however, the transitional condition might remain effective up to Reynolds number of 3000 (Patel and Head, 1969).

The total shear stress then can be estimated using the equation below:

$$\tau = \rho \upsilon \frac{d \langle U \rangle}{dy} - \rho \langle uv \rangle \tag{3.37}$$

Based on the sole dependency of τ to y, the equation 3.37 can be applied for both open and ice covered flows with an acceptable accuracy. Thus, it is possible to result that the lower boundary shear stress can be represented as: $\tau_b = \tau(0)$.

Due to the antisymmetric nature of the shear stress about the depth centerline in channels with identical upper and lower boundaries, it can be concluded that the $\tau_((h/2)) \cong 0$ and the top boundary stress is $\tau_h = -\tau_b$. Hence, the shear stress distribution from boundaries through the flow depth can be represented as:

$$\tau(y) = \tau_b \left(1 - \frac{2y}{h}\right) \tag{3.38}$$

As it is evident in the equation 3.38, the shear stress distribution is independent of the fluid properties as well as the state of fluid motion. The boundary shear stresses can be normalized based on maximum or mean velocity. The results of normalization is called *skin friction coefficient* (Pope, 2000) and can be represented as (here based on mean velocity):

$$C_f = \frac{\tau_w, \tau_h}{\frac{1}{2}\rho \bar{U}^2} \tag{3.39}$$

The total shear stress presented in equation 3.37 , is the summary of viscose and Reynolds stresses. Near boundaries, the velocity magnitude is nearly zero and therefore, the total shear stress consists of only the viscous stresses. Distancing from the boundaries, instantaneous velocity increases and velocity fluctuations emerge. For the flows in ducts (e.g. ice covered streams), assuming the similarity of the lower and upper boundaries, this process continuous up to the flow centerline where, theoretically, the maximum velocity occurs. Here, according to the equation of shear stress distribution, 3.38, the shear stress values conceptually drops to zero.

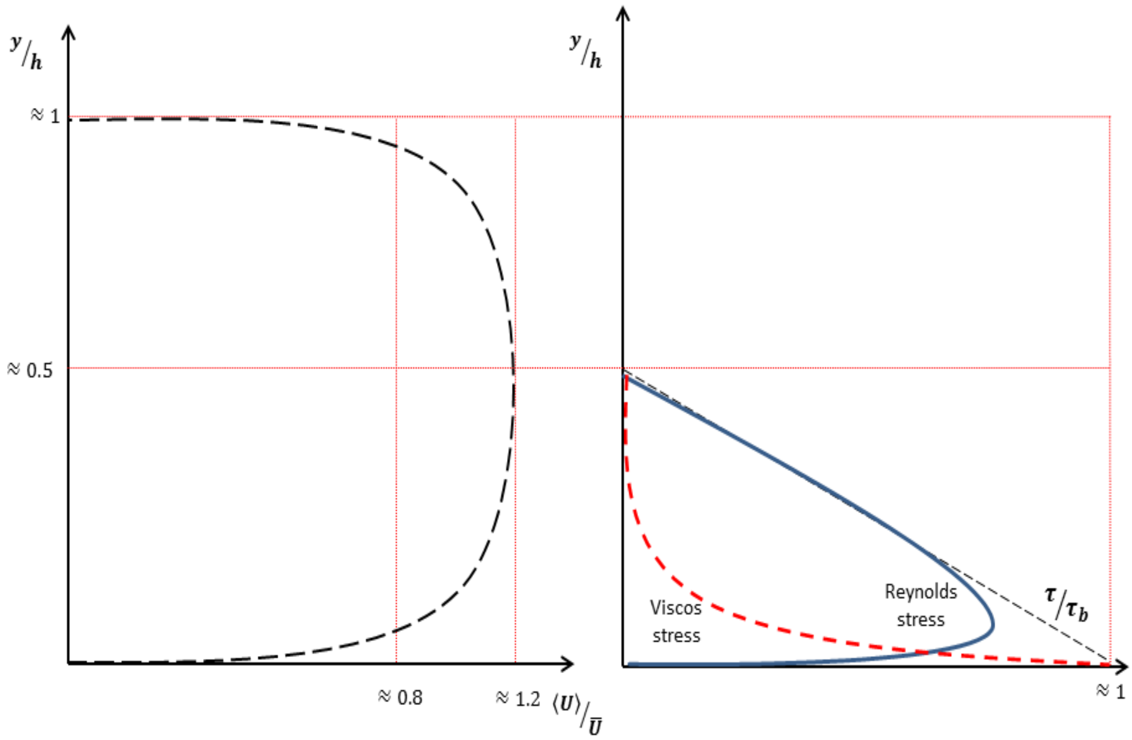

Figure 3.5: Theoretical representation of normalized velocity and shear stress distribution

The schematic representation of normalized velocity and shear stress distribution are presented in Figure 3.5. As it can be seen, in the vicinity of the boundaries, the total shear stress is mainly governed by the viscous stresses mainly due to the important effect of viscosity near the boundaries. Due to the symmetrical importance of the υ near the lower and upper (when exists) boundaries, appropriate velocity and length scales are developed to define the near boundary condition.

$$\delta_\upsilon = \frac{\upsilon}{u_t} = \upsilon\sqrt{\frac{\rho}{\tau_b}} \tag{3.40}$$

In the equation 3.40, the relationship between near boundary length and velocity scales, (δ_υ) and (u_t) respectively (called also *viscous scales* (Pope, 2000)), are defined.

$$y^+ = \frac{y}{\delta_\upsilon} = \frac{u_t y}{\upsilon} \tag{3.41}$$

This parameter is also called the *wall unit* (Pope, 2000).

Based on the similarity of the wall unit to the local Reynolds number, it can be used to quantify the relative importance of the viscosity and turbulence components in the total shear stress (Pope, 2000).

The fractional contribution of viscous and Reynolds stresses are presented in Figure 3.6. As seen in the figure, the share of viscous stress decreases distancing from the boundary and meanwhile Reynolds stress share gets more importance in the total stress.

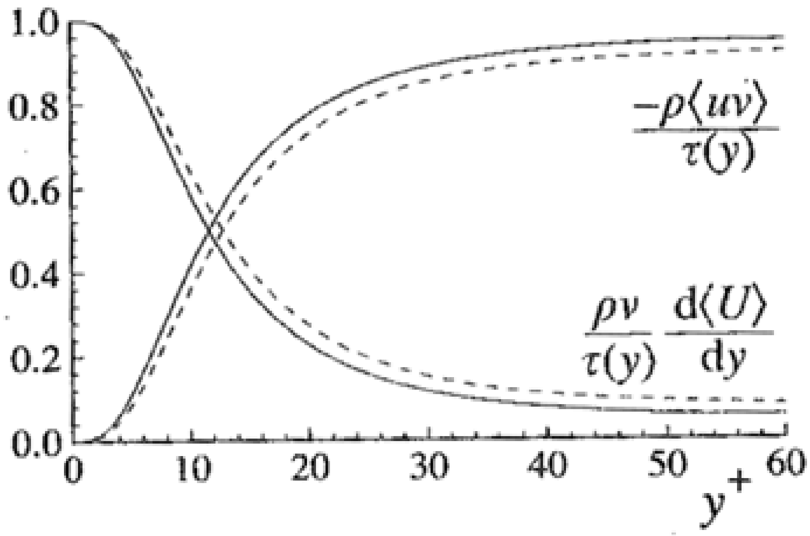

Figure 3.6: Contribution of viscous and Reynolds stresses to the total stress in wall units (Pope, 2000)

The wall unit, y^+, provides a valuable scale for defining several flow regions near the boundaries and analyze their properties. Two main regions can be addressed based on the distance from the boundary in the form of y^+; the viscous boundary region $(y^+ < 50)$ where the shear stress is directly affected by the molecular viscosity and the outer layer $(y^+ > 50)$ in which the effect of viscosity can be considered negligible . Boundary regions and layers and their associated properties are addressed in Table 3.1.

Reynolds number calculation based on shear velocity, u_* leads to a form of Reynolds number called *friction Reynolds number* and can be defined as:

$$Re_\tau = \frac{u_* h}{2\nu} \tag{3.42}$$

Substituting the equation 3.41 in the equation 3.42 leads to another representation of friction Reynolds number as:

$$Re_\tau = \frac{h}{2\delta_v} \tag{3.43}$$

Herein, the mean velocity profile and velocity gradient can be represented based on two sets of non-dimensional parameters (Pope, 2000):

$$\langle U \rangle = u_\tau \Phi \left(\frac{2y}{h},\ Re_\tau \right) \tag{3.44}$$

$$\frac{d\langle U \rangle}{dy} = \frac{u_\tau}{y}\ \Psi \left(\frac{2y}{h},\ \frac{y}{\delta_v} \right) \tag{3.45}$$

Table 3.1: Near wall boundary regions

Region	Location	Properties
Inner layer	$\frac{y}{\delta} < 0.1$	Velocity at each depth determined by shear velocity and wall unit, independent from maximum velocity and its location
Viscos boundary region	$y^+ < 50$	Significant contribution of viscosity in the shear stress
Viscous sublayer	$y^+ < 5$	Negligible Reynolds stress contribution in total shear stress
Outer layer	$y^+ > 50$	Negligible viscosity contribution in total shear stress
Overlap region	$y^+ > 50,\ \dfrac{y}{\delta} < 0.1$	Exists in large Reynolds number
Log-law region	$y^+ > 30,\ \dfrac{y}{\delta} < 0.3$	Validity of Log-law
Buffer layer	$30 < y^+ < 50$	Viscous sublayer/ Log-law buffer

In which Ψ, Φ are universal non-dimensional functions to be determined.

Both 3.44 and 3.45 equations consist of appropriate length scales for inner and outer layers which confirm the validity of the approach of selection of two non-dimensional parameters to represent the velocity profile and velocity gradient through the water depth.

Considering the equation 3.37 and showing the velocity gradient as $\varsigma = d\langle u\rangle/d\langle y\rangle$, it is possible to write the equation 3.37 in the form of Reynolds stress as:

$$-\langle uv\rangle = \frac{\tau}{\rho} - \upsilon\varsigma \tag{3.46}$$

However, the shear stress distribution is related to the boundary shear stress as equation 3.38 suggests, thus substituting equation 3.38 in the equation 3.46 leads to:

$$-\langle uv\rangle = \frac{\tau_b}{\rho}\left(1-\frac{2y}{h}\right) - \upsilon\varsigma \tag{3.47}$$

which illustrates the Reynolds stress distribution in the water depth.

Through the mean flow analysis, the kinetic energy of the fluid per unit mass can be shown as (Pope, 2000):

$$E\left(x,t\right) = \frac{1}{2}\,U\left(x,t\right).U\left(x,t\right) \tag{3.48}$$

in which the *U(x,t)* is the *Eulerian velocity.*

Substituting the Reynolds hypothesis for separation of instantaneous velocity in to mean and fluctuating components and averaging equation 3.48 results in:

$$\langle E(x,t)\rangle = \bar{E}\left(x,t\right) + k\left(x,t\right) \tag{3.49}$$

Here, the $\bar{E}\left(x,t\right)$ is the kinetic energy of the mean flow and *k(x,t)* is the turbulent kinetic energy both can be shown as (Pope, 2000):

$$\bar{E} = \frac{1}{2}\,\langle U\rangle\,.\,\langle U\rangle \tag{3.50}$$

$$k = \frac{1}{2}\,\langle u.u\rangle \tag{3.51}$$

The turbulent kinetic energy mainly determines the isotropic part of the Reynolds stress tensor but it is found that the anisotropic part also scales with the turbulent kinetic energy term (Pope, 2000).

Using the Navier-Stokes equation, instantaneous kinetic energy (left-hand side of the equation 3.49) can be rewritten as:

$$\frac{DE}{Dt} + \nabla.T = -2vS_{ij}S_{ij} \tag{3.52}$$

In which S and T, are the rate of strain tensor and the flux of energy respectively both can be shown as (Pope, 2000):

$$S_{ij} = \frac{1}{2}\left(\frac{\partial U_i}{\partial x_j} + \frac{\partial U_j}{\partial x_i}\right) \tag{3.53}$$

$$T_i = \frac{U_i p}{\rho} - 2vU_jS_{ij} \tag{3.54}$$

where p is the instantaneous pressure term in the Navier-Stokes equation.

Integrating the equation 3.54 over a fixed control volume illustrates the transfer of E from one region to another. The result of the integration process contains negative terms on the right hand side which represents the kinetic energy dissipation due to viscosity i.e. conversion of the mechanical energy to internal heat energy. Averaging equation (3.52) represents the mean kinetic energy $\langle E \rangle$, as (Pope, 2000):

$$\frac{\bar{D}\langle E \rangle}{\bar{D}t} + \nabla.\left(\langle uE \rangle + \langle T \rangle\right) = -\bar{\epsilon} - \epsilon \tag{3.55}$$

$$\bar{\epsilon} = 2v\bar{S_{ij}}\bar{S_{ij}} \tag{3.56}$$

$$\epsilon = 2v\langle s_{ij}s_{ij} \rangle \tag{3.57}$$

$$\bar{S_{ij}} = \langle S_{ij} \rangle = \frac{1}{2}\left(\frac{\partial \langle U_i \rangle}{\partial x_j} + \frac{\partial \langle U_j \rangle}{\partial x_i}\right) \tag{3.58}$$

$$s_{ij} = S_{ij} - \langle S_{ij} \rangle = \frac{1}{2}\left(\frac{\partial u_i}{\partial x_j} + \frac{\partial u_j}{\partial x_i}\right) \tag{3.59}$$

Distancing from the boundaries, the product of multiplication of Reynolds stress and velocity gradient is generally a positive quantity and is called the *production of turbulent kinetic energy* (Pope, 2000).

$$\mathcal{P} = -\langle u_i u_j \rangle \frac{\partial \langle U_i \rangle}{\partial x_j} \tag{3.60}$$

So, the mean and turbulent kinetic energy can be written in the form of:

$$\frac{\bar{D}\bar{E}}{\bar{D}t} + \nabla.\bar{T} = -\mathcal{P} - \bar{\epsilon}\ ,\ \bar{T} = \langle U_j \rangle \langle u_i u_j \rangle + \langle U_i \rangle \frac{\langle p \rangle}{\rho} - 2v\langle U_j \rangle \bar{S_{ij}} \tag{3.61}$$

$$\frac{\bar{D}k}{\bar{D}t} + \nabla.T' = -\bar{\epsilon}\ ,\ T^{'} = \frac{1}{2}\langle u_i u_j u_j \rangle + \frac{\langle u_i p' \rangle}{\rho} - 2v\langle u_j s_{ij} \rangle \tag{3.62}$$

In which ρ' is decomposed fluctuating pressure term based on Reynolds hypothesis.

For boundary layer approximation, the production of turbulent kinetic energy can be represented as (Pope, 2000):

$$\mathcal{P} = -\langle uv \rangle \frac{d\langle U \rangle}{dy} \tag{3.63}$$

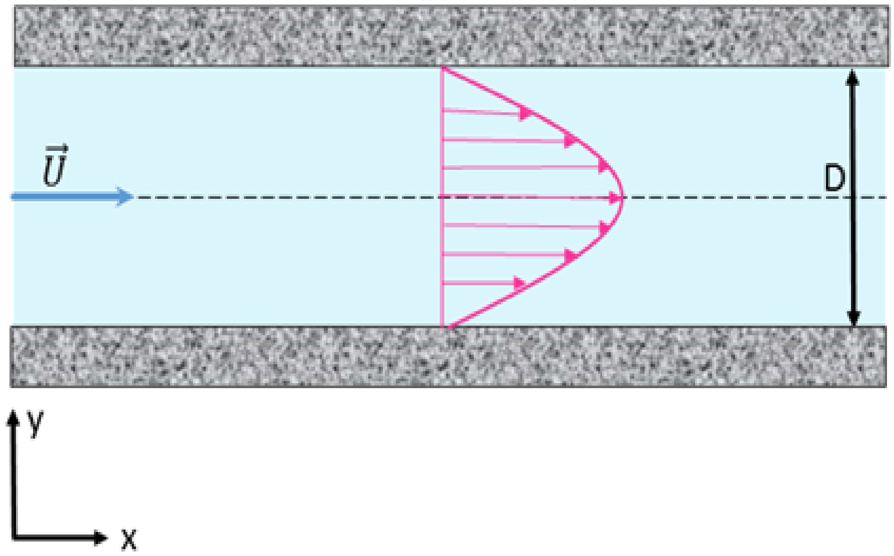

Figure 3.7: Theoretical velocity distribution for a fully developed two dimensional flow between two infinite plates

Combination of equations (3.38), (3.63) results in:

$$\mathcal{P} = \frac{\tau_b}{\rho}\left(1 - \frac{2y}{h}\right)\varsigma - \upsilon\varsigma^2 \tag{3.64}$$

As an application of the theory discussed in this, a flow between two infinite plates can be considered as the standard case of the flow between two boundaries.For a fully developed two dimensional flow between two infinite plates i.e. bed and under ice cover as shown in figure 3.7 , the momentum equation can be written as:

$$\frac{\partial P}{\partial x} = \mu\frac{\partial^2 U}{\partial y^2} \tag{3.65}$$

It should be noted that for flow condition presented in the figure 3.7, the positive vertical direction is from the lower boundary (bed) toward the upper boundary (under ice surface). This is the same positive vertical direction for ADCP recordings for this study as well.

Application of boundary conditions to the equation (3.65) leads to the velocity distribution equation as:

$$U = \frac{1}{2\mu}(\frac{\partial P}{\partial x})[y - \frac{1}{2}D] \tag{3.66}$$

As it shown, the equation (3.66) illustrates a parabolic shape for the velocity distribution with the maximum velocity locating on the centerline.

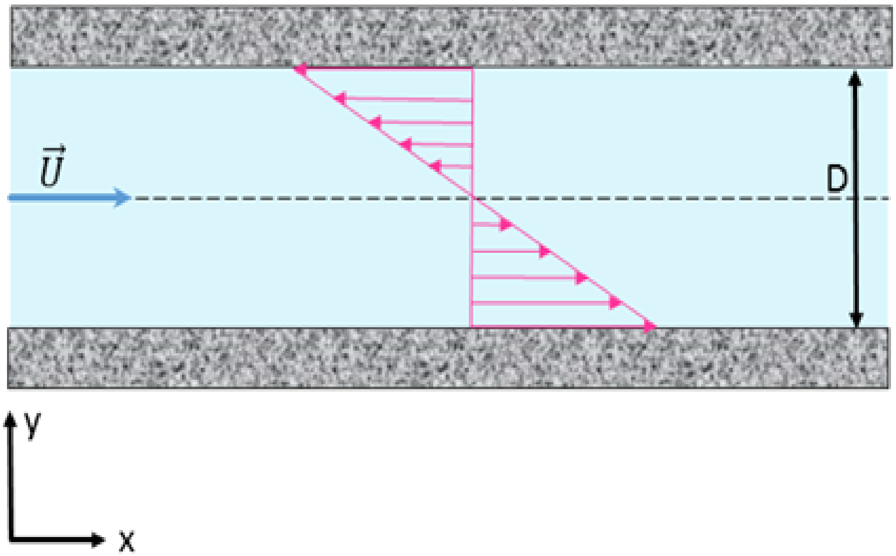

Figure 3.8: Theoretical shear stress distribution for a fully developed two dimensional flow between two infinite plates

Based on equations (3.65 and 3.66) the theoretical shear stress distribution between ice and bed boundaries can be shown as:

$$\tau = (\frac{\partial P}{\partial x})[y - \frac{1}{2}D] \tag{3.67}$$

Equation (3.67) illustrates theoretical distribution of shear stress between ice and bed. Hence, applying the flow boundaries as *y=0* and *y=D* to the equation (3.67) results in the estimation of shear stress at the boundaries as $\tau_{bed} = -1/2(\partial P/\partial x)D$ and $\tau_{ice} = 1/2(\partial P/\partial x)D$.

Considering the positive direction of the τ (normal to the y plate), the theoretical shear stress distribution between two boundaries can be represented as Figure 3.8.

3.2 River ice modeling (ICESIM/ICESIMAT)

3.2.1 Introduction to ICESIM

ICESIM model is developed by Acres International Ltd. (now Hatch Ltd.) as a computer program able to simulate the major parts of the river ice processes. The program was developed to facilitate the design of hydro-electric plants and address the ice associated problems in the Nelson River, northern Manitoba. The techniques used in the program evolved over three decades and the model has been improved in several stages with consideration of hydraulic and ice mechanics findings. The resulting comprehensive ICESIM model is a steady state, one- dimensional program, able to simulate most of the ice processes during winter under a variety of conditions and types of rivers. Several technical papers have been published in the past describing the "ICESIM" model and several aspects of its applications in river ice such as: Carson and Jonassen (1979) ,Carson (1982),Gerrard and Carson (1987),Korbaylo and Carson (1992),Breland and Carson (1995) ,Carson and Groeneveld (1997) and Judge et al. (1997).

It is notable that the utilization of numerical models does not provide precise understanding of hydraulic effects due to some phenomena like ice jam accumulation because of the practical limitations associated with the applications of such techniques. So, the model simulations are considered to be approximate that require engineering judgment both in formulating and interpreting the simulations of river ice processes.

3.2.2 Model input

Data requirements to set up and calibrate an ICESIM model are as follows. It is notable that the data requirements for winter hydraulic models are significantly more comparing to open-water models.

I. **Daily air temperatures**

   The mean daily recorded temperature thermograph is needed for each of the calibration and verification years. Air temperature data allow the model to calculate the volume of generated ice according to the freezing degree days that the river has been exposed to as well as the rate of border ice growth.

II. **Water inflow to the study reach (water discharge upstream)**

   Mean monthly flow discharges in winter (usually from October to April) are used in the ICESIM model simulations.

III. **Observed water levels over the reach throughout the winter**

IV. Observed ice front location and ice cover condition

   This information is used to roughly validate the model prediction of ice condition and related ice front location.

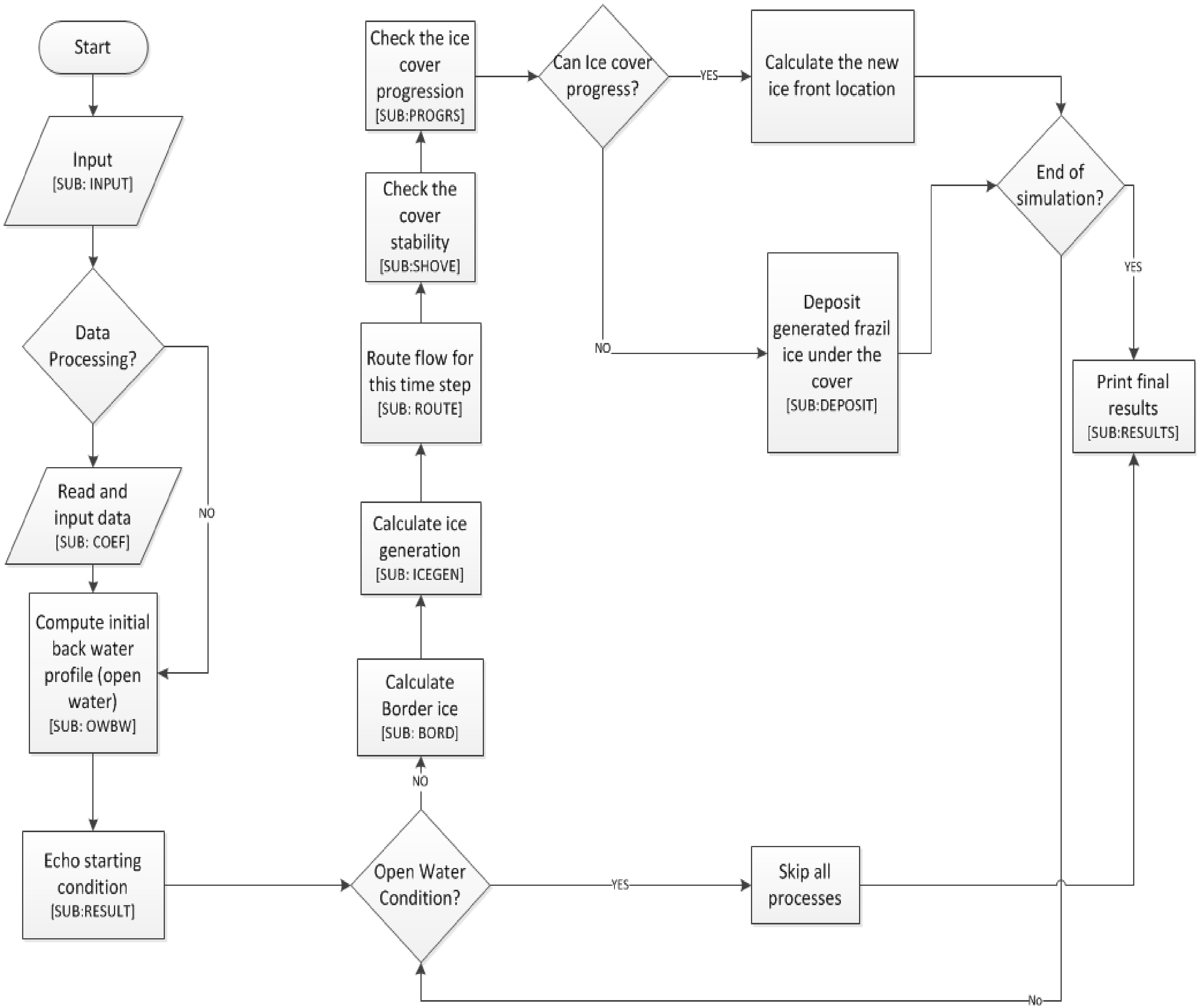

Figure 3.9: ICESIM model river ice simulation flowchart

Table 3.2: Summary of "ICESIM" main applications (Carson and Groeneveld, 1997)

Location	River	Problem Addressed	Successful Calibration	Years of Application
Limestone	Nelson	Winter ice cover effect during Conawapa G.S	Yes, within 1m to 10 m staging from ice	1974,1985,2009
Ogdensberg	St.Lawrence	Effect of extension of navigation season on ice formation	Yes, within 15 cm in 1.5 m variation due to ice	1978
Fort McMurray	Athabasca	Spring Ice jams flood mitigation measures	Yes	1982
Nipawin	Saskatchewan	Spring ice jams effect on coffer dams and bridge crossing	Yes	1984
Woodstock/Perth-Andover	St.John	Spring ice jams means to control	Yes, within 10%of total staging due to ice	1987-92
Whitehorse	Yukon	Ice jamming due to hydro plant peaking	Yes, within 15 cm in 1.5 m of staging	1993
Churchill	Churchill	construction of control weir	Yes, within 0.7m in 9 m of ice staging	1993

3.2.3 Model theory

ICESIM is formulated to simulate major physical processes, in discrete time steps, contributing to river ice processes as well as parameters affecting the water stage along the river, namely:

I. Ice generation over the open water areas along the study reach

II. Ice cover advancement by frontal progression using a Froude number criterion (the juxtaposition process)

III. Ice deposition and transport

IV. Ice erosion

V. Border ice growth

VI. Ice retreat and mechanical thickening due to forces acting on the leading edge(Shoving process)

VII. Ice cover progression due to back water effect (Packing process)

In general, model processing starts by computing the water surface profile in a given time step in order to update the hydraulic conditions according to any changes in the ice cover conditions. Ice thickness and acting hydraulic forces then are recomputed based on the new condition and the process is then repeated following the same process of computation, until a final solution is obtained for the given time step. A brief description of each physical process and its application, main equations and assumptions are as follows:

Rate of ice generation

Simulation of generated ice is a key point in model calculation because it introduces the volume of ice entered to the study reach. It is an important parameter since the rate of progression of the leading edge of an unconsolidated ice cover is a factor of ice supply entering the study reach. Two points are available for ice volume input in ICESIM:

$$V_f = \frac{L_0 B_0}{\rho_i \lambda_i} C_0 \left(T_w - T_a\right) \tag{3.68}$$

where V_f is the volumetric production of ice [m^3] , L_0B_0 is the area of open water upstream of the cross section [m^2] , C_0 is the heat transfer coefficient [$W/m^2C°$], T_W, T_a are air and water temperature [C°], λ_i is the latent heat of fusion for ice [J/kg] and ρ_i is the density of ice [kg/m^3].

Previous observations proved that the frazil ice can form in deep rivers when the surface temperature is less than or equal to 0°C but the average water temperature is about +0.6°C (Ashton, 1986). ICESIM assumes the ice generation is not possible until the average water temperature drops to 0°C. Also, ICESIM neglects the effect of super cooled water on ice generation wherein the temperature of water is below 0°C. So, some adjustments may be needed to compensate the associated effects and consider this phenomenon in interpretation of the model results.

Frontal progression and juxtaposition process

When water velocity is low, generated ice particles (frazil ice pans, slush ice or ice floes) are simply carried downstream until they are stopped by lake or sea ice cover, the existing edge of river ice or ice bridge locations. This process is called "juxtaposition". However, when the water velocity is too high to permit the floating ice particles to stop and accumulate at the edge of the existing ice cover, the incoming ice floes underturn and keep traveling downstream beneath the ice cover until the velocity decreases due to the variation in cross section geometry which allows them to deposit at physically appropriate cross sections further downstream. This process leads the ice cover frontal progression to stall at some sections for a while and continue to thicken due to incoming ice floes. A critical Froude number which is a function of velocity and depth is defined as a criterion for under turning of incoming ice floes. Typical values for critical Froude number range from 0.08 to 0.12.

Eventually, this process causes the water to stage, which subsequently lowers the Froude number, balancing and stabilizing the process at the leading edge. The juxtaposition process can then take place again and the ice cover continues to progress upstream. Ice front progression requires a minimum thickness to resist against water thrust, so the leading edge of ice cover may thicken as the cover advances upstream if it is necessary.

After ice cover thickness calculation at each cross section, water surface level and hydraulic characteristics are calculated based on *Bernoulli* and the *continuity* equations in ICESIM.

Ice front thickness can be calculated according to the following equation by Michel (1971).

$$h_j = \frac{{V_u}^2}{[2g\left(1 - \frac{\rho_i}{\rho_w}\right)(1 - P_j)]} \tag{3.69}$$

In the equation above, $h_j$is the ice thickness [m] , $V_u$is the water velocity under ice [m/s], $\rho_i$is density of ice [kg/m^3], ρ_wDensity of water [kg/m^3], $P_j$is the ice cover porosity at the location of leading ice front and $g$is the gravity acceleration [m/s^2].

In most practical situations measurements beneath the ice cover are impossible and parameters like V_u are determined based on knowledge of the flow immediately upstream of the edge. Thus, ICESIM assumes that V_u is approximately equal to $\frac{V}{\left(\frac{R_c - h_j}{R_c}\right)}$ where R_c is equal to mean hydraulic radius and V is the water velocity immediately upstream of the ice edge.

Hence, equation (3.69) above can be rearranged as follows:

$$F_r = \frac{V}{\sqrt{gH}} = [\ 2(1 - \frac{\rho_i}{\rho_w}\,(1 - P_j)\,(\frac{h_j}{H}\ )]^{1/2}\ (1 - \frac{h_j}{H}\ ) \tag{3.70}$$

Assuming $P_j = 0.73$ and $\rho_i = 920$ [Kg/m^3], equation (3.70) which is the Froude number at the leading ice edge can be simplified to:

$$F_r = \frac{V}{\sqrt{gH}} = 208\,\sqrt{\frac{h_j}{H}}\ \left(1 - \frac{h_j}{H}\right) \tag{3.71}$$

Ice deposition and erosion

Hydraulic condition determines whether frazil is deposited or eroded at the under ice surface. Under ice observations show frazil ice will be deposited at under-ice velocities $\leqslant$ 0.3m/s while erosion occurs around 1.5-2 m/s (Michel, 1971). Erosion velocity magnitude is greater than the deposition and this is because when frazil ice deposit under the cover, it tends to stick and lock in the position. Hence, the required force and consequently water velocity should be greater for removal than the deposition.

ICESIM uses simple velocity criteria to calculate the ice movement or deposition. If frazil ice is available for deposition, ICESIM estimates the hydraulic condition of all cross sections downstream of the cross section subject to the calculation. The frazil ice is deposited when it reaches a cross section where the water velocity is less than the velocity criterion. Deposition continues until velocity at the section reaches the criterion, then the remaining ice volume is transported downstream and deposited at the next low velocity location. Similarly, the possibility of ice erosion is checked during the water surface profile calculation in ICESIM. The program applies a second velocity criterion for ice to start to be eroded ($\approx$ 2 m/s).

Solid ice floes - which have greater flotation and angularity and would exist during break-up - need higher velocity variation to undergo the deposition-erosion process. Still, the criterion method implemented in ICESIM is anticipated to be valid and provide precise results, particularly during the freeze-up period when deposition-erosion is more important in ice cover advancement.

Border ice growth

Border ice growth is calculated using four optional approaches in ICESIM, which provides user flexibility according to the situation:

1. A modified empirical equation by Newbury (1968) based on data from Nelson River considering several years of severity. This method has been used with moderate success in Northern Manitoba, but should be used with care in other areas. The border ice growth equations is as follows (Newbury, 1968) :

   $$W_b = \frac{c_1}{V^{c_2}} D_d \tag{3.72}$$

   In this equation, W_b is total border ice width at a cross section [m] , V is the average velocity of flow at the cross section [m/s], $D_d$is degree-days of freezing [°C-days] and c_1, c_2 are coefficients based on the observation of the study reach supplied by the user. Reasonable values of these parameters for northern Manitoba conditions are c_1 = 0.054 and c_2= 1.5.

   The term$\frac{c_1}{V^{c_2}}$ actually represents a coefficient to relate degree-days of freezing to border ice growth [m/°C-Day].

2. Application of a constant called "Border ice factor" for border ice calculation. This value is a function of degree-days of freezing and is entered as an input to the program for border ice growth calculations.

   The factor defines the fraction of total water area that remains open and is based on field observations. This factor may be advantageous under some conditions such as consistent border ice growth along the river as well as short length of the study reach.

3. This option uses a varying border ice factor for each cross section. The factor again is a function of freezing degree-days and is obtained from field observations.

4. The final approach for border ice calculation in "ICESIM" uses an initial border ice fraction that is specified for each cross section. The border ice growth equation, as explained in 3.72, is used for additional border ice generation.

It is also important to know that if the rate of border ice generation is relatively consistent over the study reach, the two last options offer more representative simulations.

Mechanical thickening (Shoving process)

When the net downstream force on an ice cover exceeds the internal resistance of the ice cover, mechanical fragmentation (shoving) happens, which lets the ice cover to thicken to its internal equilibrium thickness. This mechanical thickening leads to ice front recession in some occasions.

Pariset et al. (1966) showed that the two major driving forces acting on the ice cover in wide rivers are: a) forces opposed by friction on underside of the cover and the component of the cover weight in the streamwise direction.

ICESIM computes required cover thickness for each cross section during the shoving calculation and this process continues in the downstream direction. Back water profile computation is the next step while the program checks the erosion velocity not to exceed the limit anywhere along the study reach. The volume of ice required to thicken all weak cross sections can then be calculated.

It is also notable that the model allows, if deemed appropriate, reduction of downstream force due to grounding of the ice cover as well as reduction due to presence of islands along the study reach.

Acting forces on the leading edge increase the stresses in the ice cover while the cover progresses upstream. These forces are hydrodynamic shearing force of flow under the cover, shearing stress of wind on the cover, weight of the ice cover along the hydraulic slope, and the hydro dynamic thrust on the cover edge. Mentioned forces must be opposed by supporting forces most of which are resistance of the cover and the resistance of the river banks, otherwise the cover will be structurally unstable and shoving will occur.

Forces exerted by the flow on the ice cover are calculated using the equations below:

1. Hydrodynamic thrust on the leading edge (Michel, 1971)

$$F_t = \left(1 - \frac{d_H}{H}\right)^2 {V_u}^2 \; BH \; \frac{\gamma_w}{2g} \tag{3.73}$$

   In this equation, F_t is the hydrodynamic thrust of the flow [N] , H is the depth of the water upstream of leading edge [m] , d_H is the depth of water under the leading edge [m] , V_u is the water velocity under the leading edge which is the mean value across the width of the channel [m/s], $B$is the width of the ice cover [m] , g is the acceleration due to gravity [m/s^2], γ_w is the specific weight of the water [9800 N/m^3].

2. Hydraulic drag of the flow on the under-surface of ice cover

   The force from fractional drag on the under-side of the cover can be computed between each cross section as (Michel, 1971):

$$F_D = \left(\frac{\gamma_w \; d_H \; S \; {n_i}^{1.5}}{2 \; {n_c}^{1.5}}\right) \; A = 4900 \; \left(\frac{d_H \; S \; {n_i}^{1.5}}{{n_c}^{1.5}}\right) \; A \tag{3.74}$$

   Where F_D is hydraulic fractional drag force [N], γ_w is the specific weight of the water (9800 [N/m^3]), S is the slope of hydraulic grade line, n_i is the Manning roughness coefficient of the underside, n_c is the composite Manning roughness coefficient of the cross section, d_H is the depth of flow under the ice cover [m] and A is under surface of the ice cover exposed to the flow [m^2] .

3. Weight of the ice cover

   Cover weight includes the weight of the ice as well as the weight of water that fills the ice cover voids. Cover weight acts along the hydraulic gradient and can be calculated based on buoyancy as follows:

$$F_w = \; \gamma_i \; V_0 \; S \tag{3.75}$$

   In the equation above, F_w is the gravitational force acting along the channel [N] , γ_i is the specific weight of ice (9020 [N/m^3]), V_0 is volume of ice cover including voids in filled with water, S is the slope of the energy grade line.

4. Wind force on the ice cover

   The force on the ice cover due to wind drag can be calculated as follows:

$$F_{wd} = \; P_w \; A \tag{3.76}$$

   Where $F_{wd}$is wind drag force [N] , P_W is the wind force per unit area of ice cover [Pa] (Positive direction is upstream to downstream) and A is the ice surface area [m^2] .

5. River bank forces

Cohesion of the ice cover to the river banks and friction of the ice cover against the river banks are categorized as resisting forces in ICESIM. Ice cover cohesion can be presented as follows (Pariset et al., 1966):

$$F_c = 2\ C_c\ t_h\ L \tag{3.77}$$

In this equation, $F_C$is the force of cohesion of ice to river banks [N] , $C_c$is the magnitude of cohesion per unit area of ice/bank interface [Pa] , t_h is average thickness of ice cover between cross sections [m] and L is the distance between cross sections [m].

The other stabilizing force, friction of the ice cover against the river banks, is the result of lateral stresses of hydraulic forces exerted to the ice cover in the streamwise direction which are partially spread laterally toward the river banks. According to the Pariset and Hausser (1966), it can be represented as:

$$F_f = 2\ f_i\ t_h\ L\ k_1\ \tan\varphi_i \tag{3.78}$$

Where F_f is the friction force of the ice to the river banks [N] , f_i is the stress in the ice cover in the direction on flow [Pa] , t_h is average thickness of ice cover between cross sections [m] , L is the distance between cross sections [m] , k_1 is a coefficient equal to the ratio of lateral stress to the longitudinal stress in the ice cover (ratio less than or equal to 1.0) and φ_i is the angle of friction of ice/bank interface.

ICESIM calculates the stress in the ice cover proceeding downstream as follows:

$$S_i = \frac{F_t + \ F_d + F_{Wd} - F_c - F_t}{t_h\ W_i} \tag{3.79}$$

In this representation, $S_i$is the stress in the ice cover [Pa] , $F_{t,..etc}$ are acting forces as defined above [N] , t_h is the ice thickness [m] , W_i is the ice cover width [m].

If the stress amount exceeds the maximum internal resistance of the ice cover, the ice front may recede but the cover thickens vertically to attain the minimum required thickness. As mentioned before this process is called “shoving” or “telescoping”. The internal resistance can be determined from Pariset et al. (1966) as follows:

$$F_{ir} = \gamma_i \left(1 - \frac{\gamma_i}{\gamma_w}\right) \frac{{t_h}^2\ W_i}{2}\ k_2 \tag{3.80}$$

Where F_{ir} is the internal resistance of ice cover [N] , k_2 is the *Rankin's passive coefficient* (greater than or equal to 1.0), t_h is the ice thickness [m] , W_i is the ice width [m] , γ_i is the specific weight of ice [9020 N/m^3], γ_w is the specific weight of water [9800 N/m^3].

Values of k_1, $\tan\varphi_i$, and k_2, which are key components of the shoving process, are not precisely known but it has been shown that the product $k_1.k_2\ .\ \tan\varphi_i$ is between 1.3 – 1.6.

Ice thickness calculation after shoving occurrence can be finalized as:

$$t_h{}' = \frac{2\ S_i}{k_2\ \left(1 - \frac{\gamma_i}{\gamma_w}\right)\ \gamma_i} \tag{3.81}$$

This calculation proceeds from upstream to downstream to the first assigned cross section and the total volume of ice required to thicken the subject cross sections is computed. Finally the time to produce this volume of ice is calculated and updated in the calculations.

Ice cover progression by ”Packing process”

The Froude number criterion for controlling the juxtaposition process is another key point in ice cover advancement as it occurs with or without the aid of deposition.

Ice cover advancement is represented by ”packing” when the rate of ice inflow is significantly higher than the transport capability under the ice cover. So, advancement can be calibrated by varying the critical Froude number while the thickening process is governed by the maximum erosion velocity limit under the ice.

Water surface profile

The one dimensional Bernoulli energy equation is used in ICESIM for calculation of the water surface profile assuming gradually varied subcritical flow (see Appendix A). The calculation begins at a known water surface elevation is used at the downstream cross section with known hydraulic conditions such as bearing capacity with/without ice, widths, areas, etc.., and proceeds upstream using an interactive standard step procedure.

ICESIM conceptual assumptions

(a) Rate of Ice Generation Equations

- No explicit allowance is made for snowfall.
- Assumes average water temperature of section must be below 0°C to generate ice. Input temperatures must be adjusted accordingly to compensate for this condition as ice generation can occur even if the average temperature is slightly above 0°C.
- ICESIM does not directly account for the reduction of ice generation area due to the insulation of the water surface by accumulating plans of slush ice.

(b) Ice Deposition

- Model does not account for buoyancy of particles, whereas this could be achieved using a densimetric Froude number.

(c) Border Ice Growth

- Section conveyance does not consider the presence of border ice.

(d) Shoving

- In calculating hydrodynamic thrust, the full width is used rather than only the fragmented cover width (i.e. assumes border ice breaks up as ice progression occurs).
- Bottom of ice cover width is used for stability calculation.

(e) Progression by Packing

- Model Assumes shoving cannot occur downstream of packing section.
- Model Allows for high cover strength and variable cohesion.

(f) Water Surface Backwater Profiles

- Assumes effect of velocity distribution for three-dimensional streamlines is negligible.
- Assumes contraction/expansion losses are negligible.
- Does not consider flow separation.

ICESIM subroutines and modules are presented in appendix B.

3.3 Introduction to the ice climate model

3.3.1 Thermal regime of river ice

River and lake ice processes are triggered by thermal variation in a water body that permits frazil crystal nucleation. Nucleation process is briefly discussed in section 2.2.1. In all nucleation cases, ice crystals are formed due to super cooling of the water body. Super cooling is due to heat transfer from the "warmer" water body to the "colder" atmosphere through the water/air interface. The heat transfer in rivers and lakes in fall and winter is controlled by atmospheric factors including air temperature, wind velocity, barometric pressure, precipitation and the most important, solar radiation which ultimately controls all climatic processes. Solar radiation that reaches the ground is called *insolation* and consists of two parts: direct solar radiation and diffuse sky radiation (Ashton, 1986).

Ice production can form ice cover in rivers only if the water velocity is less than 0.6 m/s (Ashton, 1986). In higher velocities, more than 1 m/s, hydraulic condition rules the ice cover formation since the high mixing prevents ice particle flotation and disorders the water thermal stratification. Instead, the frazil agglomeration process causes clusters of various ice forms to emerge on the water surface. Frazil clusters have greater fall velocity which causes them to rise to the water surface, As already mentioned in chapter 2, these frazil ice floes play an important role in ice cover formation in rivers. Frazil ice formation balances the heat loss of water to the atmosphere by releasing the latent heat of fusion. A large ratio, up to 1450, exists in volumetric water temperature increase by formation of a single volume of ice which illustrates the important share of turbulent heat transfer in ice particle growth (Ashton, 1986). One of the main sources of frazil ice generation in rivers is the introduction of ice crystals formed in the atmosphere in to the water, with sizes up to 100μm which is big enough to trigger the formation of ice nuclei by initial breeding (secondary nucleation) (Osterkamp and Gosink, 1983; Gosink and Osterkamp, 1983; Ashton, 1986).

Heat conduction in still water forms the ice cover through the process of static ice cover formation. Heat transfers from water to the atmosphere through the ice cover and likely snow cover on top of it in different rate in each media. As depicted in ,Figure 3.10 T_w is water temperature, T_m is ice cover temperature at the bottom which equals to 0°C and T_s is ice cover temperature at the top which is usually different than the air temperature, T_a. The parameters k_i and ρ_i are thermal conductivity and density of ice respectively, and h_i is the thermal ice cover thickness. The temperature profile can be assumed linear through the ice cover.

Heat loss causes the static ice to form in a certain rate as follows:

$$\rho_i \lambda_i \frac{dh_i}{dt} = \frac{-k_i}{h_i} \left(T_m - T_s\right) \tag{3.82}$$

where $\lambda_i$is the heat of fusion.

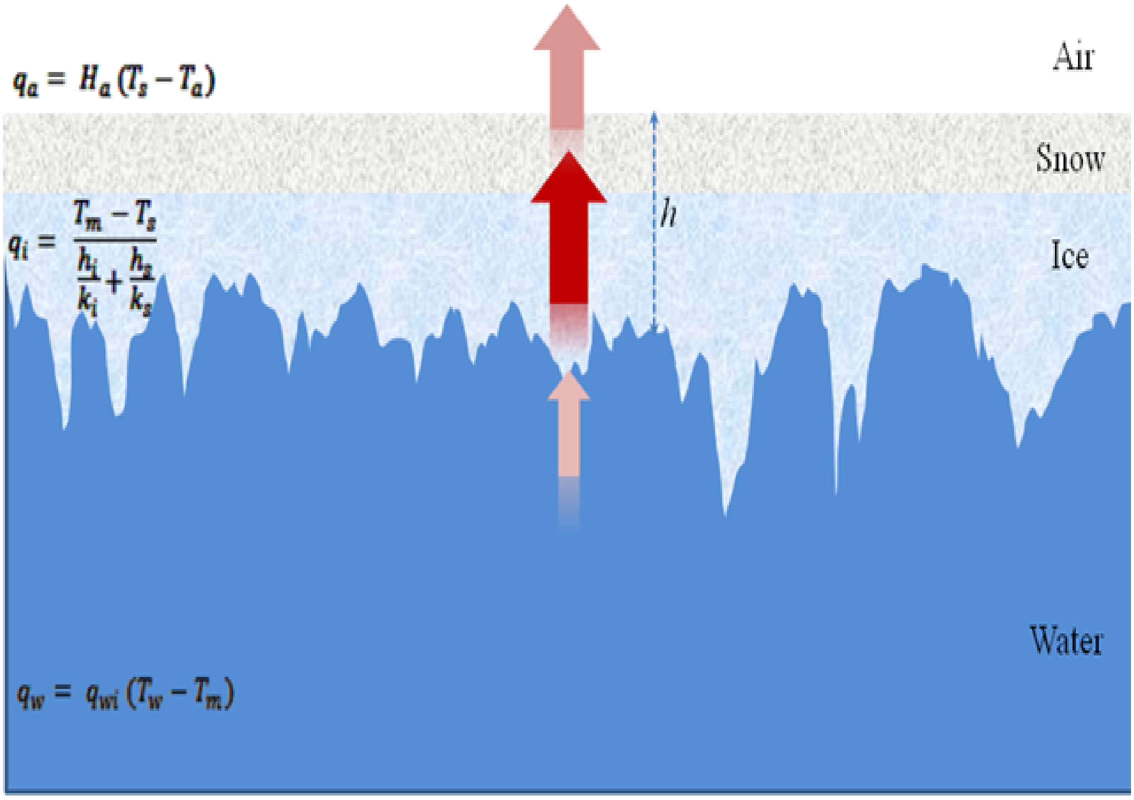

Figure 3.10: Heat transfer from water to air in ice covered rivers (after Ashton, 1989)

Integration of the above formula considering the initial condition of h_i=*0* and *t=0*, results in *Stefan*'s method for static ice formation:

$$h_i = \left[\frac{-2k_i}{\rho_i \lambda_i}\int_0^t (T_m - T_s)dt\right]^{0.5} = a\left[\int_0^t (T_m - T_s)dt\right]^{0.5} \equiv aS^{0.5} \tag{3.83}$$

Where a is an empirical equation including some factors which are not considered in the analysis and S is the cumulative time of freezing.

It is notable that the same temperature is assumed for the ice top and the atmosphere which is valid when the ice cover is thick enough (20-30 cm). This assumption is also the case in this study since the ice thickness is estimated to be more than 30 cm in most of the ice cover period.

The rate of static ice cover growth in time can be represented as (Ashton, 1986):

$$\Delta h_i = \frac{\Delta t}{\rho_i \lambda} \frac{T_m - T_a}{\frac{h_i}{k_i} + \frac{h_s}{k_s} + \frac{1}{H_a}} \tag{3.84}$$

where H_a is the heat transfer coefficient and can be found based on density of the snow and the cover (Mellor, 1978). Typically the value for $H_a$varies between 10W/m^2°C in no

Ice cover condition	a in. ($F^{-1/2}$. $Day^{-1/2}$)	a cm($^{o}C^{-1\backslash 2}$. $Day^{-1/2}$)
Windy lakes with no snow	0.8	2.7
Average lake with snow	0.5 ˜ 0.7	1.7 ˜ 2.4
Average river with snow	0.4 ˜ 0.5	1.3 ˜ 1.7
Sheltered small river with rapid flow	0.2 ˜ 0.4	0.7 ˜ 1.4

Table 3.3: Variation of constant for Stefan method (Michel (1971)

wind condition to 25 W/m^{2}°C in condition of 4 m/s wind. The parameters h_s and k_s are snow cover thickness and snow cover conductivity, respectively.

The Stefan method, also known as the degree-day method, was introduced by Stefan (1889). The Stefan method has been practically used to simulate river and lake ice thermal growth (Michel, 1971; Pivovarov, 1973). This method estimates thermal ice thickness, h_i based on the cumulative freezing degree-days of the air temperature as follows:

$$h_i = a\sqrt{D_d} \tag{3.85}$$

where a is a site specific empirical equation and D_d is the cumulative freezing degree days of the air temperature (equivalent to S in equation 3.83) .

Empirical constants of a may vary with the site but typical values according to the site specifications have been reported by Michel,1971 in Table 3.3. The Stefan equation can give acceptable results for the thickening of ice cover with small initial thicknesses (h_{i0}).

The Stefan method (Equation 3.85) is not applicable once the maximum freezing degree-days have been achieved. In other words, it is not capable to simulate the ice thickness during the decay period. Bilello (1980) suggested the use of accumulated thawing degree-days to simulate the rate of decay and ice thickness from its maximum thickness.

Bilello's equation can be summarized as follows:

$$h_i = h_{i\ max} - BD_t \tag{3.86}$$

where h_i is the ice thickness, $h_{i\ max}$ is the maximum ice thickness at the beginning of the ice decay, B is an empirical constant which is site dependant, and D_t is accumulative thawing degree-days. Even Belillo indicated that several coefficients could be used for describing the thawing process based on the meteorological conditions. However, since complete examination has not yet been performed on the method, no coefficients are suggested for estimation of ice thickness after the maximum freezing degree-days.

In general, a formula of the following form would be more appropriate than Stefan method (Shen and Chiang, 1984)

$$h_i{}^2 = h_{i0} - aD_d \tag{3.87}$$

where $h_i$is the ice thickness, h_{i0} is the initial ice thickness a is the Stefan method constant which is the site specific value D_d is the accumulative freezing degree days.

3.3.2 Modified degree-days method

Based on thermodynamics, vertical ice growth rate after ice cover formation can be described using the equation below (Shen and Chiang, 1984):

$$\frac{dh_i}{dt}\,\rho_i\lambda_i = \left[\frac{T_m - T_a}{\frac{h_i}{k_i} + \frac{h_s}{k_s} + \frac{1}{C_{ia}}}\right] - C_{wi}(T_w - T_m) \tag{3.88}$$

$\frac{dh_i}{dt}$ is the rate of ice growth in time, iρ_is the density of ice, λ_i is latent heat of fusion of ice, C_{wi} is the heat transfer coefficient from water to ice, k_i is the thermal conductivity of ice, C_{ia} is the heat transfer coefficient from ice to air.

The Stefan method (equation 3.85) is a simplified form of equation 3.88 based on freezing degree days and a case specific coefficient (a).

Comparing the two methods, the maximum value for c$a$an be calculated theoretically as:

$$a_{max} = \left(\frac{2k_i}{\rho_i\lambda_i}\right)^{0.5} \tag{3.89}$$

It is reiterating that the a value can be affected by meteorological processes such as snow fall, because the snow cover can isolate the top of the ice cover, decreasing the heat transfer and effectively lowering the a value. On the other hand, ice thickening due to processes such as mechanical thickness growth (shoving), floe under-turning and frazil accumulation increase the a value.

So, based on equations above, an ice cover thickness equation including thermodynamic elements and freezing degree-days terms can be summarized as follows:

$$h_i = -\frac{k_i}{C_{ia}} + \left[\left(\frac{k_i}{C_{ia}} + h_{i0}\right)^2 + \frac{2k_i}{\rho_i\lambda_i}\,D_d\right]^{0.5} \tag{3.90}$$

It is notable that by neglecting the terms $\frac{k_i}{C_{ia}}$and h_{i0}, equation (3-45) takes the form of the Stefan equation.

Shen (1984) noted that the term $\frac{k_i}{C_{ia}}$ is an important parameter and should not be neglected in thermal ice growth. Thermal conductivity values of pure ice can be estimated based on Dorsey (1940), who tabulated and summarized the k_i values for air temperature between 0°C to -40°C and simplified it as follows :

$$k_i = 2.21 - 0.011T_a \tag{3.91}$$

Where $T_a$is the air temperature. It is also notable Equation 3-46 does not apply if air temperature is 0°C because ice melting commences.

As shown in ,Figure 3.10 snow cover has considerable effect on thermal ice growth by affecting the thermal conductivity and resisting the heat transfer. So, considering the snow cover presence, equation (3-45) can be rewritten as:

$$h_t = -\left(\frac{k_i}{C_{sa}} + \frac{k_i h_s}{k_s}\right) + \left[\left(\frac{k_i}{C_{sa}} + \frac{k_i h_s}{k_s} + h_{i0}\right)^2 + \frac{2k_i}{\rho_i \lambda_i}\ D_d\ \right]^{0.5} \tag{3.92}$$

In this equation, h_t is the total ice thickness considering the snow cover, k_i is the thermal conductivity of ice cover, C_{sa} is the heat transfer coefficient at the snow-air interface, h_s is the snow cover thickness, k_s is the thermal conductivity of ice, h_{i0} is the initial thickness of ice, ρ_i is the density of ice, is the latent heat of fusion of ice and D_d is the accumulative freezing degree-days.

3.3.3 Thermal decay of the cover

Break up starts due to thermal effects followed by mechanical processes. Decay and weakening of solid ice cover usually happens because of increasing air temperature. When the water temperature increases up to above the freezing point, the ice cover starts to decay rapidly due to the effect of turbulent heat transfer from water to the ice cover. So the heat transfer coefficient from "warmer" water to the ice cover can be estimated based on the following equation(Shen and Yapa, 1985) :

$$C_{wi} = 1622\ {V_w}^{0.8}\ H^{-0.2} \tag{3.93}$$

Where the iC_{wi}s the heat transfer coefficient from water to ice, V_w is the flow velocity (m/s) and H is the flow depth (m).

The ice thickness at any time step of decaying period can be calculated as follows:

$$h_{j+1} = \ h_j - b - aT_a \tag{3.94}$$

In this equation, b is the decay rate and aT_a is the rate of melting at the upper part of the ice cover.

The decay rate can be estimated using the equations below(Shen and Yapa, 1985):

$$\rho_i \lambda_i \frac{dh}{dt} = -C_{ia}\left(T_a - T_m\right) - C_{wi}(T_w - T_m) \tag{3.95}$$

$$\frac{dh}{dt} = \frac{-C_{ia}\left(T_a - T_m\right) - C_{wi}(T_w - T_m)}{\rho_i \lambda_i} \tag{3.96}$$

$$b = \frac{dh}{dt} = \frac{-C_{ia}\left(T_a\right) - C_{wi}(T_w)}{\rho_i \lambda_i} \tag{3.97}$$

3.4 Alluvial channel response to river ice

Parameters and relations

Similitude of independent variables associated with the flow in alluvial channels provides a helpful approach to characterize many aspects of river ice and alluvial channel stability interactions.

For open water condition in alluvial channels, several parameters influence the flow process and resulting bed morphology, including (Ettema, 2002):

- Inflow rate of water per unit width of the channel q
- Inflow rate of sediment per unit width of the channel q_s
- Water density ρ
- Kinematic viscosity ν
- Bed sediment diameter d
- Geometric standard deviation σ_g
- Sediment density ρ_s
- Submerged unit weight $g\Delta\rho$
- Channel slope S_0

Figure 3.11 visualizes several of these parameters in an ice-covered river.

The presence of an ice cover affects channel morphodynamics, but its effect is dependent on other river characteristics such as water depth. In other words, river ice influence on channel equilibrium is inversely related to the channel size (i.e., depth). In deep flowing rivers, based on severity of the ice cover processes, river hydraulic condition, i.e. water

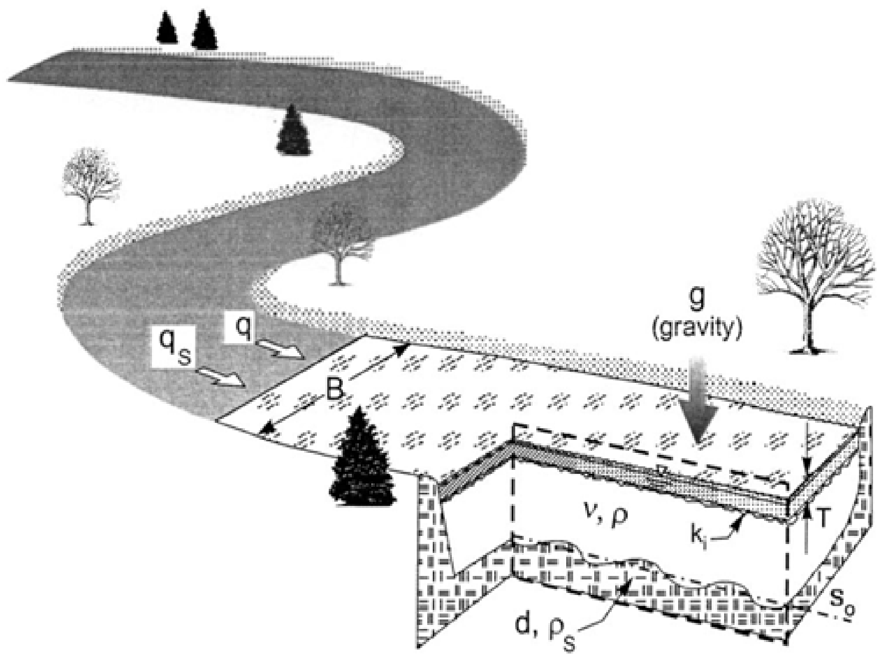

Figure 3.11: Associating variables with in alluvial channels under ice cover (Ettema 2002)

velocity and depth, may be considerably affected by the presence of a rough cover (Ghareh Aghaji Zare et al., 2015) .

A common assumption in the hydraulics of ice-covered channels is that ice covers are free floating (Ashton, 1986), and comprehensive observations confirm that this is true for most rivers (Ettema and Daly, 2004). The influence of an ice cover on river sediment bearing capacity depends on whether the cover is fixed or floating. Under floating ice covers, the river bed usually aggrades because the average velocity decreases, therefore sediment transport capacity of an ice covered channel, ,q_{sc} is less than the rate at which the sediment load is supplied to the channel, ,$q\ _s$ i.e.,$q_{sc} < q\ _s$. Conversely, when the cover is fixed and/or thick i.e. (large T/Y), the bed locally degrades because the average water velocity under the cover increases. So, $q_{sc}> q\ _s$ (Ettema and Daly, 2004). The next section describes in detail the parameters involved in river ice-morphology interaction processes.

3.4.1 Important parameters in river ice- river morphodynamics interactions

Water temperature

The physical properties of water are influenced by temperature. For example, cooling of water from 25 °C to 0 °C results in almost a 100% increase in υ and a slight variation about 0.3% in ρ (Ettema, 2002). This increases kinematic viscosity, ν, which directly reduces the Reynolds number ($Re = q/\nu$)and particle Reynolds number($Re_* = u_{*_b}d/\nu$) and thereby influences sediment transport mechanics and channel response.

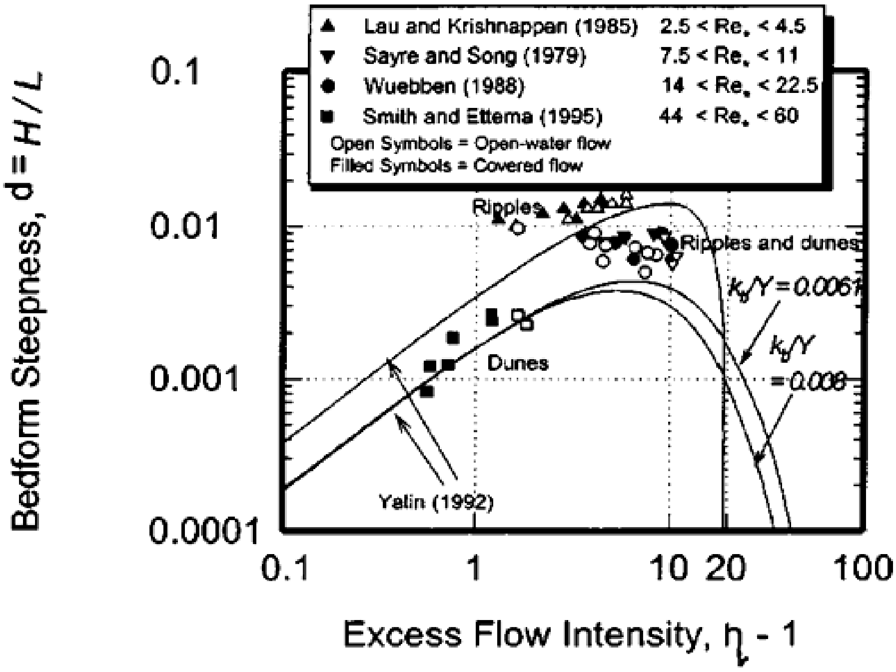

Figure 3.12: Comparison of flume data for bed form steepness and empirical open water curves developed by Yalin (1992)

Studies of Lane et al. (1949) and Colby and Scott (1965) on field investigated data and Ho (1939) and Straub (1955) ,Taylor and Vanoni (1972) and Hong et al. (1984) on flume data, all confirm that sediment transport rate increases when water temperature decreases. Increase in sediment transport rate is even more substantial when the water temperature drops below 15°C. For instance Hong et al. (1984) show based on flume data that there is an increase in mean concentration of bed sediment transport up to 7 to 10 fold when water temperature drops from 30° to 0°C. The concentration of sediment transport was probed in a bed layer where the thickness of the layer can be calculated as (Ettema and Daly, 2004):

$$t_s = d\eta^{0.5} \tag{3.98}$$

Where η is equal to:

$$\eta = \frac{\theta}{\theta_c} \tag{3.99}$$

In the equation above, θ is the Shield's parameter and θ_c is the critical value for initial entrainment of bed sediment. θ can be calculated as:

$$\theta = \left(\frac{\rho (u_{*b})^2}{g \Delta \rho d} \right) \tag{3.100}$$

where ρ is the water density, u_{*b} is the bed shear velocity, $g\Delta\rho d$ is submerged unit weight and d is the particle diameter.

Based on Hong et.al. (1984) bed level concentration of sediment movement increases significantly only if the bed layer Reynolds number exceeds twenty. Bed layer Reynolds number has been defined by Hong et. al. (1984) also as follows:

$$Re_b = \frac{u_* \ d \ \eta^{0.5}}{\nu} \tag{3.101}$$

Few studies have been performed about the erosion of cohesive sediment or clay in cold water. In this field, Raudkivi and Hutchison (1974) probed the influence of water temperature in erosion rate of cohesive sediments. They found that water viscosity and thermal energy of water in interparticle spaces decrease when the water temperature decreases. Concluded trends, which are complicated by consideration of water salinity and level of cohesiveness of particles, suggest a direct positive correlation between water temperature and erosion rate of cohesive sediments.

Bedform Geometry

Ice presence influences overall tractive force of the flow as well as the turbulence due to redistribution of the water flow pattern. Therefore the rate of flow energy exerted to the bed changes and usually reduces when the cover is free floating (Ettema et al., 2000).

Comparing flume data with empirical open water curves developed by Yalin and Selim (1992) , Ettema (2004) found that an ice cover, by reducing the excess flow intensity at the bed, reduces the bed form steepness. It was also observed that the bedform geometry conforms to the same relationship that Yalin provided for open water conditions. Figure 313shows the results of empirical and flume data comparison for bedform steepness.

The influence of ice cover presence on bedform length also was studied by Ettema (1999a), and compared to Yalin's empirical curves (1992) for open-water conditions. Results suggest that the smooth ice cover may intensify generation of macro scale turbulence in the flow, which slightly increases the frequency of structures generated from bed forms. This allows the flow structures to grow to the full depth of the flow. Consequently, the same bedform length scaling was observed in covered and open-water experiments Figure 3.12.

3.4.2 Sediment transport by ice

River ice directly causes sediment entrainment and transportation due to presence of frazil ice as well as anchor ice formation at the channel bed.

Slush ice-sediment mixture also ice-sediment clumps may be observed during the freeze-up period. The latter could be due to anchor ice formation and release at the river bed which rips off a part of bed material and entrains them to the water body.

Ettema (2004) noted that:"The amounts of sediment entrained or rafted with the ice slush and clumps can produce a substantial momentary surge in the overall quantity of sediment moved by some rivers and streams."

Frazil ice adhesion to sediment particles is the first step of sediment entrainment to the flow. Frazil mixing in the water column due to turbulence causes the frazil particles to travel deep into the water, despite the positive buoyancy of frazil. Frazil ice particles then start to accumulate on bed objects exposed to the flow and form anchor ice.

This process may happen repeatedly with a short-term frequency. Each ice formation and release event potentially increases the sediment entrainment by repeated ice-rafting events along the river reach. The entrainment mechanism has been studied by Kempema et al. (1986, 1993) using laboratory investigations. Anchor ice formation experiments were also reported by (Kerr et al., 1997).

Anchor ice formation is usually limited on fine non-cohesive bed material because these materials can not hold significant anchor ice accumulation and are easily lifted (Marcotte, 1984). Larger sediment size particles on the river bed are heavier and usually penetrate higher into the flow and are thus more influenced by water thermal condition and more exposed to frazil particles. Therefore, thicker anchor ice normally forms on coarser bed material. Vast areas of the river bed may be covered by anchor ice. As an instance, Marcott (1984) reported 20 Km^2 of the Lake Saint Louise Lachine rapids reach of the St. Lawrence river coated in layer of anchor ice up to 1.5 m thick, which when released, forms floating blocks over 6 m in length. Based on Marcotte (1984), Ettema(2003) noted it would be interesting to study if frazil and anchor ice would alter the size distribution of sediment on a channel bed.

A stabilized ice cover prevents the water body from being super cooled by exposure to the air; so, frazil nucleation due to super cooling, anchor ice formation and consequent ice rafting usually cease.

3.4.3 Ice cover effect on channel morphology

Channel morphology changes may occur over a wide range of time and length scale. For instance, some morphologic variation such as local cross section variation and meander loop cut off, bank failure and erosion can take place over a short period of drastic ice stage variation like ice jam formation and release. On the other hand, thalweg realignment may not be visible in short periods even over a medium period of time like a winter (Ettema, 2002; Ettema and Zabilansky, 2004; Ettema and Daly, 2004).

Avulsion and meander cutoff

Presence of meander loops or sub-channels around bars reduce channel conveyance which turns the reach into a potential area for ice jam formation. Irregularity in channel cross section or morphology such as high curvature significantly diminishes the ability of the reach to pass oncoming ice floes especially during the spring break-up period.

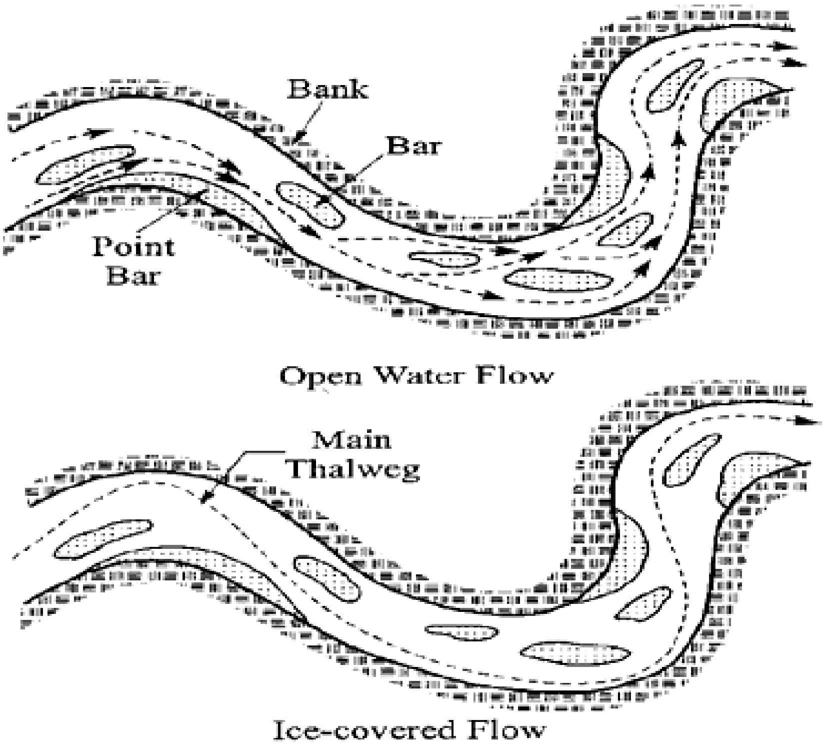

Figure 3.13: River ice impact on thalweg of sinuous braided channel,Ettema (2002)

Dupre and Thompson (1979) and Prowse (1993, 2001) suggest that scouring and avulsion due to ice jams plays an important role in shifting the distributary channels of river deltas. Zabilansky (2002) studied ice influence on channel condition and noted where freeze-up jams lead to thalweg shifts in a sinuous-braided reach of a channel, and where jam formation in tight meander bends results in bend cutoff. According to the aforementioned studies, as shown in , Figure 3.13 ice cover causes the main thalweg to be more sinuous.

River ice jams eventually raise the water stage therefore water flow can proceed over bank across the neck of the meander loop. Erodible material in the neck of the meander can easily scour, leading to meander cutoff, which shortens and steepens the channel reach. Figure 3.14 conceptually shows the effect of ice cover on meander wave length. As shown, the cover may cause the meander loops to shorten.

Alternatively, ice jam induced flooding over large, non-erodible bank material may lead to overbank sediment deposition, which increases the bank height and reinforces the meander loop. Eardley (1938) reported such a phenomenon on the flood plain of Yukon River. Ettema (1999a); Ettema and Daly (2004) also reported the same event for the Fort Peck reach of Missouri River. In this regard, he concluded that: "Overbank deposition of sediment, together with ice-run gouging and abrasion of sediment erosion from the lower portion of a bank, may over steepen riverbanks".

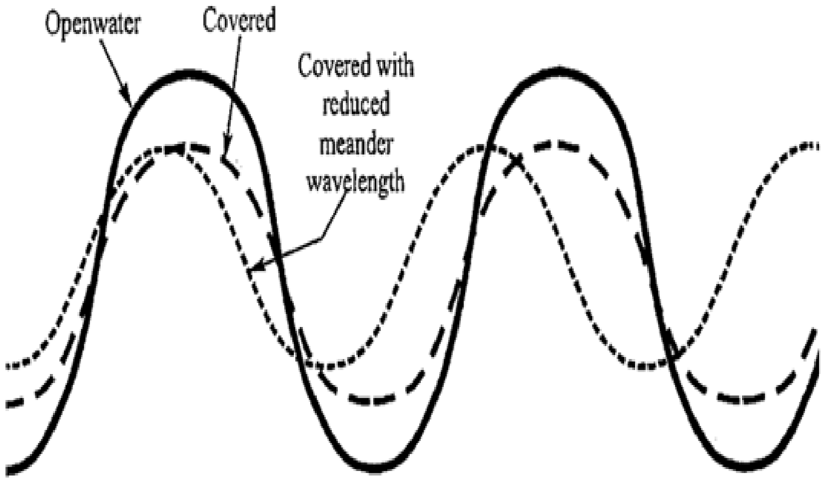

Figure 3.14: Conceptual influence of ice cover on meandering channel of uniform flow depth, Ettema (2004)

Ice cover effect on river banks

River ice presence affects river geomorphology through several geo-mechanic and loading impacts. These impacts decrease river bank resistance against hydraulic erosion and physical scouring which leads to more local sediment initiation to the channel. Some of important effects of ice on river banks are as follows.

1. Reduction in river bank strength

   Ice cover causes water stage variation. Ice cover formation and jamming processes cause the water stage to rise on a river bank, whereas cover break-up and ice jam release lower it quickly. These rapid fluctuations in water stage may reduce bank resistance against erosion due to increased seepage pressure after bank saturation and abrupt water level drop, which reduces shearing resistance of the bank material. Formation of thick ice along the river bank may affect and possibly block seepage through the bank, which leads to slight rising of the water table. Saturated banks, as mentioned, are less resistant to erosion, which leads to a zone of weakened river banks at the vicinity of the ice cover, as shown in Figure 3.15.

2. Loading of bankfast ice

   Another important factor in bank erosion due to ice is bankfast ice, which particularly affects steep banks consisting of sufficient clay to be cohesive. Zabilansky et al. (2002) reported the process along the Fort Peck Reach of the Missouri River. This erosion mechanism can be described as follows. During the break up period, water stage drops in the channel, but some ice portions may stick to the river banks and stay higher than the water surface. The cantilevered ice portions soon collapse and weaken and wrench bank materials, also carrying some of them to the water, which introduces

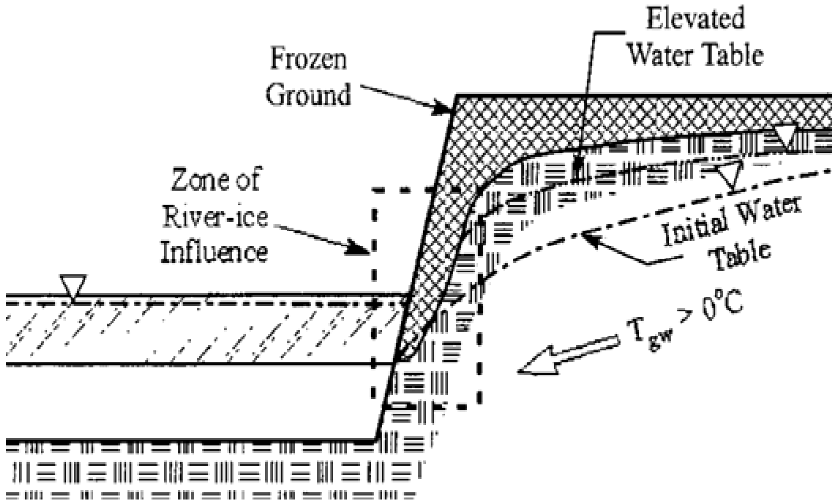

Figure 3.15: Ice cover effect on river banks with high water table, Definition of weakened river bank zone, Ettema (2002)

more suspended and bed sediment particles to the river. Figure 3.16 describes how this mechanism might weaken the bank.

Wuebben (1988b) reported a similar effect on riprap commonly termed as "plucking". During this process, bankfast ice remains attached to riprap stones, eventually transporting them while still frozen to the ice sheet. He discussed plucking concerns in design of riprap for river bank protection.

3. Ice run abrasion

Channel banks are potentially subject to heavy abrasion by ice runs following ice jam release. This gouging mainly takes place in steep channels that convey high velocity flows. The phenomenon has been studied comprehensively by Marusenko (1956),Hamelin (1979); Smith (1979); Smith and Ettema (1997); Smith and Pearce (2000); U.S. Army Engineer District (1983); Doyle (1988),Wuebben (1988b) and Uunila (1997) . Amongst them, Smith (1979) studied 24 rivers in Alberta, Canada which led him to the hypothesis that ice

runs enlarge channel cross sections at the bank-full stage by as much as 2.6–3 times those of comparable flow rivers not subject to ice runs. On the other hand, Kellerhals and Church (1980) opened a discussion against Smith's hypothesis noting that other factors made the widening effect in the channels studied by Smith (1979) which are not related necessarily to the river ice runs. Uunila (1997) also discussed that the ice jam even may protect channel from widening by causing over bank flow. Ettema (2002) also noted that for sluggish ice runs, an ice wall at the river banks may defend the bank from contacting the ice run and thereby prevent abrasion by the ice. A key determinant for the potential for channel abrasion by ice is the local morphology of the channel. For instance, sharp bends, point bars, and creek or river confluences can influence the likelihood for an ice run to contact the river bank.

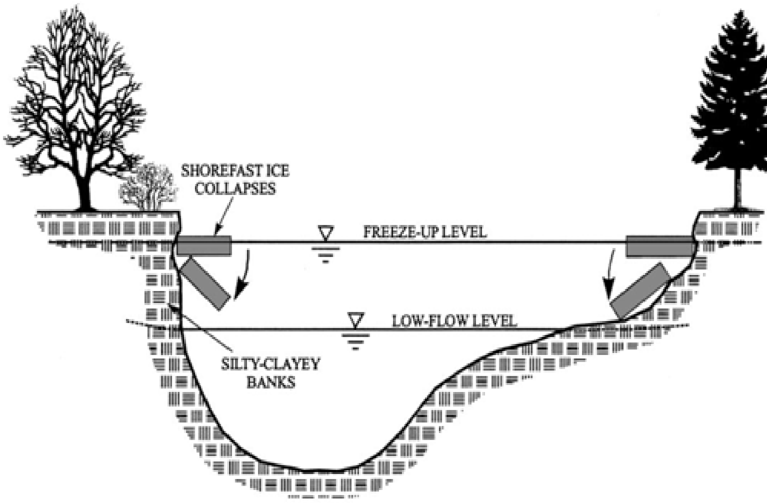

Figure 3.16: Bankfast ice effect on river banks also bank material during low flow stage, Ettema (2002)

Two main channel forms have been observed in gravelly rivers due to physical ice scouring. The first one is "ice push ridges" which are formed by heavy ice runs when sediment is shoved by the ice along the river banks and accumulates at the location of an ice jam (Bird, 1974). The shoved sediment then forms a ridge at the jam location, and when the finer sediments get washed by the flow during jam release, remnants comprised of coarser gravel and boulders remain in the ridge.

The other feature is "cobble pavement" and it forms when finer materials from the surface of the bars or banks are swept by ice and cobbles. The resultant surface is comprised of cobbles whose major axis is aligned parallel to the channel and whose size gradually decreases downstream (Mackay and Mackay, 1977). The resultant cobble pavement may extend for many miles along the banks of large northern rivers, such as the Mackenzie and Yukon (Wentworth, 1932).

Hamelin (1979) also discussed another interesting feature due to ice effect on river banks. Ice run gouging and over bank deposition of sediment may result in formation of an elevated ridge along the banks of some northern rivers. These features are called "bechevnik" in Siberian rivers, which provide an easy way to towing boats upstream by horse or man. "Becheva" means towing in Russian. Figure 3.17 shows a bechevnik at the Rimouski River, Quebec (Dubé et al., 2009).

4. Hydraulic and geo-mechanic complex impact

   Channel destabilization is not just due to hydraulic or geo-mechanic impact but mostly due to their combination. Each of those mentioned parameters may disturb channel morphology but not permanently destabilize it.

   In this regard, Ettema (2004) noted: "Sinuous-point-bar, sinuous-braided, and braided-alluvial channels are especially prone to river ice impact, especially if they have steep banks, formed of fine and partially cohesive sediments. The thalweg (or thalwegs) of

Figure 3.17: Bechevnik evidence in Rimouski River,Quebec, Dube et. al. (2009)

such channels usually lies close to the outer banks of bends, and the banks themselves are prone to border-ice loading, lack of vegetation cover typical of eroding banks!, and freeze-thaw weakening. Figure 10 illustrates this susceptibility. The thalweg lies close to the bank, such that the flow continually erodes the bank toe, thereby keeping the bank steep, and possibly undercutting the bank. Snow cannot protectively blanket the bank face. Frost penetration potentially is deep; the water table is held relatively high, and the channel shifts, destabilized". Ettema's Figure 10 has been reproduced herein as Figure 3.18.

As shown in Figure 3.18,combination of hydraulic impacts (such as thalweg shift and bank toe erosion) and geo-mechanic impacts (such as elevated seepage pressure and bankfast ice loading) may weaken the river banks mainly in channel bends which leads to overall channel destabilization.

In conclusion it is notable the literature about ice effect on alluvial channels is not extensive. Furthermore, even the entity of it is still topic of serious debate. On the other hand numerous publications discuss about the aspects of this effect namely: Marusenko (1956),Lane (1957),Lau and Krishnappan (1985),Collinson (1971),Mackay et al. (1974),Hamelin (1979),U.S. Army Engineer District (1983),Doyle (1988),Uunila (1997),Milburn and Prowse (1998),Zabilansky (2002),Ettema (1999a); Ettema et al. (2000); Ettema (2002); Ettema and Zabilansky (2004); Ettema and Daly (2004). Almost all these publications more or less contain hypotheses and conjectures. For instance, in most of them river ice properties such as thickness and roughness are considered as independent variables but it should be obvious that they may be dependent on flow as well as bed condition.

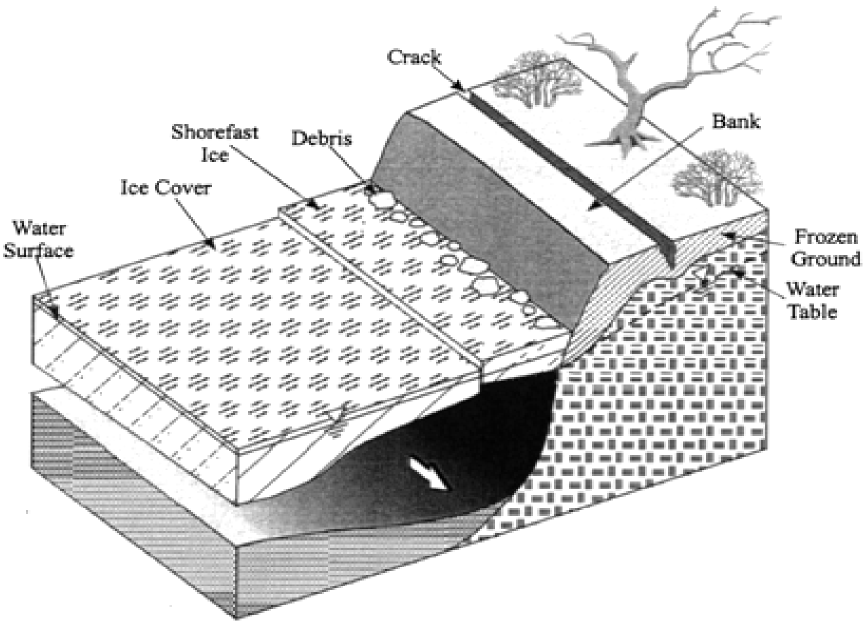

Figure 3.18: Combination of hydraulic and geo-mechanic effects on river bank destabilization,Ettema (2004)

It is clear that interactions between flow, ice and loose bed cause significant variations in river morphology in time and space and raise serious problems for scientific estimation of river characteristics (i.e. flow resistance, channel conveyance capacity and sediment transport) as well as engineering works such as design of hydro-electric generating stations and channel and bank stabilization.(Newbury and Malaher, 1973)

3.4.4 Sediment transport models

Sediment transport in rivers can be categorized in two main sets of sediment loads: suspended load and bed load.

There is no well-defined boundary between bed load and suspended load in natural streams, however, it is necessary to set a border between bed load and suspended load for mathematical representation purposes (Van Rijn, 1984).

Sediment motion in streams can be represented in three types of particle movement, all of which are governed by the value of the shear stress on the bed. They are namely:

- Rolling and/or Sliding
- Saltation
- Suspended particle motion

When the shear stress on the bed exceeds the critical value for initiation of motion, the particles will be rolling and sliding on the bed. As the shear stress increases, particles start to move by regularly jumps along the bed through the process of saltation. When the shear velocity exceeds the fall velocity of the sediment material, the particles can be lifted and transformed within the water body, more or less at the water velocity which forms the suspended load in the river (vanRijn, 1984). It is notable that, as stated, bed and suspended load transform to each other within a spectrum defined by the shear stress and turbulence in the flow. Particles remain suspended only if the vertical velocity component of the turbulent eddies compensates or exceeds the particle fall velocity (Bagnold, 1966). Suspended load is discussed in section 3.4.4 more in details.

Bed load models are generally based on the calculation of imposed force on bed materials. Bed load models compare calculated force to the critical force required for incipient motion of bed material regardless of the availability of the sediment for transport.

The bed load models are based on the laboratory observations of steady flow with uniform size distribution and hence, provided formulae are for uniform, steady flow condition.

The primary uncertainty in the application of any bed load model is the grain size distribution. Surface processes complicate the bed sediment layer structure. Processes like armoring cause the variation in the particle distribution, make it different horizontally and vertically. Figure 3.19 shows the stratigraphy of an armored bed with associating sediment layers. It is notable to remember that the surface sediment is important in defining the flow resistance, roughness measurements as well as the initiation of particle motion but the bed load transport calculations are mainly based on the subsurface sediment properties (Rennie, 2012). Bed material sampling in gravel and cobble bed rivers can be conducted through two main approaches. The sampling method is defined based on the objectives of the study. These two main methods are (Bunte and Abt, 2001):

- Surface sampling in which a preselected number of surface particles is sampled from predefined area.
- Sub-Surface sampling which samples preselected sediment volume from predefined sediment layer.

Theoretically, the surface grain size distribution seems to be more appropriate, however it is recommended to use the subsurface size distribution unless the method which is being applied is developed specifically for the surface grain size distribution (Parker, 1990; Rennie, 2012) because the primary role is to employ the same size distribution as the model is developed for.

Forces acting on a single particle situated on a slope, exposed to the flow can be categorized as Rennie (2012):

- Submerged weight of the particle acting vertically on the center of the mass of the particle. This force is result of gravity and buoyancy forces on the particle and can be described as:

$$F'_G = (\gamma_s - \gamma)\, C_1 D^3 \tag{3.102}$$

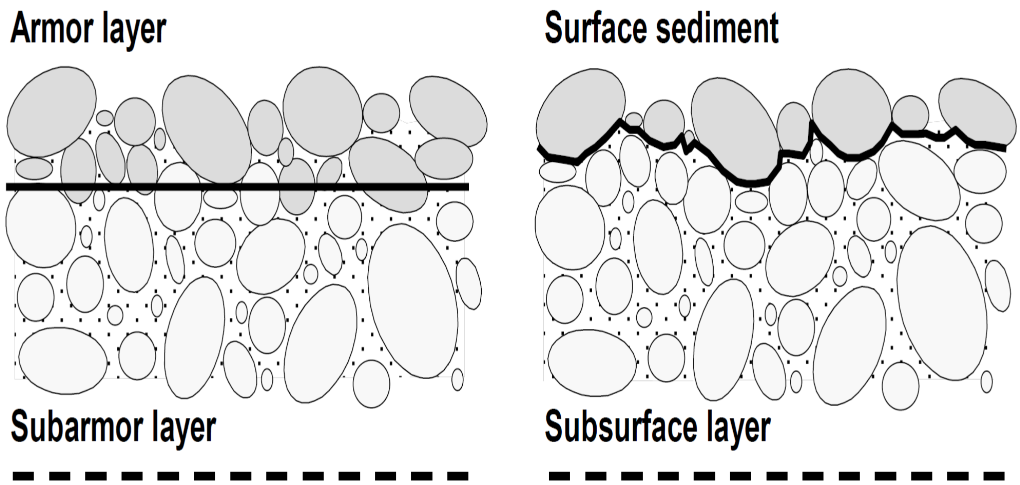

Figure 3.19: Stratigraphy of an armored bed illustrating the armor layer, subarmor layer, surface sediment and sub surface layer Bunte and Abt (2001)

in which the γ_s is the submerged specific weight of the sediment, C_1 is a form factor and D is the characteristic particle diameter.

- Drag force on the particle due to the shear stress acting on the particle at the direction of slope. The drag force can be described as:

$$F_D = \frac{1}{2} C_D \rho U^2 A_x \tag{3.103}$$

in this equation, C_D is the drag coefficient, A_x is the projected particle surface perpendicular to the flow and U is the average velocity over the same area.

- Lift force which is due to the velocity gradient between top and bottom of the particle. The lift force can be shown as:

$$F_L = \frac{1}{2} \rho C_L C_2 U^2 D^2 \tag{3.104}$$

in which the C_2 is the form factor and C_L is the lift coefficient.

Particle incipient motion starts when the sum of the moments about the active particle area is zero. Shields (1936) investigated the incipient motion of bed material and defined a relation between the two dimensionless parameters as: *particle mobility parameter and particle Reynolds number* both are expressed as:

$$F_s = \frac{{u_*}^2}{(S_s - 1)\, gD} \tag{3.105}$$

$$Re^* = \frac{u_* D}{\upsilon} \tag{3.106}$$

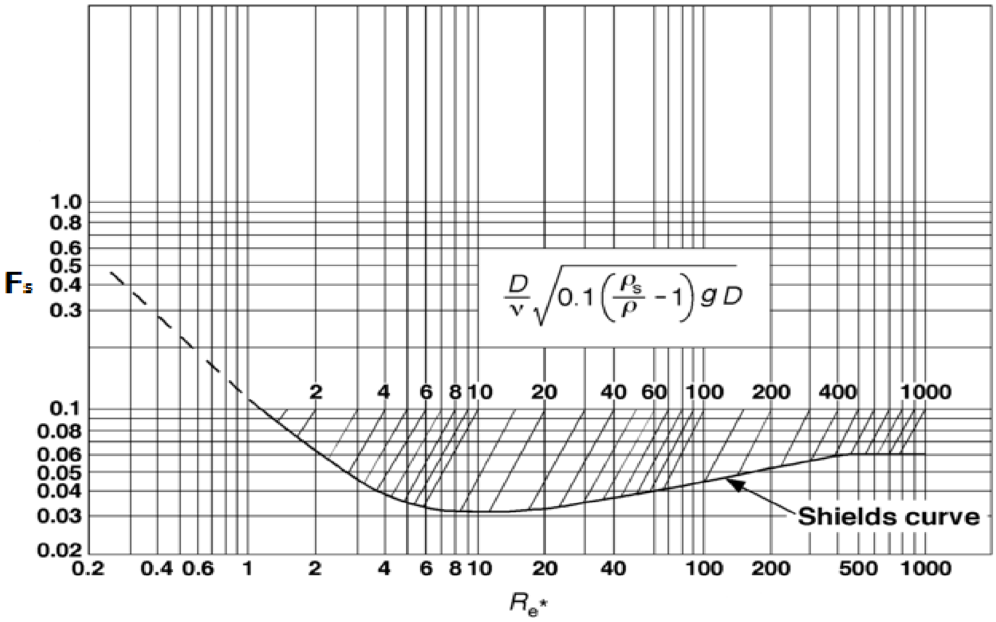

Figure 3.20: Shield's diagram (Shields, 1936)

Where S_s is the specific gravity parameter(ρ_s/ρ). He presented the results in a form of a graph well-known as Shields diagram (Figure 3.20). Based on the defined parameters above, the ratio of the critical shear stress applied on the bed as well as the critical shear stress necessary to mobilize bed material can be estimated according to the graph.

The relation between shear stresses and mass transport rate is schematically presented in the Figure 3.21.

As illustrated the figure, four main zones can be identified on the graph. No transport occurs in zone 1 and the bed materials are immobile, the shear stress on the bed material is lower than the critical shear stress. The shear stress is close to the critical value in zone two means that the transport begins and single stones start to move. Shear stress increases in zone 3 and partial transport is starting, however, largest grains are still immobile. The mass transport rate increases as the shear stress exceeds more than the critical value. General transport takes place in zone 4. In gravel bed rivers, this stage is associated with mobilized bed surface in discrete patches.

Bed load models

Several bed load models are considered in this study to calculate the bed load during the ice cover condition. They are generally based on the specification of a force that can mobilize the grains. Another important assumption made in the bed load models is that the transport is the direct function of the force rather than the availability of the sediment. The models formulation is based on uniform steady flow condition. The bed load models of this study are described in the following:

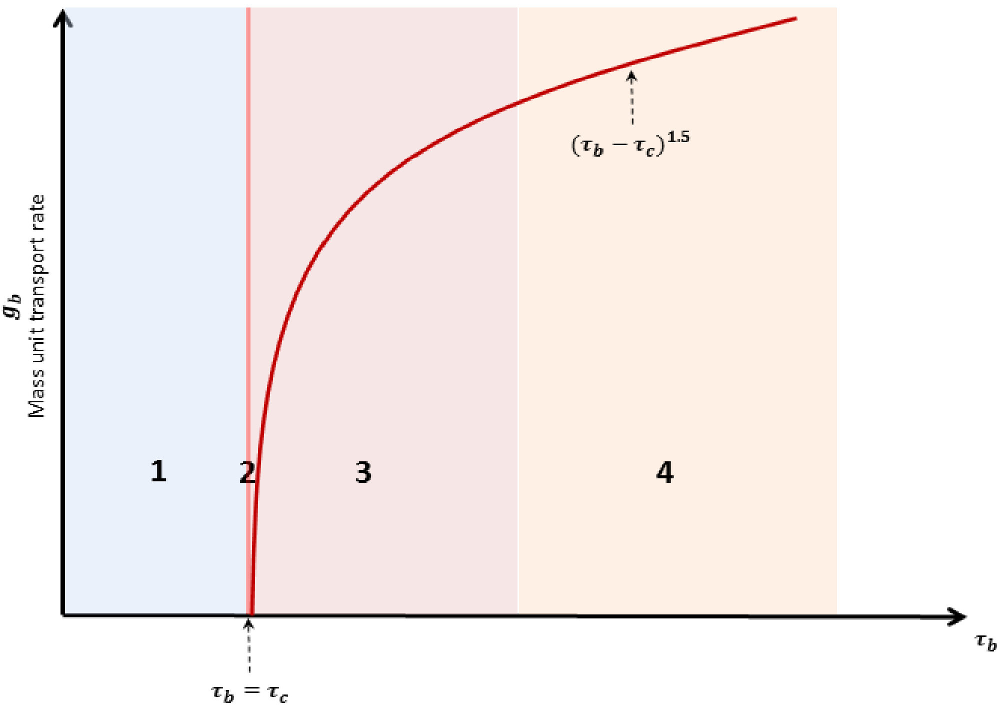

Figure 3.21: Schematic representation of shear stresses and mass transport rate

Meyer-Peter and Müller (1948), MPM model:

The MPM method is developed for gravel bed rivers with the range of particle diameter as *d=0.4-28.65 mm* based on large flume experiments. Model is restricted for non-suspended bed material. It generally can be represented as:

$$g_b = 8\rho_s g^{0.5} {d_m}^{1.5} \sqrt{\frac{\rho_s - \rho}{\rho}} \left[\frac{\tau \left(\frac{k}{k'}\right)^{1.5}}{\left(\rho_s - \rho\right) g d_m} - 0.047 \right]^{1.5} \tag{3.107}$$

in this equation, g_b is the mass unit transport rate (kg/m.s) and ρ_s is the sediment density. d_m is the representative particle size and can be defined as:

$$d_m = \sum P_i d_i \tag{3.108}$$

in which P_i is the proportion of the bed surface sediment comprised by the size fraction and d_i is the particle size geometric mean as:

$$d_i = \sqrt{d_{max} d_{min}} \tag{3.109}$$

The *(k/k')* factor shows that the model accounts the sediment transport just due to the grain shear stress, not the total stress. On the other mean, the resistance due to bed forms has no effect on sediment motion. The factor can be represented as:

$$\frac{k}{k'} = \sqrt{\frac{f'}{8}}\,\frac{V}{\sqrt{gRS}} \tag{3.110}$$

in which the *f'* is the friction factor which can be found from Moody diagram using the Reynolds number (Re=4VR/ρ) and the relative roughness representation defined as: $K_s = d_{90}/4R$.

Meyer-Peter and Müller (1948) reported the range of *(k/k')* between 0.5 and 1.

Assuming the maximum value for the factor, the MPM formula can be simplified as:

$$g_b = 8\rho_s g^{0.5} {d_m}^{1.5} \sqrt{\frac{\rho_s - \rho}{\rho}}\,\left(\tau^* - {\tau_c}^*\right)^{1.5} \tag{3.111}$$

$$\tau^* = \frac{\rho {u_*}^2}{{\gamma'}_s d_m} \tag{3.112}$$

in which the τ_c^* is equal to 0.047 which is typical value for experimental sediment mixture. γ_s' is the sediment submerged specific weight and can be calculated as: $\gamma_s' = {\rho'}_s.g$ where the ρ_s' represents the submerged density of bed material.

Einstein (1950) model:

The model is based on the probabilistic concept of bed material movement previously developed by Einstein (1937). The model is applicable to sand and highly mobile gravel beds. The model is derived for the uniform bed material range of *d=0.785 -28.65 mm*. However, the model is limited to steady, uniform flow and plane bed condition.

Einstein introduced the hiding function (ξ) concept in order to modify the grain mobility in mixed beds. Through this concept, it is assumed that the probability of grain entrainment (P) is equal to the probability that the instantaneous lift force on an individual particle exceeds the particles submerged weight.

The lift force is calculated based on velocity measurement at 0.35 $\varkappa$ in which the $\varkappa$ is the characteristic grain size and can be calculated as:

$$\varkappa = 0.77\Delta \qquad if\ \frac{\Delta}{\sigma'} > 1.8 \tag{3.113}$$

$$\varkappa = 1.39\ \sigma' \qquad if\ \frac{\Delta}{\sigma'} < 1.8 \tag{3.114}$$

Here, Δ is apparent roughness diameter and σ' is the thickness of the laminar sublayer. Hiding factor modifies the entrainment of the smaller particles (d_i) since they lock in the intersections of larger particles. Hiding factor thus can be represented as a function of particle diameter and characteristic grain size.

The model is developed based on the calculation of two parameters; non-dimensionalized transport rate (φ_*) and flow intensity parameter (ψ_*) which are defined as:

$$\varphi_* = \frac{g_b}{\rho_s \sqrt{(S_s - 1)\, g d^3}} \tag{3.115}$$

$$\psi_* = \xi \daleth \frac{\beta^2}{{\beta_x}^2} = \xi \daleth \frac{\beta^2}{{\beta_x}^2} \; (S_s - 1) \frac{d}{SR'} \tag{3.116}$$

In the equation above, $\daleth$ is the pressure correction for modifying the lift of particles in mixed beds, S is the slope, R' is the hydraulic radii related to the grain roughness.

For the fully rough flow, Einstein modified the log-law for both smooth and rough boundaries by introducing a correction factor, x. Thus, taking the velocity at $0.35X$, the modified log-law can be represented as:

$$\frac{U}{U'_*} = 5.75\{log_{10}(10.6\frac{x\varkappa}{K_s}) \tag{3.117}$$

In which the U'$_*$ is the *grain shear velocity* and K$_s$ is the grain size (d$_{50}$). Hence, the β^2, β_x^2 can be calculated as:

$$\beta^2 = \{(log_{10}(10.6))^2 \tag{3.118}$$

$${\beta_x}^2 = (\{log_{10}(10.6\frac{x\varkappa}{K_s}))^2 \tag{3.119}$$

Values for $\daleth$ (shown as Y in the figure)and x (shown as N in the figure) and ξ are represented in Figure 3.22 . It is notable that the values for Δ can be defined as: $\Delta = K_s/x$.

Einstein-Brown (1950)model:

This model is the simplified version of Einstein model and is widely used for sand and fine gravel rivers. The method is based on an empirical relation between φ and ψ as follows:

$$\varphi = \frac{g_b}{{}_1\rho_s \sqrt{g(S_s - 1){D_s}^3}} = \begin{cases} 2.15\; e^{\left(\frac{-0.391}{\tau^* {d_{50}}}\right)} & if \quad \tau^*{}_{d_{50}} < 0.093 \\ 40\; (\;\tau^*{}_{d_{50}})^3 & if \quad \tau^*{}_{d_{50}} \geq 0.093 \end{cases} \tag{3.120}$$

In the equation above, D_s is the representative grain size ≈d$_{50}$ and F$_1$ is a parameter related to the particle fall velocity ($\mho$) and can be defined as:

$$\mathrm{F}_1 = \sqrt{\frac{2}{3} + \frac{36\; \mho^2}{g{D_s}^3(S_s - 1)}} \tag{3.121}$$

For gravel bed rivers, F$_1 \simeq 0.82$.

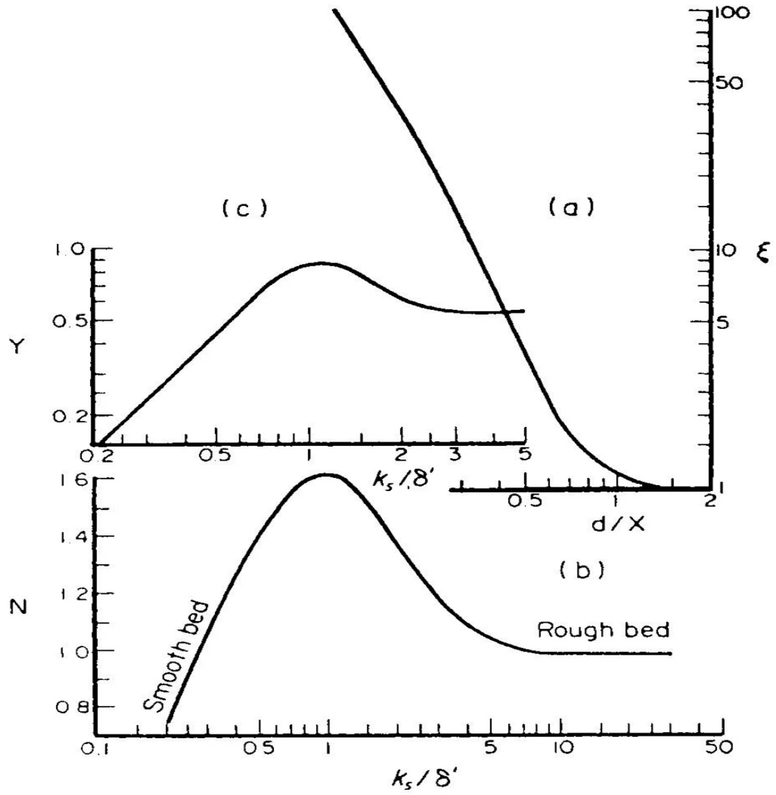

Figure 3.22: Pressure correction factor and hiding factor in Einstein method (Raudkivi, 1998)

Yalin (1963)model:

Yalins model is derived for the particle range of *d=0.315 -28.65 mm* considering the saltation mechanics and using d_{50} for sediment mixture.

$$g_b = \frac{\left[(\gamma_s - \gamma)\, d_{50}\right]^{1.5}}{g\rho^{0.5}} \,(0.635)\, s\ \tau^{*0.5} \left[1 - \frac{1}{as}\ \ln\left(1{+}as\right)\right] = 0.635\,(\rho_s - \rho)\, d_{50} u^{*} s \left[1 - \frac{1}{as}\ \ln\left(1{+}as\right)\right] \quad (3.122)$$

in which:

$$\tau^{*} = \frac{\tau}{\gamma(S_s - 1)d_{50}} = \frac{u^{*2}}{g(S_s - 1)d_{50}} \quad (3.123)$$

and

$$a = 2.45\ \frac{{\tau^{*}}_c^{\ 0.5}}{S_s^{\ 0.4}} \quad , \quad s = \frac{\tau^{*} -\ {\tau^{*}}_c}{{\tau^{*}}_c} \quad (3.124)$$

Bagnold (1980)model:

Bagnold model is developed for sand and gravel bed rivers. The model calculates the total sediment load based on the rate of energy expenditure in flow to move the bed material.

In this model the stream power is calculated and its erosive effect on the bed material is evaluated. The stream power and bed load work rate are calculated as:

$$\omega = \tau \ \bar{u} \tag{3.125}$$

$$W = \tau \ U_b = \ e_b \ \tau \ \bar{U} = m'_b \ g \ \bar{U}_b \tan(\alpha) = i_b \tan(\alpha) \tag{3.126}$$

In this equation, m'$_b$ is the bed load submerged mass per unit area and therefore, the term $m'_b \ g$ represents the submerged bed load stress. The term i$_b$ is the submerged weight per meter per second and $\tan(\alpha)$ is the friction resistance transport.

In the Bagnold model, the e$_b$ is the efficiency of the completed work on the bed and considering the carpet layer transport (entire bed surface moving, very rare in gravel bed rivers), Bagnold estimated the e$_b \simeq 0.1$. Here, the total sediment load can be calculated as:

$$i = i_b + i_s = \ \omega \left[\frac{e_b}{\tan(\alpha)} + e_s \frac{\bar{U}_s}{\mho} (1 - e_b) \right] \tag{3.127}$$

In the equation above, i$_b$ and i$_s$ are the bed and suspended loads and $\frac{\bar{U}_s}{\mho}$ is the ratio of suspended particle velocity to the particle fall velocity.

Difficulties associated with the parameterization of the model are resolved using an empirical approach which led to the estimation of sediment load as follows:

$$g_b = \frac{S_s}{S_s - 1} g_{br} \left[\frac{\omega - \omega_c}{(\omega - \omega_c)_r} \right]^{1.5} \left[\frac{y}{y_r} \right]^{-\frac{2}{3}} \left[\frac{d}{d_r} \right]^{-\frac{1}{2}} \tag{3.128}$$

in which the ω and ω_c are calculated as:

$$\omega = \gamma Y S \bar{U} \tag{3.129}$$

$$\omega_c = 5.75 g [0.04 \ \rho \ (S_s - 1)]^{1.5} \left[\frac{g}{\rho} \right]^{0.5} d^{1.5} \ \log \left[\frac{12 \ Y}{d} \right] \tag{3.130}$$

Parameters in the equation above can be summarized as:

$g_{br} = 0.1 kg.m^{-1}.s^{-1}, (\omega - \omega_c) = 0.5 N.m^{-2}.m.s^{-1}, Y_r = 0.1m, d_r = 0.0011m$

which g$_{br}$ is the efficiency, d is the sediment diameter and Y is the total depth. Finally it is notable that Bagnold assumed the $\tau_c^* \simeq 0.04$. The subscript r, indicates the reference value from flume experiments (Williams, 1970).

Modified Ackers-White (1982) model:

The Ackers-White model is developed for sand and gravel bed rivers with *d=0.04-4.94 mm*. The current model (White and Day, 1982)is the modified version of the original (Ackers and White, 1973) model. The model calculates the fraction of the total bed load for each grain size and sums it for all grain sizes to reach the total transport. Empirical coefficients of the model are determined using flume experiments. The model can be represented as:

$$g_{bAW} = \sum_i g_{bi} \tag{3.131}$$

In this equation which represents the general method of the total bed load transport (g_{bAW}), i is the size fraction and g_{bi} is the fractional bed load transport which can be calculated as:

$$g_{bi} = G_{gri}\ \rho_s\ u\ (\frac{u}{u^*})^{n_i}\ D_i\ p_i \tag{3.132}$$

In this equation, D_i is the geometric mean particle size of size fraction i and p_i is the fractional proportion in the bed. Term of G_{gri} is called the dimensionless fractional transport parameter and is calculated as:

$$G_{gri} = C_i\ \left[\left(\frac{F_{gri}}{A_{ii}}\right) - 1\right]^{m_i} \tag{3.133}$$

F_{gri} is called the mobility number and can be defined as:

$$F_{gri} = \frac{u^{*n}}{\sqrt{g\ D_i(S_s - 1)}}\ \left[\frac{u}{5.66\ \log(\frac{10\ Y}{D_i})}\right]^{1-n_i} \tag{3.134}$$

and

$$A_{ii} = A_i\ \left[0.4\ (\frac{D_i}{D_A})^{-0.5} + 0.6\right] \tag{3.135}$$

$$D_A = 1.6\ D_{50}\ (\frac{D_{84}}{D_{16}})^{-0.28} \tag{3.136}$$

Coefficients n_i, A_i, m_i and C_i can be calculated using the following:

$$1 \leq D_{gri} \leq 60\ : \begin{cases} n_i = 1 - 0.56\ \log D_{gri} \\ A_i = \left(\frac{0.23}{D_{gri}{}^{0.5}}\right) + 0.14 \\ m_i = \left(\frac{9.66}{D_{gri}}\right) + 1.34 \\ C_i =\ 10^{(2.86\ \log(D_{gri}) - \left(\log(D_{gri})\right)^2 - 3.53)} \end{cases} \tag{3.137}$$

$$D_{gri} \geq 60 \ : \begin{cases} n_i = 0 \\ A_i = 0.17 \\ m_i = 1.5 \\ C_i = \ 0.025 \end{cases} \tag{3.138}$$

Parameter D_{gri} is called the fractional dimensionless grain diameter and is calculated as:

$$D_{gri} = D_i \left[\frac{g\,(S_s - 1)}{\upsilon^2}\right]^{1.3} \tag{3.139}$$

Van Rijn (1984) model:

The van-Rijn bed load model is developed for sand bed rivers and is derived for the range of *d=0.2-2 mm*. The model is found to be more applicable for subsurface sediment material distribution (Rennie, 2012).

$$g_{bVR} = 0.053\ \rho_s\ D_{50}\ \sqrt[1.5]{(S_s - 1)\,g}\ \frac{T^{2.1}}{{D_*}^{0.3}} \tag{3.140}$$

In the equation above, T is the transport stage parameter:

$$T = \frac{\left[u'^{*2} - {u'^*_{cr}}^2\right]}{{u'^*_{cr}}^2} \tag{3.141}$$

where u'^* and u'^*_{cr} are grain shear velocity and critical grain shear velocity.

D_* is the scaled particle parameter and can be calculated:

$$D_* = \ D_{50}\left[(S_s - 1)\,\frac{g}{\upsilon^2}\right]^{\frac{1}{3}} \tag{3.142}$$

The grain shear velocity is:

$$u'^* = \frac{\bar{U}}{5.75\log_{10}\left[\frac{12\ Y}{3\ D_{90}}\right]} \tag{3.143}$$

Parker et al. (1982) model:

The Parker model is developed based on the equal mobility concept for gravel bed rivers with *d=0.6-102 mm*. The equal mobility concept means that the size distribution of the bed load equals to the subsurface sediment.

The Parker model can be illustrated as:

$$g_b = \frac{w^*(Y\ S)^{1.5}\ g^{0.5}\ \rho_s}{S_s - 1} \tag{3.144}$$

w^* is the dimensionless total bed load and is calculated as:

$$w^* = {w^*}_r\ G\left[\phi_{50}\right] = 0.0025\ G\left[\phi_{50}\right] \tag{3.145}$$

where

$$\phi_{50} = \frac{{\tau^*}_{50}}{{\tau^*}_{50r}} \tag{3.146}$$

and

$$\tau^*{}_{50} = \frac{\tau}{\rho\ \left(S_s - 1\right) g\ d_{50}} \tag{3.147}$$

$$\tau^*{}_{50r} = 0.0876 \tag{3.148}$$

In which the d_{50} refers to the subsurface size distribution.

Here, the parameter $G[\phi_{50}]$ can be calculated as Parker (1990):

$$G\left[\phi_{50}\right] = \begin{cases} 5474\left(1 - \frac{0.853}{\phi_{50}}\right)^{4.5} & for\ \ \phi_{50} > 1.59 \\ e^{14.2\ (\phi_{50}-1) - 9.28\ (\phi_{50}-1)^2} & for\ \ 1 \le \phi_{50} \le 1.59 \\ {\phi_{50}}^{14.2} & for\ \ \phi_{50} < 1 \end{cases} \tag{3.149}$$

Parker (1990)model:

Andrews and Parker (1987) modified the original Parker model by introducing a new function as reduced hiding function, $f(\mathrm{D}_i/D_{50})$. The most important effect of this function is to modify the shear stress imposed up on the particles. The model is converted from the original Parker et al. (1982) model to accounts the surface size distribution since the surface materials are exposed to the flow. The model can be expressed as:

$$w^*{}_{si} = \frac{\left(S_s - 1\right) g\ g_{bi}}{\rho_s\ \left(\frac{\tau}{\rho}\right)^{1.5}\ F_i} = 0.00218\ G\left[\phi\right] \tag{3.150}$$

$$g_b = \sum_i g_{bi} \tag{3.151}$$

where

$$\phi = \varpi \phi_{sgo}\ g_o\left(\sigma_i\right) \tag{3.152}$$

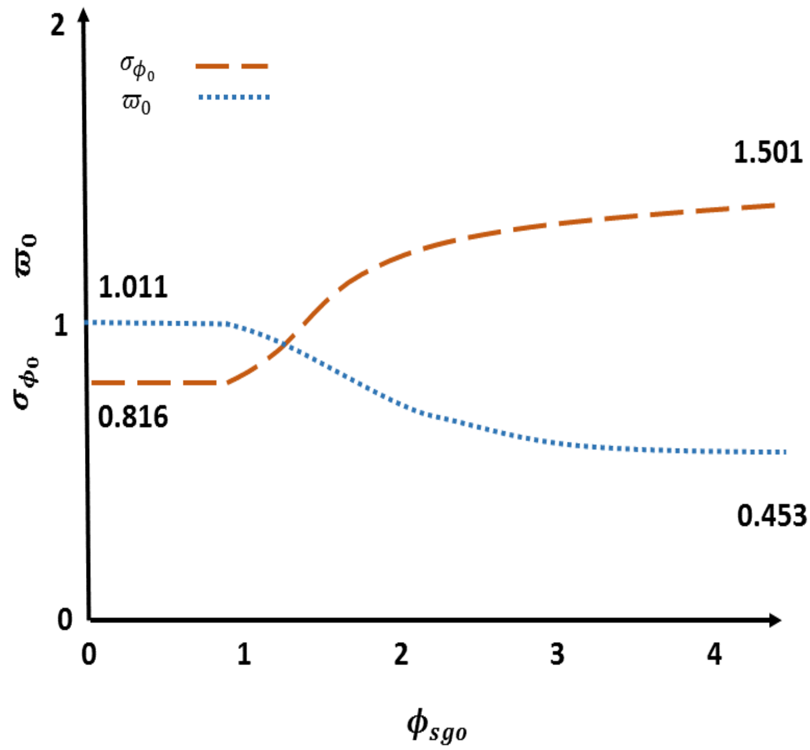

Figure 3.23: Values for $\sigma_{\phi_0}$and ϖ_0 are plotted versus ϕ_{sgo}, After Parker (1990)

and hence,

$$G\left[\phi_{50}\right] = \begin{cases} 5474\left(1-\frac{0.853}{\phi_{50}}\right)^{4.5} & for \quad \phi_{50} > 1.59 \\ e^{14.2\ (\phi_{50}-1)-9.28\ (\phi_{50}-1)^2} & for \quad 1 \leq \phi_{50} \leq 1.59 \\ {\phi_{50}}^{14.2} & for \quad \phi_{50} < 1 \end{cases} \tag{3.153}$$

In the equation 3.152, ϖ is called modified straining function and can be calculated as:

$$\varpi = 1 + \frac{\sigma_\phi}{\sigma_{\phi_0}}\ (\varpi_0 - 1) \tag{3.154}$$

where σ_ϕ is the arithmetic standard deviation of the surface size distribution:

$$\sigma_\phi = \sqrt{\sum [\frac{\ln(\frac{D_i}{D_{sg}})}{\ln 2}]^2 \mathcal{F}_i} \tag{3.155}$$

In the equation above, $\mathcal{F}_i$ is the percent representation of size fraction i in the surface. Values for σ_{ϕ_0} and ϖ_0 are plotted versus ϕ_{sgo} and are shown in Figure 3.23.

The non-dimensionalized bed shear stress, ϕ_{sgo} can be calculated from the following:

$$\phi_{sgo} = \frac{\tau^*{}_{sg}}{\tau^*{}_{r\ sg}} = \frac{\tau}{0.0386\ (\rho\,(S_s - 1)\ \ g\ D_{sg})} \tag{3.156}$$

Where the D_{sg} is the surface geometric mean.

$$D_{sg} = e^{\sum[F_i\ \ ln(D_i)]} \tag{3.157}$$

Finally, the reduced hiding function, $g_o(\sigma_i),\ is:$

$$g_o\,(\sigma_i) = \ g_o \left[\frac{D_i}{D_{sg}}\right] = \left[\frac{D_i}{D_{sg}}\right]^{-\beta} = \left[\frac{D_i}{D_{sg}}\right]^{-0.0951} \tag{3.158}$$

Wilcock and Crowe (2003) model

The model is based on the surface sediment size distribution.

$$w^*{}_{si} = \frac{(S_s - 1)\,g\ g_{bi}}{\rho_s\ (\frac{\tau}{\rho})^{1.5}\ F_i} = \begin{cases} 0.002\ \phi^{7.5} & for\ \phi < 1.35 \\ 14\ (1 - \frac{0.894}{\phi^{0.5}})^{4.5} & for\quad \phi \geq 1.35 \end{cases} \tag{3.159}$$

$$g_b = \sum_i g_{bi} \tag{3.160}$$

In which the $\phi = \tau/\tau_{ri}$ where τ_{ri} is the reference shear stress for each grain size fraction. The reference shear for the mean grain size, τ^*_{rm}, is:

$$\tau^*{}_{rm} = 0.021 + 0.015\ e^{(-20\ \ P_s)} \tag{3.161}$$

Where $\mathcal{P}_s$ is the sand present on the bed surface. Hence,

$$\tau_{rm} = \ \tau^*{}_{rm}\ \ (S_s - 1)\ \ \gamma\ D_{sm} \tag{3.162}$$

$$D_{sm} = \ e^{\sum[F_i\ \ ln(D_i)]} \tag{3.163}$$

Here, the reference shear stress can be calculated as :

$$\tau_{ri} = \ \tau_{rm}\ \left[\frac{D_i}{D_{sm}}\right]^b \tag{3.164}$$

and the empirical function of b can be shown as:

$$b = \frac{0.67}{1 + \ e^{\left[1.5 - \ \frac{D_i}{D_{sm}}\right]}} \tag{3.165}$$

Suspended load models

An important factor in sediment particles suspension is the particles fall velocity. As long as the vertical component of the flow turbulence remains equal to or higher than the particle fall velocity, the sediment particles remain suspended. The particles terminal fall velocity is dependent on the diameter and density of the particles and can be expressed as (Yang, 1996):

$$\mho = \sqrt{\frac{4}{3}\,\frac{1}{C_D}\;g\;D\;(S_s-1)} \tag{3.166}$$

In this equation C_D is the drag coefficient and based on what is represented in the above equation, it can be represented as:

$$C_D = \frac{4}{3}\left[\frac{\mho\;D}{\upsilon}\right]^{-2}\left[\frac{\upsilon}{g\;D^3\;(S_s-1)}\right]^{-1} \;=\; \frac{4}{3}\;[Re_w]^{-2}\;[G]^{-1} \tag{3.167}$$

Re_w is the particle Reynolds number and G is the sedimentation parameter. The drag coefficient can be calculated using the graph represented by Simons and Şentürk (1992) as shown in Figure 3.24:

However, simpler formulation for estimation of particles fall velocity is developed by Stokes (Yang, 1996). The equation known as Stokes law, is developed for approximately spherical particles which are large enough to overcome the Brownian motion and are falling in uniform velocity:

$$\mho = \frac{(S_s-1)\,g\;D^2}{18\;\upsilon} \tag{3.168}$$

Rather than what has discussed above, the particle fall velocity is dependent on other parameters such as suspended sediment concentration. Generally, for fine sediment particles, a cluster or closely spaced particles fall faster than single particles, but the dense cloud of particles will fall more slowly due to a process of jamming. Considering the fact discussed, the fall velocity can be adjusted as (Rennie, 2012) :

$$\mho = \mho_0\;(1-\mathcal{C})^{\beta} \tag{3.169}$$

Where the $\mathcal{C}$ is the sediment concentration (m^3/m^3). The factor β is a function of grain shape, particle Reynolds number, or non-dimensional grain size (D^*) as:

$$D^* = D\Big[(S_s-1)\frac{g}{\upsilon^2}\Big]^{\frac{1}{3}} \tag{3.170}$$

Here, the β can be calculated as:

$$\begin{cases} \beta = 4.56\;,\;\; D^* < 40 \\ \beta = \frac{7.478}{D^{*0.129}}\;\;\; 40 < D^* < 8000 \\ \beta = 2.35\;,\;\; D^* > 8000 \end{cases} \tag{3.171}$$

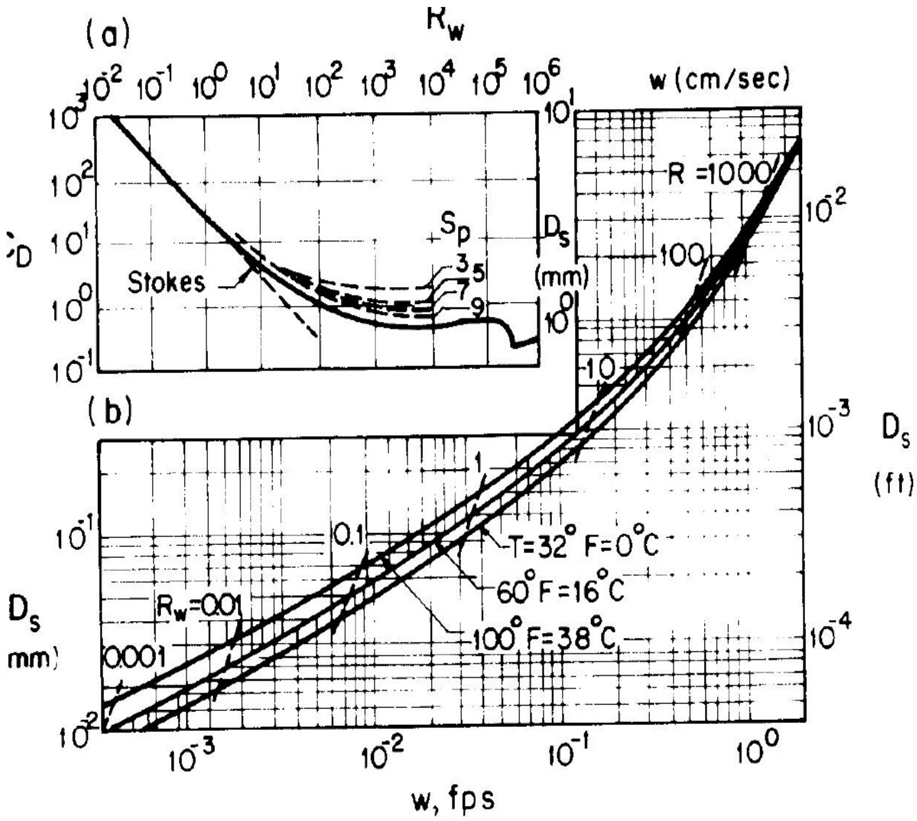

Figure 3.24: Coefficient C_D drag versus Reynolds number Re_w for spheres and natural sediments with shape factors equal to 0.3, 0.7 and 0.9 (Simons and Şentürk, 1992)

vanRijn (1984) suspended load model:

Van-Rijn presented a model to calculate the total shear based on calculated grain and form roughness. Such an approach makes the calculation of bed slope unnecessary prior to the suspended load calculation. vanRijn solution is presented in the following:

$$D^{*} = D_{50}\left[(S_s - 1)\frac{g}{\upsilon^2}\right]^{\frac{1}{3}} \tag{3.172}$$

where similar to the vanRijn bed load model, D^{*} is the scaled particle parameter.

The grain shear velocity can be calculated as:

$$u'^{*} = \frac{\bar{U}}{5.75\ \{log_{10}\left[\frac{12\ Y}{3\ D_{90}}\right]} \tag{3.173}$$

Thus, the transport stage parameter, T, can be calculated as:

$$T = \frac{\left[u'^{*2} - {u'^{*}_{cr}}^{2}\right]}{{u'^{*}_{cr}}^{2}} \tag{3.174}$$

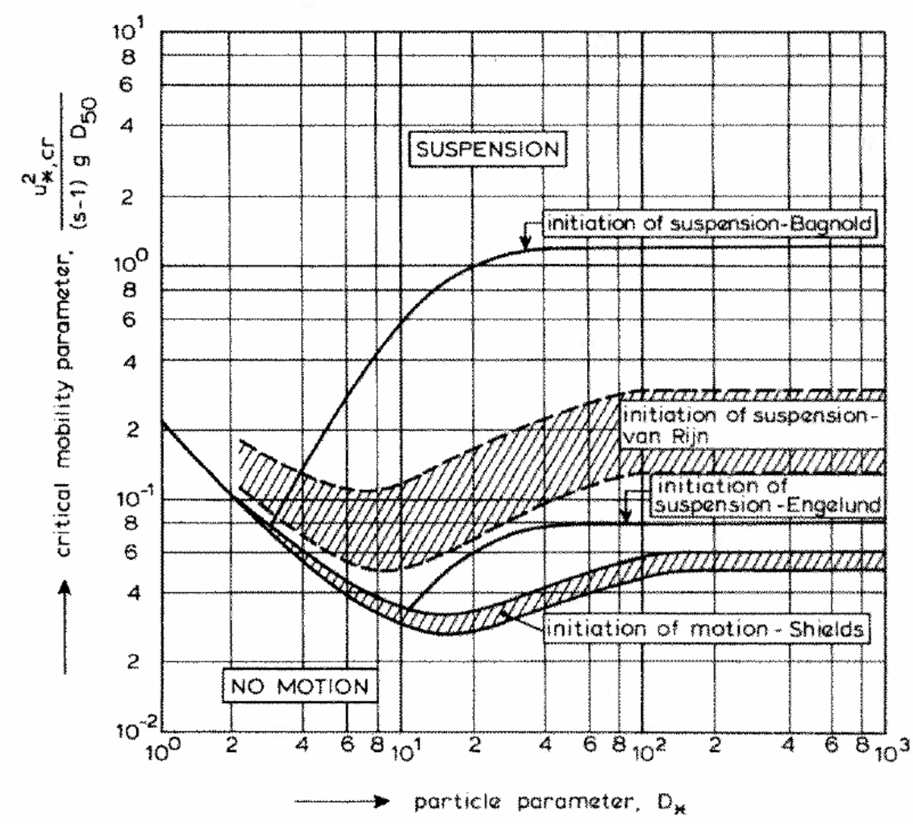

Figure 3.25: Initiation of motion and suspension (vanRijn, 1984)

In the equation above, u'^{*}_{cr} can be calculated from Shields diagram (Figure 3.20) or the Figure 3.25 .

vanRijn then calculated the suspended load by integrating the product of the concentration profile and the velocity profile:

$$g_s = \int_a^Y CU\ dz \tag{3.175}$$

in which a is the reference height, Y is the total flow depth and z is the height above the bed. vanRijn defined two parts for concentration profile through the integration process:

$$\mathcal{C} = \mathcal{C}_0 \left[\frac{a(Y-z)}{z(Y-a)}\right]^{\zeta} \quad for \quad \frac{z}{Y} < 0.5 \tag{3.176}$$

$$\mathcal{C} = \mathcal{C}_0 \left[\frac{a}{(Y-a)}\right]^{\zeta} e^{-4Z\ (\frac{\zeta}{Y}-0.5)} \quad for \quad \frac{z}{Y} \geq 0.5 \tag{3.177}$$

In these equations, ζ is the suspension parameter and is defined as:

$$\zeta = \frac{\mho}{\beta \kappa u^{*}} \tag{3.178}$$

where, β represents the ratio of sediment to fluid diffusivity and is shown as:

$$\beta = \frac{\epsilon_s}{\epsilon} \tag{3.179}$$

vanRijn modified the suspension parameter, ζ, and diffusivity ratio, β, as:

$$\zeta^{'} = \zeta + \varphi^{'} \tag{3.180}$$

in which

$$\varphi^{'} = 2.5 \left[\frac{\mho}{u^*}\right]^{0.8} \left[\frac{C_a}{C_0}\right]^{0.4} \quad for \quad 0.01 < \frac{\mho}{u^*} < 1 \tag{3.181}$$

and

$$\beta = 1 + 2\left[\frac{\mho}{u^*}\right]^2 \quad for \;\; 0.1 < \frac{\mho}{u^*} < 1 \;,\; \beta_{max} = 3 \tag{3.182}$$

In the equations above, $\mathcal{C}_0$ is the maximum concentration of astatic bed equals to 0.65.

The reference height is calculated in vanRijn method as:

$a = 0.5\ \Delta \quad or \quad a = k_s$ with the minimum of 0.01Y

Where, Δ is the bed forms height. Hence, the concentration at the reference height, $\mathcal{C}_a$, can be calculated as:

$$\mathcal{C}_a = 0.015\ \frac{D_{50}\ T^{1.5}}{a\ D_*^{\ 0.3}} \tag{3.183}$$

As shown in equations 3.181 to 3.182, both $\varphi^{'}$ and β are dependent to the particle fall velocity, which is defined as:

$$\begin{cases} \mho = \frac{(S_s-1)g\ D_s^{\ 2}}{18\ \upsilon} & for \;\; D_s < 100\ \mu m \\ \mho = 10\ \frac{\upsilon}{D_s}\ \left\{\left[1 + \frac{0.01\ (S_s-1)g\ D_s^{\ 3}}{\upsilon^2}\right]^{0.5} - 1\right\} & for \;\; 100\ \mu m < D_s < 1000\ \mu m \\ \mho = \sqrt{1.1\ (S_s-1)\, g\ D_s} & for \;\; D_s > 1000\ \mu m \end{cases} \tag{3.184}$$

Here, D$_s$ is calculated as:

$$D_s = D_{50}\ \left[1 + 0.011\ (\sigma_g - 1)(T - 25)\right] \tag{3.185}$$

Which σ_g is the geometric standard deviation and is calculated in van-Rijn solution as:

$$\sigma_g = 0.5\left(\frac{D_{84}}{D_{50}} + \frac{D_{16}}{D_{50}}\right) \tag{3.186}$$

Considering the Log-law velocity distribution, substituting the defined parameters in equations 3.176 to 3.186 in 3.175 leads to:

$$g_s = \frac{u^* C_a}{\kappa} \left[\frac{a}{(Y-a)}\right]^{Z'} \left\{ \int_0^{0.5\ Y} \left[\frac{Y-z}{z}\right]^{Z'} ln(\frac{z}{z_0})\ dz + \int_{0.5\ Y}^{Y} e^{-4Z'\left(\frac{z}{Y}-0.5\right)}\ ln(\frac{z}{z_0})\ dz \right. \tag{3.187}$$

which necessities the numerical integration. However, vanRijn offered an integrated version which accounts for $\pm$ %0.25 of the full model if 0.3$\leq \zeta' \leq$ 3.0 and 0.01$\leq$a/Y $\leq$0.1 as:

$$\mathcal{F} = \frac{\left[\frac{a}{Y}\right]^{\zeta'} - \left[\frac{a}{Y}\right]^{1.2}}{\left[1-\frac{a}{Y}\right]^{\zeta'} (1.2-\zeta')}$$

and finally

$$g_s = \mathcal{F}\ \bar{U}\ Y C_a\ \rho_s \tag{3.189}$$

Chapter 4

Methodology

4.1 Field apparatus and measurements

4.1.1 Introduction to the Lower Nelson River

Nelson River, as one of the great Canadian rivers, collects water from interior Canada and empties it to Hudson Bay after flowing through the Canadian Shield of northern Manitoba (Newbury and Malaher, 1973). The main bed of the river is located in a valley eroded by several historical glaciations at the boundary of two major geological zones; the Superior and Churchill provinces of the Canadian Shield (Newburry and Gaboury, 1993). The Nelson system is located between approximately 45.5°N to 57°N latitude and 90°W to 117.5°W longitude. The watershed drains to Lake Winnipeg from the eastern slopes of the Rocky Mountains and the prairie provinces at the west, northern Ontario at the east, and Minnesota and North Dakota at the south. Nelson River then carries its continental collection northeast to Hudson Bay (Benke and Cushing, 2011) . Total drainage area of the system is more than one million square kilometers of central North America, about 892,300 km^2 of Canada and 180,000 km^2 of the United States. Nelson River has a long history of exploration starting from mapping of the river shores in hope to find the Northwest Passage to India by the early 1600s. In spring 1611, a man called Henry Hudson, his son and seven others were cast drifted by a mutinous crew somewhere on a vast northern bay, later to be named after him as Hudson Bay. A year later, Sir Thomas Button was appointed to find lost Capitan Hudson. During his mission, he winter camped at the mouth of a large river and called it Nelson River after his ship master, Robert Nelson, who died there (Marsh, 1999) . Even before European exploration, the Nelson River area was occupied by at least 39 different aboriginal societies since the glaciers retreated 7000 to 9000 years ago (G. Dickson cited in Rivers of North America). The area dynamically occupied by northern Dene and southern Cree people during 1000 years domination periods.

The Nelson River catchment includes 11 major subcatchments. The largest are (Canada. Department of Energy and Branch, 1978; K and Sykes, 1982):

1. Saskatchewan (335,900 km^2; 334,100 km^2 Canada, 1800 km^2 United States)

Figure 4.1: Lower Churchill River between Southern Indian Lake and Hudson Bay before diversion in to Nelson River (up), after diversion (75% of the flow) (down) (Photo: A.P. Wiens, Rivers of North America)

2. Red-Assiniboine (287,500 km^2 ; 138,600 km^2 Canada, 148,900 km^2 United States)
3. Winnipeg (135,800 ; 106,500 km^2 Canada, 29,300 km^2 United States)
4. Main-stem Nelson (89000 km^2 all Canada)

The Churchill River catchment is also diverted to the Nelson River catchment (Figure 4.1) for long-term hydropower development in the Lower Nelson (Newbury et al., 1984). The two catchments are far apart for most of their length but at Southern Indian Lake (Churchill) and Rat-Burntwood River (Nelson), the two rivers get close. The idea of diversion of the Churchill River to the Nelson River first emerged in the 1950s and materialized in the mid 1970s by diverting 75% of the Churchill River to the Nelson River (Hecky and Guildford, 1984).

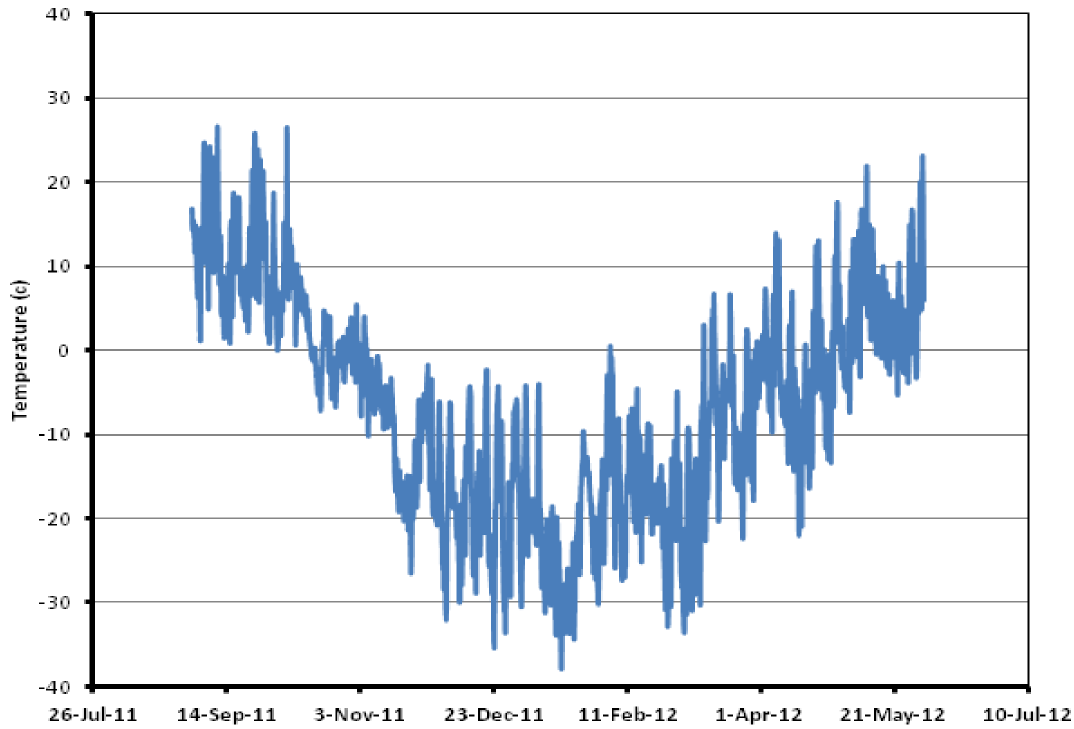

Figure 4.2: Temperature at Gillam Airport, Lower Nelson River during Fall 2011 - Spring 2012

Lake Winnipeg, which is a remnant of the glacial lake Agassiz, is the origin of the main stem of Nelson River(Newbury, 1990). Nelson River main stem length is 680 km between Lake Winnipeg and Hudson Bay. The First 350 km from Lake Winnipeg is called Upper Nelson River which consists of a complex series of lakes. Two major dams are located in this reach of the river , Wuskwatim (2012) and Jenpeg (1979). The lower 150 km of the river emerged as marine intrusion zone above the sea level since the last glaciations (Benke and Cushing, 2011).

Climate condition of the Lower Nelson River can be categorized as continental characterized by short, cool summers and long cold winters (Province of Manitoba, 1974). Mean daily temperature at peak summer ranges from 17.5°C in southern part to 12.5° C at the northern part and in peak winter varies from -22.5°C at southern part to -27.5°C at the mouth of the river. Annual precipitation is about 500 mm which mostly occurs from May to October 4.2. Usually less than 25 mm per month falls during the winter months.

Land use of Lower Nelson River basin can be categorized as 47 % of cropland, 32 % of forest, 6 % of shrubland, grassland and savanna and 7 % of urban and industrial (Revenga et. al. 1998 cited in Rivers of North America).

Nelson River main stem discharge is being significantly altered by regulation plants which raises the importance of accurate interpretation of run off at Lower Nelson River before and after regulation. This is mainly important at Kelsey and Limestone generation stations (Benke and Cushing, 2011). Average annual discharge of Limestone Generation

Station is calculated as almost 3700 m^3/s in 2012-2013 (H.Ahmari, Manitoba Hydro, Personal communication).

The Study reach of this research is Lower Nelson River (LNR) between Limestone Generating Station (LGS) and Gillam Island at the mouth of the river, just upstream of the estuary in Hudson Bay. The river in this reach is regulated, semi-alluvial, fast flowing without any lakes, and is characterized by high banks reaching to 50 meters height in some locations. Water surface elevation drop is about 43 meters over this 102 km reach, of which almost 30 m occurs over the first 28 km by several sets of rapids. The remaining 13 m drop takes place over the lower portion. Thus, the slope of the upper portion is about S=0.0011 and for the lower part is S=0.00018.

Previous observations on the Lower Nelson River demonstrate that in most years a continuous ice cover propagates upstream, reaching approximately 100 km from the estuary to just downstream of LGS. Ice floes generated in the study reach accumulate on the ice cover edge in the Nelson River Estuary where flow velocity diminishes, approximately 10 km downstream of Gillam Island. The ice front propagates upstream of Gillam Island typically in mid to late December, although ice progression upstream of Gillam Island has been reported as early as mid November and as late as mid February (Rennie and Ahsan, 2010) . Along portions of the LNR, no woody vegetation exists within several meters of the river bank, presumably due to ice scouring processes. This evidence suggests that ice processes have a major influence on the Lower Nelson River. The study site for this research is located upstream of Jackfish Island, about 50 km upstream of Gillam Island. River width in this location is about 1 km and depth is about 10-12 meters depending on both the time of year and the time of day due to hydropeaking fluctuations. Bed material is mainly gravel and cobbles, with interstitial sand patches (Figure 4.3) (Moore et al., 2013),(NorthSouthConsultants, 2010).

4.1.2 Instrumentation

This study used acoustic techniques to study the ice cover influence on river hydraulics and sediment transport. For this purpose, a Teledyne RD Instruments 1200 kHz Workhorse Sentinel Acoustic Doppler Current Profiler (ADCP) and a 546 kHz Shallow Water Ice Profiling Sonar (SWIPS) were installed looking upward on a moored bottom mount and deployed under the ice cover. Flow velocities along each beam axis are obtained in range-gated bins based on the Doppler shift of the backscattered sound, and a three-dimensional Cartesian velocity is obtained in each range bin using a coordinate transform. Refer to (Simpson, 2001) for more details on ADCP principles and operation.

The ADCP collected data as ensemble averages in 25 cm bins. The first measurement bin was centred at 0.4 m above the ADCP, and thus 1.04 m above the river bed. Each ensemble consisted of an average of 50 pings with a 7.5 min time step between ensembles.

The SWIPS is a programmable instrument designed for autonomous long-term deployment to gather information of floating objects in the water including all forms of river ice. Similar to an ADCP, backscatter intensity of emitted sound, which is a function of range and reflectivity, is used to detect the particles, and the instrument includes sensors for

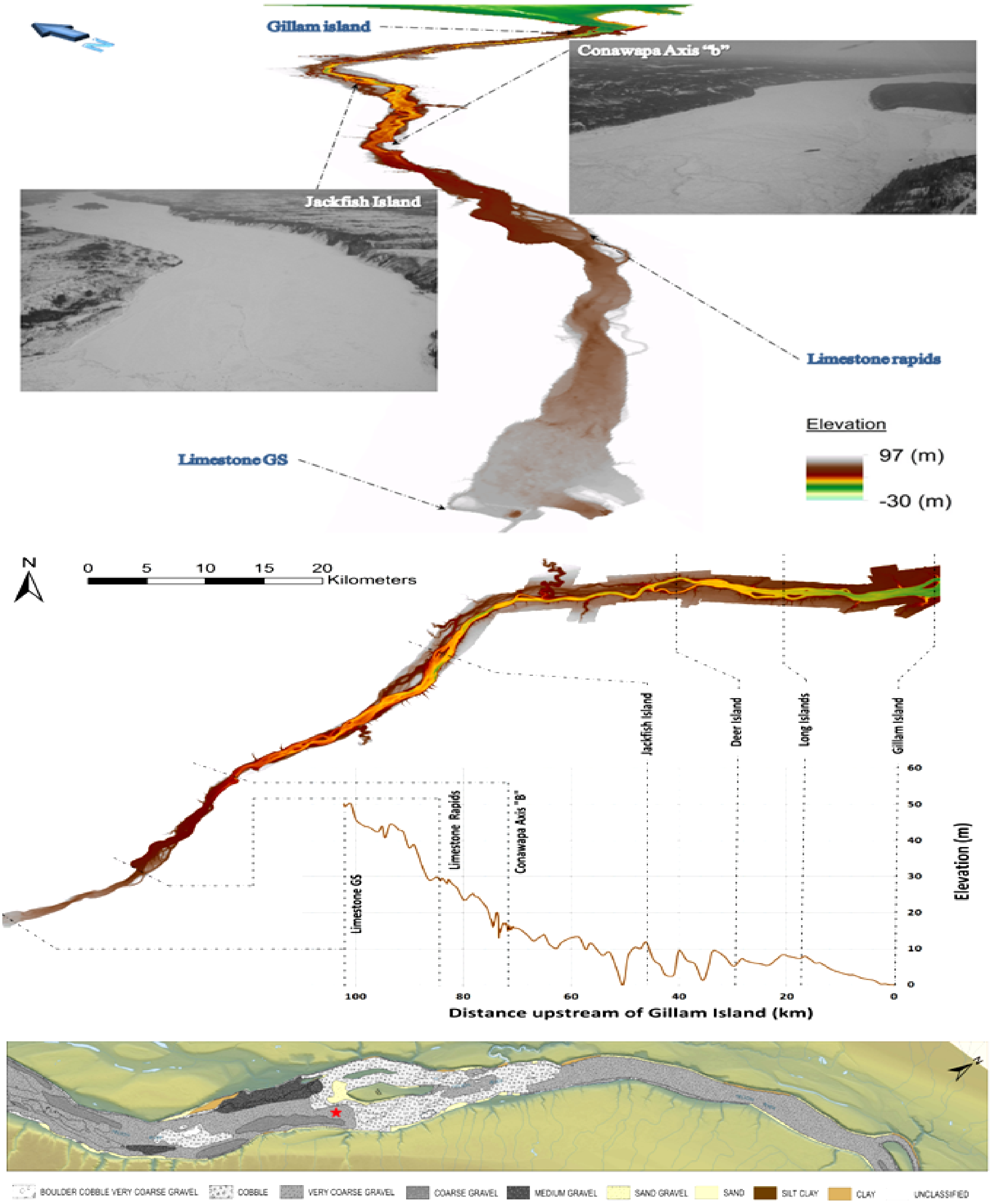

Figure 4.3: Lower Nelson River between Limestone Generating Station and Gillam Island, Location of river features (top), Bed elevation (middle) and map of bed material at the deployment site (red star)(NorthSouthConsultants, 2010)

measuring the pressure, temperature and transducer tilt during the deployment. However, the SWIPS does not utilize the Doppler effect to calculate velocities. The SWIPS was programmed to collect data at a 64 kHz digitization rate (0.01 m/sample) with a 150 μs pulse length. Four distinct phases of 30 days duration were employed for data acquisition, with a different gain setting employed for each phase.

Field investigations of this study were conducted through three field campaigns in March 2012- June 2012, September 2012- July 2013 and February 2015- July 2015. Instruments were programmed specifically each year in order to collect data through a designed procedure, providing appropriate information for a specific type of river ice cover and flow analysis Appendix C). In all three measurement campaigns the instruments were deployed in a deep pool upstream of Jackfish Island, which minimized influence of anchor ice on the bottom-mounted instrument pod. For the first and third field campaigns the instrument pod was deployed through the ice cover, whereas for the second campaign the instrument pod was deployed by boat in open water conditions. Due to the difficulties of instrument deployment in this challenging environment, the bottom pod was located in slightly different locations within the pool each year (6298715 N, 469474 E). The bottom pod was retrieved by boat in the early summer of each campaign year. Retrieval was facilitated by inclusion within the instrument pod of an automatically released retrieval buoy and acoustic ping locater. The following analyses were performed at each year on the data collected by the acoustic instruments:

1. Analysis of water surface elevation during the open water and winter periods (ADCP, SWIPS; 03/2012- 06/2012, 09/2012- 07/2013 and 02/2015- 07/2015).
2. Analysis of flow velocity (ADCP; 03/2012- 06/2012, 09/2012- 07/2013 and 02/2015- 07/2015)
3. Ice cover thickness and condition/stage analysis (SWIPS- ADCP; 03/2012- 06/2012, 09/2012- 07/2013 and 02/2015- 07/2015)
4. Effect of ice cover on boundary shear stress (ADCP- SWIPS; 03/2012- 06/2012)
5. Analysis of composite hydraulic resistance in ice covered streams (ADCP- SWIPS; 03/2012- 06/2012)
6. Effects of ice cover formation and progression on turbulent structures in ice covered rivers (ADCP; 09/2012- 07/2013 and 02/2015- 07/2015)
7. Analysis of suspended sediment concentration using acoustic backscatter intensity (ADCP; 03/2012- 06/2012)

It should be noted that in the second field campaign an effort was made to include spatial variations in collected data along the study reach. Specifically, a second instrumented bottom pod was deployed further upstream at the Conawapa axis DX [460353.04 E, 6288879.16 N]. However, due to the technical difficulties associated with the safe and successful retrieval of the instruments, this bottom pod could not be recovered. Consequently, no further attempt was made to deploy at a second site. Instead, the instruments were deployed at the location of the first year where geomorphological characteristics of the river cross section met the study project requirements and ensured the successful accomplishment of the retrieval procedure.

4.2 Ice cover effect on river hydraulics

4.2.1 Ice cover effect on boundary shear stress and velocity distribution

Addition of a new boundary layer to the top of the stream in form of an ice cover can influence hydraulic and morphologic characteristics of these rivers. Ice cover development affects water velocity magnitude and distribution, water stage and conveyance capacity, channel morphology and sediment transport. Estimation of boundary shear stress is essential for many river engineering problems. Shear stress acting on the boundaries resists flow and can significantly affect the conveyance capacity of the river. Flow resistance increases in the presence of an ice cover because of the additional boundary layer on top of the stream (Ettema and Daly, 2004). Shear stress also plays an important role in movement of materials at the upper boundary, including frazil ice floes during stages of freeze-up, and ice floes and slush ice during the stage of ice cover break-up. Motion and deposition of ice floes under the ice cover may lead to formation of hanging ice dams (Davar et al., 1998) or even ice jams which can alter the flow stage drastically and causes flooding events (Sui et al., 2010). Estimation of boundary shear stress is usually achieved by indirect methods based on theoretical and empirical assumptions, such as use of the local horizontal component of pressure gradient force (i.e., the depth-slope product), or velocity profile measurement and utilization of the law of the wall (Whiting and Dietrich, 1990) . Estimation of boundary shear stress based on the pressure gradient force is not applicable for local estimation in many natural rivers because it requires uniform flow with minimal convective acceleration, which is often not the case (Dietrich and Whiting, 1989). Alternatively, if velocity profiles can be defined near the boundaries, the boundary shear stress can then be calculated from the log-law (Kironoto et al., 1995). In the presence of an ice-cover, which results in boundaries at the bottom and top of the stream, two velocity profiles can be assumed. Each velocity profile extends from the respective boundary to the location of maximum velocity, so two individual logarithmic relations between velocity magnitude and depth can be fitted to the main profile (Larsen, 1969; Ashton, 1986).

4.2.2 Boundary shear stress from depth-slope product

Boundary shear stress (τ_b) can be expressed as a function of boundary shear velocity (u_*):

$$\tau_b = u_*^2 \, \rho \tag{4.1}$$

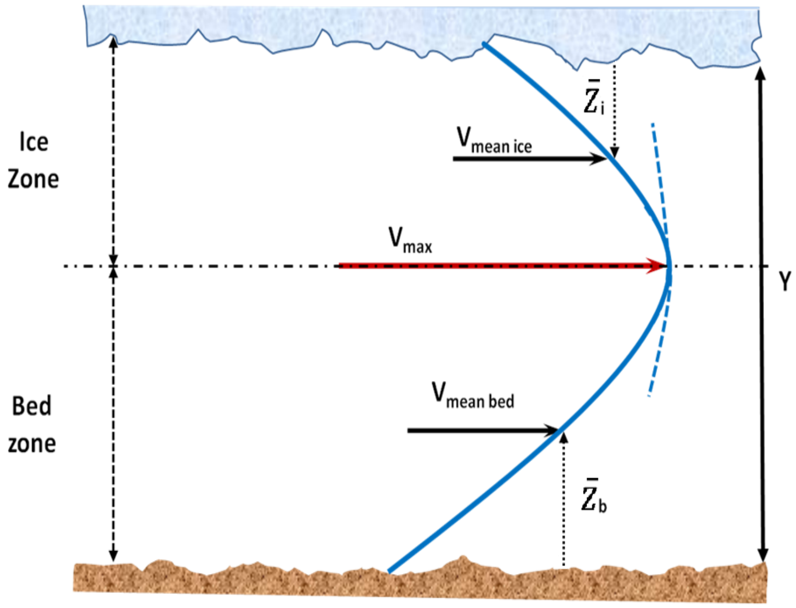

Figure 4.4: Definition of theoretical velocity profile under ice cover (after Larsen 1969)

where ρ is the water density. Boundary shear velocity can be calculated using the following expression (Henderson, 1989):

$$u_* = \sqrt{gRS_f} \tag{4.2}$$

where g is the gravity acceleration, S_f is the energy grade line and R is the hydraulic radius. Equation (4.2) can be applied to wide rivers by replacing the hydraulic radius, R by water depth, Y. However, application of (4.2) to estimate local shear velocity in natural streams is fraught with difficulty, including specification of the cross sectional gradient of streamwise velocity which affects parameters in (4.2) (Smart et al., 2002).

4.2.3 Logarithmic analysis of water velocity profiles

Previous studies and field measurements show that logarithmic velocity profiles can extend over much of the flow depth in open channels (Smart, 1999). In ice covered streams, however, the stream cross section can be divided into two main parts: a lower area where the velocity distribution is controlled by the lower boundary (i.e., the bed), and the upper zone that is controlled by the upper boundary which is the bottom of the ice cover. In both zones the stream-wise gravity force is opposed by the shear force on the boundaries. As shown in Fig 4.4, these two zones are divided by the location of maximum velocity, thus the maximum velocity location forms a velocity isoline between the two zones (Larsen, 1969).

Herein, we employ the log-law to estimate the shear velocity at each boundary. Prandtl (1925), Von Kármán (1930) and Millikan (1938) divided time averaged vertical profiles of streamwise velocity into an inner, log and outer layers as shown in Fig. 4.5 (Smart et al., 2002). The log portion can be described by:

$$u/u_* = (1/\kappa)\ln(z) + (1/\kappa)\ln(30/k_s) \quad (4.3)$$

where z is the distance from the boundary at which the velocity is u, k_s is equivalent sand roughness of the boundary (Nikuradse, 1933), and κ is the Von-Karman constant. Although the universality of the Von-Karman constant is under question for fluvial streams (Gaudio et al., 2010), generally $\kappa \approx 0.4$, and thus the same value is used in this work. Flow in rivers is often rough so the thickness of viscous sub-layer (within the inner layer) is negligible. Inner layer thickness is theoretically two to five times the bed roughness height (Raupach et al., 1991; Nikora et al., 2007).

Outer layer thickness has been estimated to cover up to 80 % of the depth in the presence of smooth boundaries (Nezu and Rodi, 1986). However, Cardoso et al. (1989) demonstrated that the the log-law can be applicable throughout the flow depth in gravel-bed rivers. This includes gravel-bed streams with both small and large roughness scale (Ferro and Baiamonte, 1994) as well as rivers with mobile bed (Whiting and Dietrich, 1990; Song et al., 1994). Even in gravel-bed rivers with non-uniform flows, the log-law holds in the zone near the boundary (Kironoto et al., 1995). For example, in their field study of non-uniform flows in gravel-bed rivers, Afzalimehr and Rennie (2009) observed that the range of the upper limit of applicability of the log-law varied between 22 % and 68% of the flow depth from the bed .

In cases where the logarithmic profile extends almost to the flow surface (Keulegan, 1938), integration of (4.3) from the location of zero velocity (Z_0) to the location of maximum velocity (total depth (Y) in open water condition), yields the average velocity over the depth (U_m), Maximum velocity (U_{max}) and equivalent bed roughness (k_s) as follows (Calkins et al., 1982):

$$U_m/u_* = (1/\kappa)[\ln(30Y/k_s) - 1] \quad (4.4)$$

The maximum velocity in the profile ,U_{max} can be calculated as:

$$U_{max}/u_* = (1/\kappa)\ln(30Y/k_s) \quad (4.5)$$

Dividing equation (4.4) by (4.5) results in an equation for k_s as follows:

$$k_s = 30Ye^{[-1/(1-(U_m/U_{max})]} \quad (4.6)$$

Finally, substituting k_s from (4.6) in (4.5) yields:

$$u_* = \kappa(U_{max} - U_m) \quad (4.7)$$

Three approaches are available to estimate u_* as the representation of boundary shear stress from the equations above:

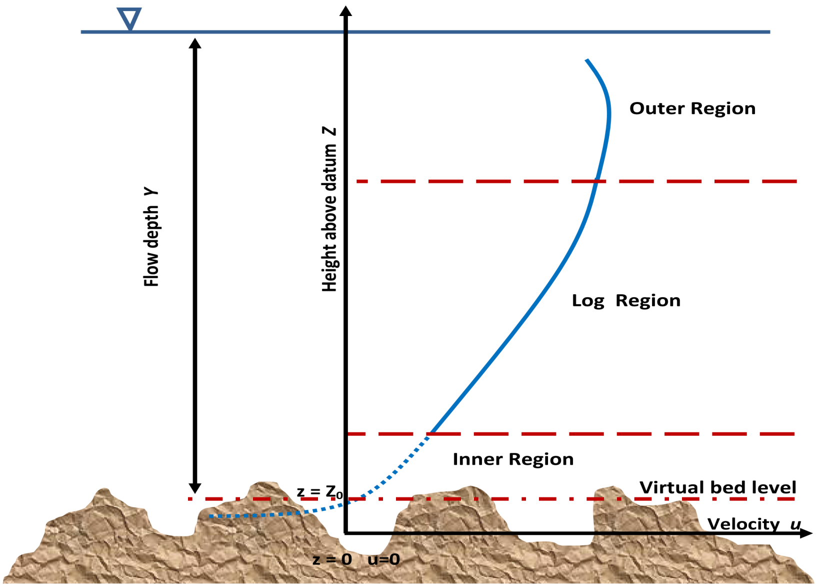

Figure 4.5: Schematic division of water velocity profile in depth to three main regions, scheme is presented based on Smart et al. (2002)

- Estimating of boundary shear velocity u^* using (4.4) or (4.5) which requires an estimation of either maximum or average velocity and equivalent sand grain roughness, i.e k_s.
- Plotting the velocity magnitudes versus the log of depth values and fitting a straight line through the data. Based on (4.3), the fitted linear line slope yields u_*, and then the intercept provides k_s.
- Estimating of maximum and average velocity, then shear velocity can be calculated directly using (4.7) without estimation of slope of the velocity profile

In this study, the logarithmic velocity distribution is assumed to be applicable throughout the turbulent flow region to the maximum velocity location (Figure 4.4). Using the second of the proposed methods, two lines are fitted to the velocity-log depth data, from which shear velocity and local boundary shear stress (equation 4.1) are estimated for both the lower boundary at the river bed and the upper boundary at the bottom surface of the ice. The third method is also utilized for comparison.

4.2.4 Application of acoustic techniques for turbulence studies in open channels

The main technique that is used in this research to study the turbulence in open channels is called the Variance Technique and is developed by Stacy et.al 1999. The technique is developed for application of broadband ADCPs to resolve the turbulent quantities. The process of calculation of water velocity in BB ADCPs is discussed in section 3.1.2.

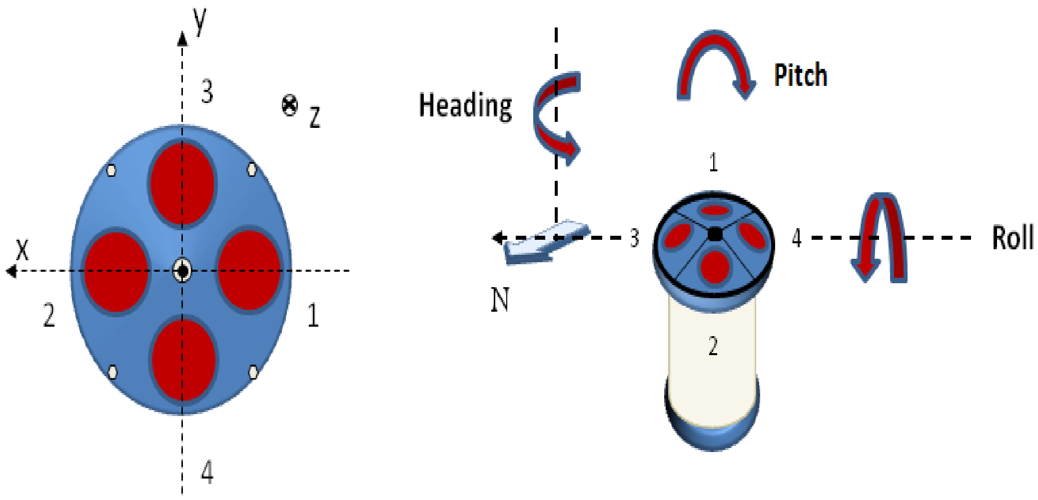

Figure 4.6: ADCP beam numbering and orientation-tilting description

ADCP coordinate system

The ADCP records the water velocity in four sets of coordinate axes, each of them are controlled by the EX internal command. The beam configuration utilized in definition of the coordinate system for an upward looking ADCP is shown in Figure 4.6 .Transducer numbering and alignment as well as the concepts of ADCP tilting are illustrated in the figure. Looking at the face of the instrument, the transducers are labeled clockwise as 3-1-4-2 . Based on mentioned transducer labeling, two horizontal axes are defined as axis x from transducer 1 to transducer 2 and axis y from transducer 4 to transducer 3. The vertical axis lies along the axis of symmetry of four beams pointing toward the pressure case (pointing downward viewing the transducers from above).

Tilt of the instrument around the three principal axes are Heading ($\mathcal{H}$), Pitch (Φ) and Roll (Ψ), as shown in positive sense in the Figure 4.6. Briefly, heading is the angle of beam number 3 to the magnetic north while the pitch and roll are tilting of transducers 3 and 2 to the hypothetical horizontal plate, respectively.

I. Radial Beam Coordinates (BM1, BM2, BM3, BM4): these set of velocity components are recorded directly by each transducer in (mm/s) and are usually referred as raw velocity measurements. This coordinates system is selected by EX00. command in ADCP programming interface (BB Talk). The velocity is recorded as positive if the flow is toward the transducer. Since each transducer records the velocity independently, the velocity axes in this coordinate are not orthogonal.

II. Instrument Coordinates (X, Y, Z): this coordinate system is selected through the EX01. command. The horizontal and vertical axes (x,y,z) are orthogonal and as described before.

III. Righted Instrument Coordinates (Ship coordinates- S, F, M): the ship coordinates consists of the orthogonal starboard, forward and mast. However, they usually are known as pitch, roll and yaw axes. This coordinate system can be set using the EX10. command assuming the beam number 3 pointing the forward, for an upward looking ADCP, the axes can be defined as:

$$S\text{=-}X,\ F\text{=}Y,\ M\text{=-}Z$$

IV. Geographic or Geodetic Coordinates (E, N, U): this set of orthogonal coordinate axes provides a stable reference frame for ensemble averaging and hence is the commonly used coordinate system. The Geodetic axes system is selected by the EX11. command and is named as East, North and up.

Velocity information is recorded in Geodetic coordinates (East, North and Up [E,N,U] directions) in this study (using the EX11111 command, which translates for : Geodetic coordinates, Pitch and Roll transformation, three beam solution, bin mapping) and therefore they should be converted back to horizontal (X,Y) and vertical (Z) direction in order to calculate the beam velocities (u_1 to u_4). To perform such a transformation in the coordinates of ADCP data, the inverse rotation matrix should be applied on the recorded data. The rotation matrix ($\mathcal{M}$) is the combination of three rotations as the order below:

-Ψ about the y axis which levels beam 2 (levels the x axis).

-Φ about the leveled x axis which levels beam 3, and finally

H about the z axis which corrects the heading.

Therefore, the rotation matrix can be illustrated as:

$$M = \begin{bmatrix} \cos(H) & \sin(H) & 0 \\ -\sin(H) & \cos(H) & 0 \\ 0 & 0 & 1 \end{bmatrix} \begin{bmatrix} 1 & 0 & 0 \\ 0 & \cos(\Phi) & -\sin(\Phi) \\ 0 & \sin(\Phi) & \cos(\Phi) \end{bmatrix} \begin{bmatrix} \cos(\Psi) & 0 & \sin(\Psi) \\ 0 & 1 & 0 \\ -\sin(\Psi) & 0 & \cos(\Psi) \end{bmatrix} = \tag{4.8}$$

$$\begin{bmatrix} \{cos(H)cos(\Psi)+sin(H)sin(\Phi)sin(\Psi)\} & \{\sin(H)cos(\Phi)\} & \{cos(H)cos(\Psi)-sin(H)sin(\Phi)sin(\Psi)\} \\ \{-sin(H)cos(\Psi)+cos(H)sin(\Phi)sin(\Psi)\} & \{cos(H)cos(\Phi)\} & \{-sin(H)cos(\Psi)-cos(H)sin(\Phi)sin(\Psi)\} \\ \{-cos(\Phi)sin(\Psi)\} & \{sin(\Phi)\} & \{cos(\Phi)cos(\Psi)\} \end{bmatrix}$$

When the internal pitch sensor is selected (EZxxx1xxx in BB-talk, EZ1111101 in this study), the true pitch is modified using the internal sensor recorded pitch value (ϕ) using the following expression:

$$\Phi = \arctan(\tan\phi . \cos\Psi) \tag{4.9}$$

It is notable that for an upward looking orientation, 180° must be added to the measured Ψ before it is used to calculate the rotation matrix.

So, the inverse transformation, from geodetic coordinates to the instrument coordinate velocity is given by the matrix $\aleph$ the inverse of M as (ADCP coordinate transformation, TELEDYNE RD Instruments, 2010):

$$\vec{V}_{XYZ} = M^{-1}.\vec{V}_{ENU} = \aleph.\vec{V}_{ENU} \tag{4.10}$$

In which, $\aleph$ is:

$$\aleph = \begin{bmatrix} \{-cos(H)cos(\Psi) - sin(H)sin(\Phi)sin(\Psi)\} & \{sin(H)cos(\Psi) - cos(H)sin(\Phi)sin(\Psi)\} & \{cos(\Phi)sin(\Psi)\} \\ \{cos(\Phi)sin(H)\} & \{cos(H)cos(\Phi)\} & \{sin(\Phi)\} \\ \{sin(H)sin(\Phi)cos(\Psi) - sin(\Psi)cos(H)\} & \{cos(H)cos(\Phi)\} & \{-cos(\Phi)cos(\Psi)\} \end{bmatrix} \tag{4.11}$$

Acoustic depth cell mapping was activated for the current study which provides adjustments for pitch and roll corrections. This option essentially enhances the spatial resolution of the average velocity profile by re-mapping and correcting each beams cell range from the actual to the nominal depth. Therefore, planar velocity components are possible to analyse in terms of variance more accurately. However it should be noted that since the bin mapping was activated during the data acquisition period, application of the transformation matrix does not necessary result in reproducing the original beam velocities but calculates a good approximation of the horizontal velocity component at each elevation which makes the variance technique applicable to calculate the Reynolds stress.

Application of inverse rotation matrix described above to the velocity recordings in geodetic coordinates leads to the calculation of the velocity in instrument coordinates (X, Y, Z, Error velocities). As explained in Section 4.2.4 , in order to estimate turbulence parameters, beam velocities are required, which are therefore calculated using equations 3.5a to 3.5d.

Acoustic techniques for turbulence studies:

Considering the ADCP configuration as it is demonstrated in Figure 4.7 , two planar velocities of u and v can be calculated as Stacey et al. (1999):

$$u = \frac{(u_3 - u_4)}{2\sin\theta} \tag{4.12}$$

$$v = \frac{(u_1 - u_2)}{2\sin\theta} \tag{4.13}$$

The variance techniques utilized in this study to calculate the turbulence statistics was outlined by Tropea (1983) and Lohrmann et al. (1990) and improved for BB ADCPs by Stacey et al. (1999). The technique relies on the along beam variance of measured velocities at opposite beams . Note that in the configuration presented in the figure, beam 3 and

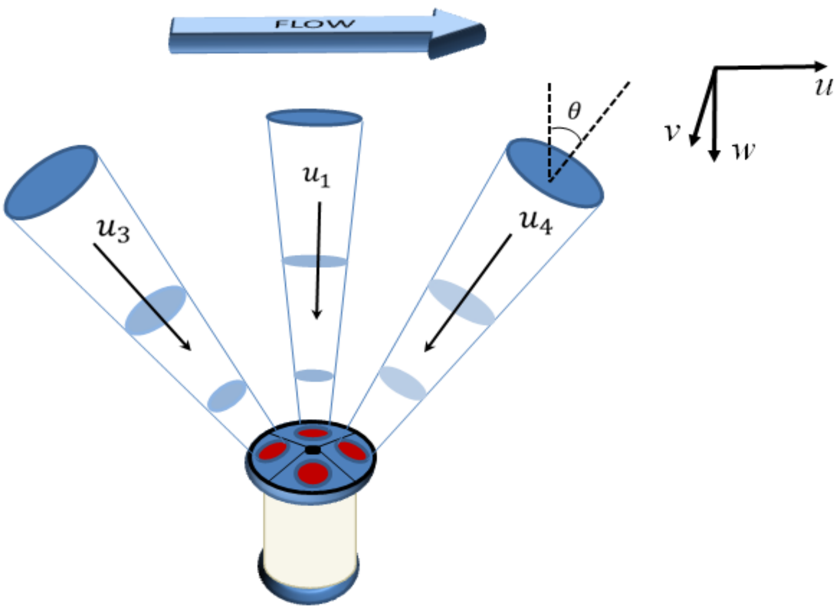

Figure 4.7: Beam velocities and orthogonal water velocity components relative to the ADCP

beam 4 velocities are positive and negative respectively while the beam 1 and beam 4 (through the figure- not represented) are zero (flow is in the beam3-beam 4 axis).

The deployed ADCP in this study, as described before, was equipped with four monostatic transducers, each inclined at 20 degrees to the vertical ($\theta = 20$). Therefore, as shown in Figure 4.7, measured velocity at any range from the transducer along each beam (equations 3.5a to 3.5d) is a weighted sum local horizontal and vertical velocity components (Stacey et al., 1999).

Application of Reynolds hypothesis for each beam velocity separates the beamwise velocity in to mean and fluctuating components. Mean velocity is calculated over an ensemble averaging window:

$$u = \bar{u} + u^{'} \tag{4.14}$$

and similarly

$$u_i = \bar{u}_i + u_i^{'}, \quad i = 1, 2, 3, 4 \tag{4.15}$$

Here, the variance of the along-beam velocity components can be calculated as:

$$\bar{u_1}^2 = \bar{v'}^2 sin^2\theta + \bar{w'}^2 cos^2\theta + 2v'\bar{w}' sin\theta cos\theta \tag{4.16}$$

$$\bar{u_2}^2 = \bar{v'}^2 sin^2\theta - \bar{w'}^2 cos^2\theta + 2v'\bar{w}' sin\theta cos\theta \tag{4.17}$$

$$\bar{u_3^2} = \bar{u'^2} sin^2\theta + \bar{w'^2} cos^2\theta + 2\bar{u'w'} sin\theta cos\theta \tag{4.18}$$

$$\bar{u_4^2} = \bar{u'^2} sin^2\theta - \bar{w'^2} cos^2\theta - 2\bar{u'w'} sin\theta cos\theta \tag{4.19}$$

Now, the principal and cross stream Reynolds stresses can be calculated as (Stacey et al., 1999):

$$\bar{u'w'} = \frac{\bar{u'_3{}^2} - \bar{u'_4{}^2}}{4 sin\theta cos\theta} \tag{4.20}$$

$$\bar{v'w'} = \frac{\bar{u'_1{}^2} - \bar{u'_2{}^2}}{4 sin\theta cos\theta} \tag{4.21}$$

Using the anisotropy ratio of turbulent field and the summary of the variances, the turbulent statistics such as turbulent kinetic energy components (summary of the variances) can be calculated as:

$$d_u{}^2 = \frac{1}{2}\left(\bar{u'_3{}^2} + \bar{u'_4{}^2}\right) = \left(\bar{u'^2}\ sin^2\theta + \ \bar{w'^2}\ cos^2\theta\right) \tag{4.22}$$

$$d_v{}^2 = \frac{1}{2}\left(\bar{u'_1{}^2} + \bar{u'_2{}^2}\right) = (\bar{v'^2}\ sin^2\theta + \ \bar{w'^2}\ cos^2\theta) \tag{4.23}$$

On the other hand, for steady, unstratified flow, the total shear stress analytically can be shown as (Nezu and Nakagawa, 1993):

$$\frac{\tau}{\rho} = -\bar{u'w'} + \upsilon\frac{\partial\bar{u}}{\partial z} = u_*{}^2\left(1 - \frac{z}{H}\right) \tag{4.24}$$

Hence, assuming the local balance between the energy production and dissipation, it can be shown (Nezu and Nakagawa, 1993):

$$\bar{u'^2} = 5.29\ u_*{}^2 e^{-2\frac{z}{H}} \tag{4.25}$$

$$\bar{v'^2} = \ 2.66 u_*{}^2 e^{-2\frac{z}{H}} \tag{4.26}$$

$$\bar{w'^2} = \ 1.61 u_*{}^2 e^{-2\frac{z}{H}} \tag{4.27}$$

Using the equations above, Stacey et al. (1999) showed that the anisotropy of the turbulent field can be calculated as:

$$\frac{\bar{v'^2}}{\bar{u'^2}} = 0.5 \tag{4.28}$$

$$\frac{\bar{w'^2}}{\bar{u'^2}} = 0.3 \tag{4.29}$$

Also, the turbulent kinetic energy can be calculated according to the equations 4.22, 4.23 and 4.25-4.27 as:

$$q^2 = \ 9.56{u_*}^2 e^{-2\frac{z}{H}} \tag{4.30}$$

Stacey et al. (1999) showed that the principal Reynolds stress is unbiased by the Doppler noise. However, the estimation of turbulent kinetic energy is biased by the variance of the noise (σN^2), in which, N is the random variable of the Gaussian white noise.

Studying the histogram of the turbulence intensity estimators (d_u^2, d_v^2), they calculated the bias as 34 cm^2/s^2 which is consistent with the per-ping error of 5.8 cm/s reported by RDI(Instruments, 2010; Stacey et al., 1999) .

Finally, considering the Reynolds hypothesis noted in equation 4.15, the Reynolds shear tensor can be represented as (Tilston et al., 2009):

$$\tau'_{R.S} = \sqrt{0.5 \sum_{i,j} (\tau_{R.Si,j})^2} \tag{4.31}$$

In which, the $\tau_{R.S}$ is the standard instantaneous Reynolds stress component:

$$\tau_{R.Si,j} = -\rho u'_i u'_j \tag{4.32}$$

4.2.5 Ice cover effects on river conveyance capacity

One of the important aspects of river ice influence on hydrodynamics is its effect on conveyance capacity. This effect leads to important operational problems, some of which are as following (Ashton, 1986):

1. Appropriate water releases from upstream water reservoirs or dams according to the water demands for hydropower generation, and urban, industrial and agricultural water consumption.

2. Hydraulic measurement issues due to disturbance of stage-discharge relations caused by complete or partial ice coverage of control reach, and

3. Early mechanical break-up due to rapid water staging in ice covered channels, which can lead to ice jam formation and release which increases the chance of severe flooding.

Amongst the important factors that determine a channel's conveyance capacity, hydraulic resistance of a covered reach is a factor that varies directly according to the condition of the ice cover.

Ice cover presence increases the hydraulic resistance in different ways namely (Ashton, 1986):

- Total channel resistance increases due to the additional resistance of the upper boundary layer induced by the ice cover.
- Thickening and stabilization of the ice cover may lead to local cross section reduction, especially when large protrusions of ice form under the surface of the consolidated ice cover.

Stabilized ice cover has been observed to increase the energy loss up to 62% and to decrease the discharge up to 29% in covered channels compared to open channel condition with the same water level (Ohashi and Hamada, 1970; Pratte, 1979).

Analysis of channel conveyance capacity under the ice cover

Two main analytical approaches are usually employed to calculate of hydraulic resistance in partially or totally covered streams: the *Manning* equation and the *Darcy-Weisbach* equation. The important factors that influence conveyance capacity are addressed in the Manning equation, which for ice covered streams can be expressed as (Chow, 1959):

$$Q = \frac{1}{n_c} A \ R_c^{\frac{2}{3}} \ S^{\frac{1}{2}} \tag{4.33}$$

where Q is discharge, n_c is the resistance coefficient for covered cross section, A is the cross section area, R_c is the hydraulic radius for covered cross section, and S is the slope of the energy gradient. An empirical equation for hydraulic radius estimation has been adopted for various covered conditions including open water to completely covered flow regimes. The equation can be stated as follows for rectangular channels (Tang and Davar, 1985):

$$R_c = \frac{Y_t \ .W}{2Y_t + W(1 + \frac{a}{100})} \tag{4.34}$$

where Y_t is the total flow depth, W is the cross section width, and a is the percentage of the cover.

The Darcy-Weisbach flow resistance equation can be expressed as (Chow, 1959):

$$H_l = f_c \frac{L}{4R_c} \cdot \frac{V^2}{2g} \tag{4.35}$$

where H_l is the head loss in length L, f_c is the Darcy-Weisbach friction factor for the entire composite section, L is the length of the reach, and V is the mean velocity in the channel. The energy grade line slope, $S = \frac{H_l}{L}$, can be defined by applying(4.35) for a specific length between two cross sections of the river.

Using an extension of classical pipe flow for prismatic, straight uniform channels, f functionally can be shown (Chow, 1959):

$$f = [R_n \ , \ \frac{\epsilon}{4R} \ , \ S.F] \tag{4.36}$$

where R_n is the Reynolds number, $\varepsilon/4R$ is the ratio of absolute roughness (ε) to the hydraulic radius (m/m), and S.F is the shape factor depending on the channel cross section geometry.

Equating velocity in equations (4.33) and (4.35) yields:

$$n_c = \frac{{R_c}^{\frac{1}{6}}}{\sqrt{\frac{8g}{f_c}}} \tag{4.37}$$

Considering (4.36) and (4.37), n_c theoretically must be a function of the Reynolds number, shape factor and the ratio of absolute roughness to the hydraulic radius, not just the boundary roughness alone. Flow in natural rivers is usually turbulent, thus Reynolds number is large enough not to be an important factor. Furthermore, shape factor can be neglected if the channel cross section is assumed to be rectangular. On the other hand, $\varepsilon/4R$ affects the resistance, thus it can be concluded that for a given ε, n_c and f depend on the flow depth as well.

Other channel features such as topography, channel irregularities, bed material transport, vegetation, etc. make estimation of a representative value of ε difficult, thus the resistance is most frequently expressed in terms of bulk estimates of Manning's coefficient n (Barnes, 1967).

Hydraulic resistance in ice covered streams

Presence of an ice cover and its consolidation complicates the precise estimation of the resistance to flow as it causes the flow regime to change from open water flow to partially covered and finally to the closed channel flow. The change in flow regime raises some basic difficulties in flow regime definition and accompanying assumptions for hydraulic calculations. A common assumption made in hydraulics of open channel flow is the uniform flow regime which is expressed as $S_o = S_w = S_f$, where S_o is the bed slope, S_w is the water surface slope, and S_f is slope of the energy grade line (i.e., the friction slope). Although this assumption is also widely used in covered flow regimes (Tang and Davar, 1985; Ashton, 1986), its application to ice covered rivers is tenuous at best The fundamental challenge in estimation of flow resistance in ice covered channels is to define the relative and combined influence of the ice cover and the channel bed on the composite total flow resistance.

Introduction to common methods for composite resistance calculation

A review of available methods for composite resistance calculation is provided in 2.2.3. Here three common methods of Larsen, Hancu and Belkon-Sabaneev are chosen as the most common methods for composite resistance calculation according to Uzuner and Kennedy (1976) and Ashton (1986).

I. *Belkon-Sabaneev*'s method

Belkon (1938) used a power-law velocity distribution with an exponent of 1.5 for the cross section of both ice and bed zones. The separation line between two areas was adopted as the maximum velocity location. He also assumed $V_c = V_i = V_b$. The Belkon-Sabaneev method can be expressed as follows:

$$n_c = n_b.\left[\frac{1+\frac{2}{3}\left(\frac{P_i}{P_b}\right)\left(\frac{n_i}{n_b}\right)^{\frac{3}{2}}}{1+\left(\frac{P_i}{P_b}\right)}\right] \tag{4.38}$$

where P_i and P_b are wetted perimeters for the ice and bed zones respectively.

II. *Hancu*'s method

Hancu investigated flow in wide rectangular channels with unequal wall roughness values. He established a relation between the total roughness of flow cross section and boundary roughness values based on the velocity defect law. As noted above, he assumed that the composite shear stress is an average of ice and bed zone shear stresses. Hancu's method is illustrated as:

$$n_c = \frac{n_b}{\sqrt{2}}\left(\frac{R_c}{R_b}\right)^{\frac{1}{6}}\left[\left(\frac{V_{mean_b}}{V_{mean_c}}\right)^2+\left(\frac{V_{mean_i}}{V_{mean_c}}\right)^2\left(\frac{n_i}{n_b}\right)^2\left(\frac{R_b}{R_i}\right)^{\frac{1}{3}}\right]^{\frac{1}{2}} \tag{4.39}$$

III. *Larsen*'s method:

Larsen applied a logarithmic velocity distribution and Manning equation to ice and bed zones separately and provided an equation for composite roughness estimation (Larsen, 1969). The main assumption in his method is equality of energy grade line slope in ice and bed subsections and the total cross section i.e. $S_c = S_i = S_b$. Simplification of Larsen's method leads to a simple form of the Sabaneev equation (Ashton, 1986). The Larsen method can be written as follows:

$$n_c = \frac{0.63 n_b\left(\frac{Y_i}{Y_b}+1\right)^{\frac{5}{3}}}{\frac{n_b}{n_i}\left(\frac{Y_i}{Y_b}\right)^{\frac{5}{3}}+1} \tag{4.40}$$

where Y_i and Y_b are the total depths of the ice and bed zones.

In the following, a new method to estimate composite roughness is developed based on measured velocity profiles. Using four months of continuous field measurements collected under ice cover using acoustic instruments, the validity and applicability of the main assumptions employed in the new theoretical method are evaluated. Results of this method are compared to observed total flow resistance and values obtained using previous methods.

Introduction to a new approach for composite resistance calculation

Assuming the logarithmic distribution of the velocity profile from the boundary surface to the location of maximum velocity as shown in Figure 4.4 , a line can be fitted to the measured velocity data in the form of $u = \alpha \ln(z) + \beta$. Values of shear velocity and equivalent sand roughness can be calculated from the slope and intercept of the fitted line as (Calkins et al., 1982):

$$u_* = \alpha\kappa \tag{4.41}$$

$$k_s = 30e^{\frac{-\beta\kappa}{u_*}} \tag{4.42}$$

Manning roughness coefficient for both upper and lower boundaries then can be calculated using Strickler's empirical equation as follows (Vischer, 1987):

$$n_{i,b} = 0.0047{k_{s_{i,b}}}^{0.167} \tag{4.43}$$

where n_i and n_b are respectively the Manning roughness for upper ice-cover *(i)* and lower bed *(b)* boundary layers.

Composite roughness calculation

The velocity defect law can be defined as :

$$V_{max} - u = \sqrt{\frac{\tau}{\rho}}\,\frac{1}{\kappa}\,\ln\left(\frac{z}{Y}\right) \tag{4.44}$$

Mean velocities for the bed and ice zones can be calculated by integrating equation (4.44) from the boundary surface to the location of maximum velocity. So, maximum velocity and mean velocity for each section can be written as (Stevenson, 1963):

$$\bar{U}_i + \frac{u_{*i}}{\kappa} = \bar{U}_b + \frac{u_{*b}}{\kappa} = V_{max} \tag{4.45}$$

where the overbar indicates the vertically averaged mean. The boundary shear stress for each zone as a function of the associated Darcy-Weisbach resistance coefficient can be calculated using:

$$\tau = \frac{\rho}{2}\,\frac{f}{4}\,U^2 \tag{4.46}$$

On the other hand from continuity equation, we know:

$$U_c.A_c = U_b.A_i + U_b.A_b \tag{4.47}$$

Applying the momentum equation, total slope of the energy grade line, S_{fc} can be defined as:

$$A_0.\rho.g.S_{fc} = \tau_i.P_i + \tau_b.P_b \tag{4.48}$$

in which $\tau_i = \gamma.R_i.S_{fi}$ and $\tau_b = \gamma.R_b.S_{fb}$. Hence, the 4.48 can be written as:

$$S_{fc} = \frac{A_b}{A_c}.S_{fb} + \frac{A_i}{A_c}.S_{fi} \tag{4.49}$$

$$\tau_0 = \gamma.R_c.S_{fc} = \gamma.\frac{A_c}{2(b+y_c)}.(\frac{A_b}{A_c}.S_{fb} + \frac{A_i}{A_c}.S_{fi}) \tag{4.50}$$

Assuming $2(b+y_c) = P_c$, two new terms in 4.50 can be introduced as:

$$R'_b = \frac{A_b}{P_c}\ ,\ R'_i = \frac{A_i}{P_c} \tag{4.51}$$

Substituting U from (4.46) in (4.47) and arranging it for f_c leads to:

$$f_c = \frac{\tau_c}{\left(\frac{\tau_i}{f_i}\right)\left(\frac{Y_i}{Y_c}\right)^2 + 2\sqrt{\frac{\tau_i\tau_b}{f_i f_b}}\left(\frac{Y_i Y_b}{{Y_c}^2}\right) + \left(\frac{\tau_b}{f_b}\right)\left(\frac{Y_b}{Y_c}\right)^2} \tag{4.52}$$

Using 4.50 to 4.51, 4.52 can be rewritten as:

$$f_c = \frac{\gamma\ (R_i S_{fi} + R'_b S_{fb})}{\left(\frac{\tau_i}{f_i}\right)\left(\frac{Y_i}{Y_c}\right)^2 + 2\sqrt{\frac{\tau_i\tau_b}{f_i f_b}}\left(\frac{Y_i Y_b}{{Y_c}^2}\right) + \left(\frac{\tau_b}{f_b}\right)\left(\frac{Y_b}{Y_c}\right)^2} \tag{4.53}$$

The friction slope can be written as:

$$S_f = \frac{{u_*}^2}{gR} \tag{4.54}$$

Using the definition for S$_{(fi)}$ and S$_{(fb)}$ presented in 4.54, 4.53 can be written in the form of:

$$f_c = \frac{\frac{R'_i}{R_i}{u_{*i}}^2 + \frac{R'_b}{R_b}{u_{*b}}^2}{(\frac{u_{*i}}{\sqrt{f_i}}\frac{y_i}{y_c} + \frac{u_{*b}}{\sqrt{f_b}}\frac{y_b}{y_c})} \tag{4.55}$$

According to (4.45) to (4.55), the composite roughness coefficient for a channel cross section can be written as:

$$f_c = \frac{(\frac{R'_i}{R_i})\left(V_{max} - \bar{U_i}\right)^2 + (\frac{R'_b}{R_b})\left(V_{max} - \bar{U_b}\right)^2}{\left(\frac{(V_{max}-\bar{U_i})}{\sqrt{f_i}}.\frac{y_i}{y_c} + \frac{(V_{max}-\bar{U_b})}{\sqrt{f_b}}.\frac{y_b}{y_c}\right)^2} \tag{4.56}$$

Equation(4.37) can be used to convert fc to an equivalent Manning's composite roughness n_c. Applicability of equation (4.56) for composite roughness calculation is tested through a field campaign and results are presented in section 5.2.2.

4.3 Acoustic techniques for estimation of suspended sediment concentration

Using the shear velocity estimation from equation (4.3), vertical concentration profiles $c(z)$ for all grain sizes can be obtained from the equation below (Moore et al., 2013):

$$c\,(z) = \; c_a\left(\frac{(H - z)}{z}\;\frac{a}{(H - a_\alpha)}\right)^{P_n} \tag{4.57}$$

in which c_a is the references concentration of the specific size of sediment at the reference height a_α($\cong$ average value of k$_s$ from the velocity profiles), H is the water depth and is P_n the Rouse number which can be represented as:

$$P_n = \frac{\omega_s}{\beta\kappa u_*} \tag{4.58}$$

In the equation above, $\beta \approx 1$ is ω_s the fall velocity.

The reference concentration for sediment size d can be calculated as (van Rijn, 1982):

$$C_a = 0.015\frac{d}{a_\alpha {d_*}^{0.3}}(\frac{{u_*}^2 - \;{u_{*cr}}^2}{{u_{*cr}}^2})^{1.5} \tag{4.59}$$

Where d_* is the non-dimensional diameter and u_{*cr} is the critical bed shear velocity for each grain size.

Equation (4.59) provides the concentration of each size of sediment for a given shear velocity in respect to the height from the bed. Integration of equation (4.57) over the grain size distribution of the bed sediment provides the total concentration of suspended sediment from the bed up to the location of maximum velocity (zone of equation (4.3) applicability, refer to 4.2.1).

Since the ADCP records the backscatter intensity (section 3.1.4) not the concentration, theoretical backscatter intensity should be related to the concentration of each size of sediment. For this purpose, the equation provided by Thorne and Meral (2008) is applied to the recorded backscatter data. The equation is mainly developed for backscatter from sand sized sediment and can be represented as:

$$S_v\left(z\right) = 10\log\left[\frac{{n_w}^4}{2\pi}\left(\frac{e-1}{3e}+\frac{g_d-1}{2g_d+1}\right)^2\right] + \ 10\log\left[\int c\ (z,d)(\frac{d}{2})^3 p(d)\partial d\right] \quad (4.60)$$

Where is $S_v\left(z\right)$˜the theoretical backscatter power per unit volume, n_w is the acoustic wave number, e is the ratio of elasticity of the particles to water and g_d is the ratio of the particles density to the water. The first term is a constant accounting for the sediment properties. Term $c\left(z,d\right)$ is the concentration of particles of diameter d at height z.$p(d)$ is the probability density function of the grain size distribution by volume of the bed material.

Recorded intensity in counts E, can be converted to the measured backscatter power per unit volume using the following equation (Moore et al., 2013):

$$S_v\left(z\right) = \Psi - PdBW - 10\log\ \left(b_s\right) + K_cE + 20 + 2\alpha r \quad (4.61)$$

Where Ψ is the instrument specific constant equals to -135 dB, $PdBW$ is the transmit power [dB] , K_c is a coefficient equals 0.43 dB/counts, r is the distance from transducer and α is the attenuation coefficient. The term $10\log\left(b_s\right)$ normalizes the measured volume to 1 m^3 while the term K_cE converts the intensity recorded in counts to dB referenced to $1\mu\ Pa$.

Equation (4.61) applicability is limited to the condition that the signal exceeds the noise level by at least 10dB. Recorded data showed that the equation was valid for the measurements of this study. According to the beam deflection angle, 20°, radiance can be represented as : $r = \frac{z}{\cos 20°}$.

Assuming that the vertical distribution of particle sizes continues to be a function of fall velocity and shear velocity of the flow, the difference between measured and predicted backscattering strength can be interpreted to be due to variation in concentration of the similar sized sediment. Thus the observed concentration can be calculated based on a combination of theoretical concentration and the difference in observed and predicted (Moore et al., 2013):

$$C_{obs} = \ C_{th} \times 10^{\frac{(S_{v_{obs}} - S_{v_{th}})}{10}} \quad (4.62)$$

In the equation above, C_{obs} and $S_{v_{obs}}$ are the observed concentration and backscatter strength while C_{th} and $S_{v_{th}}$ are representing the theoretical values of the same parameters.

Chapter 5

Results

5.1 Ice cover effect on river Hydraulics

5.1.1 Ice observations

Acoustic results presented about analysis of ice condition and river hydraulic are all investigated through a field campaign of 2012 winter. ADCP and SWIPS setting for all field studies are presented at Appendix C.

Analysis of the ice cover suggests break-up started to occur in mid April in the study year (2012) and the process continued until mid May, when break-up typically occurs on the Lower Nelson River (Ghareh Aghaji Zare et al., 2013). Briefly, LANDSAT and NASA MODIS satellite images (Figure 5.1) of the LNR were collected for the break-up period and studied to clarify the division of the ice stages.

These images revealed that the ice cover disappeared from the study site sometime between May 10^{th} and May 13^{th} when the complete open water condition began. Similarly, based on direct observations, the ice cover broke up on April 21^{st} at a measurement station (Conawapa Axis"B"), approximately 22 km upstream of the study site. The ADCP temperature sensor data during and after the break-up period revealed that water temperature increased from 0°C to 3°C - 4°C after May 10^{th} when the ice cover started to release. Finally, changes in water level and surface backscatter (Figure. 5.10-a) suggest the ice cover fully released on May 13^{th}. Thus, the break-up period on the LNR began in April, although complete break-up and cover removal at the study site appears to have occurred on May 13^{th}(Ghareh Aghaji Zare et al., 2013; Moore et al., 2013). Ice thickness was also calculated throughout the campaign using water level and the elevation of lower surface of the ice cover from a 546 kHz Shallow Water Ice Profiler Sonar (SWIPS) (Ghareh Aghaji Zare et al., 2013; Moore et al., 2014). The ice thickness was observed to increase at the end of April. It is reasonable to suggest that higher discharge during spring freshet increased the thrust on the cover, causing the cover to start to fracture and mechanically thicken until it reached sufficient thickness to resist against the higher thrust exerted on the body of the cover by the increased discharge velocity. This process of mechanical thickening is called

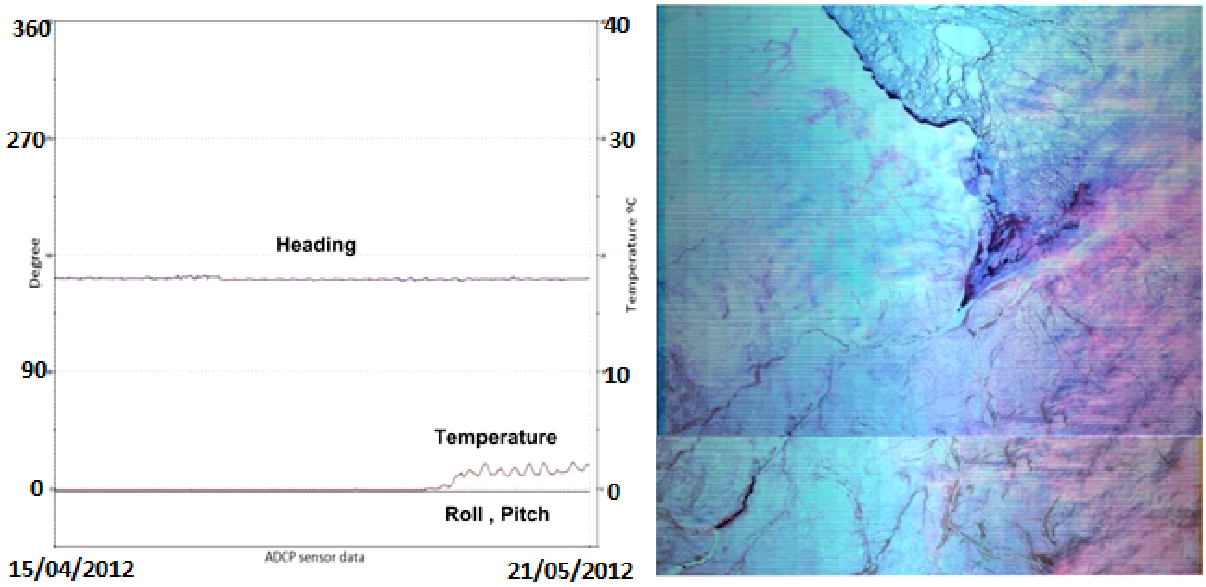

Figure 5.1: (a) ADCP sensor data between mid April to late May, (b) Satellite Image (LANDSAT) of study reach, April 2012

shoving, in which the ice edge starts to retreat downstream from its original location and thicken in downstream cross sections (Davar et al., 1998). Shoving roughens the ice cover lower surface with large jagged ice protrusions, which impede flow near to the boundary (Beltaos, 1995a).

Reviewing backscatter intensity results also reveals severe freeze-up condition during the 2013-2014 winter. Figure 5.2 shows the backscatter intensity data (not range corrected)for all four beams during the 2012-2013 winter field campaign.

Some features are very distinctive in this figure. First of all, several null windows appear early in winter separated with narrow bands of recorded data between November 12th, 2012 to late January 2013. According to the nature of the recorded values (uniform distribution in the depth) the phenomenon can be interpreted as the slush ice presence during the freeze-up period in the year of study. This is also consistent with the field observations most of which are indicating the presence of a severe slush ice condition during the winter at the early and late stages of the stable ice cover. As shown in the figure, slush ice expanded over the depth of the water within the blank distance of the instrument (60 cm from the transducer) blocking the propagation of sound pulses in to the water and consequently stopped the instrument recordings. However, water surface elevation is recorded constantly during the freeze-up period (solid blue line in the figure) indicating that the instrument was not physically blocked (anchor ice is not formed on the instrument).

According to the backscatter information presented in Figure 5.2, the freeze-up period is estimated to have continued until late January in the year of study. Formation of the stable ice cover over the study site is accompanied by a higher resistance to the flow resulting in the significant increase in the water surface level. As shown, water level raised up to

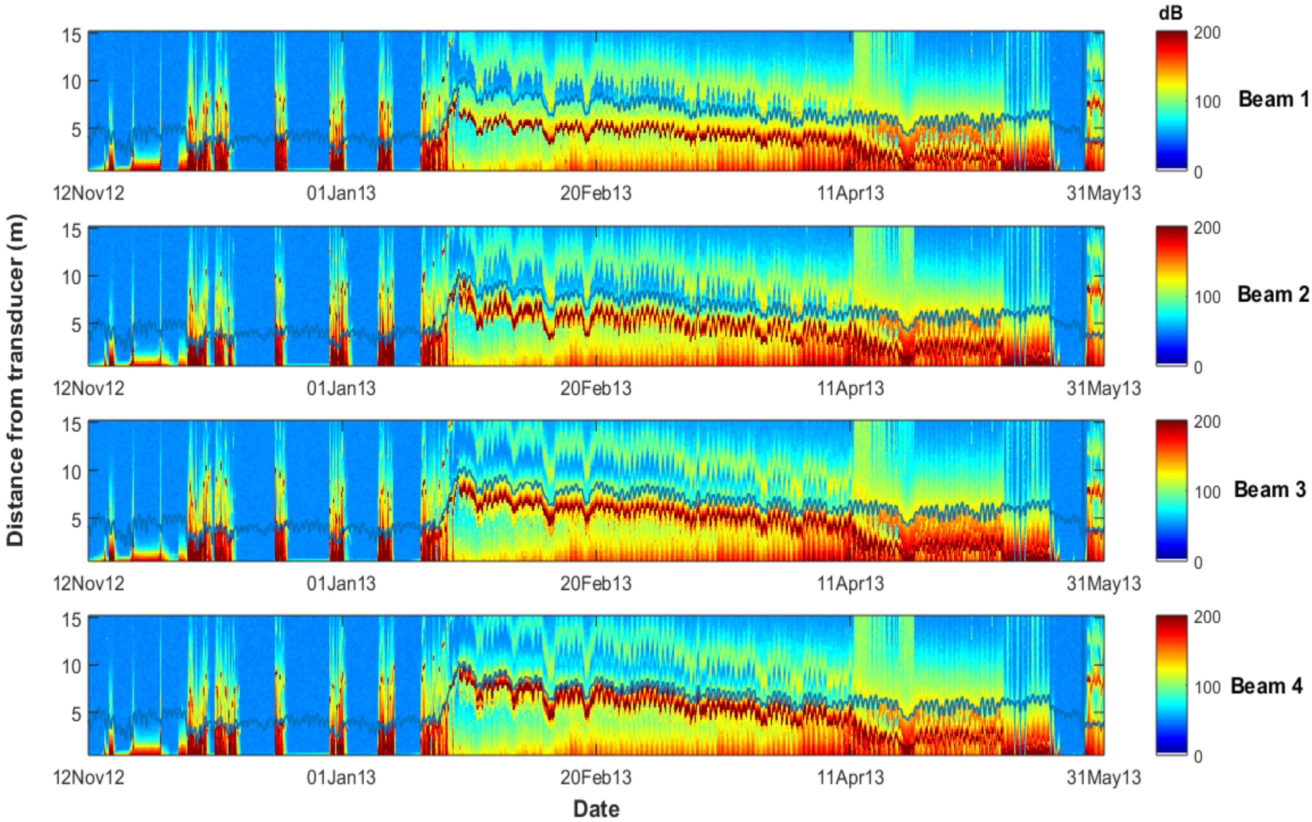

Figure 5.2: Backscatter intensity data for 2012-2013 winter in dB, showed for all four beams

5 meters within a week by the formation of stable ice cover. The stable ice cover period continued until late May 2013 at the deployment site.

The second important observation is about the evolution and development of the ice cover during the stable ice cover period i.e. stabilization period (late January to mid-April). During this period, the ice cover bottom location can be identified by a very narrow band of very high backscatter intensity in all beams. Since the beams at the elevation of bottom of the ice may be up to 10 meters apart, information presented in the figure can be used to estimate the spatial variation of the ice bottom location i.e. ice thickness at the study site. As seen, the thickness of the ice in all beams remains relatively constant in time by early April. It means that the ice cover stabilized at the deployment site during this period. The trend of water surface elevation is also considerable during this period. As seen, the water surface elevation slowly but constantly decreases in time. This is another indication of the cover stabilization. As time passes after the rigid ice cover formation, water reshapes the undersurface of the ice cover by smoothening of the cover or eroding specific areas exposed to the higher water velocities. This phenomenon is more obvious during the ice jam formation when the ice blocks come in contact with river boundaries and temporarily block. High water velocities then erode the cover and eventually lead to the formation of ice grooves under the cover in the flow direction(Wong et al., 1985; Beltaos, 1995a). Such a process increases the conveyance capacity of the covered channel (though not significantly) either by reducing the hydraulic resistance to the flow or increasing the hydraulic radius. Therefore the backwater effect caused by the formation of the stable ice cover decreases in time.

Starting with the break-up period (can be seen around April 11th), higher water velocities (which will be shown later (Figure 5.9) and therefore higher hydraulic thrust on the cover, thickens the cover mechanically. Thicker ice with rougher under cover surface increases the resistance to the flow again and the decreasing trend of the water surface elevation stops. The thickening process lowers the ice bottom location in the water to very close to the transducer (vicinity of the blank distance). Considerably thick cover accompanying with slush ice presence eventually stops the instrument from data recording during the end of the break-up period and another null window occurs around the end of May. Eventually, ice cover is removed by the start of June and water surface elevation returns to the open water period elevation of about 4 meters at the deployment site.

A full cycle of ice cover formation and removal (though not continuous due to some lost data windows during freeze up and break-up) was observed during the 2012-2013 study year at the deployment location illustrating the ice cover formation stabilization and removal.

Spatial averaged (over 4 beams) ice cover thickness estimation for the winter 2013 is presented in Figure 5.3. Three main stages are obvious in this figure. First, the stable ice cover period, between late January to almost mid-April, when the ice thickness remained around 2 meters, experiencing very little variation which is presumably due to temporary ice deposition and erosion. Starting with the thermal break-up period, a sudden increase is observed in the ice thickness values. This is likely due to the processes of thermal weakening followed by the mechanical thickening. As a result of the combination of these two processes, thermally weakened ice cover started to fragment and reconsolidate at the location and hence mechanically thicken to resist against the higher water velocities and shear stresses under the ice cover. Notably higher water velocities (will be shown later in figure) are also observed immediately prior to this stage, indicating the thermal break-up started at the site or upstream sections. The ice cover condition then became fairly stable until the end of April and early May. Starting the dynamic stage of mechanical ice cover break-up, the ice cover almost doubled in thickness to 5.5 meters due to accumulation of break-up ice runs and slush ice introduction from upstream sections. The ice cover thickened to such a degree that the ice bottom location lowered to the blank distance of the ADCP (within 60 cm from the transducer) resulting in the formation of an obstacle to the sound and disturbed the data recording process. Since the ice thickness is calculated based on the location of the underside of the cover (as discussed in section 3.1.5), no ice thickness is calculated during this period (Not shown in Figure 5.3). Nevertheless, considering the nature of the phenomenon and the logic described above, the zero ice cover thickness recordings during this period can be interpreted as even higher ice cover thicknesses. The frequency of appearance of zero ice thickness values increases in time making the graph more complicated to distinguish and thus the rest of the break-up period is not represented in the figure, although this trend can be clearly followed in Figure 5.3.

Investigating the ice cover thickness estimation using all four beams individually showed more or less the same trend in ice thickness. Interestingly, ice cover thickness estimation

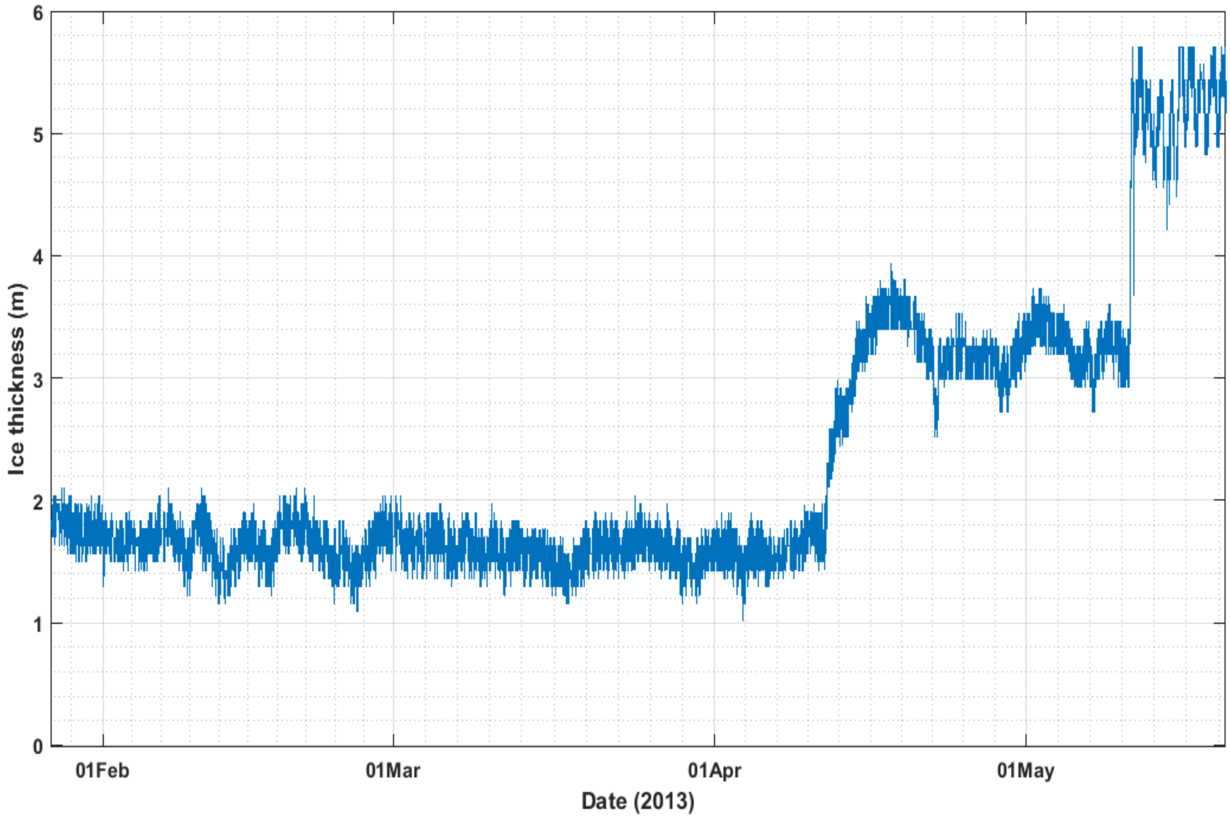

Figure 5.3: Ice thickness estimation for the deployment site during the winter 2013

varied up to 2.5 meters between the four beams indicating the spatial variation in ice cover thickness during the stable ice cover period at the deployment site. Ice cover thickness estimation at beam 2, is the closest to the beam averaged ice cover thickness while the beam 4, the most downstream relative to the deployment location, showed the lowest ice thickness values. Considering the fact that the estimation of ice cover thickness using individual beams are several meters (up to 15 meters for diagonal beams and 9 meters for adjacent beams) apart from each other, Figure 5.4 can be interpreted as the spatial variation of ice thickness at the study site during the stable ice cover period considering the fact that the tilt variation during this time was negligible. Interestingly, during the thermal break-up and mechanical fragmentation and reconsolidation processes, the ice cover thickness values tend to an almost equal value. This observation suggests the formation of an equilibrium ice cover at the site during the late stages of the ice cover period when the cover characteristics were mostly governed by the hydraulic conditions of the study reach.

During the 2015 deployment year, the instrument was deployed after the ice cover formation. Figure 5.5 shows the backscatter intensity for all beams during the 2015 field campaigns. In contrast to the inconsistencies in backscatter data during the 2013 field study, in 2015, backscatter intensity was continuous and consistent between beams during the one month deployment.

Ice cover thickness during the stable ice cover period of 2015 field campaign, showed

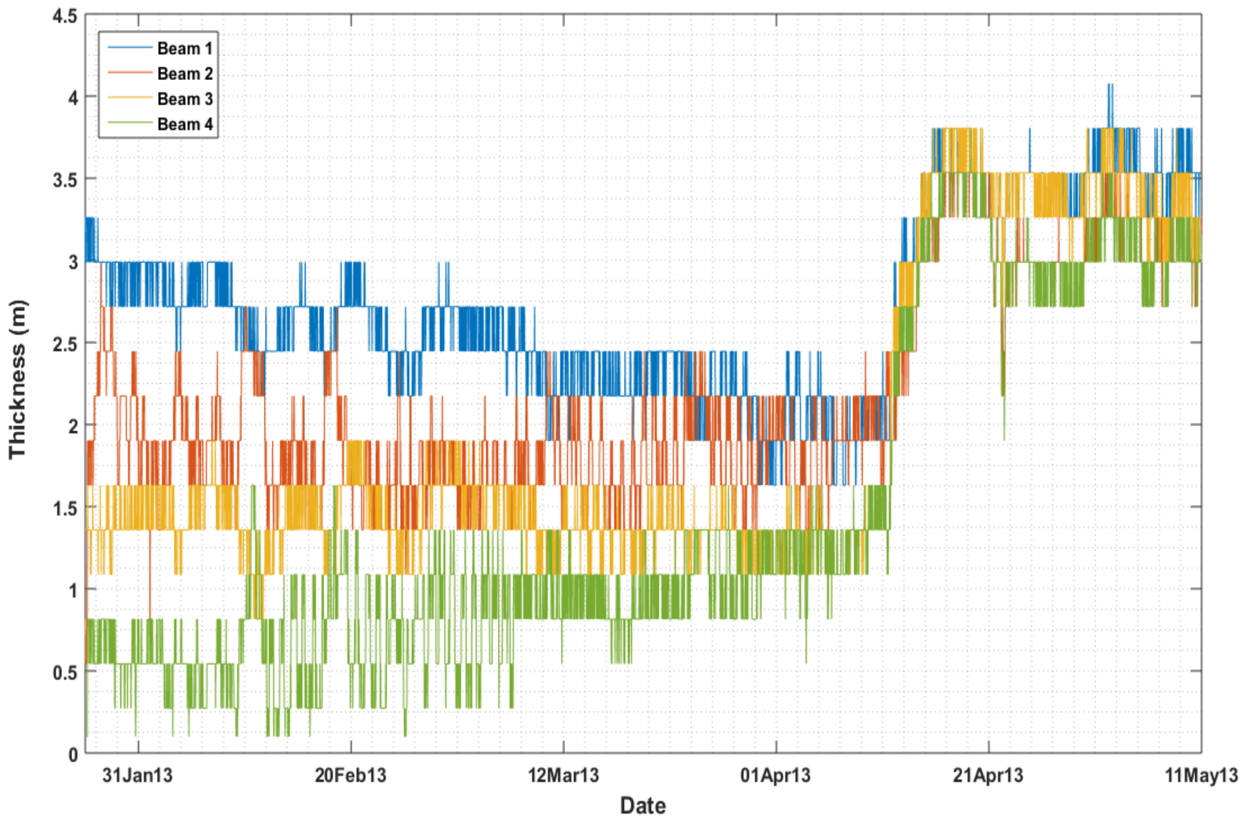

Figure 5.4: Estimation of ice thickness variation using individual beams during the ice cover period, 2013

changes in matter of a centimetres (10 to 50) due to periodic cycles of hydropeaking at LGS (Figure 5.6). The variation could be due to the temporal deposition of the ice floes under the ice cover during the low peaking times. During the flow acceleration phase of the hydropeaking cycle, deposited, but not consolidated, ice floes are washed away from their location and are carried downstream with the flow. Comparing the stable ice cover periods between 2015 and 2013 winters, ice cover thickness were significantly smaller (about one sixth) during the March 2015 campaign. Field observations during the deployment also confirm the calculated values for the ice cover thickness It is evident in Fig 5.5 that beam 4 tended to have higher backscatter intensity than beam 3, which itself was higher than beams 1 or 2. Beam 4 was downstream of the mount, and beam 3 was upstream of the mount. Note that both roll and pitch values were constantly less than 3 during the deployment period (not shown here), thus the discrepancy is not due to instrument tilt. Therefore considering the velocity profiles for individual beams (will be shown in Figures 5.20 and 5.21), relative difference in the backscatter intensity in beams 1 and 4 can be interpreted as the cross sectional variation in the concentration of suspended material. It appears that greater sediment transport occurred along the stream path line at the bottom mount than on either side of the mount.

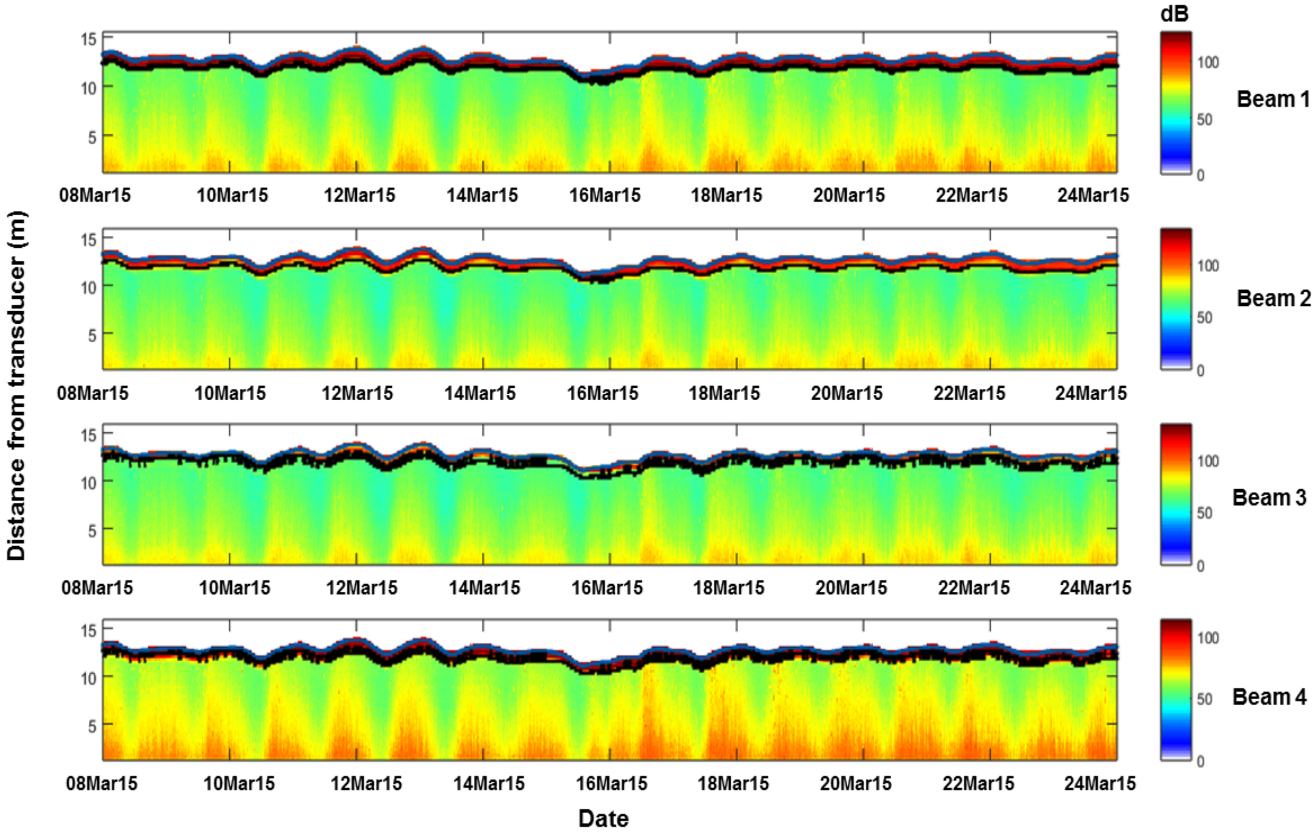

Figure 5.5: Backscatter intensity for all four beams during the stable ice cover period of 2015

5.1.2 River hydraulics under different ice stages

The main effect of ice cover on river hydraulics can be found through the analysis of flow velocity during the ice cover period. As discussed in sections 2.5.1 and 4.2.1, ice cover presence alters the flow velocity in terms of magnitude and distribution. This necessitates the detailed analysis of flow velocity under the ice cover period to better understand the variations in flow hydraulics.

Flow velocity is measured during different river ice cover conditions through out this study mainly as; stable ice cover and break-up (2012 study), freeze up, stable ice cover and break-up (2013 investigations) and stable ice cover (2015 study).

Water velocities are presented (for all study years) and analyzed in particular (for the first study year, 2012) in this section.

Figure 5.7 show the raw recorded velocity magnitudes for the total ice processes stages in 2012-2013 study year.

As discussed in section 2.5.2 and 3.1.3, ADCP recordings in instrument coordinates includes three main velocity components as well as the error velocity which increases with greater inhomogeneity in flow velocity between beams. As shown in Figure 5.7, the same missing windows appeared in velocity recordings as in the backscatter intensity values.

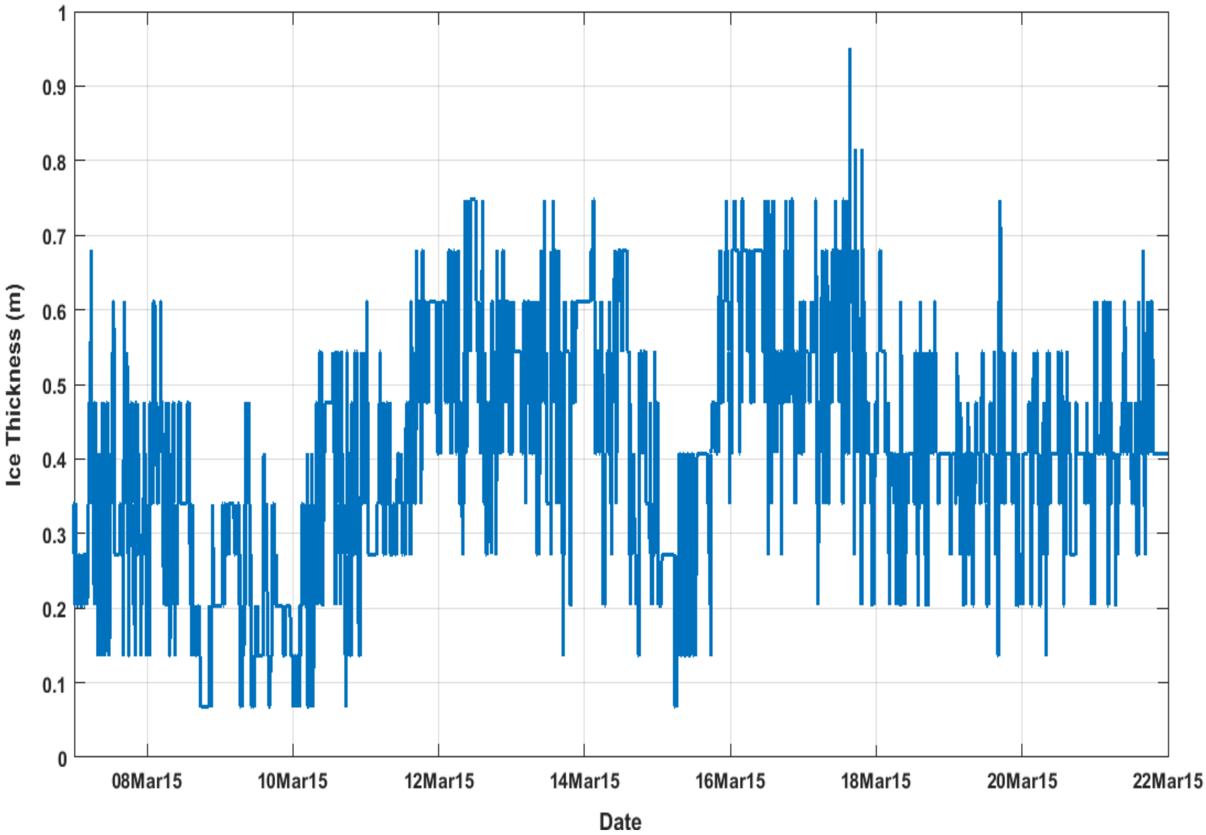

Figure 5.6: Ice cover thickness estimation during the stable ice cover period of 2015

However, before the ice cover formed over the study reach (late January), when the ADCP was able to record, relatively high streamwise water velocities were recorded. According to the figure, at the start of the ice cover period, the water surface elevation raises and streamwise water velocity decreased . The ice cover is presented in velocity recordings in the form of white (null) bands of recordings which shares the same shape as was observed in backscattered intensity data. Streamwise water velocity increased around mid-April, while the null band gets narrower and lower in water depth accompanied with higher recorded velocities just before the start of mechanical break-up. This is an indication of higher streamwise water velocity, which likely contributed to mechanical ice cover thickening (shoving process). Another interesting feature appeared during the mechanical thickening period; the , ADCP recorded velocities in the cells where representing the ice cover in all directions. Though the recorded velocities are physically meaningless, they are indication of sound pulse penetration in to the cover which can be interpreted as different nature (less dense material) of the cover compared to the stable ice cover period. This can also be seen in Figure 5.2 , where relatively high backscatter intensity values were observed above the ice cover during this period. This observation supports the interpretation of the nature of the cover during the break-up period as porous cover i.e. slush ice which is consistent with other field observations at the deployment site.

It is notable that Figure 5.7 shows the unfiltered velocity recording and therefore velocity magnitudes are recorded to a certain elevation above the water surface elevation

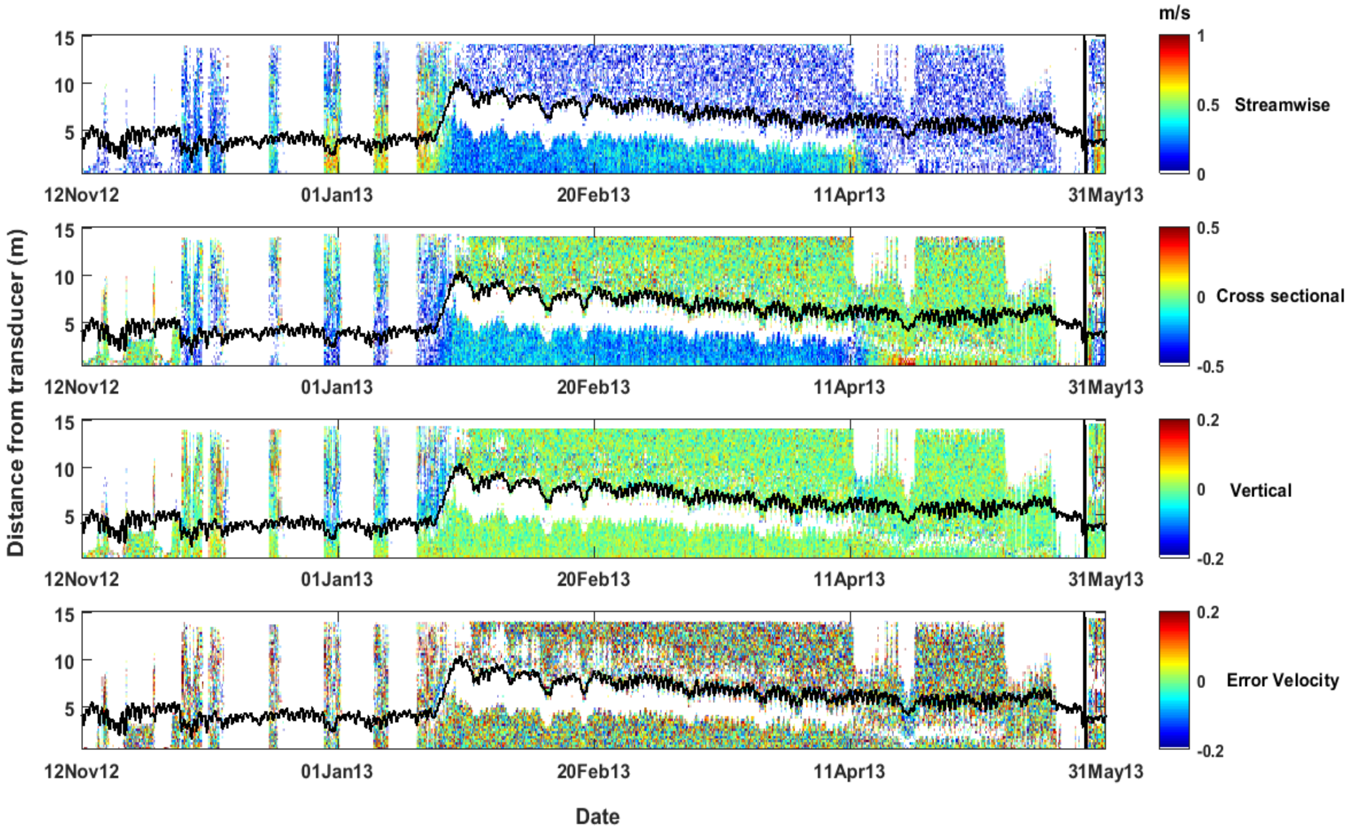

Figure 5.7: Orthogonal ADCP velocity recording

(solid black line). This is due to the echo of the sound pulses which bounce back and forth from the boundaries (water surface/ice undersurface) and since the time of reception of the bounces are different, the instrument reads them farther from the transducer. However, since these values are not representing any physical velocity, they are filtered in the velocity analysis .

An interesting feature appeared in the cross sectional velocities. Whereas the streamwise velocity decreased due to the thickening of the ice cover at the start of break-up, cross sectional velocity is observed to increase . This could be an indication of flow obstacle formation, in which an obstacle blocks the main stream and deviates the flow from the path it was flowing. Combination of very thick, porous ice cover (presented in both backscatter and velocity data) as well as very low streamwise velocity and instead higher cross sectional velocity can be reasonably related to the formation of an ice jam at the study site during the end of the break-up period. Ice jam formation was also observed during the 2012 field campaign at the ADCP recordings (as will be discussed in detail in sections 5.1.3 and 5.1.4)

Vertical water velocity is observed to fluctuate between positive and negative values which is an indication of medium turbulence intensity in the flow. Turbulent structures will be discussed later in the section 5.3). No specific trend is observed in error velocity and the values are found to be distributed randomly.

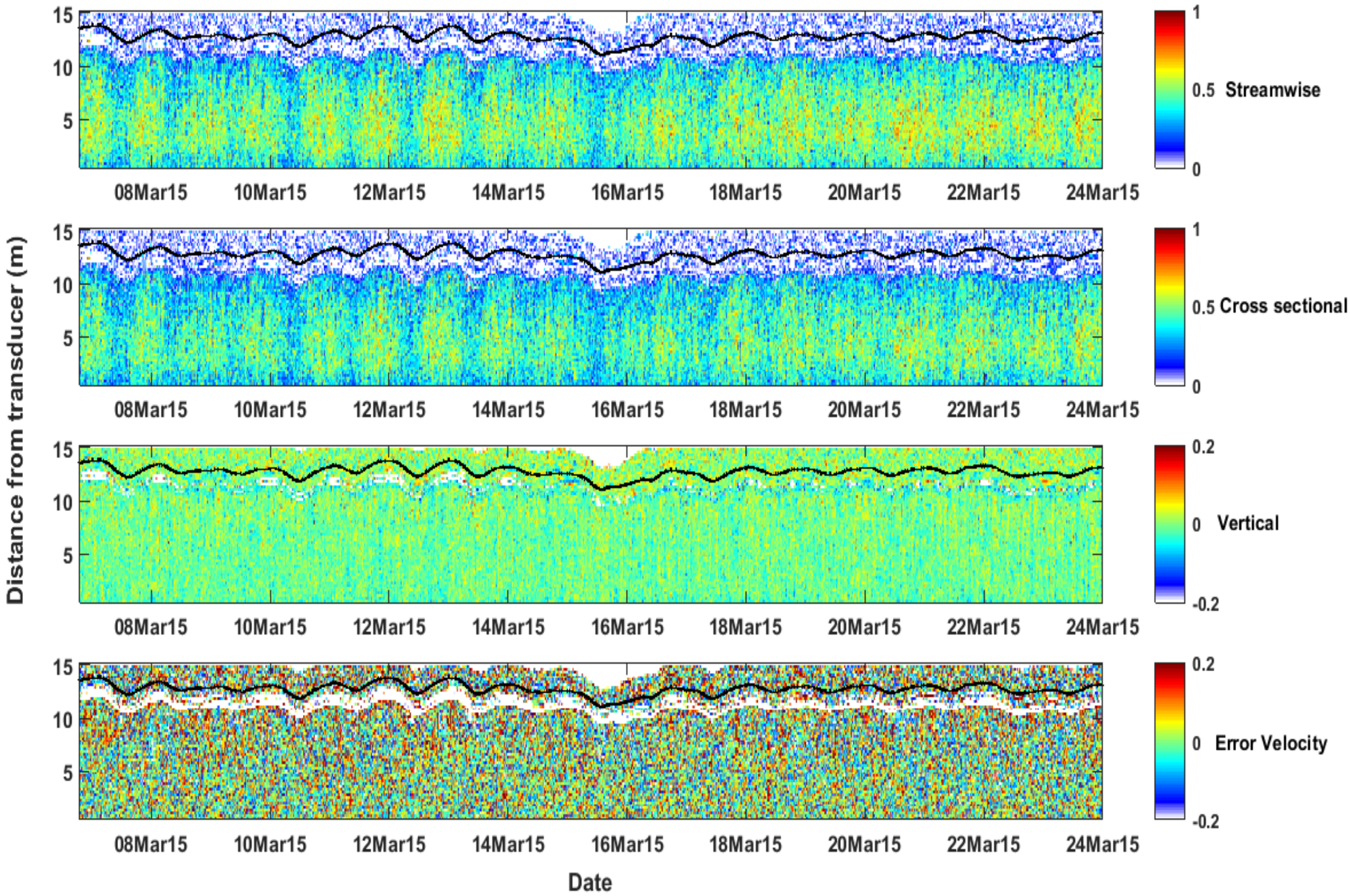

Figure 5.8: Orthogonal ADCP velocity recording, 2015

The ADCP recorded orthogonal velocities during the stable ice cover of 2015 winter are presented in Figure 5.8. Considerably less variation in ice cover thickness was observed at the deployment area during the data acquisition period of 2015 campaign, leaving the recordings as a consistent, less variant set of information. Even though the ice thickness was significantly less during the stable ice cover period compared to 2013 investigations, water is observed to stage higher . Even though the deployment locations were not exactly the same but they were close enough to represent the general sense of the ice cover condition at the deployment location through the deployment years. This could be an indication of physical downstream blockage of the flow, making the flow condition more stable during the study period. However, since the data acquisition period was significantly shorter during the 2015 data, ice cover condition analysis would be restricted to the recording time window which increases the uncertainty level of the ice cover condition analysis for the longer period of winter.

A sequence of higher water velocity is obvious in both streamwise and cross sectional velocity recordings which is clearly due to the hydropeaking operations of Limestone Generating Station. Though this effect is clearly obvious in 2012 (will be shown later) and 2015 data, it is not observed in 2013 orthogonal and consequently mean velocity data (Figure 5.9). This can be described based on the ADCP data recording program. In 2013, the ADCP was programed to work in a burst mode with relatively short periods of high frequency data recording in order to analyse the turbulent structures in the flow. Due to the long period of deployment, the instrument was set to stand by for relatively long period of time between the bursts. This enabled the instrument to record high frequency variations in the flow but the data are not recorded during long periods and thus the data resolution for low frequency phenomena is lost. As a result, ADCP lost the velocity trend in low frequencies (daily basis sequences like hydropeaking) in the recordings.

Figure 5.9 shows the velocity magnitude during the stable ice cover period of 2013 at the deployment site. The velocity data are filtered for the elevations above the water surface elevation. Ice bottom location is also averaged for four beams (presented in section 5.1.1) and superimposed on the velocity data. Almost the same trend as observed in streamwise velocity is apparent in the graph. Even though the hydropeaking effect on water surface elevation is obvious in the figure, the similar effect is barely traceable in the velocity magnitude variation. However, ice cover thickness variation in time, specifically as the break-up evolves, is more clear in this figure. The increase in water velocity observed during the early stages of break-up and subsequent amplification during the ice jam formation are better represented in this figure. Due to the significant difference in ice bottom location between the four beams (represented in Figure 5.4) during the stable ice cover period (before April 11^{th}), mean velocity recordings are not extended to the average ice bottom location . In the other word, (velocity values were not consistent through the beams with the same distance from the ADCP transducer), but However, the inconsistency diminishes while the more equilibrium ice cover condition takes place over the deployment site (beam estimated thickness values converge to the fairly identical value during the break-up).

Consistent observations of mean water velocity magnitude and orthogonal velocity magnitude are made in velocity recordings in 2015. Hydropeaking effect on mean water velocity is more obvious in Figure 5.9. Ice cover thickness variation was insignificant during the recorded ice cover period, however, slight variation in ice thickness is estimated through the cycle of hydropeaking and low peaking due to the deposition/erosion of the frazil ice and ice floes under the existing ice cover. The effect and frequency of operational cycle on ice thickness variation will be discussed and analyzed in section 5.2.1.

Figure (5.10) shows the ice cover condition, mean water velocity and maximum water velocity location under the ice cover period during 2012 field investigations.

Daily oscillations in the water surface elevation were observed (Figure. 5.10-b,solid black line), which are due to hydropeaking operations at Limestone Generating Station (LGS) upstream. Daily water surface fluctuations were on the order of 2 meters, and were accompanied by water velocity fluctuations. During the stable ice-cover period, hydropeaking caused depth averaged water velocity to vary between 0.35 m/s to 0.65 m/s, and maximum velocity magnitudes to vary from 0.4m/s to almost 0.75 m/s (Figure. 5.11-a).Water discharge at the cross section is also calculated based on time shifting of released discharge at LGS almost 50 km upstream of the study site. Discharge results are also presented in Figure. 5.11-b). The average and maximum velocities fluctuated within a constant range during the ice cover period, but at the start of the break up period, they rose significantly until they reached their maxima (more than1 m/s) at the end of April. This could be due

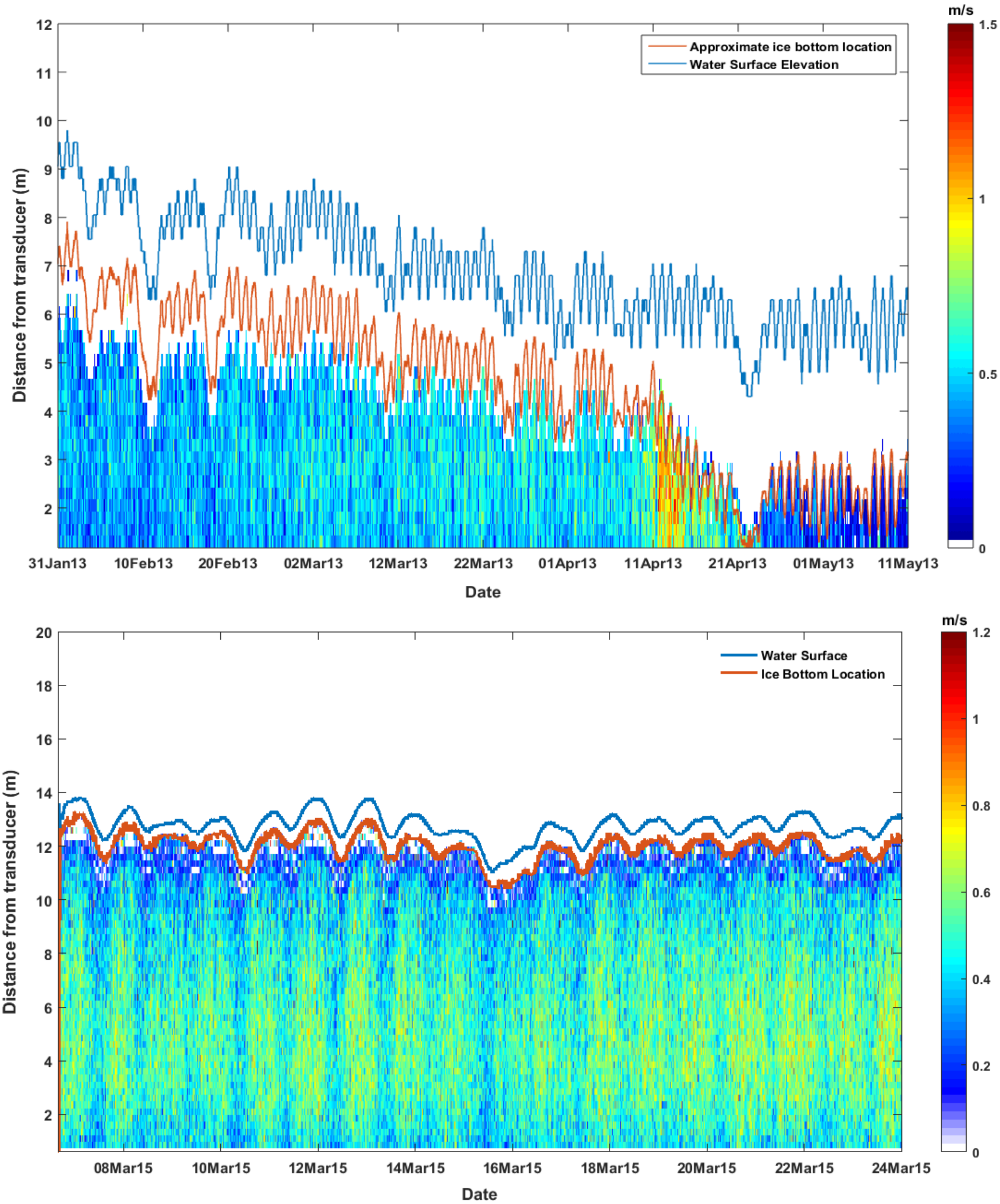

Figure 5.9: Mean water velocity magnitude under the ice cover, top: 2013, bottom: 2015

to introduction of new freshet water to the system, which caused a slight rise in water surface elevation between late April and early May.

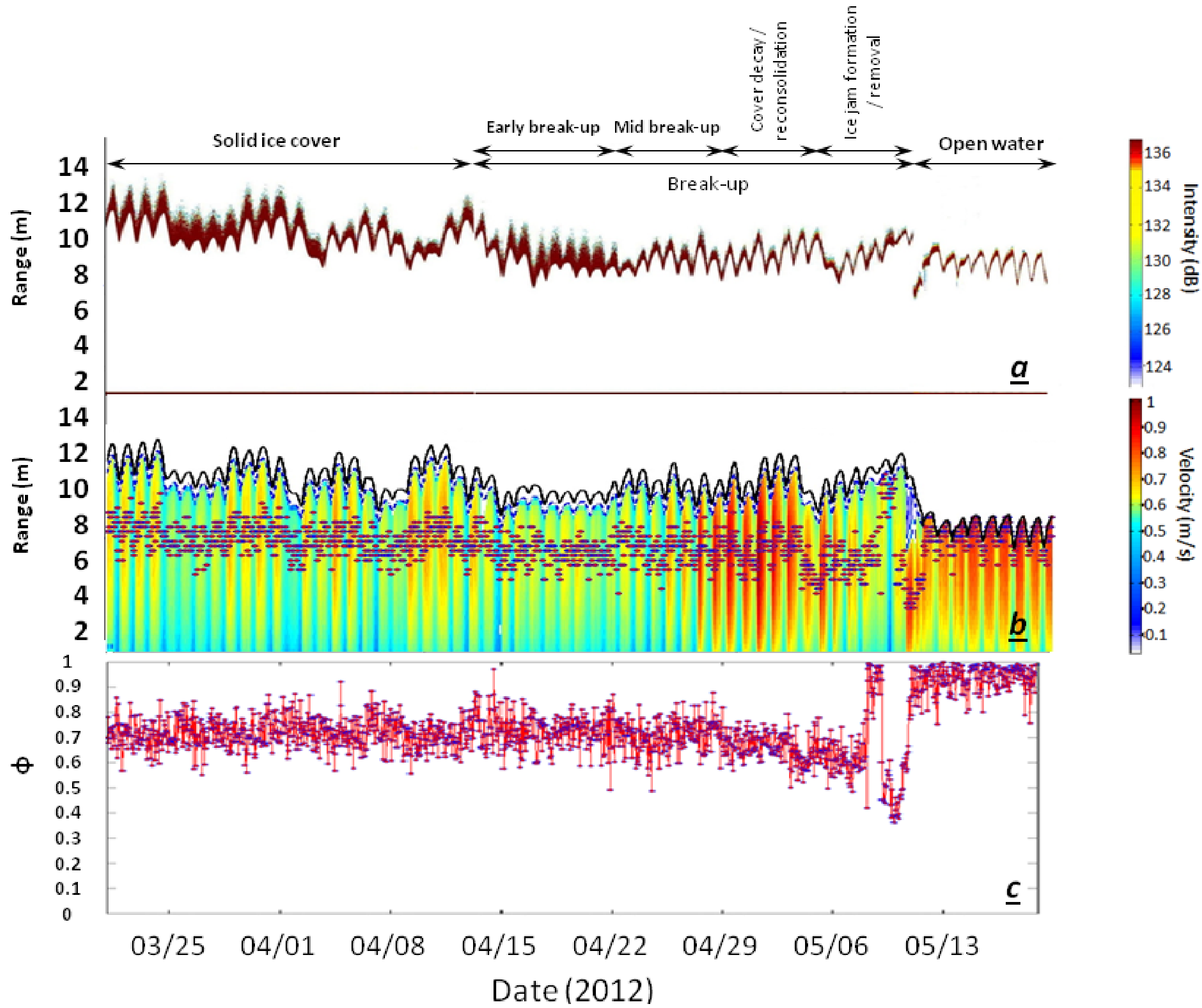

Figure 5.10: (a) River ice condition based on SWIPS data, (b) Water surface location(black solid line) undersurface of the ice cover (dotted blue line), water velocity and maximum velocity location as colored dots, and (c) normalized maximum velocity location over the study site

The elevations of the maximum velocity in the vertical profile in each ensemble are also shown as dots in Figure. 5.10-b. The location of the maximum velocity differentiates the ice zone from the bed zone portions of the water column. The non-dimensional ratio of the maximum velocity location over the depth, ϕ, is also calculated (Figure. 5.10 -c). It is notable that average water velocity was observed to be about 5% higher in the ice zone than in the bed zone (values are not shown) . This is particularly true during the stable ice cover, when the maximum velocity occurred in the upper half of the water column depth, roughly at $\phi = 0.7$ (Figure. 5.10-c).

During the break-up period in late April, higher volumes of water flow resulted in higher

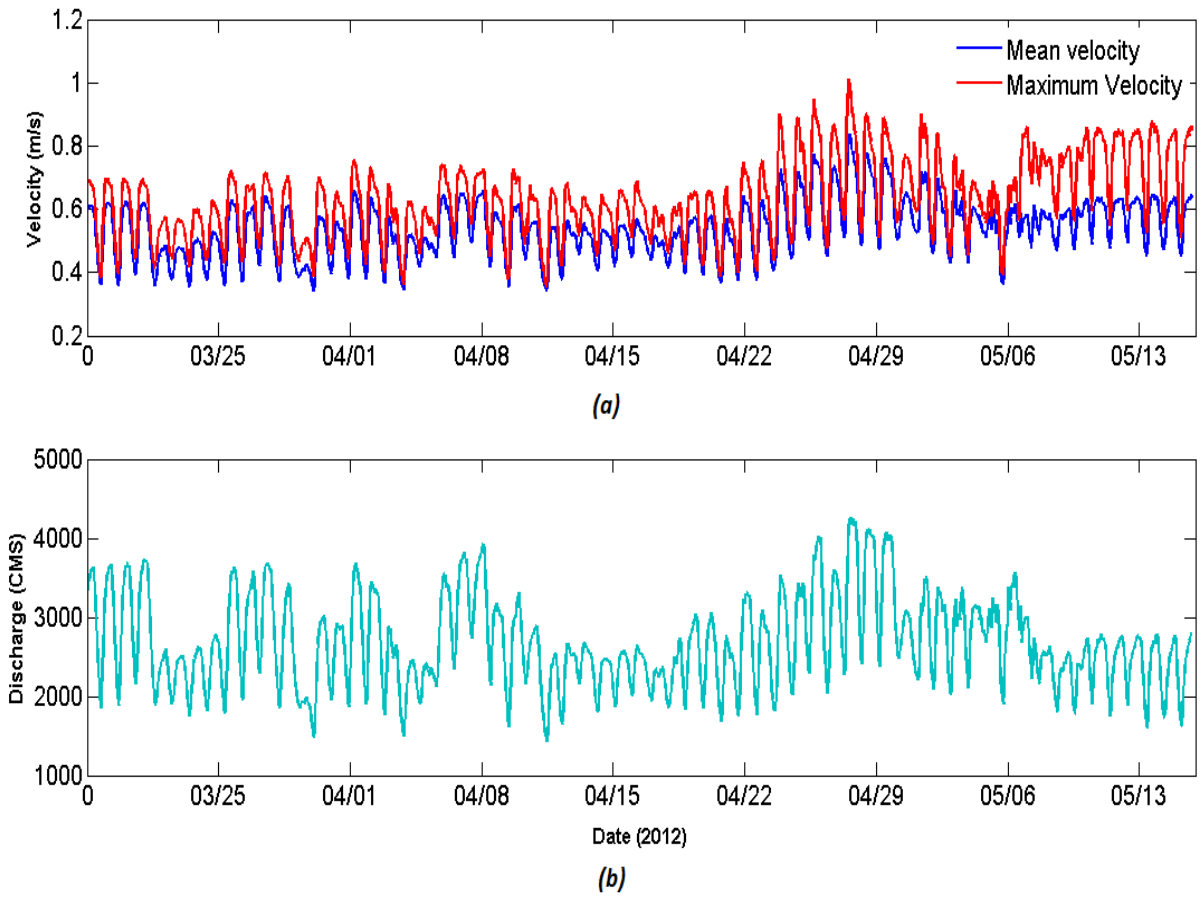

Figure 5.11: Variation of maximum and average velocity (a) and water discharge (b) during the study period

velocities (Figure. 5.10-b), and roughening of the upper boundary due to ice shoving pushed the maximum water velocity location deeper into the flow. This is observed in early May (Figure. 5.10 **b** and **c**). On May 7^{th}, ϕ briefly equalled 1, suggesting a brief ice-free period occurred at the sampling site. The value of ϕ then dropped dramatically to 0.40 on May 10^{th}, and then returned to 0.95 of the depth on May 12^{th}, and remained at values near 1 for the remainder of the measurement campaign. These observations suggest that an ice jam started to form briefly on May 8^{th}, and then the ice cover finally was removed afterwards when the jam released suddenly on May 12^{th} .

The possibility of the presence of an ice jam is corroborated by the fact that the water surface rose immediately before May 10 th and then suddenly plunged on May 12^{th}. This suggests the sudden presence and subsequent rapid removal of a flow obstacle (i.e ice jam).

This analysis of the ice-cover suggests that velocity profile measurements cover several different ice-cover conditions: i.e., solid ice cover, different ice cover break-up stages such as cover decay and reconsolidation, ice jam formation and release and open water.

The data set thus provides comprehensive coverage of many of the key stages of ice cover. This provides the opportunity for comparing boundary shear stress with an ice

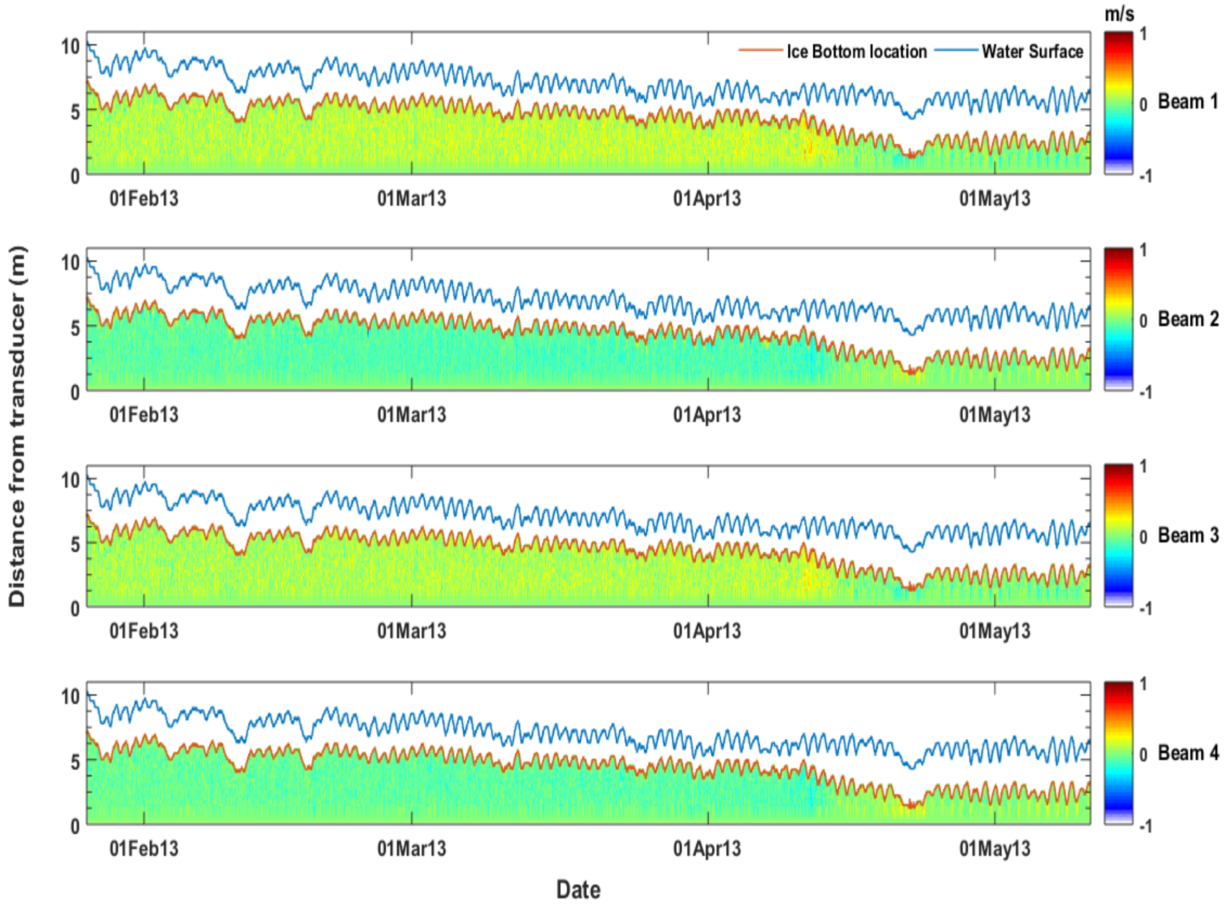

Figure 5.12: Beam velocity recordings for 2013

cover versus various dynamic conditions during break-up.

Using the equations presented in section 3.1.3, equations 3.4a to 3.5d, velocity recordings in instrument coordinates can be converted to calculate the beam velocities for each individual beam during the data acquisition period. These data are used to apply the variance technique to calculate the turbulence in the flow (as discussed in section 4.2.4).

Beam velocities for each individual beam during the ice cover period of 2013 are calculated and then extrapolated to the flow boundaries. Results are presented in Figure 5.12 . The relative location of the ice bottom and water surface are more distinctive in the figure.

As shown, recordings are consist with positive (beams 3 and 1) and negative (beams 4 and 2) values for separate beams. The sign of recordings are defined based on the beam direction. For beams looking upstream (water flows toward the beam), since the Doppler shift between two propagated signals is positive i.e. backscattering particles are getting closer to the transducer, the velocity values are recorded as positive. Vice versa, the beams looking downstream (water flows away from the transducer) receive negative Doppler frequency between two emitted sound pulses and hence, the velocity recordings are recorded as negatively signed values.

As shown, the beam pair of 1 and 3 velocities are recorded in positive whereas pair 2

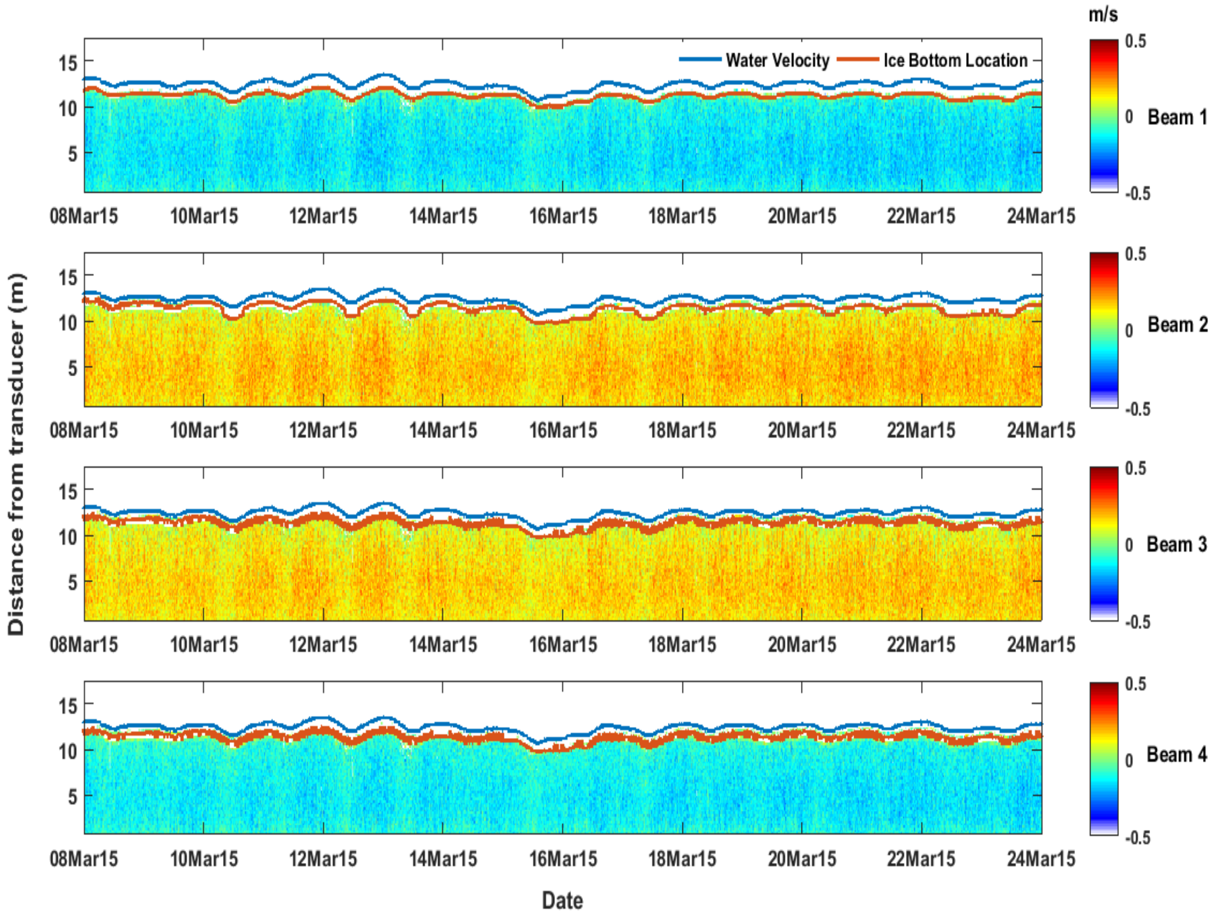

Figure 5.13: Beam velocities during the stable ice cover period of 2015

and 4 velocities are recorded as negative values. An interesting feature of change in flow direction can be identified in beam velocities as well. As seen, starting at break-up, the signature of recorded values in all beams reverses, which is an indication of drastic change in flow direction during the early stages of break-up . As previously described, this can reasonably related to the formation of an obstacle to the flow resulting in a complete flow direction change.

Based on the sign of the recorded velocities in all four beams, relative change in the flow direction can be observed in all beam velocities compared to the period prior to the start of break-up and shoving/ice jam formation stage.

Figure 5.13 shows the beam velocities during the stable ice cover period of 2015. As it is obvious in the figure, beams 2 and 3 recorded the positive velocities. The other pair of beams 1 and 4 were facing downstream during the deployment and recorded the negative velocities. Hydropeaking effect on velocity magnitudes is clear in both positive and negative values. Relatively similar ice cover condition is observed in all four beams which stays constant throughout the study period. Therefore, the effect of the ice cover on flow pattern is observed to be very low amongst the beams.

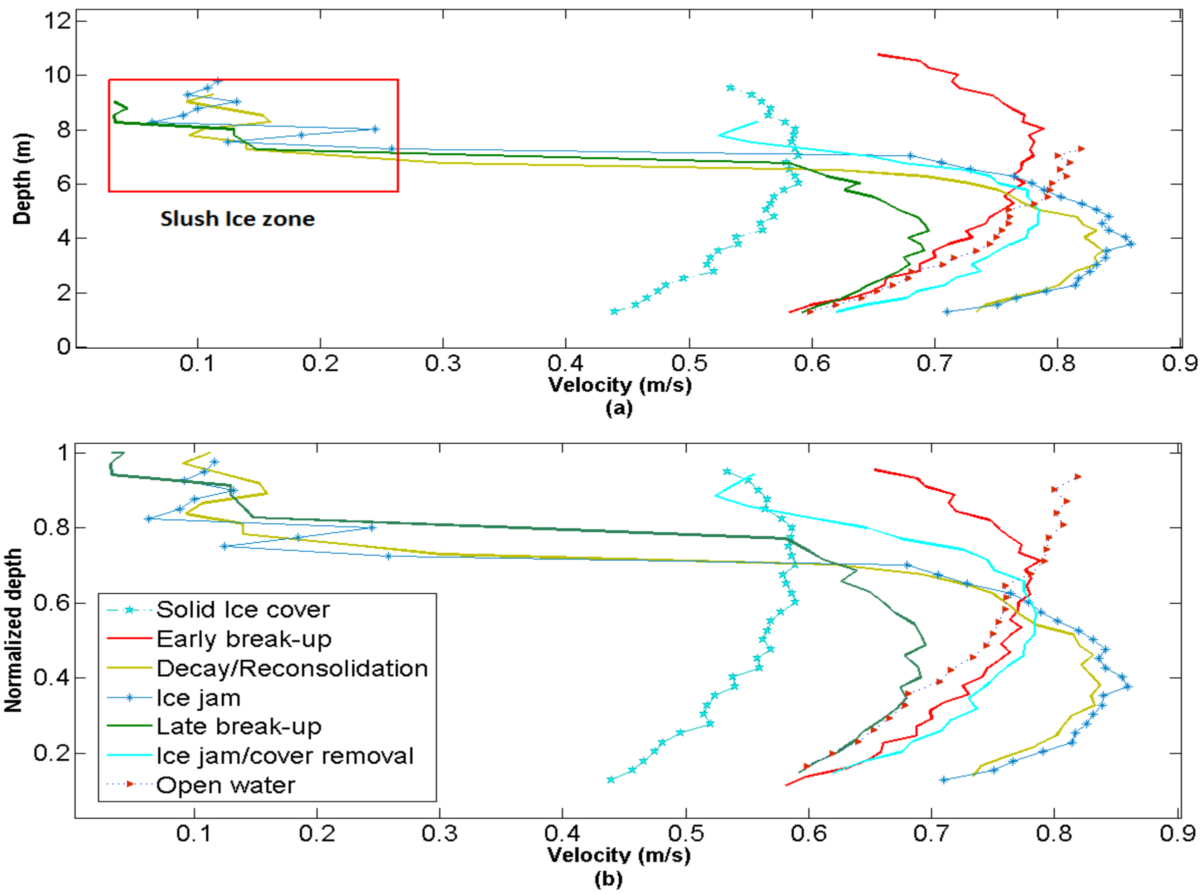

Figure 5.14: Velocity profiles for different ice stages as a function of depth (a), normalized depth(b) .

5.1.3 Velocity profiles in various ice-cover stages

Individual one-hour averaged water velocity profiles representative of each ice cover stage are shown in Figure. 5.14. Under stable ice-cover, observed velocity profiles demonstrated a double boundary layer U shaped profile, with maximum velocity pushed down into the water column.

Similar U shaped profiles were observed during thermal weakening of the ice cover in the early break-up period, but velocity magnitudes were greater. A deeper U shape was observed during the apparent ice jam period at the study site (between May 9^{th} to May 11^{th}, when greater ice surface roughness pushed the maximum velocity even further down. Finally, as expected, the open water profiles had maximum velocity near the water surface. Several of the profiles during the break-up period displayed a low velocity, zero stress zone at the upper boundary adjacent to the ice cover (Figure 5.14, slush ice zone).

This zone likely indicates the presence of a layer of moving materials below the ice cover during the last ice cover stages. According to the occurrence period and persistence of the phenomenon as well as the velocity distribution through the layer of the moving materials, it can be interpreted as "slush ice" underside of the stable, rigid ice cover. Upper and

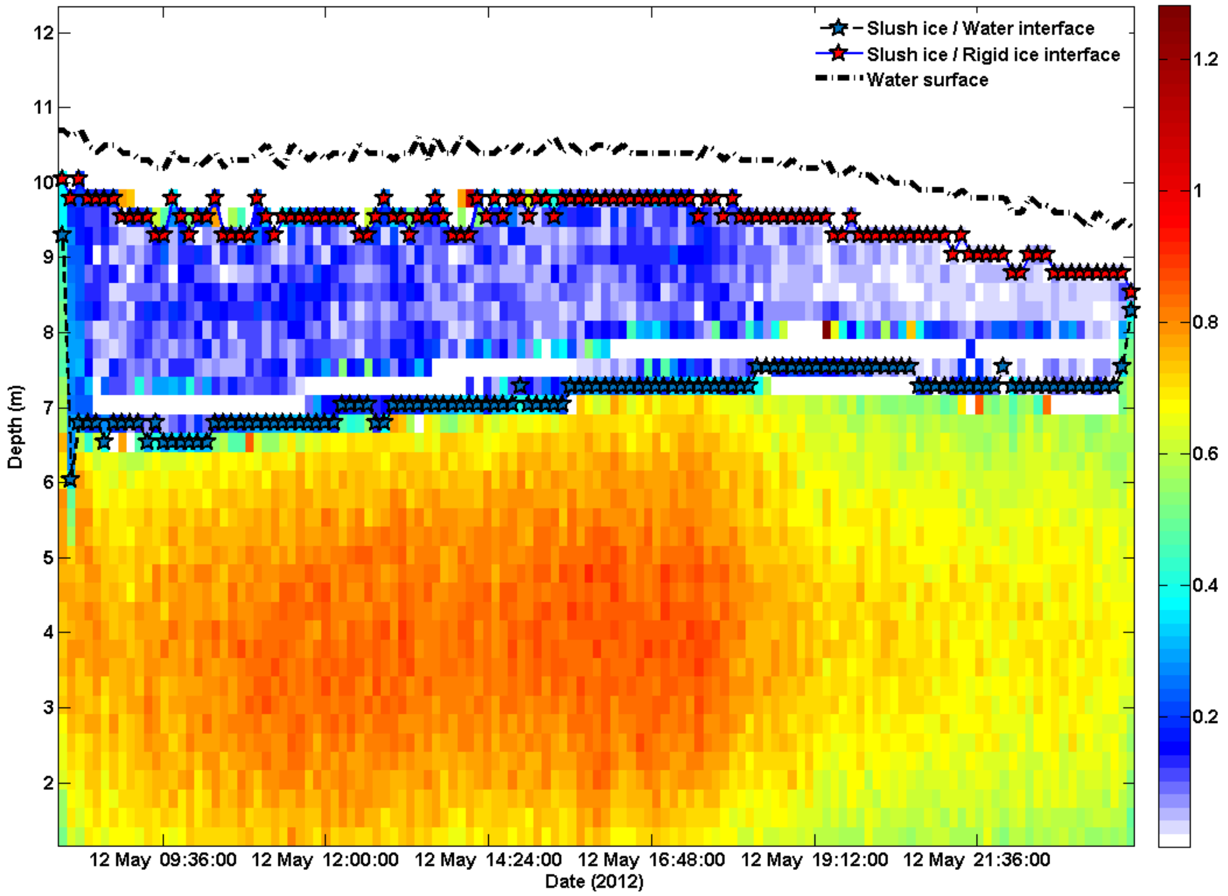

Figure 5.15: Slush ice layer and "water / slush ice" and "slush ice / rigid ice" interfaces in the study reach over the scale of hours.

lower interfaces of the aforementioned layer as well as water surface elevation during the occurrence period are represented in Figure 5.15. Upper and lower boundaries of the layer are of rigid ice and water body respectively. This interpretation is corroborated by physical observations at the same study site in March, 2014 of a 1 m thick layer of slush ice below the ice cover. Furthermore, slush ice presence during the break-up period has been observed elsewhere (Nezhikhovskiy, 1964; Beltaos, 1995b, 2001) . Nezhikovsky (1964, cited in Beltaos 1995), provides a method to calculate the roughness of slush ice accumulation on the underside of a solid ice cover.

Our measurements of velocity profiles showed that the slush ice thickness reached up to 25% of the total water depth and about 50% of the ice zone depth in some situations at the study site. Since the presence of slush ice introduces a phase change in the water column, the log-law may not be applicable through the entire water column because of the velocity distribution in the slush zone. Thus, fitting the log-law through the entire ice zone depth could lead to incorrect estimates of the shear velocity and shear stress. When slush ice is present, the boundary surface is the moving slush ice surface instead of the rigid ice cover. Therefore, shear velocity and shear stress estimation was performed with and without consideration of slush ice presence underside of the solid cover by separating

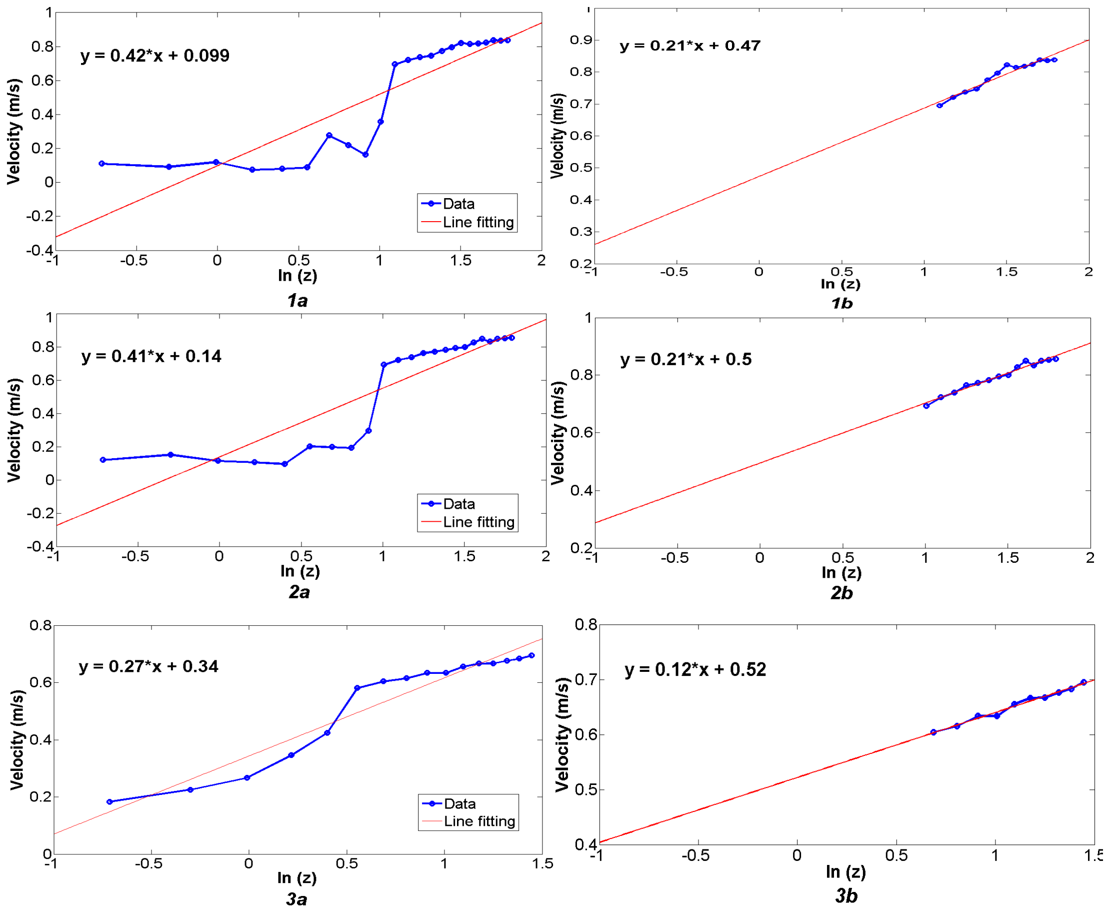

Figure 5.16: Logarithmic representation of velocity profiles during different ice stages: a) with and b) without slush ice consideration for (1) decay/reconsolidation, (2) ice jam, and (3) cover break-up periods

the velocity profiles in water column.

Results of curve fitting for both scenarios are presented in Figure. 5.16. The coefficient (slope) and intercept of the fitted lines are illustrated with and without slush ice consideration (**a** and **b** series respectively) for three different ice stages, including the decay/reconsolidation period (Figure. 5.16-1), ice jam (Figure. 5.16-2) and cover break-up and removal (Figure.5.16-3). It is clear that the velocity profile is not log-linear in the slush ice zone. Therefore, log-law application through the whole water/slush column causes overestimation of the fitted line slope and intercept, which results in over estimation of shear velocity by a factor of about two. Hence, three approaches were chosen to estimate the shear stress during the slush ice presence (Figure 5.17).

- The first approach (***a*** in Figure 5.17) is linear line fitting to the velocity-log depth profiles using equation (4.3) over the total depth of ice zone.

- The second approach (***b***) is estimation of shear velocity from the maximum velocity and average velocity of the ice zone using equation (4.7).

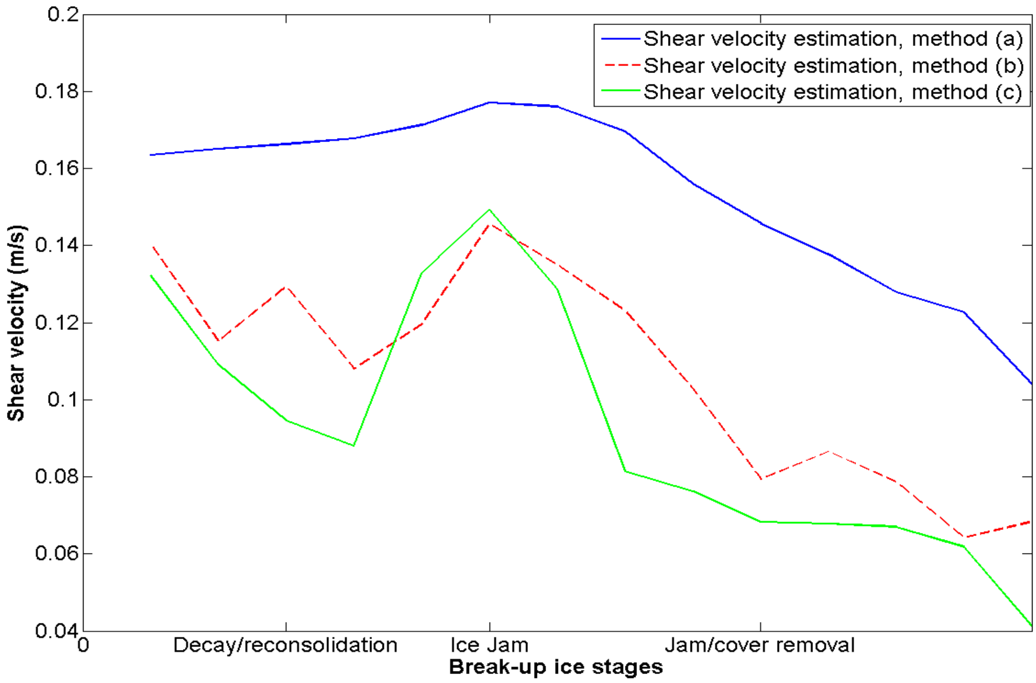

Figure 5.17: Comparison of shear velocity results estimated by: a) line fitting to the semi-log velocity profiles using equation (4.3), b) use of maximum and average velocity with equation (4.7), and c) line fitting to semi-log velocity profiles using equation (4.3)without the slush ice zone

- The third approach (***c***) estimates shear velocity using equation (4.3) with the ice zone velocity profile excluding the slush zone.

Figure 5.17 demonstrates that method ***a*** consistently overestimates the shear velocity compared to methods ***b*** and ***c***, which yield similar shear velocity estimates. Based on this assessment, equation (4.3) was used for all shear velocity estimates, but the slush zone was excluded when present (method ***c***). Interestingly, calculation of Manning roughness for slush ice period (n≈ 0.07-0.08) using three mentioned log-law approaches, fits perfectly with the values that Nezhikovsky (1964) calculated for 2-3 meters thickness accumulation of dense slush ice (Beltaos, 1995a).

Figure 5.20 shows the beam velocity profiles through the water depth during several stages of the ice cover in 2013 as Stable ice cover period (two first profiles),Thermal break-up initiation, mechanical break-up start and Ice jam formation. As discussed before, velocities in beams 2 and 4 were recorded as negative values.

Due to the higher sampling frequency, data are ensemble averaged in order to reduce the noise level in data presentation, however the shape of the profile is expected to remain intact through the process of ensemble averaging.

Analysis of the velocity profile distribution between the several ice cover stages reveals

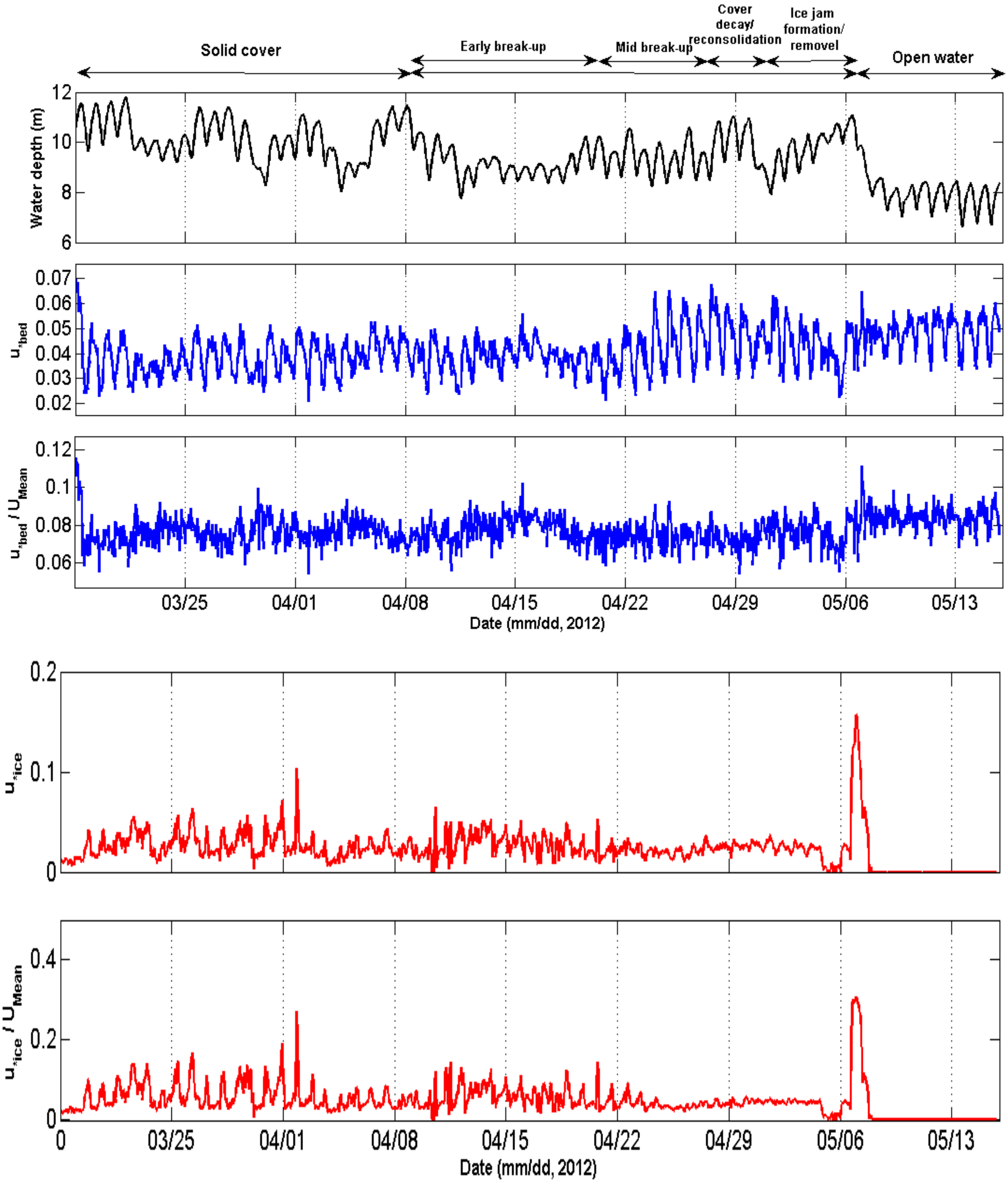

Figure 5.18: Water depth and Shear velocity estimation (using method $\boldsymbol{c}$) for upper and lower boundaries (ice and bed).

that the velocity profiles follow the expected shape of the profiles for ice covered flows during the major parts of the study period. However, some differences are traceable between different stages. Ice thickening process is clearly seen in the vertical extent of the velocity

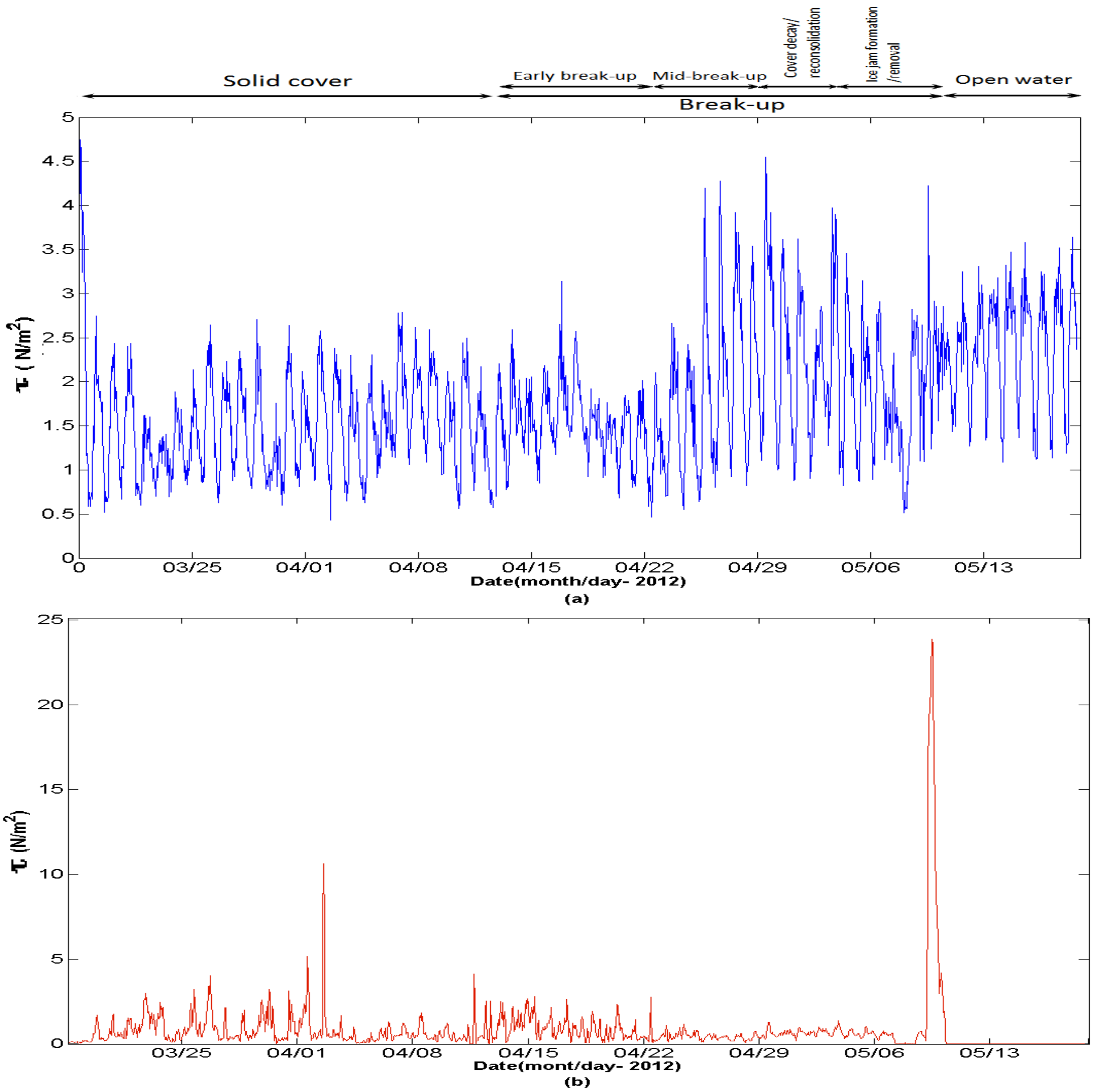

Figure 5.19: Shear stress values for lower (a) and upper (b) boundaries (bed and ice cover undersurface) using method ***c***

profiles. As the time passes and the cover thickens, the extent of the velocity profile decreases and its shape changes to the be more U shape profiles. During the break-up period, the profiles followed the most distinctive shape with the maximum velocity location occurring at a relatively lower location. This is observed in both positive and negative recorded velocities. After the formation of thick ice cover i.e. mechanically thickened cover, the velocity magnitudes decreased and lower gradient is observed through the data.

Since the ice cover experienced significantly lower variation in terms of thickness and roughness during the stable ice cover period of 2015, velocity profiles are observed to follow more consistent shape during the data recording period (Figure 5.21). As discussed before,

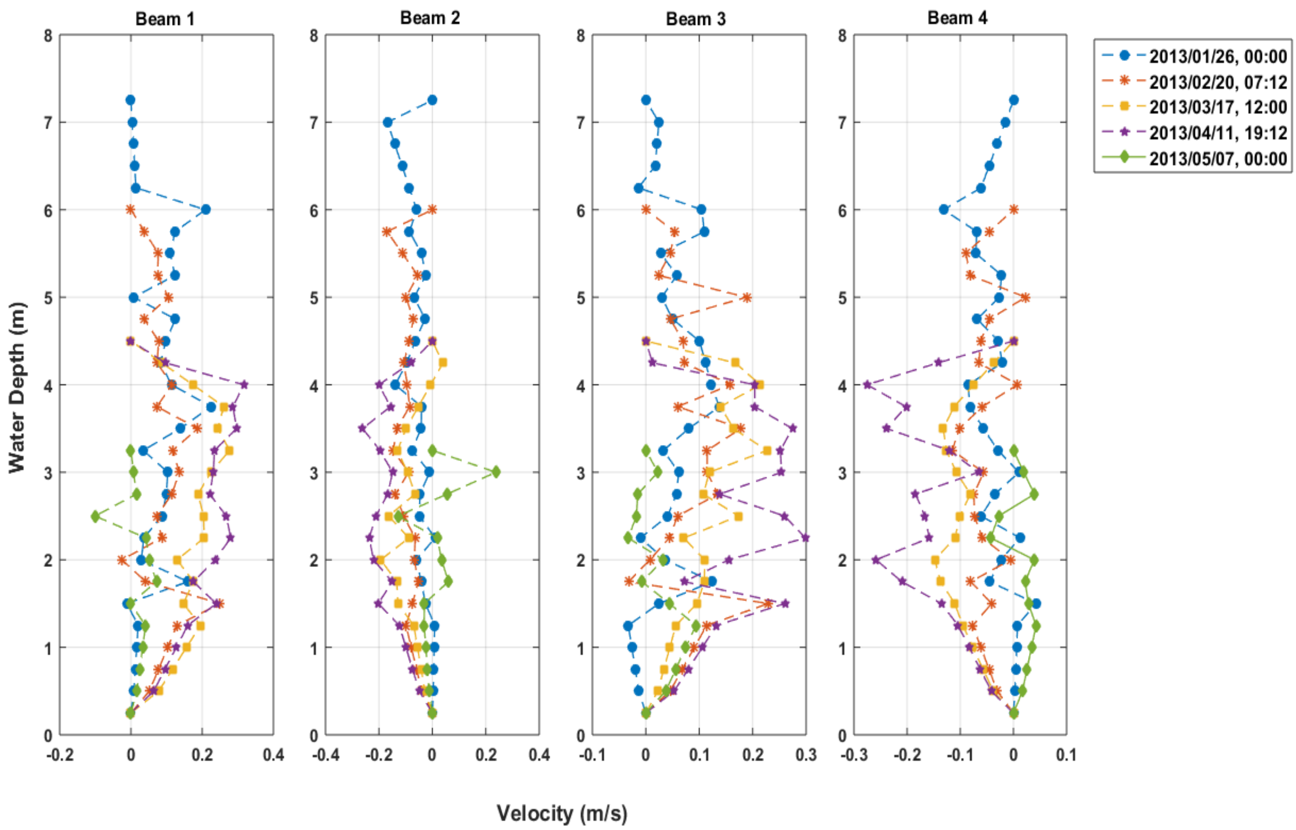

Figure 5.20: Velocity profiles during several ice cover stages

beam 2 and beam 3 recorded positive velocities indicating that they were facing upstream. Except for the early stage of the data recording, velocity gradient was found to be very similar throughout the study period. Maximum water velocity location and magnitude was also found to be similar between all the recorded profiles during the study period of 2015, all of which suggesting the insignificant variation on upper boundary roughness. It should be noted that the presented profiles, due to the constant interval between them, are presenting the low flow velocity profiles of the hydropeaking cycle. Velocity profiles during the acceleration phase of the hydropeaking periods followed the same pattern but with higher maximum velocity magnitude.

5.1.4 Shear velocity and bed shear stress during break-up

To the best of our knowledge, these will be the first estimates of boundary shear stress during ice break-up, when it is thought that the greatest sediment transport occurs (Ghareh Aghaji Zare et al., 2014; Beltaos et al., 1994; Prowse, 1993)

Figure. 5.18 presents the calculated values of local shear velocity for both the lower and upper boundaries (bed and ice cover) at the deployment site throughout the study period. Normalized shear velocity u_*/U_m, is presented for both cases as well. Diurnal oscillations due to hydro peaking are apparent in the shear velocity estimates. Bed shear velocity

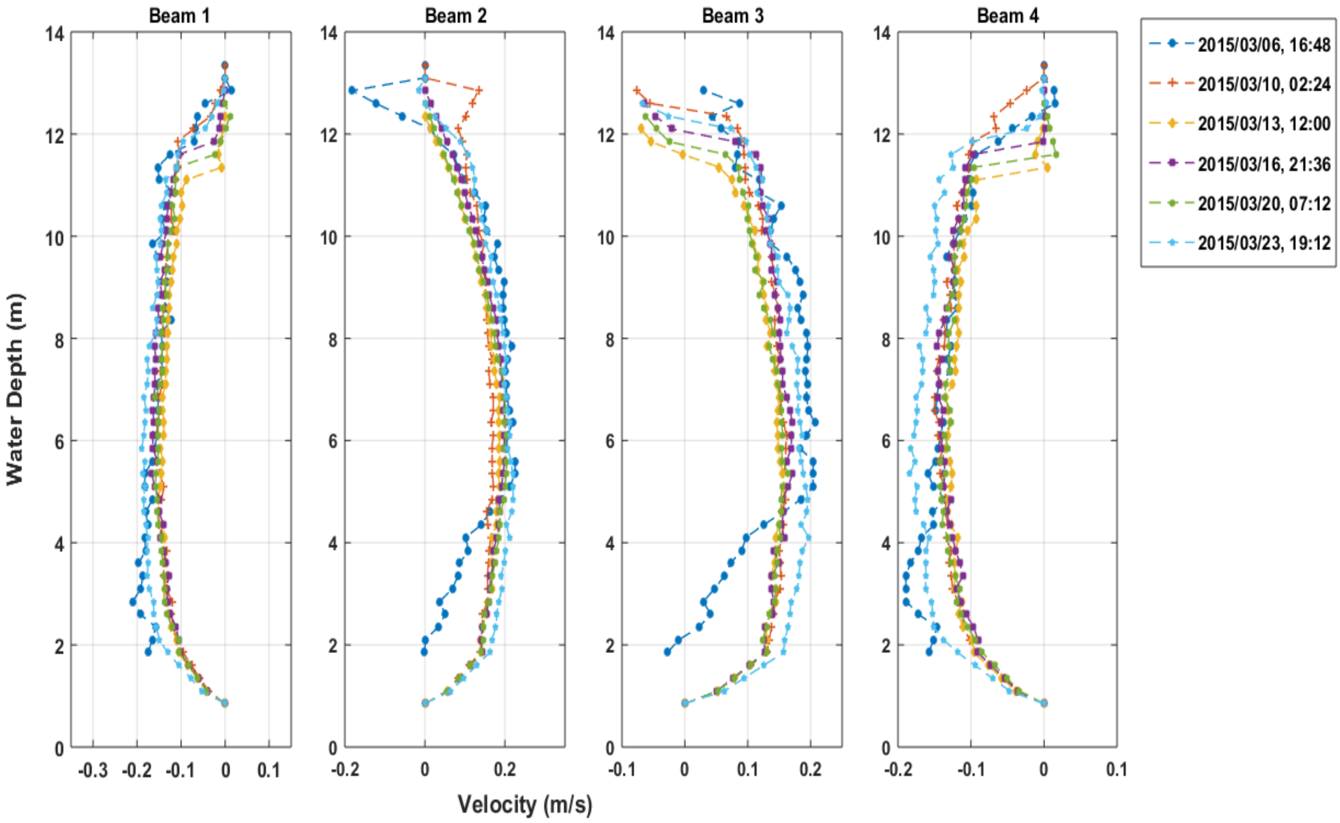

Figure 5.21: Velocity profiles during several ice cover stages

magnitudes varied between 0.025 m/s to 0.055 m/s with an average of 0.038 m/s during the stable ice cover.

At the beginning the break-up period in late April during which we expect that there was increased freshet flows and cover decay and reconsolidation episodes, bed shear velocity began to rise until it reached a maximum of 0.067 m/s. Bed shear velocity then decreased from late April until the first week of May, but increased and underwent another peak value on May 10^{th}, likely associated with formation of an ice jam at the site. Bed shear velocity decreased again on May 13^{th} with full ice cover release and commencement of open water conditions. It fluctuated diurnally afterwards. As expected, averaged bed shear velocity was greater in open water conditions than in the stable ice cover period.

Variation of shear velocity on the upper boundary is also shown in Figure 5.18-a. Dramatic oscillations in upper boundary shear velocity were observed, with values ranging from near zero to 0.1 m/s during the period from late March to late April. Minor fluctuations were observed between April 22^{nd} and May 7^{th}, then very high values occurred during the period which has been interpreted as ice jam formation. Upper boundary shear velocity was not calculated for open water conditions that followed release of the ice jam since there was no upper boundary.

Boundary shear stress can be calculated using equation (4.1) from the estimated shear velocity magnitudes. Figures 5.19-a and 5.19-b show the calculated local upper and lower

Table 5.1: Average Shear Stress (standard deviation in parentheses) on river boundaries using method $\boldsymbol{c}$, (N/m^2)

	Stable ice cover	Early break up	Mid break up	Ice cover removal and reconsolidation (including shoving process)	Ice jam	Open water
Ice cover	0.79 (0.9)	0.84 (0.62)	0.52 (0.23)	0.59 (0.26)	23.87 (8.8)	______
Bed	1.51 (0.59)	1.54 (0.45)	2.19 (0.90)	2.02 (0.74)	2.27 (0.76)	2.4 (0.60)

boundary shear stresses at the study site, and Table 5.1 provides a summary of average and standard deviation of boundary shear stresses during each identified ice cover stage. Average bed shear stress for the period of April 22nd to May 7th was 2.0 N/m^2. As expected, higher bed shear stress values were observed in the open water period after May 13th than in the stable ice cover period before April 22nd. The shear stress on the under ice surface averaged 0.79 N/m^2 during the stable ice cover, 0.65 N/m^2 during the break up, and up to 24 N/m^2 for the ice jam. Before temporal averaging, peak upper boundary shear stress on the ice cover (results not shown here) was 11 N/m^2 in the stable ice cover period and almost 30 N/m^2 during ice cover break-up on May 10th. It is worth noting that using method $\boldsymbol{a}$ as opposed to method $\boldsymbol{c}$ would overestimate shear stress by about 20%.

Regardless, the ice cover shear stress during ice jam formation was observed to reach to a value almost twice that expected based on previous investigations (Calkins, 1983; Calkins et al., 1982).

Results of multiple comparison test on shear stress data using Bonferroni correction during different ice stages are represented in Figure 5.22. It is clear that, shear stress values during at least one stage (ice jam period) are significantly different than others. Mean value for each group is represented by symbols in the middle of the group intervals. Two means are significantly different if their intervals are disjoint. Results, also prove that the ice jam period is significantly different.

Also as shown in Figure 5.22, average shear values during the mid break-up period including the mechanical break-up period are significantly different than early break-up

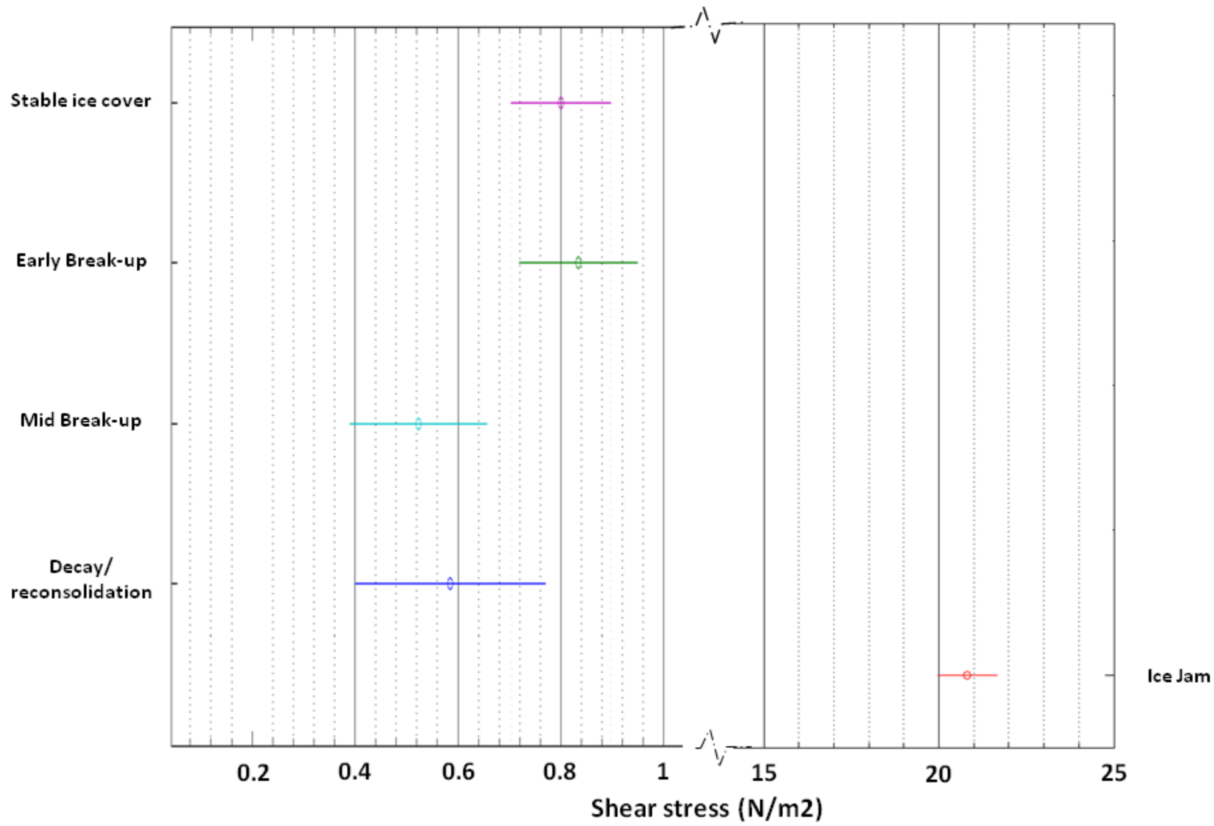

Figure 5.22: Bonferroni corrected multi comparison test on under ice shear stress during important ice stages.

period as well as stable ice cover. No significant difference in under ice shear stress values has been observed between stable ice cover and early break-up periods. Average shear stress values are also significantly different between reconsolidation and ice jam periods.

Ice cover effect on river hydraulics can be summarized and discussed through different ice stages as follows:

I. **Solid ice cover**

Flow velocities in mid-winter under the stable ice cover were relatively low, thus the shear stress on the under surface of the ice would have been mainly affected by the condition of the ice cover during the solid cover period, rather than the velocity. Significant variations in upper boundary shear stress were calculated during this period which could have been due to ice deposition and erosion processes at the lower surface of the ice cover associated with diurnal flow fluctuations due to hydropeaking. It is possible that the thickness of the ice cover and its roughness varied diurnally due to accumulation of moving ice particles under the existing cover when the water velocity was low and their erosion when the velocity was high. Flow velocity has two simultaneous effects on boundary shear stress during this time. First, during stable ice cover period, flow velocities are low at this site during the low flow cycles of the hydro-peaking operation of the upstream LGS, which permits floating ice particles to deposit under the ice surface and thicken the cover. A newly formed thicker cover initially has a rougher surface and higher shear stress observed immediately after frazil deposition which is consistent with previous theoretical expectations (Calkins et al., 1982). Second, accelerated flow due to hydropeaking at the upstream hydroelectric station (LGS) or reduction of the cross sectional area, would smoothen the cover undersurface by increasing the ice transport capacity at the cross section (Shen and Wang, 1995) . Therefore, it is suggested herein that variation in shear velocity and shear stress on the stable ice cover is dependant on a combination of hydraulic and climatic factors e.g. water velocity and upstream frazil generation (Ghareh Aghaji Zare et al., 2014).

II. **Break-up**

At the beginning of the break up period, the upper boundary shear velocity began to decrease while the bed shear velocity increased slightly; this could have been due to smoothening (erosion) of the under surface of the ice due to higher velocities. However, later in the break-up process during the mechanical thickening process (shoving), under ice shear velocity increased in time until it reached the maximum of 0.18 m/s during the ice jam formation. In the open water condition after jam removal, variation of hourly average bed shear velocity ceased.

The results demonstrate and affirm that the break-up period consists of highly dynamic ice stages. Higher water velocities occurred in late April (Figure 5.10-a and Figure 5.11-a) during the ice break-up period, presumably due to increased freshet flows. It is reasonable to suggest that higher velocities caused higher thrust on the ice cover, thus the cover started to fracture and mechanically thicken to be able to resist against increased thrust force. This shoving process would have led to formation of a rough, jagged under surface of the ice, and this rough boundary can explain the observed migration of the maximum velocity deeper in the water column (Figure 5.10 a,b). Observed phenomenon of effect of ice cover condition on maximum velocity location is consistent with laboratory finding of Crance and Frothingham (2008) and Sui et al. (2010). These processes resulted in slightly higher shear stress values on the upper boundary at the ice undersurface during this period (first week of May comparing to the last week of April) (Figure 5.19-b). Furthermore, calculated bed shear stress (Figure 5.19-a) also increased during the break-up, which could be due to higher velocity occurrence in this period. This finding has important implications for sediment entrainment and transport during break-up.

Water velocity has an important role in cover thickening/reformation during break-up period, which is mainly a mechanical effect due to high thrust forces. Even though ice deposition-erosion processes are still in progress during break-up, the range of velocity values required for these processes would be significantly different. Frazil particles can deposit under the ice cover due to their low density and high tendency to agglomerate and stick to objects. Therefore, deposition and erosion of frazil is easier during solid ice cover and thus variation in under ice surface condition and resultant shear stress would be higher. Ice floes, as they are during break up, are more buoyant and angular, therefore, higher water velocity variation is necessary to erode and deposit the break up ice floes. (Judge et al., 1997). Previous studies have found that frazil depositions starts around 0.3 m/s and less, while frazil erosion occurs around 2m/s, but for break-up floes this range would be shifted to higher velocity magnitudes (Michel, 1971; Michel and Ramseier, 1971).

III. **Ice jam**

Ice jams form when large floes jam in narrower cross sections. They form rough and temporarily stable obstacles, and cause the water surface to rise rapidly and even inundate upstream flood plains in some cases. Their sudden release can cause large water surges [jave] traveling downstream and these surges can be the main causes of spring flooding in northern rivers. For instance, wave speed and peak magnitude attenuation of an ice jam release surge have been studied on the Athabasca River, Alberta, Canada (Kowalczyk and Hicks, 2003). Jasek (2003) also noted a surge on the Athabasca River, in which the river rose 17 m in 1 hour and the surge traveled at 5 m/s downstream after jam release (Jasek, 2003).

It appears that an ice jam formed and released at the study site in the days immediately prior to full release of the ice cover. This ice jam resulted in high boundary shear stresses on both the bed and ice undersurface, with a remarkably high estimated value of nearly 25 N/m^2 on the upper boundary. During the late stages of the break-up period, bed shear velocity and consequently bed shear stress then decreased slightly in time due to ice jam formation, which was accompanied by water staging (increased water surface elevation), and decreased velocity magnitudes (as shown in Figure 5.11-a and Figure 5.18-a). As the jam grew at the section, water passed through a smaller area, thus maximum velocity value for each profile and consequently the shear velocity on the bed started to increase until it reached its maximum before the jam released. After ice jam release, bed shear velocity remained statistically steady during the open water condition.

IV. **Slush ice** The velocity measurements suggested the presence of slush ice during the break-up period. According to the velocity profiles during the late break-up (Figure 5.14 and Figure 5.15), slush ice started to accumulate during the decay/reconsolidation period. The thickness of the ice/slush ice layer, reached a maximum of about 3.00 m during the last ice cover stages, i.e. ice jam formation. The slush ice was subsequently flushed downstream during jam/cover removal.

The shear velocity and stress calculated in the presence of slush ice can be considered as the shear stress at the boundary of water and slush ice. The log-law did not represent the velocity distribution over the entire water column in the presence of slush ice (Figure 5.17), therefore the log law for velocity profile analysis should be implemented with caution in this situation. In this study, a method was developed to use equation (4.3) excluding the slush ice zone. This is similar to use of the log-linear layer above the zero stress wake zone induced by vegetation (Raupach et al., 1991) or large scale roughness such as cobbles (Nowell and Church, 1979). Error in estimation of boundary shear stress using equation (4.3) with the entire ice zone velocity profile was as large as 20%. During the slush ice period, estimation of shear velocity using equation (4.7) with the maximum and average velocity magnitudes yielded values similar to use of equation (4.3) in the log-linear region excluding the slush ice, thus use of equation (4.7) appears to be reliable in the case of presence of slush ice. This suggests the values of both the average and maximum velocities are relatively unaffected by the presence of the slush ice layer according to our measurements. This may not be true in some cases, such as shallow waters or in conditions where the ratio of the cover thickness (including the slush ice) to the total water depth is significantly high or all other conditions for which high rates of slush ice are suspected to contribute to cover formation (e.g. during freeze-up).

5.2 Composite hydraulic resistance in an ice covered stream

Considering the maximum velocity location as a key indicator of ice and bed zones, velocity profiles were identified from the upper and lower boundaries up to this point respectively. Application of log-law (equations (4.3), (4.41), (4.42) and (4.43) from the boundary surface to the location of maximum velocity provides information to calculate the shear velocity, u_* and equivalent boundary roughness, Ks for under surface of the ice and bed. Many other investigators also used log-law for velocity distribution for both ice and bed zones (Levi, 1948; Synotin, 1965; Hancu, 1967; Larsen, 1969; Tesaker, 1970; Ismail and Davar, 1976). According to what discussed in part 4.2.3, it is applicable to illustrate the velocity distribution in an ice covered river with an acceptable accuracy. Thus, this approach has been implemented to define the boundary roughness as well as calculation of the composite resistance for this study.

Manning roughness coefficients (n_i, n_b) for each boundary was determined using equation (4.43). Finally, total composite roughness was calculated using equation (4.56).

Velocity profiles during the ice cover period are presented in Figure 5.23 , demonstrating that profiles reasonably matched with the logarithmic velocity distribution. In most cases the estimated roughness values indicate the flow was fully rough turbulent, suggesting the ice boundary profile was fully rough turbulent for the majority of the fully ice-covered period. Furthermore, application of the transitionally rough form of the log-law velocity profile [Garcia, 2008] during transitional periods would not have influenced shear velocity estimates, but the smallest values of ice roughness would have been estimated to be somewhat greater.

5.2.1 Estimation and analysis of composite hydraulic resistance

Calculated Manning roughness values for the ice cover and the bed and their ratio are shown in Figures 5.24 *a* and 5.24 *b*. Although ice cover roughness was sometimes significantly greater than the bed roughness (up to a factor of four times), generally n_i was less than n_b. Estimated bed Manning roughness values remained almost constant for the whole

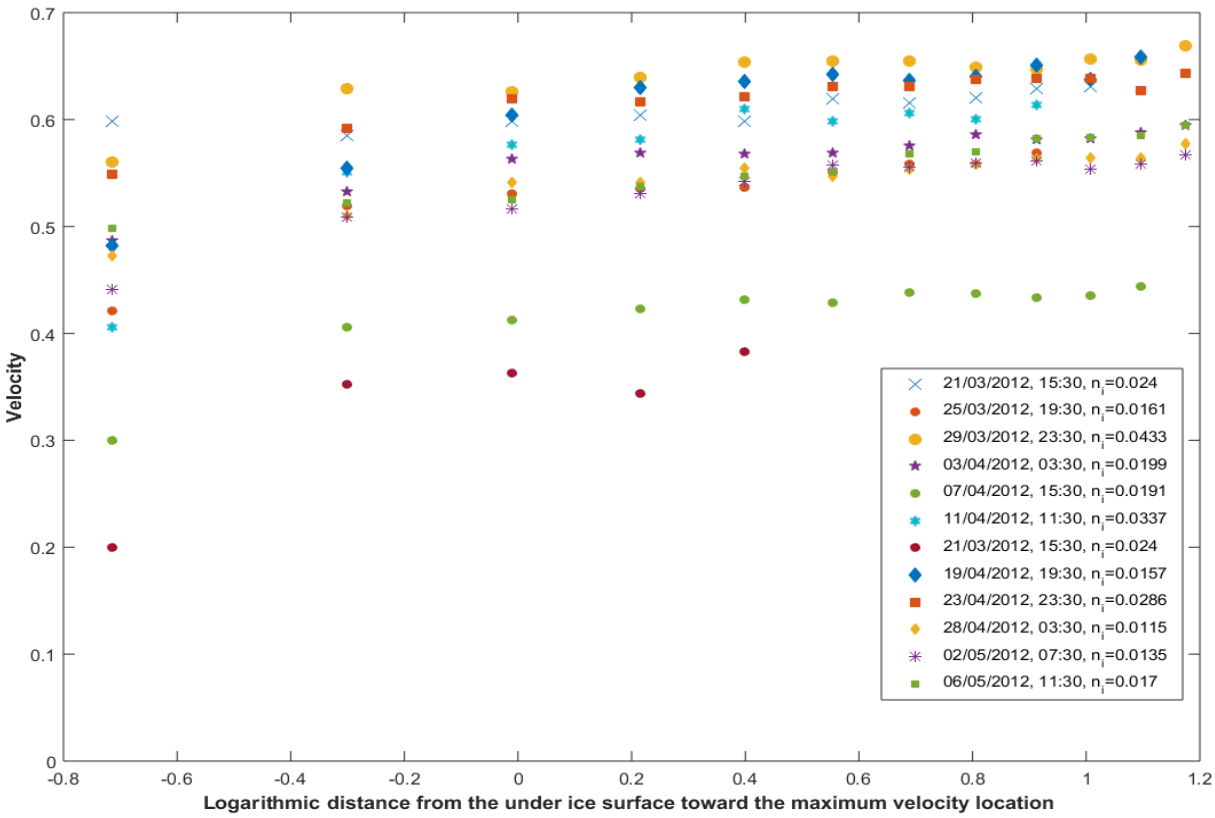

Figure 5.23: Logarithmic representation of velocity distribution for several ice cover stages and calculated Manning's roughness coefficient for each profile

period. On the other hand, periodic variation in ice cover roughness is apparent in Figure 5.24-a, which could be due to a cyclic process of smoothening and roughening of the ice cover. Frequent deposition and erosion of ice particles (frazil ice) beneath the existing cover, dictated by hydraulic factors such as velocity, may be the main reason for such a high variation in roughness of the ice cover under surface.

To validate this hypothesis, the periodic behaviour of the ice roughness time series was studied and frequency-domain cross-spectral correlations between ice roughness and depth averaged mean velocity and average depth were calculated (Figure 5.26-a,b). Welch's Overlapped Segment Averaging (WOSA) spectral periodogram method was used for this purpose (Welch, 1967; Oppenheim et al., 1989). The magnitude squared coherence (MSC) was calculated to identify significant correlation frequencies between ice roughness and velocity or depth. Significant correlation at a given frequency can be deemed positive or negative based on the cross-spectral phase lag at that frequency. In Figure 5.26 phase lags (in radians) are shown for frequencies in the vicinity of the peak coherence frequency.

For 16 to 20 degrees of freedom (18 in this study), coherence is significant if it is higher than 0.3 (Koopmans, 1995; Rennie and Hay, 2010). The 0.3 line is drawn on the MSC graphs. As seen in figure 5.26, the most significant coherence was observed at the frequency of $\simeq 1.12*10^{-5}$ Hz (i.e., an oscillation period of 24 hours) for all MSC estimations. This

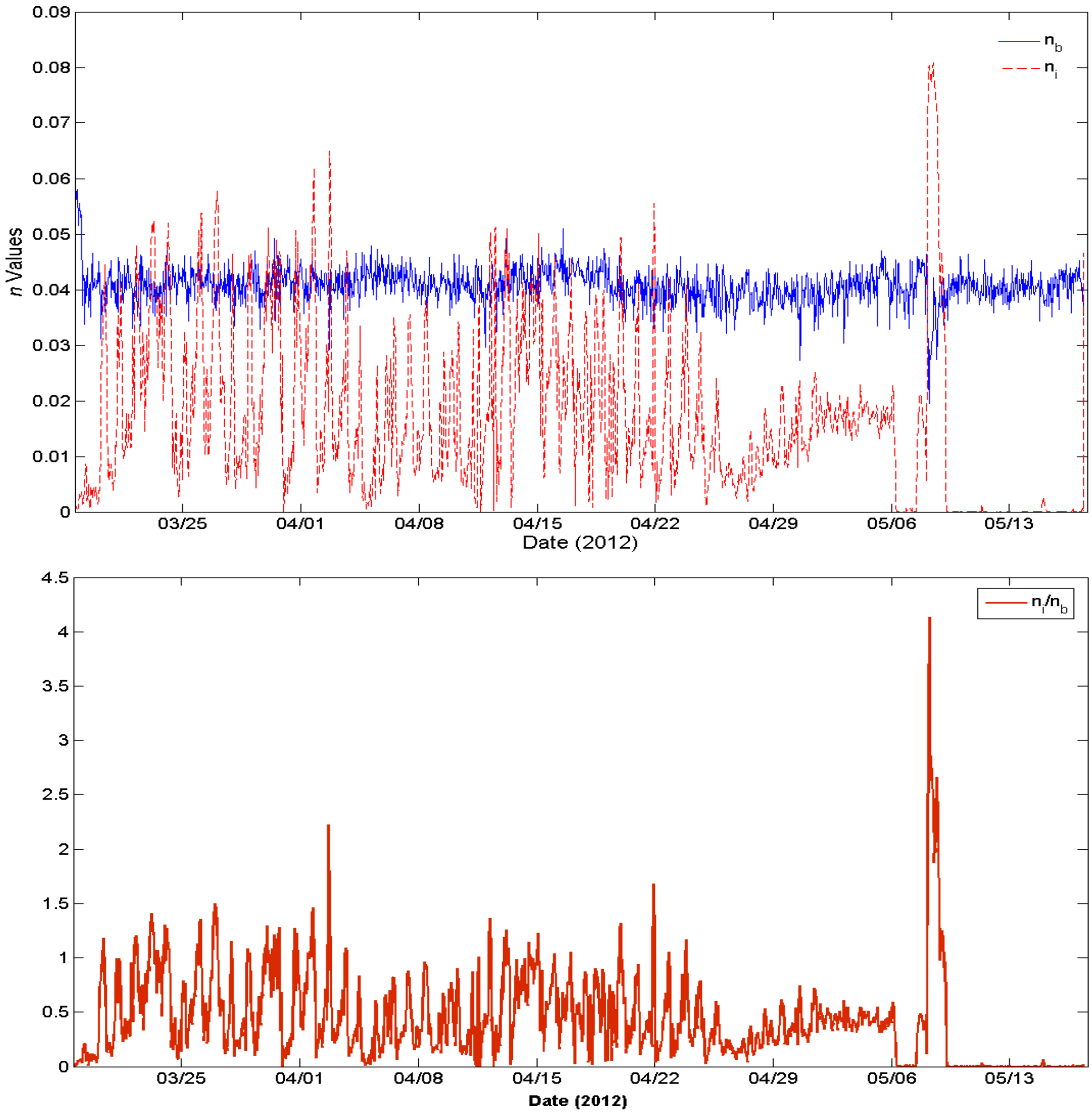

Figure 5.24: Estimated boundary roughness coefficient for bed and under ice surface (a), ice to bed roughness coefficient ratio (b)

is an indication of periodic coherency between under ice roughness values and hydraulic characteristics in a daily scale which is equal to the frequency of daily hydro-peaking oscillations. Strong ice roughness coherency (MSC = 0.58) was observed with mean water velocity (Figure 5.26-a) and average depth values (Figure 5.26-b). Calculated phase lags at the peak coherence frequency were -π radians for mean velocity and $-\pi/2$ radians for the mean depth, suggesting that ice roughness was inversely related to both mean velocity and mean depth. This may be explained according to the cycle of hydro peaking. During periods of increased flow release from LGS, the water velocity and water depth increased simultaneously (Figure 5.10). We hypothesize that increased water velocity eroded and smoothened the under ice surface, which resulted in the observed inverse relation between under ice roughness and mean water velocity. Due to coincidence of occurrence of high

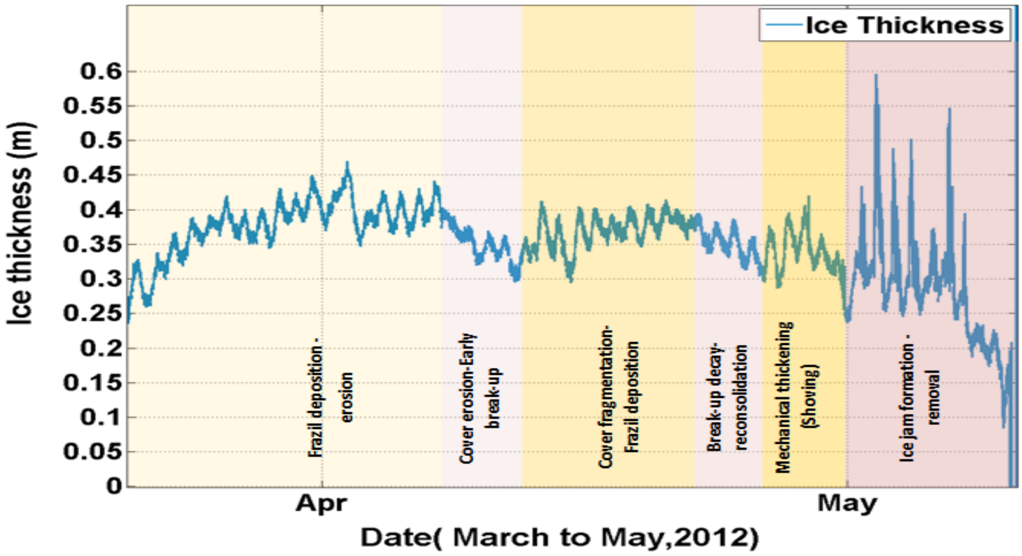

Figure 5.25: Rigid ice thickness estimation at the study site for April- May 2012, Open water periods are excluded

velocity and high depth during hydropeaking, the same relation is also expected for water depth (Figure 5.26-b). Even though an inverse correlation between ice roughness and flow depth is evident in figure 5.26-b, the phase lag is less than the phase lag between ice roughness and velocity. This suggests that during each hydropeaking cycle, decreased velocity first roughens the ice surface by allowing the frazil particles to deposit under the cover and then flow depth increases consequently.

The influence of under ice roughness on normalized location of maximum velocity can be seen by comparing Figures 5.24-top and 5.10-c. During break-up, ice roughness increased while the location of maximum velocity decreased until they reached their respective extreme values during the ice jam formation period.

The energy grade lines for ice and bed zones were also calculated for the study period using equations (4.3) and (4.54) (Figure 5.27). Higher values of energy grade line (S_{fi}) in the ice zone were observed during the stable ice cover period compared to the energy grade line of the bed zone (S_{fb}). The highest value of S_{fi} occurred during the period of ice jam formation and release, up to six times greater than during the stable ice cover period.

Using water discharge (calculated based on time shifting of released discharge at LGS) and cross section geometry, total resistance for the cross section was calculated using equation (4.33).

Due to the remoteness of the study site, local water surface slope measurements are not available. Averaged bed slope over a 10 km long reach is calculated to be about 10^{-4} . However, due to the location of the deployment site, the reach averaged river morphology may not be a good representation of the channel morphology at the deployment site. This might be even more significant during the ice cover period when the left channel (looking downstream) may get completely blocked by ice, which would create a back water effect

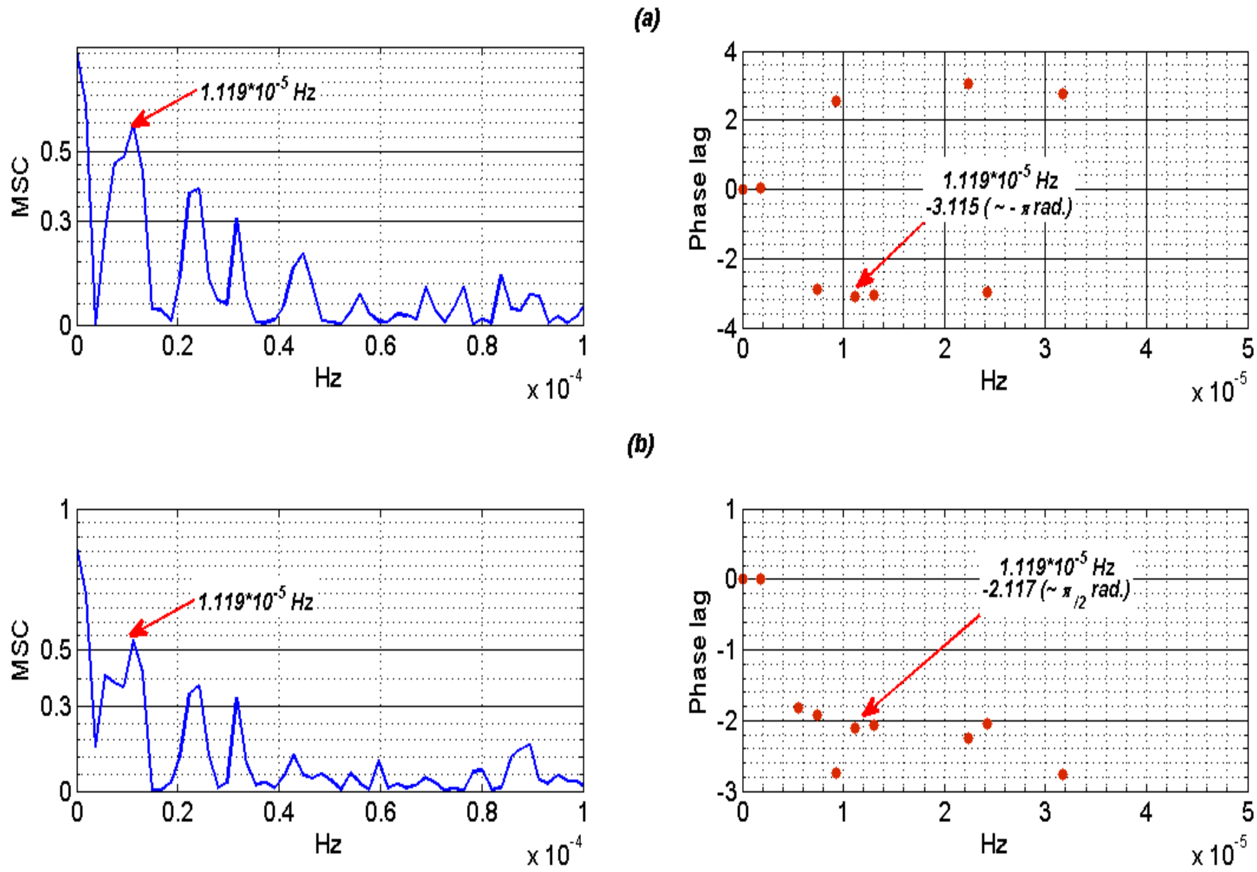

Figure 5.26: Magnitude squared coherence (MSC) and phase lag between under ice roughness and (a) mean velocity, (b) water depth during the ice cover period at the study site

influencing the energy grade line at the deployment site (deployment site information is presented in Figure 5.28).

Hence, the average value of local energy grade line slope calculated for the bed (S_{fb}) during the ice cover period is considered as the total grade line slope in the Manning equation for calculation of the hydraulic roughness coefficient during the winter (represented as n_s). It is worth noting that this average value of S_{fb} ($3\text{x}10^{-5}$) was similar to the local bed slope at the deployment site (Figure 5.27) measured over a short longitudinal length of about 250 m. This estimated local slope is about one third of the long reach averaged bed slope value used in the original paper.

Cross section hydraulic resistance (n_s) is compared to the resistance coefficients for bed (n_b) and under ice surface (n_i) in Figure 5.29. It is noteworthy that $n_s \approx n_b$ during the open water period when n_i=0, which provides confirmation of n_b estimated with the log-law method.

In Figure 5.30, the estimated cross section hydraulic resistance for the study reach during the ice cover period is used to evaluate calculation of composite resistance (n_c) calculated from common methods (equations (4.38), (4.39), and (4.40)), as well as the new

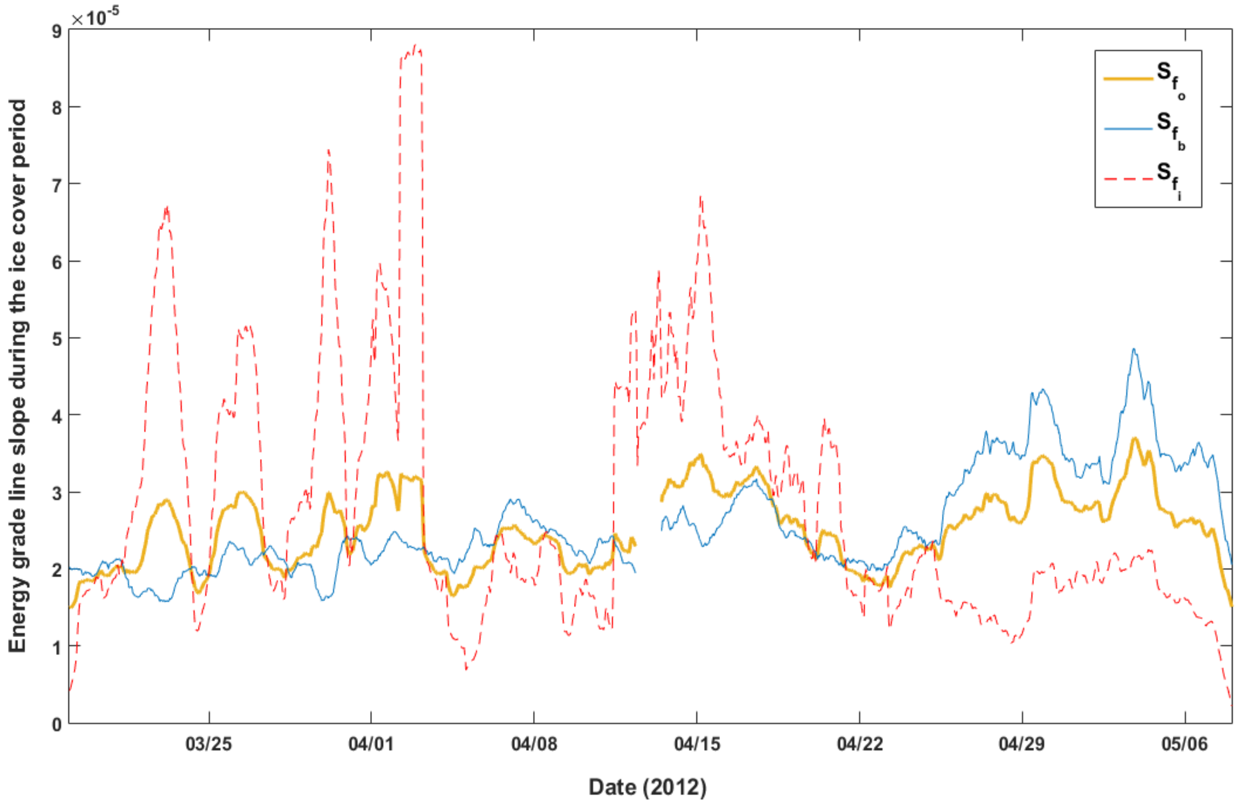

Figure 5.27: Energy grade lines for ice and bed zones

equation (equation (4.56)).

Composite hydraulic resistance is studied as a part of this thesis using field investigations through several ice stages. Based on the initial results of the application of composite resistance equations, a theory is developed considering the potential source of errors in commonly used methods to describe the total hydraulic resistance during stable ice cover. Findings of this study regarding the composite resistance topic can be discussed in some aspects.

Flow velocities were relatively low during the stable ice cover period compared to the break-up and particularly the open water condition. Since the study site is located in a regulated reach of the Nelson River, fairly stable discharge was flowing through the cross section during the hydro-peaking and off-peaking periods. Therefore, even though variation in water surface elevation and water velocity magnitudes were observed in a daily cycle, hydraulic characteristics such as mean velocity and water surface elevation fluctuated within a certain range for extended periods (e.g. stable ice cover period and open water condition). On the other hand, flow characteristics showed abnormal variation during the dynamic stage of break-up, which included important sub-stages such as mechanical thickening and ice jam formation and release.

Comparing the stable ice cover period and open water condition, two important features immediately appear; first, lower mean velocities during the stable ice cover and second, higher water surface elevation during the same period, both of which can be considered as

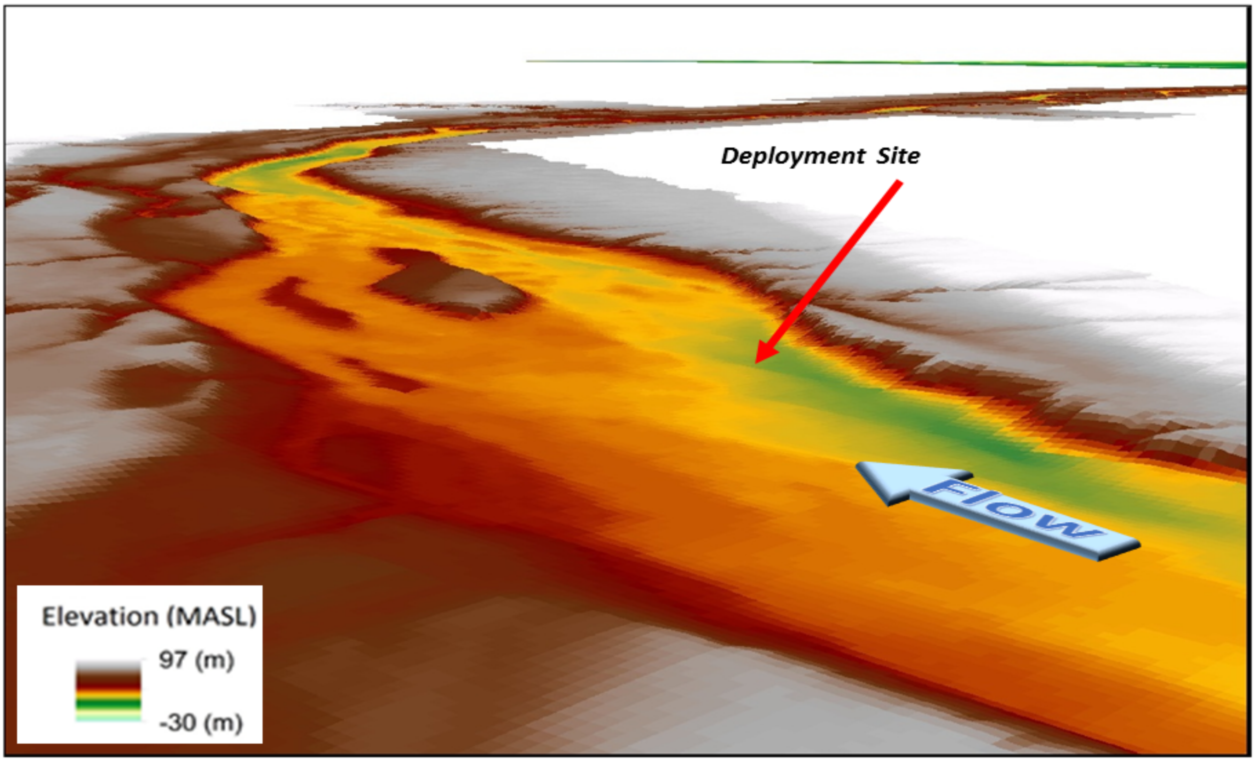

Figure 5.28: Three dimensional representation of the instrument deployment site in comparison to the river geometry

a clear sign of increased hydraulic resistance to the flow. This can be described as a result of the introduction of a new boundary layer to the top of the stream during the stable ice cover. Although discharge released from LGS (hydorpeaking) was fairly constant during the study period, lower mean and maximum velocities and depth values were observed during the stable ice cover than the open water condition. This can reasonably be related to the existence of higher resistance to the flow in the ice-covered condition.

Estimated Manning roughness coefficient for the bed and the under surface of the ice showed that the bed roughness had minimal variation, remaining almost constant around 0.04, which according to the bed material is in the range of the expected Manning roughness coefficient for such a river bed (Figure 4.3) (Chow, 1959).

On the other hand, significant variation in ice cover roughness was observed, mainly before the end of April during the stable ice cover. Frequency analysis demonstrated that these oscillations followed a diurnal cycle and were inversely related to associated changes in water velocity and depth (Figure 5.26). It is reasonable to relate these variations to a periodic process of smoothening and roughening of the under surface of the stable ice cover during hydropeaking oscillations. During the low flow condition (off-peaking of LGS), lower velocity flow permits floating ice particles, mainly frazil ice crystals, to accumulate and deposit immediately below the under surface of the ice, temporarily thickening and roughening the cover. Accelerated flow during the discharge release from LGS starts to smoothen the under surface of the cover by physically eroding the cover or melting the

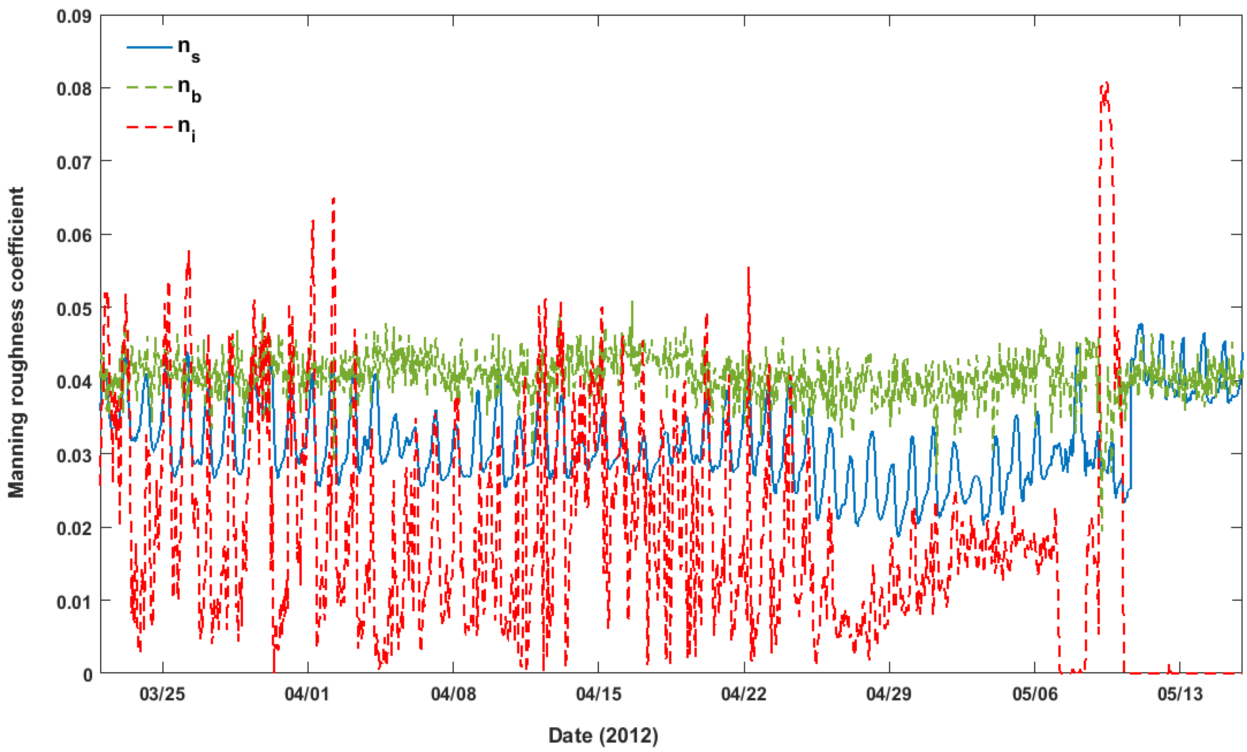

Figure 5.29: Estimated hydraulic resistance for the cross section and bed (top) and under ice roughness (bottom) values during ice cover and open water periods

ice protrusions by changing the thermal budget. Analysis of the velocity and under ice roughness time series suggests that the process of deposition and erosion of ice particles continuously occurred during the stable ice cover period. The same variation was also observed in boundary shear stresses as well (Ghareh Aghaji Zare et al., 2015) which is consistent with the theoretical expectations (Calkins et al., 1982).

During the break-up period, higher water velocities occurred. However, decrease in maximum velocity location and rising trend of ice roughness values showed that the under surface of the ice roughened in time (Figure 5.10). It is notable that between the solid ice cover period and start of the break-up the under ice roughness decreased on average, which may have been due to the initial smoothening effect of increased water velocity on the under surface of the ice. Still, as break-up progressed the under surface of ice roughened even as the velocity increased. It is reasonable to conclude that the higher velocities exerted higher thrust on the ice cover, thus the already smoothened ice undersurface started to fracture and thicken mechanically by the shoving process. Mechanical shoving leads to the formation of a more jagged under surface of the ice cover, and usually causes the retreat of the ice cover leading edge during the freeze-up period or emergence of open water patches during the break-up period.

Velocity ranges for frazil ice deposition and erosion have been found to be around 0.3 m/s for deposition and about 2 m/s for erosion (Michel, 1971). It is notable that the ice deposition-erosion process is still in progress during the break-up period but with different

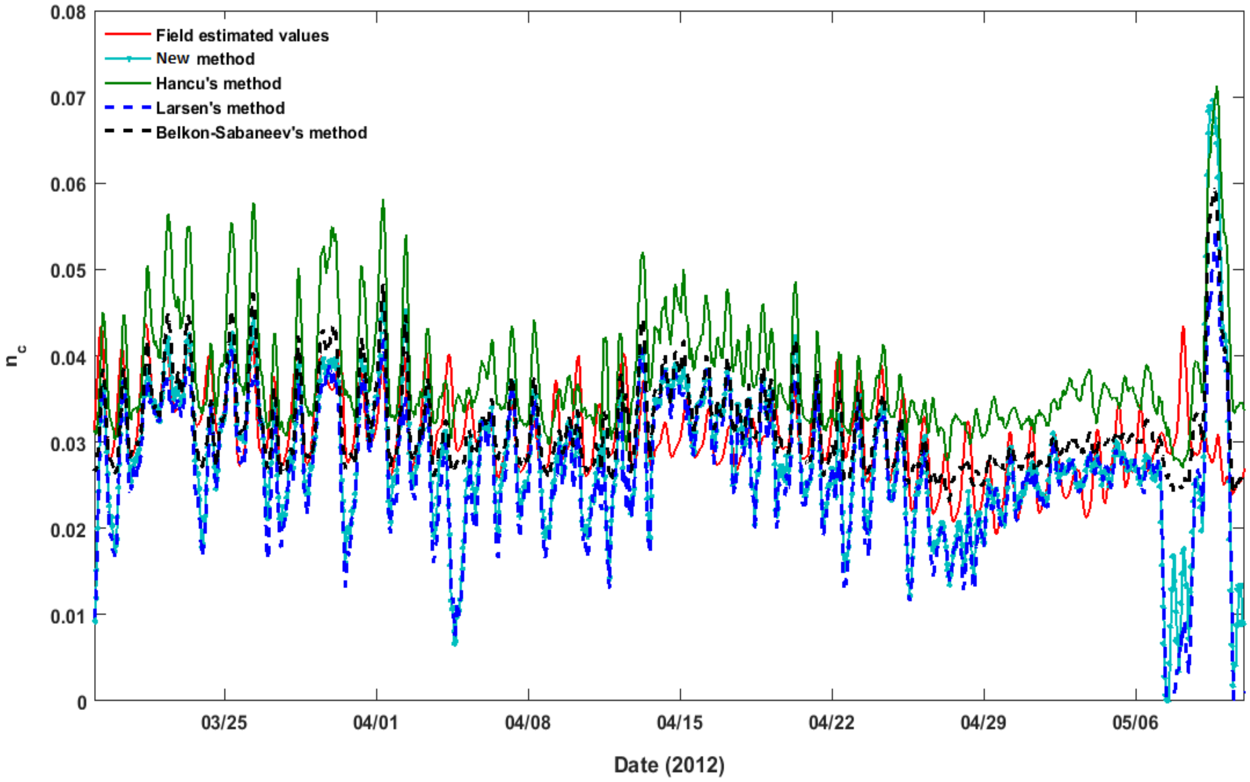

Figure 5.30: Composite resistance estimation using different methods comparing to the estimated field values

required range of velocity, due to the different nature of ice floes during freeze-up, stable ice cover and break up period. During the freeze-up period, ice floes are mainly frazil ice crystals, which tend to agglomerate and can deposit on the under surface of the ice due to high natural tendency to stick to the objects in the water. Break-up ice floes are bigger in size and more angular and buoyant–but less likely to stick together. Increased angularity and stickiness both encourage deposition. The end result is that higher velocities are required for deposition (under turning the incoming floes and depositing under the cover) and erosion (deposited and locked ice fragments) during the break-up period (Judge et al., 1997). Overall, study results suggest in higher flow velocities ice roughening/thickening often is due to mechanical fragmentation processes (shoving) rather than ice deposition and thermal thickening. An ice jam forms a temporary obstacle to the flow and leaves a very small part of the river cross section open. The open area has a very rough upper boundary, which is the under surface of the ice jam, due to the jam material.

Ice jams usually form when large fragmented floes jam in narrow sections of the river. So, due to the nature of the jam, a very rough surface would be anticipated for the upper boundary. During the late break-up, fragmentation of the cover led to the formation of temporary open water condition at the study site. Open water condition clearly can be recognized in Figures 5.10-b,c and 5.24 by the location of the maximum velocity ($\varphi \approx 1$) and the estimated under ice surface roughness ($n_i = 0$). It appears that this open water condition was followed by the formation of the ice jam since the water started to stage slightly during the open water period and meanwhile the water velocity decreased. The phenomenon then followed by occurrence of very high water velocity observations as well as the lowest rate of the normalized maximum velocity location (around 0.4), immediately before the jam release, which is an indication of high resistance to flow during this period. The highest values for ice roughness were estimated for this period as well, reaching up to 0.08, which was almost twice the average calculated roughness coefficient for bed (around 0.04). Immediately after the jam release, the water surface dropped and the maximum velocity location jumped to near the water surface, which are signs of open water condition initiation.

5.2.2 Composite resistance calculation

As expected as a result of backwatering and associated increased water depth during the ice cover period, lower energy grade line values were observed for the bed zone compared to the open water condition (Figure 5.27). Importantly, different energy grade line slopes were observed for the ice and bed zones during the ice cover period, which counters the typical assumption of equal ice and bed zone energy grade line slopes. In other words, $S_{fi}=S_{fb}=S_o=S_{bed}$ is not a valid assumption. The energy grade line slope for the ice zone was substantially higher than for the bed zone during the stable ice cover. Shear velocity and shear stress magnitudes followed the same trend during this period (Ghareh Aghaji Zare et al., 2015) but with smaller difference between the bed and ice zone shear velocities.

Estimated Manning bed roughness coefficient values (Figure 5.24) were consistent with observed bed material substrate (Figure 4.3) . Furthermore, the composite resistance for the cross section estimated using the newly proposed Equation 4.56 was fairly close (Figures 5.30) to the estimated total resistance (n_s in Figure 5.29) comparing the results of other methods and exceeded the individual bed and under ice roughness values during the ice covered condition. After ice cover removal the estimated total composite resistance equaled the bed roughness (Figure 5.29). These results suggest that the total composite resistance coefficient is a combination of bed and under ice roughness, and should be representative of higher resistance during the ice cover period.

Results of composite resistance estimation using the equations of Sabaneev (4.38), Hancu (4.39), Larsen (4.40) and the proposed equation (4.56) show a fairly similar estimation of composite roughness between equations 4.38, 4.40 and 4.56 but equation 4.39 is found to slightly overestimate the composite resistance to the flow.

The difference in prediction of composite resistance in discussed methods is mainly due to the assumptions used in the methods, which include:

1. Equality of the mean velocities for subsections and the total mean velocity, i.e., $V_t=V_i=V_b$ (Chow, 1959; Carey, 1966; Komura and Sumbal, 1967; Secil Uzuner, 1975). Validity of this assumption has been questioned before (Chee and Haggag, 1984). According to the findings of this research, which are based on field measurements for different ice cover stages, this conclusion is not a valid assumption to apply

in natural streams. The difference between V_i and V_b was more than 10% on average, and was sometimes as much as 20%. It appears that the applicability of the equal mean velocity assumption is restricted to prismatic, laboratory flumes with the same boundary material.

2. Equal hydraulic radius, i.e., $R_t=R_i=R_b$ (Secil Uzuner, 1975). Depending upon the depth measurements for ice and bed zones and the location of maximum velocity, it can be concluded that the assumption of $R_i=R_b$ connotes $n_i=n_b$. This is a simplified case in composite roughness calculation that was not observed in our measurements (Figure 5.29). Alternatively, the hydraulic radii have been assumed in literature to equal half of the total depth (Larsen, 1969; Beltaos et al., 2012). This assumption is mathematically more reasonable, and was used by Larsen (with zone depth substituted for zone hydraulic radius (Secil Uzuner, 1975; Ashton, 1986). Still, the present results demonstrate that φ did not usually equal 0.5, which renders invalid this assumption.

3. Equality of energy grade line slope for subsections and the total cross section i.e. $S_{fi}=S_{fb}=S_{fo}=S_o$ (Larsen, 1969; Ashton, 1986). This research demonstrates that this assumption is not correct. First, S_{fi} differed from S_{fb}. Second, the energy grade line for the bed zone was often substantially less than the bed slope (Figure 5.27). Since the water depth increases and mean zone velocities decrease during the ice cover period compared to the open water period, it is reasonable to anticipate lower values for the total energy grade line slope during the ice cover period.

These observations suggest that the assumptions for hydraulic radius and energy grade line slope employed in a total composite resistance formulation must be considered carefully when implementing the Manning formula in ice-covered conditions.

In general, flow depth increases and flow velocity decreases in the presence of an ice cover due to the increased flow resistance imposed by the additional boundary at the flow surface. A higher composite resistance value is required to represent the increased resistance. However, implementation of the assumptions such as $y_i=y_b=y/2$ and $S_{fi}=S_{fb}=S_{fo}=S_o$, as used by Larsen, necessitate implementation of a total roughness coefficient that is less than the bed roughness in order to maintain flow continuity (Figure 5.30). According to the results of this research, the increase in water depth during the ice cover period was not enough to compensate the effect of decreased hydraulic radius, thus with the (inaccurate) assumption of equal energy grade line slopes, the coefficient of resistance in the Manning formula n_c, must be decreased to keep the discharge per unit width constant (continuity). This approach is conceptually unsatisfactory since the estimated n_c values drop often to values less than bed roughness, indicating the resistance during the ice cover period is even less than the open water resistance. This is clearly contradictory with the observations of higher depth values and lower velocities during the ice-covered period, both of which indicate increased flow resistance.

The theoretical approach for estimation of composite resistance presented in this research avoids all of the common assumptions, and is based on analysis of the effect of the ice cover presence on hydraulic characteristics such as velocity and water depth. Observations of velocity profiles are required to determine the ice and bed roughness values, as well as the mean velocities in the ice and bed zones, the maximum velocity in the water column, and the hydraulic radii and flow depths of the ice and bed zones. The primary assumption is that the total friction slope equals the sum of the friction slopes for the ice and bed zones. Higher values of the ratio of n_c/n_b estimated by the proposed method show the increased total hydraulic resistance during the stable ice cover period, as expected. The proposed method resulted in higher variation of n_c estimates compared to the previous methods. These oscillations are due to sensitivity to the presence of the mean and maximum velocity and depth terms for ice and bed zones in the formulation.

Finally, it should be noted that the presented equation is not applicable for open water conditions where the upper boundary resistance coefficient is technically zero.

5.3 Turbulence structures in ice covered rivers

As shown in the previous section, velocity profiles corresponding to the different ice stages, more specifically during the dynamic stages of the break-up, showed relatively clear asymmetry (Figure 5.20). Starting with the mechanical break-up which was associated with higher water velocity, maximum velocity distinctively increased and occurred relatively deeper in the water column.

Based on what is described in section 3.1.3 through the equations (3.5a) to (3.5d) and 4.20 and 4.21 , using the variance technique, Reynolds stress is calculated as the main representation of the turbulence in the flow during the ice cover period. Results of the principal Reynolds stress calculation for the 2013 and 2015 study period are represented in the Figure 5.31.

Reynolds stress values are calculated up to the highest bin in the water column with a value for the velocity. As it is obvious in the figure, the velocity values are not extended to the flow boundaries. This is mainly due to two main limitations of acoustic techniques in velocimetry; first, the blank distance and second the saturation of the backscatter sound near the boundary which disables the ADCP to measure the velocity correctly near the under ice bottom. Both linear and log-linear velocity extrapolations are applied to extrapolate the velocity profiles to the boundaries (results presented in Figures 5.12 and 5.13). Considering the fact that the Reynolds stress is calculated based on the difference between instantaneous velocity magnitudes and mean velocity, Reynolds stress calculation using the synthetic near boundary velocities (extrapolated values) is found to be unreliable and thus is neglected. On the other hand, the ice bottom location, as presented before in Figures 5.12 and 5.13, is not equal and therefore, the last bin containing the meaningful velocity for each beam is different. Hence, the Reynolds stress profile near the ice bottom is calculated only if all four beams had a recorded velocity value in the the bin at that elevation. This caused the Reynolds stress extent to be slightly lower in water depth (about a meter from the boundaries) and can be considered as the limitation of field measurements. Considering all the intrinsic restrictions of the application of acoustic measurements for Reynolds

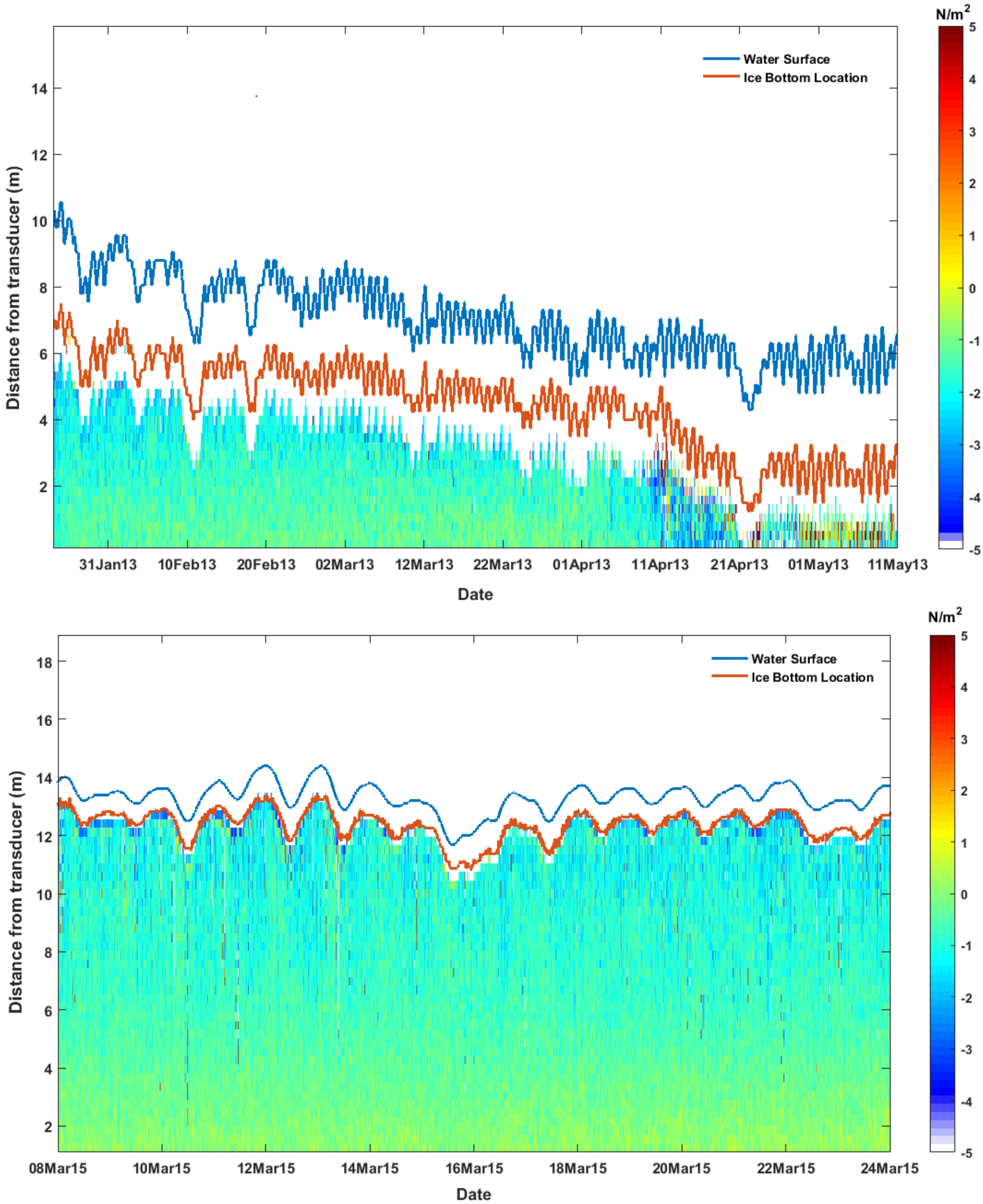

Figure 5.31: Principal Reynolds Stress calculated during the ice cover period, 2013 top and 2015 bottom

stress estimation, recorded data and calculated profiles still cover a considerable portion of the water column, making the results applicable for Reynolds stress analysis.

Data are hourly averaged in this study for all study years. For this purpose, recorded ADCP data are ensemble averaged to represent data as an average in an hour of data recording. Analyzing ensemble averaged principal Reynolds stress, presented in Figure 5.31, the following can be noticed and discussed.

Before the dynamic break-up starts (around mid-April), a decreasing trend in Reynolds stress can be noticed in the water column from the bed toward the undersurface of the ice. Such a trend can be clearly followed in the Reynolds stress profiles presented in Figure 5.32. As also can be seen, the zero Reynolds stress location in the profiles often occurs in the lower portion of the flow depth (Figure 5.31). Such an observation is consistent with the location of the maximum velocity in the flow depth, (even though the locations of maximum velocity and zero Reynolds stress do not necessarily strictly match. This is an indication of the rough nature of the upper boundary which causes the maximum velocity to be pushed down in the water column. During the mechanical break-up period, some anomalies are observed in Reynolds stress values and their distribution through the depth, including negative values. Recall that anomalies were also observed in beam velocities during this period (Figure 5.12). Both the Reynolds stress and water velocity anomalies during break up can be reasonably related to flow deviation due to partial/complete water passage blockage.

Reynolds stress distribution results were more consistent in 2015 (Figure 5.31), largely because the ice cover condition remained almost constant during the study period . As seen in the figure, higher colour coded values appeared near the lower boundary and decreasing gradient of the Reynolds stress values is observed as the bins distance from the river bed. Higher Reynolds stresses (absolute stress value) are expected to occur near the under ice surface. It is notable that the color coding representation includes the sign of the values. What can be seen in the figure can be briefly described as the presence of greater positive values near the bed and greater negative values near the under ice surface. It also should be restated that the negative sign of stress values near the under ice cover is due to the utilized coordinate system with the positive vertical direction upward.

In order to examine the hypothesis about the Reynolds stress distribution, sample profiles during the several ice stages of 2013 and 2015 are presented in Figure 5.32. More or less the same trend for Reynolds stress distribution can be observed in the profiles. Values start from positive values (notice that the data are not extended to the boundary but to the relative elevation of 0.2), and decrease in water depth. The zero Reynolds stress location varies between the profiles but is around half of the depth in most conditions. As discussed previously, the location of zero Reynolds stress can be defined as the location of ice and bed zone separation. Based on the temporal window that is selected between the profiles, the aforementioned criterion can be followed to distinguish between various river ice conditions based on the depth of ice and bed zones. The last profile corresponds to the stage identified as the ice jam formation period. As seen, the Reynolds stress values follow a completely different pattern mainly due to the drastic change in flow direction during this stage.

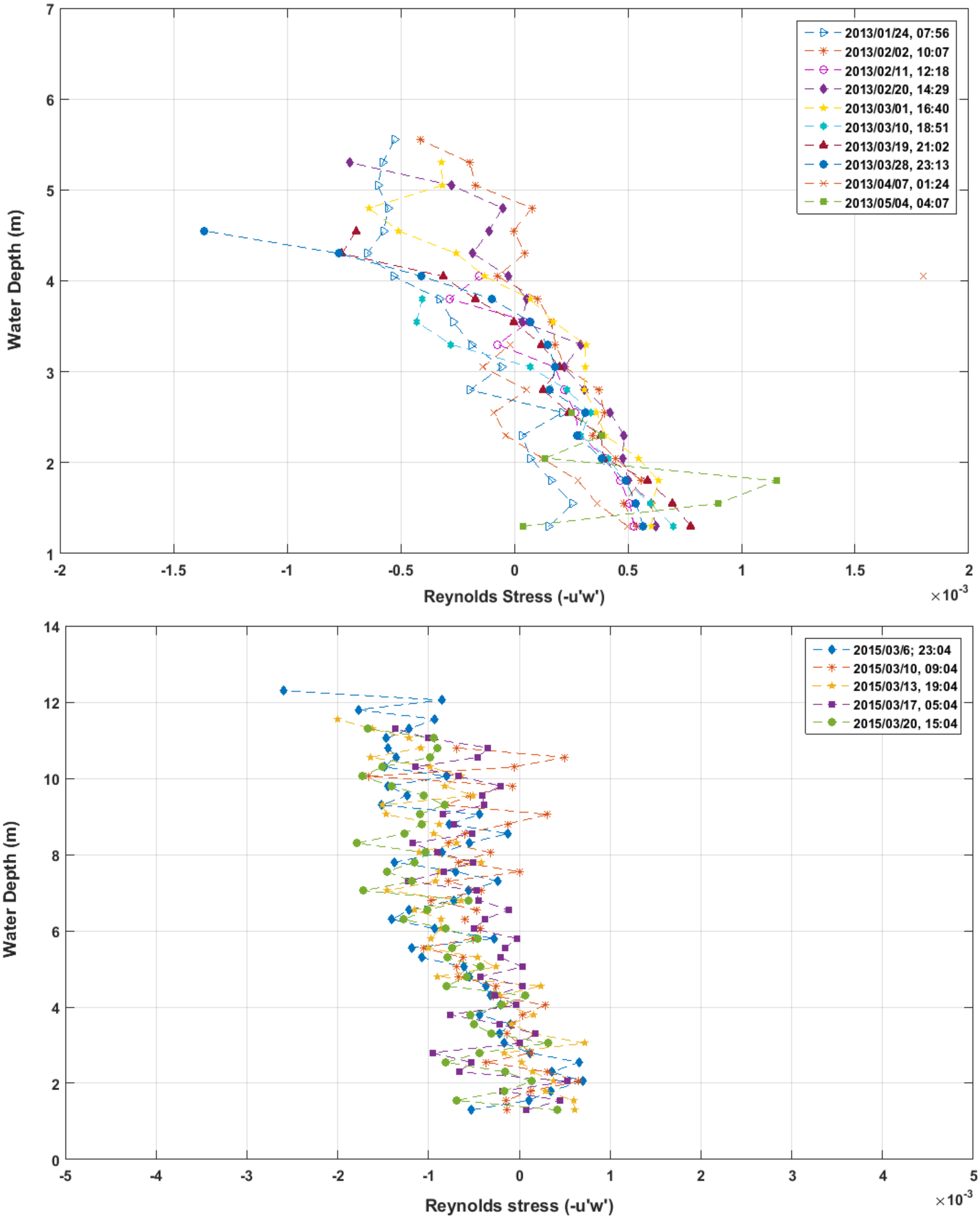

Figure 5.32: Principal Reynolds Stress distribution during different ice stages, 2013 top and 2015 bottom

In 2015 however, Reynolds stress distribution trend experiences little variation between profiles and mostly show a similar trend. As it is seen, the Reynolds stress profile during the ice cover period is clearly affected by the presence of the ice cover. Excluding the near boundary values, the negatively sloped trend of data results in negative Reynolds stress values near the upper boundary . This is an indication of increased turbulence level in the vicinity of the upper boundary layer. Higher turbulence level and consequently higher turbulence production near the ice cover can be interpreted from the results. According to what is presented in sample profiles, some Reynolds stresses are expected to be even higher than the corresponding near bed positive values indicating the possibility of higher turbulence level near the ice cover. Considering the fact that the balance between boundary roughness conditions defines the turbulent flow structures in the water column, coherent turbulence structures with higher correlation between the streamwise and vertical flow fluctuations is expected to occur in the ice zone during the formation of rough cover over the study reach.

Figure 5.33 illustrates the Reynolds stress tensor magnitude (equation 4.31), calculated for both 2013 and 2015 data acquisition periods. The Reynolds stress tensor magnitude can be considered as an indication of the turbulence intensity on the flow boundaries. In Figure 5.33, the magnitudes of Reynolds stress tensor are calculated through the water depth up until to the last bin containing meaningful beam velocities in all beams. Reynolds stress tensor magnitude is then calculated based on the Reynolds stress values. Finally, the Reynolds stress magnitudes are extrapolated to the boundaries. Since the results of equation (4.31) are all positive magnitudes, the trend of data distribution can be extrapolated to the boundaries without introduction of noise due to the signature of the Reynolds stress values, i.e., the direction of the flow velocity component. Presence of coherent turbulent structures with higher correlation between principal and cross-sectional Reynolds stresses can be better presented in the form of the Reynolds stress tensor magnitude. As it is shown, turbulence level near the upper boundary is considerably higher than lower in the flow. This is a clear indication of higher turbulence production near the undersurface of the ice cover. Since all the acoustic measurements were limited to a distance from the bed, Reynolds stress and Reynolds stress tensor could not be extrapolated to the bed successfully and therefore are not included in the presented results.

Regarding the higher turbulence intensity near the ice, it should be noted that the higher turbulence can be the result of two main factors. The most important parameter in the case of this study was the effect of hydropeaking and consequently the share of water velocity in the turbulence intensity calculation in both ice and bed zones. Temporary higher turbulence intensity is observed at the start of the break-up period as it can be seen in 2013 analysis results.

The second important factor is the condition of the ice cover. Ice cover condition can be discussed in two main categories. First, the roughness of the ice cover which determines the asymmetry in the ice and bed zones extent through the water depth. As a consequence, the upper boundary condition, assuming relatively constant bed roughness, determines the rate of production of macro turbulent coherent structures in the flow.

On the other hand, non-equilibrium ice cover condition alters the flow pattern and

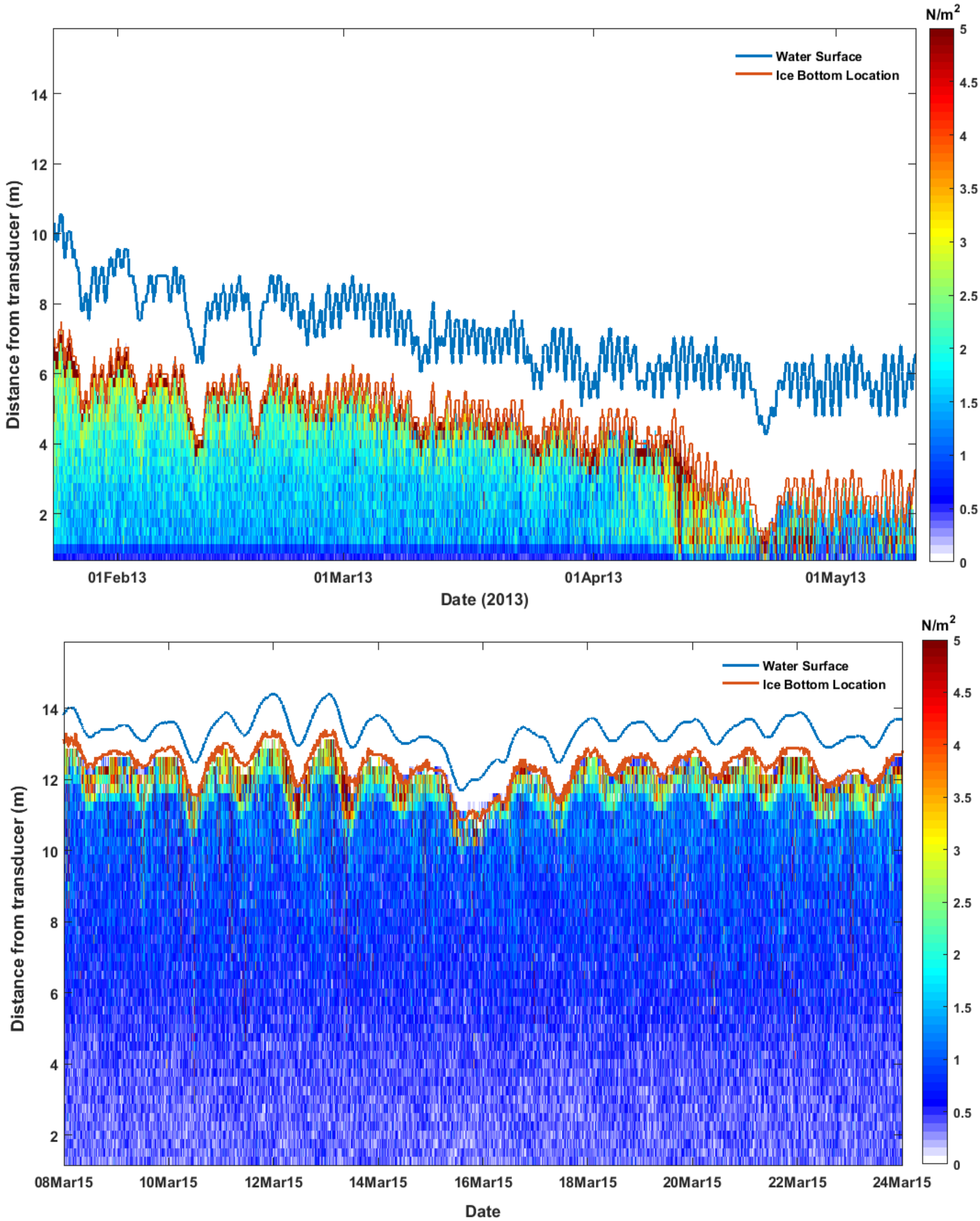

Figure 5.33: Calculated Reynolds Stress tensor during the ice cover period, 2013 top and 2015 bottom

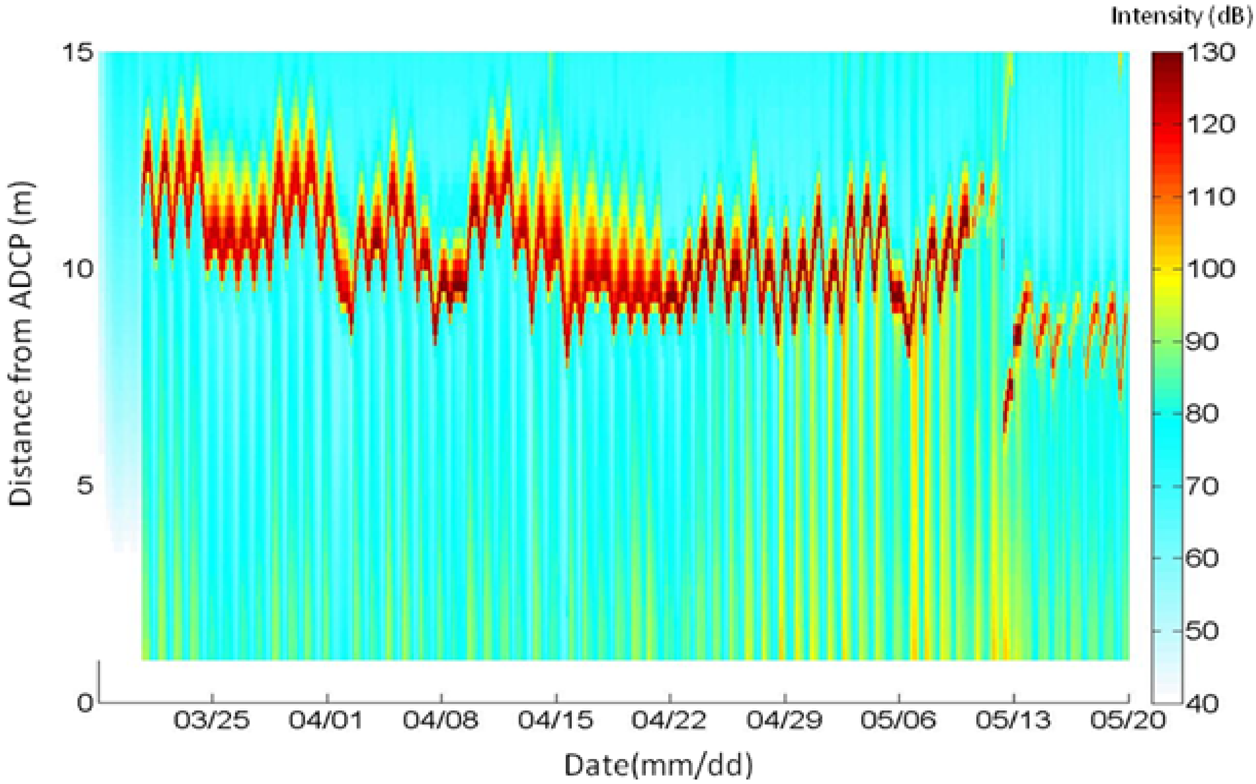

Figure 5.34: Intensity of back scattered sound shows solid surface (ice and water surface) and influence of suspended particles in water.

differs the correlation between the turbulent structures and streamwise/crosssectional turbulence intensities. As an instance, higher water velocities observed at the start of break-up contributed to the increase of Reynolds stress tensor magnitude, not by increasing the principal Reynolds stress but by altering the flow pattern and thus increasing the cross-sectional Reynolds stress.

It can be concluded that the ice cover presence varies the flow field in both hydraulic resistance and spatial non uniformity, emphasizing the considerable effect of ice cover morphology on flow structure in ice covered streams.

5.4 Sediment flux calculation

Figure 5.34 shows ADCP data for intensity of back scattered sound from suspended particles in water under stable ice cover condition and also during the break-up period. The intensities were range corrected for acoustic spreading and absorption (section 4.3).

According to figure 5.10, ADCP data show that the complete break up occurred near May 10 at the study site as it was interpreted by SWIPS data (Figure 5.10-a). it is assumed that suspended particles were sediment particles, which is a reasonable assumption for measurements in late winter and spring. Assuming that grain size distribution of

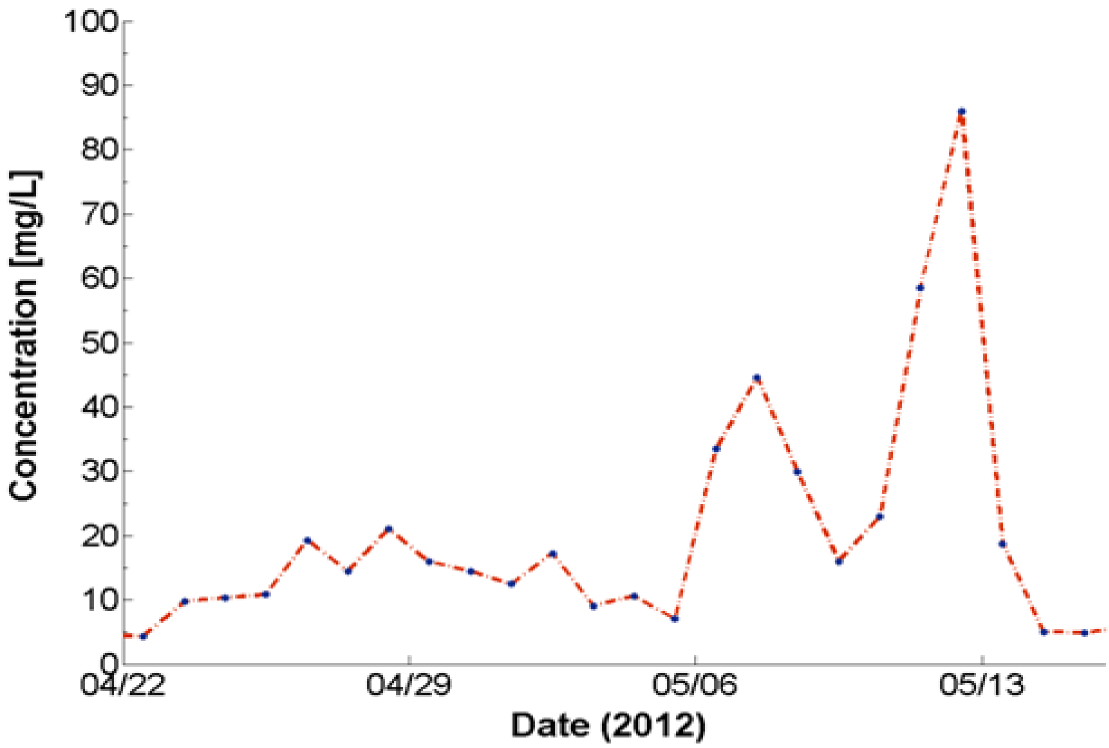

Figure 5.35: Estimates of the daily average concentration measured at 2.24 m from the bed during breakup 2012

suspended sediments was reasonably constant as a first approximation, higher intensities in the water column can be interpreted as an indication of higher concentration of suspended particles. Some higher intensities were observed near the bed which can be interpreted as an indication of bed material suspension.

Figure 5.35 shows daily averaged values of concentration of suspended sediment in mg/L which are estimated from acoustic data during the break up period using regular inversion techniques (Moore et al., 2013). This figure presents the measurements made at 2m above the bed. As seen daily averaged concentration increases from around 7 mg/L to 90 mg/L which is about 10 times higher.

According to Figures 5.34 and 5.35, following results are understandable: First, diurnal variation in sediment concentration is apparent, which corresponds to flow stage variation associating with hydro-peaking. The same oscillations in mean and maximum velocity are also possible to see in Figure 5. Thus, flow acceleration associated with hydro-peaking appears to increase sediment concentration. Estimated concentration values based on ADCP backscattered data also show that the concentration fluctuates between less than 5mg/L in the morning to almost 30 mg/L in the evening during winter months. Second, dramatic increase in suspended sediment concentration is observed at break up which reaches up to 10 times of the suspended sediment under stable ice cover. This high suspended sediment concentration can be observed from the bed to the ice/water surface during hydro-peaking events in the break-up period.

5.5 Numerical simulation of river ice using the ICES-IMAT

5.5.1 ICESIM model calibration

The majority of ICESIM processes use empirical equations with coefficients that should be calibrated to get the best simulation of observed conditions. Modified coefficient help the model to reproduce observed historical data such as water level and more importantly ice propagation rate and thickness. The first model calibration is open water condition modifications by varying the Mannings n- value of the bed to match the water level data. Subsequently, the calibration of complicated winter condition takes place.

ICESIM calibration has been performed for 16 years of available data (1993-2009). Winter 2010-11 is selected as validation year and winter 2012 is selected for verification year. Adopted main factors for ICESIM calculation have been shown in Table 5.2.

Parameter	**Value**
Maximum water velocity for under cover ice deposition	1.0 m/s
Minimum water velocity for undercover ice erosion	2.5 m/s
Maximum Froude number for Juxtaposition	0.12
K2- Coefficient of internal strength of ice (equals to Rankin Passive coefficient for soils)	7.2
K1- Ratio of lateral or longitudinal stress in ice cover , Φ -Internal angel of friction of ice mass	K1.tanΦ= 0.18
Manning's "*n*" value for ice cover	0.015- 0.13

Table 5.2: "ICESIM" calibrated ice formation parameters.

Results of calibrated ICESIM simulation for a day in the measurement period are shown in Figure 5.36, which compares the predicted to in-situ measurements of ice bottom location and water surface elevation at one location in the study reach on March 25 2012 to represent model ability in river ice simulation. Note that the measurement location near Jackfish Island is in a relatively flat part of the reach.

As shown, the model simulated the water surface elevation and ice bottom location reasonably accurately, although ICESIM slightly over-predicted the water surface elevation and ice bottom location over the deployment site. Given the one dimensional steady-state nature of the model, and considering that the model employs an equilibrium condition assumption for uniform river ice thickness across the cross section, the model produced acceptable results in comparison to real measurements at the deployment site.

River ice can be expected to vary across a section. For a symmetrical cross section thicker ice is found at river banks, due to presence of border ice and the more quiescent

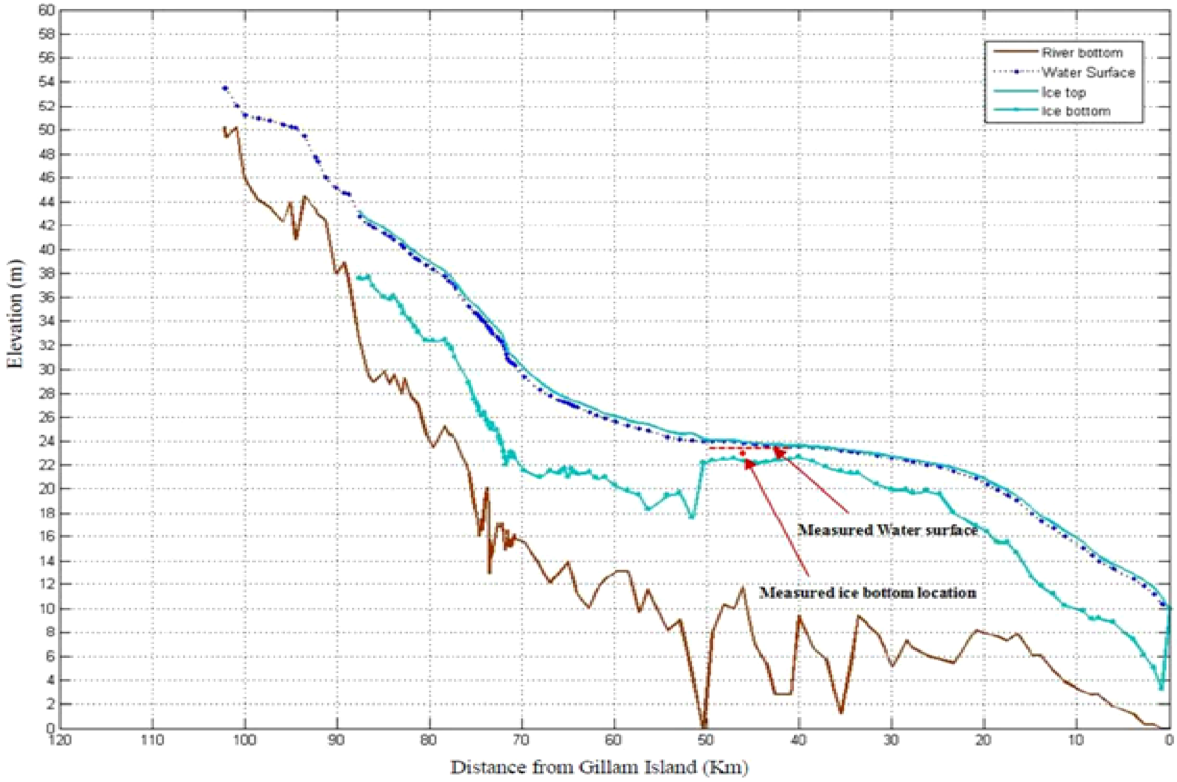

Figure 5.36: ICESIM simulation model results and real measurements at day 177 of simulation (25/03/2012)

environment of river banks, which allows for more vertical growth. Thinner ice is usually present in the middle of the section, due to more turbulent water flow and higher velocities that preclude thermal thickening, although mechanical thickening (shoving) can occur, particularly in steep reaches. On the other hand, the in-situ acoustic measurement is local in nature, thus does not represent the river ice and river hydraulic conditions all across the river cross section. The spatial domain of the ice thickness measurement is limited to some meters. For the vertical beam SWIPS this is a function of beam spreading angle. For the ADCP, this is a function of beam spreading angle and the beam angle from vertical, thus the spatial domain is a circle with the diameter almost equal to the deployment depth. Given the potential for spatial variation in ice thickness across a section, utilization of a localized in situ measurement may lead to some discrepancy between predicted and observed ice thickness as the model results provide an estimated average cross sectional ice thickness.

It is also notable that the estimation of starting point of ice progression, i.e. the time that ice front reaches the Gillam Island from Nelson River estuary, is a key point in model simulation. Therefore, wrong estimation of the time may leads to significant difference in model results in ice thickness aspect as well as propagation distance and rate. In the other word, model is highly sensitive to this factor.

Over estimation in ice thickness renders the model slightly imprecise in propagation

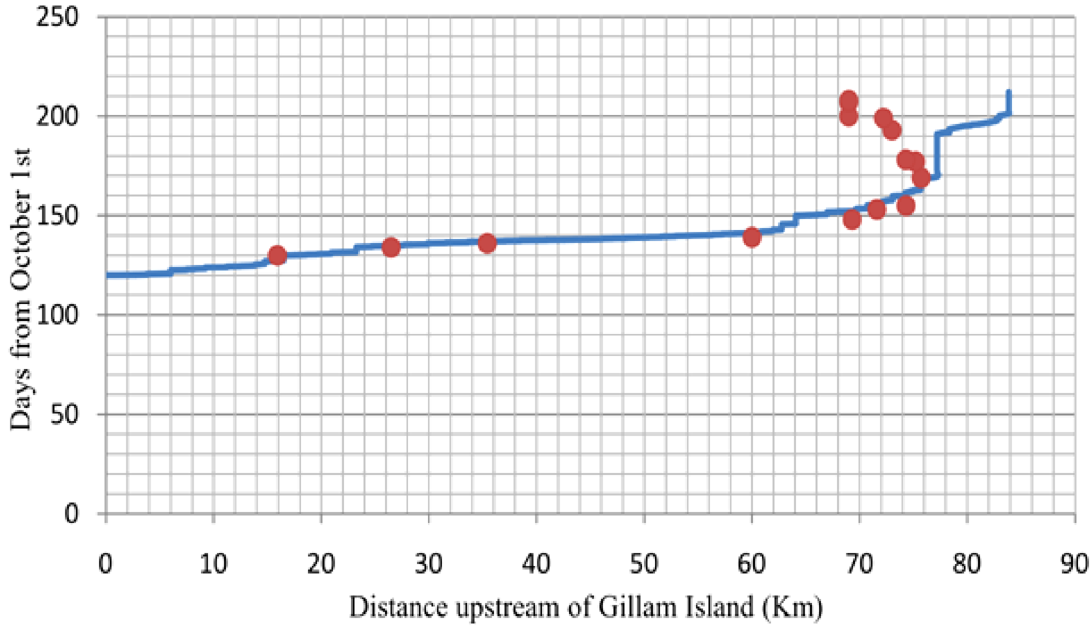

Figure 5.37: Ice front locations for ICESIM simulation period (2012)- "Red Dots" are ice front locations according to satellite images

rate, especially at the end of the ice period when the thermal weakening starts. Thermal decay weakens the thinner parts of cover as much as they cant resist against the weight of upstream thicker ice cover and start to fragment. This process makes the ice front to recede as shown in Figure 5.37. Therefore, over estimation in ice thickness affects model accuracy in final ice stages even though the model shows almost accurate simulation during propagation and stabilization periods. NASA-MODIS images for the study period considered as the validation data for ice propagation simulations in ICESIM. Downloaded satellite images analyzed in different color spectrums in ArcGIS in order to provide higher resolution data in water/ice determination process.

5.5.2 ICESIM-ICESIMAT conversion

The ICESIM code was initially developed by Acres International in the 1960s for Nelson River ice studies. The code has been programmed in FORTRAN 77, 90 and 95. The model is composed of one main control file ICEMAIN and 11 modules (14 subroutines). The main file, ICESIM utilizes subroutines in order to perform individual simulation tasks. Climatic data (air temperature) is the most important input for the simulation of river ice formation, and is required over 212 days starting from October 1st to May 1st. Ice cover simulation starts from the December 12^{th} (day 73), when based on the previous observations, ice cover reaches from the Hudson Bay to Gillam Island.

The study reach is characterized as 121 cross sections, and cross section geometry of all cross sections (surveyed and interpolated) is addressed in a text file called XSEC-

DATA.PRO. The definition of cross section geometry information is presented in Appendix D. Input variables for ICESIM are defined in a text file format including several cards addressing the variables. Input variables and their calibrated values for ICESIM/ICESIMAT are presented in Appendix E.

Results of ICESIM are also presented in text file format which must be post processed. A Matlab code is developed to process the ICESIM results and present the ice thickness over the study reach for several time steps through the simulation. Figure 5.36 was produced by the developed code representing the elevation of ice cover top and bottom as well as the water surface elevation.

As a part of this study, ICESIM has converted from FORTRAN to a Matlab based code including 31 sub-files and functions to perform the simulation. The Matlab based code, called ICESIMAT, uses the same input and geometry files and simulates the ice process over the same number of cross sections along the study reach. A Graphical User Interface (GUI) has also been designed for ICESIMAT, which makes the application of the model more user-friendly. The GUI provides the representation of the simulation results and eliminates the post processing of results.

5.5.3 ICESIMAT performance

Ice cover formation and decay

As described in section 5.5.2, through this study, the ICESIM model is improved to simulate the entire river ice processes, river hydraulics under the open water and ice covered condition as well as the sediment transport in ice affected streams. The new model is called ICESIMAT which stands for the Matlab version of the ICESIM model. The new model is developed through some steps most of them are in form of enhancements to the previously developed ICESIM and ICEDYN models. As the first step of these improvement steps, a post processing code is developed to extract, read and process the simulation results of ICESIM and ICEDYN models.

The ICESIM and ICEDYN models both were programmed to provide the simulation outputs in the text format which necessities a laborious post processing procedure through the Excel spreadsheets. During the first step of the improvement, a Matlab code called ICERESULTS developed to by-pass the post processing analysis and export the user defined results. Results of ICERESULTS code is partially presented in Figure 5.36 . The code is developed and provided to facilitate the industrial model applications for engineering purposes by the main applicant, Hatch Ltd.

As the second step, a separate Matlab code is developed to run the main Fortran codes of ICESIM/ICEDYN. Through this interface, the user defines the input variables (instead of editing the text file of input variables), runs the model and post process the results. This step is designed to fasten and assist the model calibration process. However, the main computational engine remains the Fortran code.

Due to the relative difficulty in code modifications through several involving Fortran computational subroutines, the main simulation program is decided to be converted to

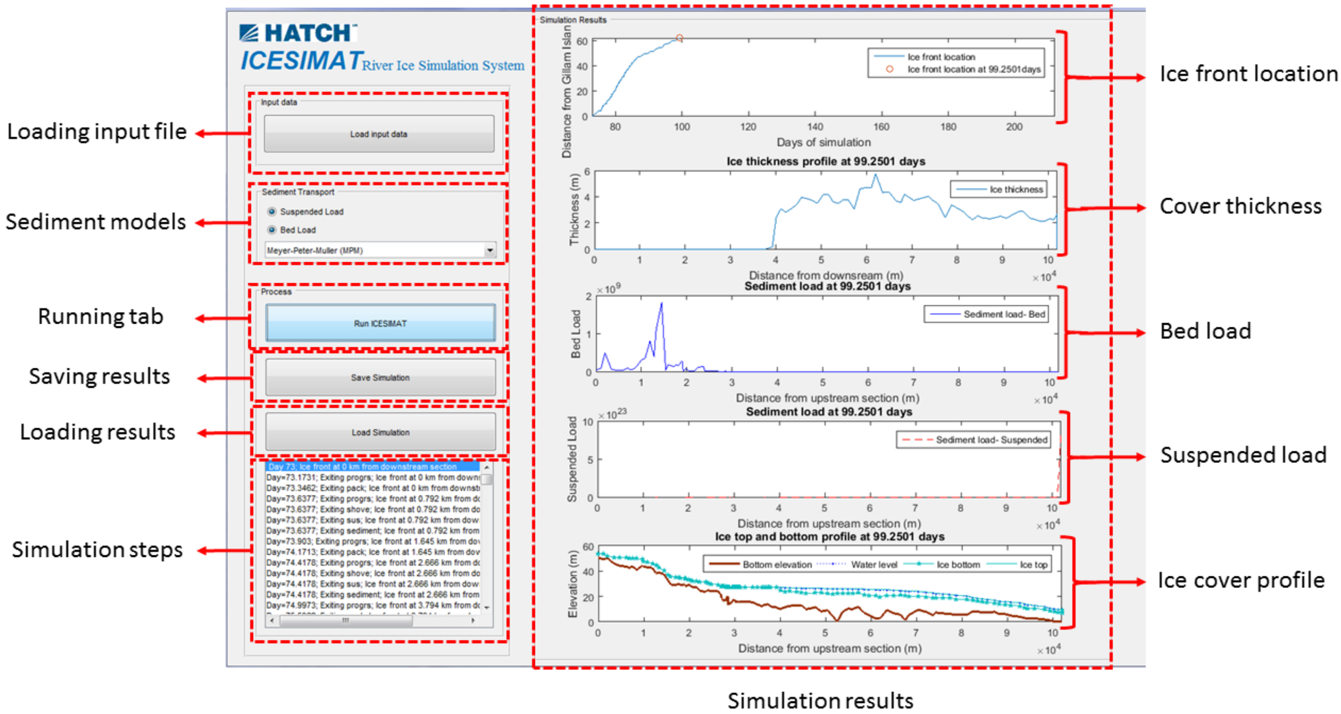

Figure 5.38: ICESIMAT Graphical User Interface

Matlab in order to increase the consistency of the model parts as well as providing a more robust platform for further improvements. Hence, the ICESIM model is completely converted to Matlab. The new version of ICESIM debugged and verified with the Fortran version to assure the similarity of the results. In consultant with the original owner of the model, the new model is named ICESIMAT.

Further improvements then designed to increase the model performance and flexibility, mainly improvement of the model capability in the simulation of the entire river ice processes as well as the sediment transport under the ice cover and open water regimes. Therefore, the main improvement of the ICESIMAT compared to the ICESIM model can be categorized as the model capability in the simulation of the river ice break-up period (excluding the river ice jam simulation) and calculation of sediment load. A graphical user Interface (GUI) is also designed for the program to post process and present the results of each simulation time step while the model is running, also to save each time step as well as saving the entire simulation at the end. The saved simulation are also possible to be loaded through the GUI in order to review or further analyze the simulation results.

Figure 5.38 shows the main parts of ICESIMAT graphical user interface (GUI). As it can be seen, the main simulation results are presented in 5 main graphs each of them representing a single or multiple simulation results.

The first graph illustrates the ice front location while the ice cover propagates upstream. The second graph represents the Ice cover thickness along all the simulation cross sections. The third and fourth graphs show the suspended sediment load and bed load respectively.

The Last graph is a multi-feature graph representing the ice cover profile, water surface elevation, ice cover top and ice cover bottom locations. All above-discussed results are also possible to recall in the GUI for each simulation time steps after the simulation is completed by selecting the eligible simulation time step from the simulation steps window.

ICESIMAT calculates suspended sediment load using the Van-Rijn method. Bed load is possible to be calculated using several models for bed load calculation which can be selected from a drop-down menu under the bed load radio button in the ICESIMAT GUI. All the models used in the sediment calculation processes in ICESIMAT are conceptually discussed in sections 3.4.2 and 3.4.4.

Ice thickness calculation is performed in ICESIMAT through the processes described in section 3.2.3. During the thawing period, the model starts to estimate the thermal weakening of the ice cover using the equations and approaches described in section 3.3.3.

The simulation procedure and the sequence of calculations will be briefly described in the following. The concept of the calculations are discussed in sections 3.2.1 to 3.3.3.

River ice simulation in ICESIM/ICESIMAT starts by the calculation of volumetric production of frazil ice in open water reaches exposed to the cold air. For this purpose, the rate of frazil ice generation is calculated using the equation 3.68. In order to calculate the rate of volumetric frazil ice generation at each cross section, the open water area upstream of the target cross section must be calculated. Accumulative frazil ice volume then can be calculated by summing the volume of the frazil ice over the area between the cross sections. Ice cover formation starts by two main processes, border ice formation and ice bridging. As discussed before, the border ice forms in areas where the water velocity is relatively low. Border ice growth is calculated in the model through the processes discussed in section 3.2.3.

Ice floes start to accumulate at the most downstream cross section based on two bridging criteria both must be met before the bridging can be assumed to occur:

1. The Accumulative Freezing Degree Days must be equal to or lower than -141° C prior to the bridging. Such an initial cold weather period guarantees the promotion of growth of sufficient border ice at the bridging site to narrow the cross section enough to trigger the bridging process.

2. Minimum daily ice volume arriving to the cross section should be met in order to satisfy the internal stability of the cover. The model uses the internal stability equation developed by Pariset et al. (1966) in order to estimate the minimum frazil ice concentration necessary to establish bridging through arch formation in the narrowed channel. The equation can be represented as follows:

$$\frac{t}{Y} = f(\frac{Q^2}{C^2 BY4}) \tag{5.1}$$

in which t is the ice thickness, Y is the mean hydraulic depth, Q is the total discharge, B is the top width of the cross section and C is the Chezy coefficient.

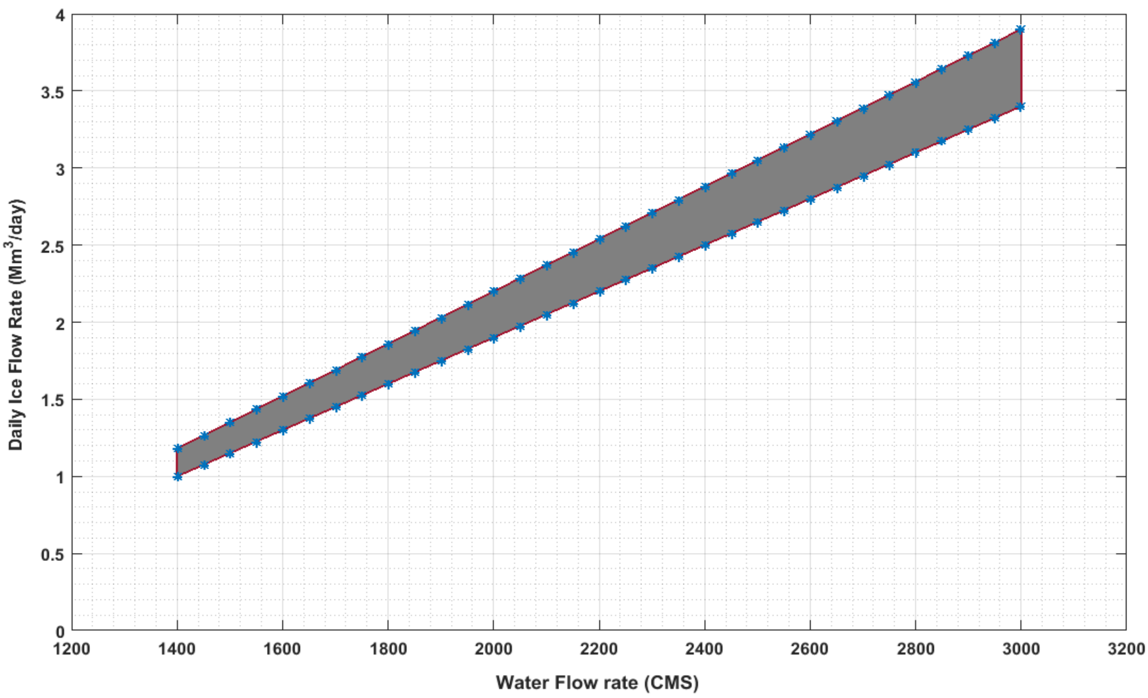

Figure 5.39: Estimated ice flow rate necessary to create bridging at the downstream boundary of the model

In essence, the model seeks to balance the forces tend to drive the ice process in the channel versus the forces which resist the ice cover progression, mainly the flow thrust and streamwise component of the ice cover weight.

The graphical representation of the relation between the required ice concentrations as a function of river discharge for a range of flows potential to occur in Lower Nelson River is presented in Figure 5.39.

The figure is specified by a strip of promoting ice concentration which defines the minimum, potential and definite ice floe concentration for the starting of the bridging and initiation of the cover progression. In Figure 5.39 , areas above the potential strip provide sufficient ice for the bridging to start whereas the areas below it indicate the insufficient ice floe. All volumes lower than the potential margin, would leave the simulation reach at the downstream boundary.

When the both criteria met and the bridging starts, the model starts the accumulation process of incoming ice floes at the bridge location. In order to the juxtaposition process to start, the model assesses the hydraulic condition at each cross section to evaluate the possibility of the ice deposition at the leading edge. Juxtaposition process and ice advancement parameters are described in sections 3.2.1 to 3.2.3.

If the hydraulic condition permits, the ice floes are deposited at the simulation cross section to the point that the variation in hydraulic condition (velocity) exceeds the predefined threshold. Then the deposition process stops and incoming floe either starts to juxtapose at the leading edge or under turn and travel under the existing ice cover. At each time step, the model evaluates the ice cover resistance to the exerted forces at the location of the cross section and adjusts the cover thickness to provide enough resistance to balance the forces through the process of mechanical thickening (shoving). The model then re-evaluates all the cross sections in terms of stability and satisfaction of velocity and Froude number criteria and modifies the water surface elevation accordingly. Through the modification of water surface elevation (backwater effect calculation), the model defines the potential cross sections where the hydraulic condition allows for ice floes to be deposited. The algorithm then deposits the excessive frazil ice volume and progresses to the next cross section along the simulation reach. Extra generated ice volumes leave the simulation reach at the location of the outflow boundary.

Juxtaposed volume of the ice defines the progression rate toward upstream. The model simulates the cover progression and advancement of the leading edge of the cover through the repetition of the aforementioned steps until the ice cover reaches to the most upstream extent which is defined based on the hydraulic conditions of the cross section. From that point on, the ice floes under turn, traveling under the cover until they finally are deposited or leave the reach. Such a condition results in stable ice cover formation over the simulation reach.

Starting the thermal break-up period, the ICESIMAT balances the thermodynamic budget of the water-ice and air as shown in Figure 3.10. Different heat transfer patterns between the thermal break-up and stable ice cover periods, causes the cover to melt and decay. The model calculates the rate of decay based on the equations presented in section 3.3.1, then re-estimates the internal strength of the updated thickness of the ice as well as the new balance of forces on the cover.

Through the stability calculation, if the cover thickness provides enough resistance to the active forces on the cover, the thickness at the cross section is defined as the final thickness for the calculation time step, otherwise, the model thickens the cover mechanically to the thickness enough to stand the new balance of forces through the process of Shoving. The frazil ice production rate is reduced during the break-up period due to the positive air temperatures (frazil ice source will be limited to the eroded ice from upstream cross sections). Hence, the mechanical thickening of the cover leads to retreating of the ice in upstream cross sections or, if the cross section is the leading edge of the ice, retreating to the more downstream cross sections. It is also notable that if the thrust on the ice cover is less than the bank resistance (equation 3.77), the ice cover will not be transferred to the downstream cross sections, but stays in place (grounding) and will be decayed through the thermodynamic processes.

The process of thermal decay and shoving eventually results in complete cover removal over the study reach.

Figure 5.40 shows the simulation results in the study area in 3 main stages of formation, stabilization, and removal. As it can be seen in the figure, the ice cover propagates upstream from Gillam Island (downstream boundary of the simulation) through the processes of juxtaposition which relocate the leading edge of the ice cover toward upstream until the cover reaches to the most upstream extents where hydraulically would be possible for the

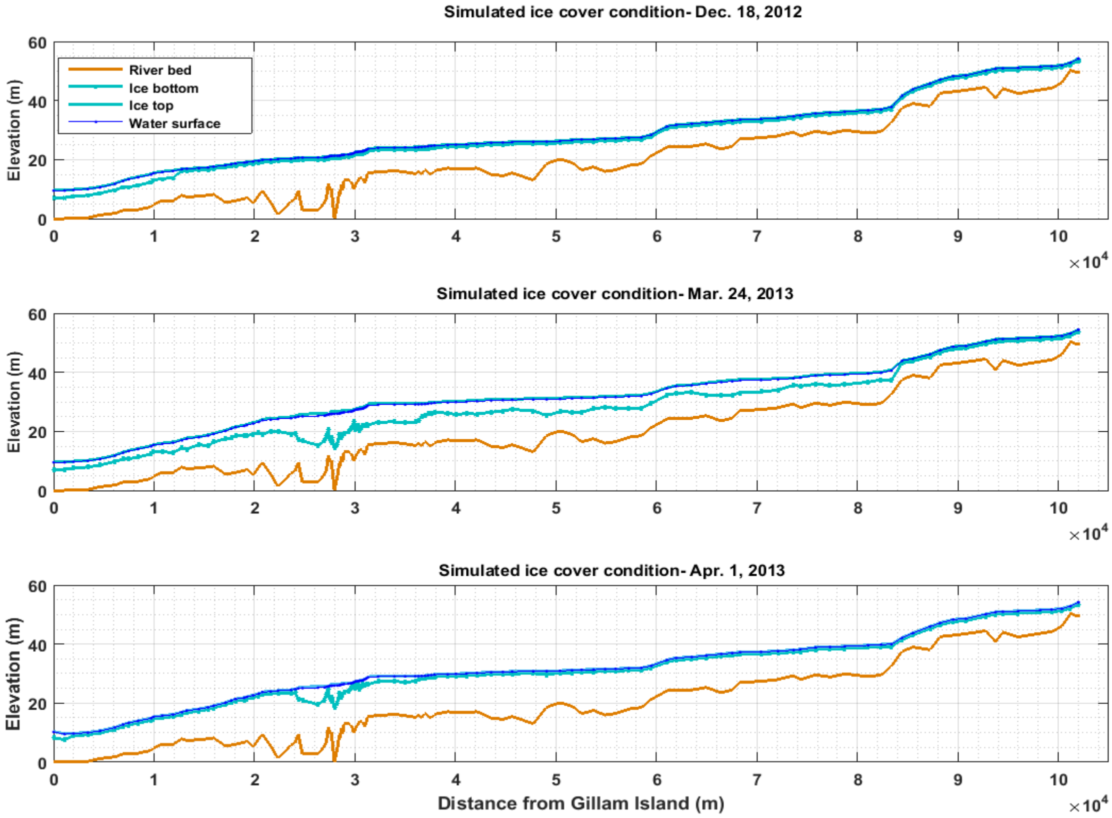

Figure 5.40: Representation of ice cover processes through 3 stages of progression, stabilization and removal in ICESIMAT

cover to extend. Then, the generated ice volume would pass the leading edge (under turning) and be deposited in downstream cross sections where the hydraulic condition meets the deposition limits. The process of propagation is presented in the top subplot of Figure 5.40.

Ice deposition under the existing cover as well as the cover adjustment through the mechanical thickening, forms the stable ice cover over the study reach as it is shown in the middle subplot of Figure 5.40 . During the state of stable ice cover, ice cover thickens and thins according to the thermal and hydraulic parameters of the flow, but likely to be stable in terms of thickness and propagation extent if no drastic variation in temperature or flow occurs.

Starting the break-up period, ice cover decays and retreats as described before. Therefore, the cover state and condition differ according to the new thermal and hydraulic condition. The ice cover removal can be noticed from the difference between the cover condition at two days of simulation presented in middle and bottom subplots of Figure 5.40.

Ice thickness variation in three different locations along the reach for the study period

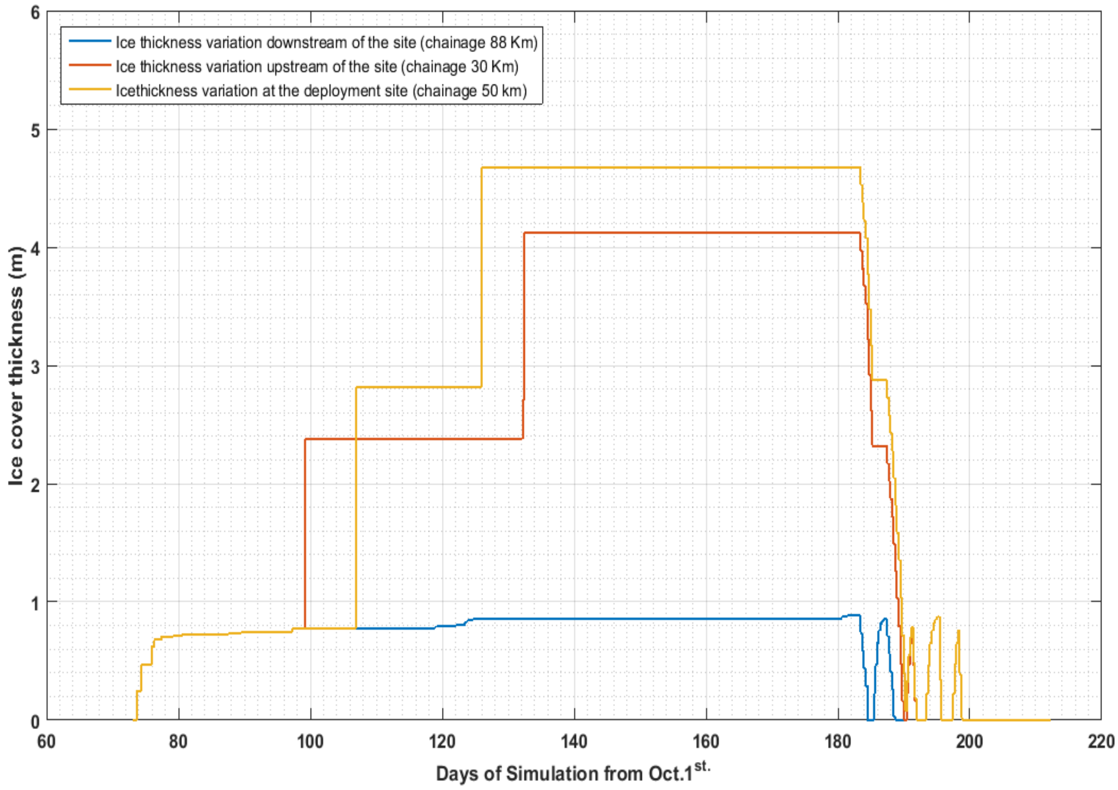

Figure 5.41: Ice cover thickness variation in three different locations along the study reach relative to the deployment site

is presented in Figure 5.41.

As it can be seen clearly in the figure, ice cover thickness varies drastically at different locations along the river reach. This is mainly due to the different involving parameters in ice cover at various locations. Hence, depending on how dynamically or statically the cover forms, it may evolve to different cover thicknesses to maintain the force balance on the body of the cover. Some very interesting features can be addressed in this figure, worth more detailed discussion. A feature which appears at the first look is the similarity in the start of ice cover formation between the presented locations though the cover forms in different rate. This is mainly due to the border ice growth and the approach that is taken in the model to calculate the border ice formation through the simulation. For the presented run, the approach 2 of the border ice growth is considered during the model calibration (refer to section 3.2.3 - border ice growth). Through this approach, as previously discussed, the border ice growth is calculated using the border ice factor which relates the border ice growth to the Accumulative Freezing Degree-Days (AFDD) at the study reach. The AFDD is assumed to be uniform along the study reach and consequently, applying the border ice factor results in the formation of border ice at the same rate and thickness for all the simulated river cross sections. However, considering other approaches described in the abovementioned section leads to the formation of the border ice at a different magnitude

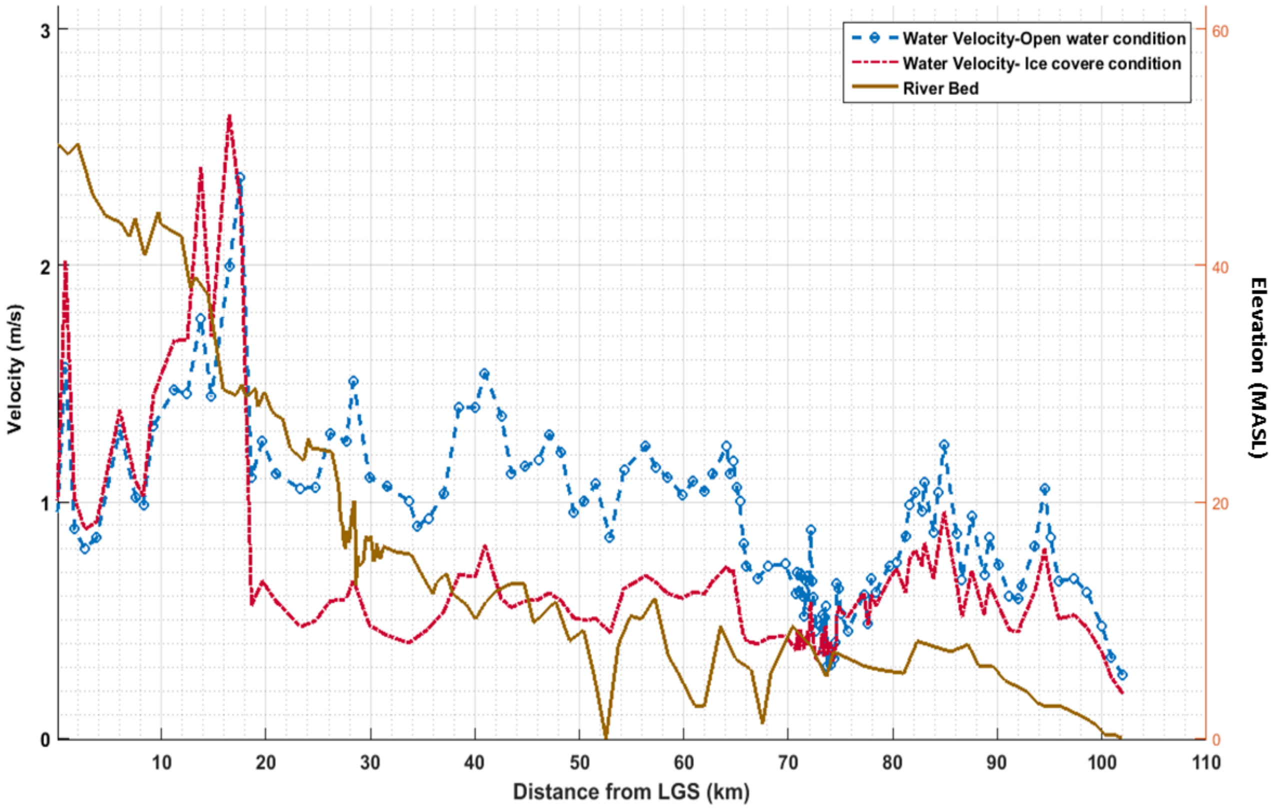

Figure 5.42: Simulated water velocity along the study reach during the open water and stable ice cover periods

and rate between the cross sections. Selecting the method of border ice simulation is based on the direct observations or experience/ interpretations of the user from the study site and varies between different simulation cases.

The second important feature that can be noticed in the cover thickness results is the significant difference between the ice cover thickness values upstream and downstream of the deployment site. As described before in section 4.1.1, simulation reach (Lower Nelson River) experiences two sets of different bed slopes before the estuary at the mouth of the Hudson Bay. Hence, different hydraulic conditions affect the cover, causing it to from in different cover thicknesses. Due to the relative similarity between the deployment location and upstream site in terms of ice thickness, they decayed at almost the same rate. However, the downstream cross section experienced completely different decay process both in terms of timing and value.

The other important feature showed in the figure is the formation and removal of mechanically thicken ice covers over the simulation sites presented in the figure, during the break-up period. These mechanical thickened ice covers are showed in the form of peaks in the ice cover thickness before the complete removal. It is notable that the ICESIMAT model is not capable of simulation of the ice-jam formation during the freeze-up and

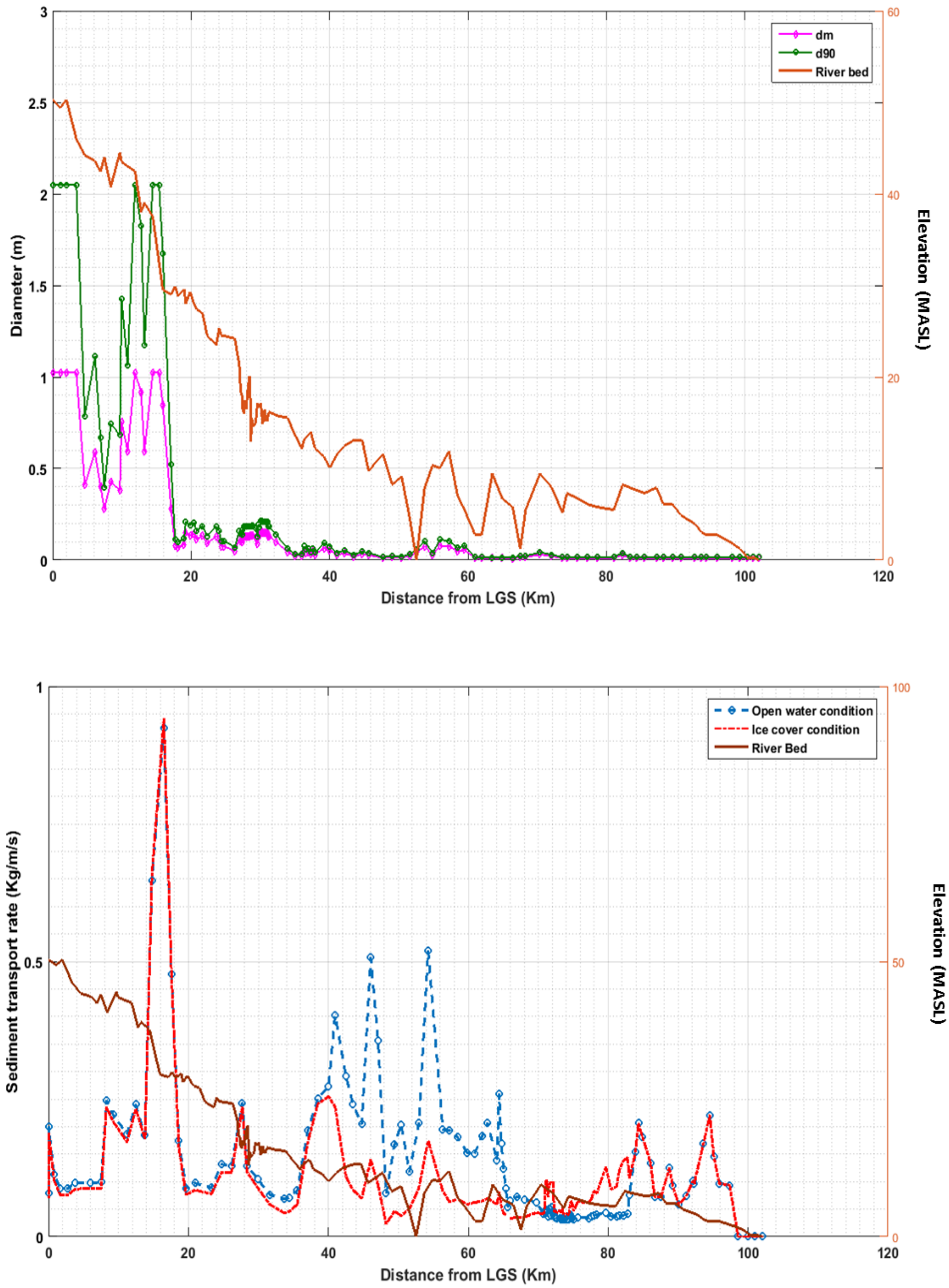

Figure 5.43: Representation of bed material size and distribution along the study reach (top) and simulated sediment transport rate during the open water and stable ice cover periods (bottom)

break-up periods and therefore, the calculated ice cover thickness during the break-up period is based on equilibrium cover thickness calculation.

This describes the reason that why even though the timing and duration of the peaks vary, the thickness values are almost identical. It is because, at the current stage, the ICESIMAT simulates the ice cover removal process using a series of equilibrium, steady ice cover formation at the sites where the open water emerges while the ice cover is still present in adjacent cross sections. As a results, the cover will thicken only to the thickness enough to resist the thrust forces at the time of simulation based on the ice volume available from upstream cross sections.

River hydraulic condition plays an important role in defining the stage and condition of the cover. It is particularly important in ice cover modeling since the model calculates the ice cover thickness based on the water velocity and elevation at each cross section. Figure 5.42 shows a comparison between the water velocity in all simulation cross sections during two stages of open water and ice covered conditions.

As shown in the figure, ICESIMAT calculates the water velocity during the ice cover period lower than open water period. These results show the model consistency with the theory in terms of ice cover on water velocity magnitudes and also match the field observations of velocity, ice bottom location and water surface elevation (refer to Figure 5.41 as well).

The simulated lower water velocities can be explained by the further resistance added to the stream on the top of the flow in places where the ice cover formed. However, higher simulated water velocities on upstream cross sections, beyond the cover extent, can be described as the results of higher water stages occurred due to the backwater effect from the downstream ice covered cross sections. Notably, the hydraulic simulation of ICESIMAT during the open water stages are also compared with HEC-RAS during the model calibration process (not shown here) and the results found to be almost identical.

According to the variation in water velocity i.e. shear stress, the sediment load estimation in the river is expected to be different between ice cover and open water conditions. As previously discussed and showed in sections 5.1.3 and 5.1.4, lower water velocities and shear stresses observed during the stable ice cover period cause the sediment load rate to diminish, except for the break-up period when the initiation and transport rate significantly increase due to the highly dynamic stages of flow and ice cover.

Figure 5.43 (top) shows the bed material distribution and sediment load estimation for the study reach during the open water condition as well as the ice cover period. Comparing the results, it easily can be seen that the sediment transport occurred at a lower rate at the study reach during the ice cover period. Two important points are to be remembered here in terms of presented sediment transport rate; first, the calculated sediment rate is based on the vanRijn method for suspended and Wilcock-Crowe method for bed load. Hence, the ICESIMAT at the current stage is developed for non-cohesive bed material through the suspended load calculations though a fairly wide range of methods is included for bed load estimation.

Second, the ICESIMAT is limited to a single model application for the calculation of bed load over the study reach even though the cross sections are quite different in terms of bed material size and distribution. As it can be seen in the figure, d_m and d_{90} of the bed material change from the scale of meters to fairly small values in terms of millimeters (from bolder/very large gravel to the particles in size of sand or smaller). This may cause some discrepancies and eventually inaccuracies in the estimation of sediment transport. Therefore, the calculated sediment transport rate, at the current version of the model, should be considered cautiously. However, based on the particle size and distribution at a specific cross section, the user can select the most appropriate method for bed load simulation. Applying the proper model for the bed load calculation based on the cross section material would increase the model accuracy.

Chapter 6

Conclusions

The aim of this thesis was to study and define the river ice processes and their influences on river hydraulics and sediment transport. To achieve this purpose we utilized acoustic techniques and instrumentation to perform field investigations on a regulated river in northern Manitoba, known as Lower Nelson River. Nelson River is the forth longest river in Canada and has been regulated by Manitoba Hydro since 1957 through 6 hydroelectric generation stations, four of which are located along the Lower Nelson River (downstream of lake Winnipeg to Hudson Bay). Lower Nelson River is well known for long and severe ice cover formation during the cold period of the year which emphasizes the importance of detailed and comprehensive studies of river hydraulics under such a condition. Considering the fact that at least 4 more hydroelectric projects are planned to be constructed on the reach studied in this thesis, the findings and results of this study can be well implemented for future projects.

Due to the remoteness of the study site, autonomous acoustic techniques found to be the most suitable and applicable approaches for this study. Furthermore, little has been found in the literature addressing the capabilities and limitations of this approach for the study of river ice and its associated consequences on stream flow. Thus, this study is interpreted to provide valuable experiences in the development of specific techniques for the application of acoustic techniques in ice covered rivers both in terms of investigations of river hydraulics and sediment transport studies.

Considering the main subjects of this thesis, two types of active sonars are selected to be deployed in the field investigations to record several parameters of ice cover formation and flow hydraulics through a time span from late fall to mid-summer at the deployment location. Acoustic Doppler Current Profiler (ADCP) is defined as the backbone of field investigations in this thesis while further information regarding the ice cover condition in time recorded using a Shallow Water Ice Profiling Sonar (SWIPS). Instruments deployed through 4 annual field campaigns at the study site in order to provide enough temporal window potentially covering the most ranges of the ice cover stages. Both of the instruments of this study are programmable and thus according to the objectives of the investigations at each year, were programmed.

The deployed instruments work on different frequencies which enabled us to monitor both river and ice in dual frequency improving our understandings of the ice cover and river hydraulics complications.

Recorded information was extracted and analyzed in order to study specific ice related issues in the river which improved the general understanding of riverine processes and interaction during the ice covered period.

Major findings of this study are summarized in a series of study subjects each described briefly in the following.

6.1 River ice formation

Using bi frequency approach for long term observation and measurement, the ice cover formation and evolution studied at the deployment site during the winters of 2012 to 2015. Ice cover formation, progression, stabilization and removal were observed and analyzed using the acoustic backscatter data. Appropriate techniques were selected and implemented in order to estimate the ice cover thickness as well as the stage. According to the analyzed information, different types of ice cover during various stages were distinguished and described in terms of their hydraulic characteristics . Results provided us important information about the specific hydraulic feature associated with different ice cover stages the form of acoustic backscattering. This enabled us to separate different and study each stage individually as well as in combination with other stages. This process, helped us to compare the ice cover formation theories with field measurements. Amongst all river ice cover stages, the important stage of the ice cover break-up period, including the transformation of the stable ice cover to ice floe/slush as well as the formation of ice jams, are well presented in data and results of the analysis.

6.2 River ice influence on flow velocity

As it is proven theoretically ice cover is expected to alter the velocity distribution in affected streams. This is because of the introduction of a new flow boundary to the top of the river during the stable ice cover period. Such a process was clearly observed in our study as well. Mean velocity magnitude was estimated to be lower during the stable ice cover period due to the additional resistance to the flow. However, study results demonstrated that the introduction of the freshet water as well as the mechanical thickening of the ice which results in the reduction in flow area and caused the flow to accelerate locally. Therefore, higher water velocities were observed at the deployment site when the ice cover experienced dynamic variations in thickness. This pattern was specifically intense in the years that the ice jam formed during the break-up period.

Velocity distribution also was observed to vary between open water condition and ice cover period as well as throughout different ice cover stages. A higher degree of curvature in the vertical velocity distribution was observed during the stable ice cover period compared to open water condition . Velocity gradient was also found to be directly related to the ice cover condition. We observed higher water velocity during the dynamic stage of break-up and more importantly during the ice jam formation.

6.3 Shear stress in ice covered streams

We believe that this is the first work that shows the estimation of shear stress imposed on the boundaries of an ice covered river especially during different ice stages. Results of this work helped us to better define the importance of the ice cover formation in shear stress distribution in ice covered rivers. The current study also proved the reliability and flexibility of acoustic methods for long-term and comprehensive hydraulic measurements.

Results clearly showed the effects of different ice cover stages in relation to shear stress magnitudes on river boundaries. These findings helped us to expand our understanding of river hydrodynamics during the ice cover period. Results demonstrated that the bed shear stress during the ice cover period is less than during the open water condition which proves that the upper boundary layer presence has a diminishing effect on bed shear stress. Average estimated bed shear stress increases during break-up to (2.00 N/m^2) comparing to the stable ice cover (1.51 N/m^2) and reaches a maximum during open water condition (2.04 N/m^2).

Based on the analysis results, we showed that the shear stress on the upper boundary layer experiences drastic variation in different stages. Higher variation was observed in shear stress on ice undersurface during stable ice cover than break-up period (excluding ice jam). This is interpreted to be mainly due to frazil ice deposition and erosion during the low and high velocity diurnal cycles based on hydro-peaking. Results also provided more clear aspects of ice cover existence and its spring break-up effects on channel systems which can be utilized in numerical modeling of the ice covered streams, ice cover propagation and recession, sediment transport especially in covered or semi covered streams and other environmental aspects such as riparian biota.

6.4 River Ice influence on stream conveyance capacity

The current research includes a field estimation of hydraulic resistance in an ice-covered flow. To the extent of our knowledge, this study can be categorized as a first attempt in several aspects. For the first time, boundary resistance was estimated in an ice-covered river using continuous direct measurements of river hydraulic characteristics such as velocity profiles and water depth. The log-law was used for velocity profiles in the ice and bed zones to estimate the ice and bed roughness values. The measurements were conducted on a regulated river subject to hydropeaking operations, which resulted in diurnal cycling of flow depths and velocities. The measurements were performed for different ice stages including stable ice cover and the very dynamic stages of breakup and river ice jam formation and release. Very high values of under ice roughness were observed during the ice jam, and high water velocities were observed during breakup. Variation of under ice roughness was analyzed, leading to the supposition that ice deposition and erosion occurred during the stable ice cover period as a result of flow variations induced by hydropeaking. Commonly employed assumptions about ice and bed zone velocity values, hydraulic radii and energy grade line slopes were demonstrated to be highly sensitive to the local flow condition. Consequently, common methods for estimation of the composite hydraulic resistance were found to be inadequate under a range of ice-covered conditions.

Finally a theoretical formulation for total composite resistance was developed based on the field measurements in order to calculate the boundary roughness. The proposed formulation was tested and demonstrated to provide accurate estimations of composite resistance compared to available approaches.

6.5 Turbulence structures in ice affected streams

Turbulence mixes water through the entire depth and thus plays an important role in the process of ice cover formation in rivers. This is mainly by affecting the process of super cooling which alters the heat transfer from water to the atmosphere as well as transporting the frazil nuclei deeper in to the water. On the other hand, turbulence applies stress to the flow boundaries and thus is expected to affect the sediment initiation and transport. Presence of the ice cover on top of the river changes the river hydraulic characteristics mainly by affecting the velocity distribution. Consequently, the turbulence parameters are expected to be influenced by the presence of the ice cover. Different ice stages have differing effects on flow hydraulics, therefore it is reasonable to anticipate different levels of turbulence during various stages of the ice cover.

Understanding of the turbulence structures, hence, is an important step to clarify the ice cover effects on rivers. Therefore the topic was planned to be a part of this study. For this purpose, during the winters of 2012-13 and 2014-15, ADCP was programmed to acquire proper data (in terms of frequency of recordings) required for turbulence analysis. The obtained data covered the main stages of the ice cover (freeze-up, stable cover, break-up) and the open water condition as well. ADCP data were extracted and analyzed to study the turbulent structures in ice covered streams. Reynolds stress magnitude and distribution were the subject of a particular interest in this research. Variation in Reynolds stress magnitude helped us to better define the effect of ice cover condition on turbulent flow characteristics. Reynolds stress distribution also followed the theoretical pattern that is expected for the fully developed flow between parallel boundaries. Reynolds stress tensor was also calculated and analyzed during different ice cover stages as well.

6.6 Sediment transport in ice covered rivers

Variation in water velocity and shear stress has a direct effect on sediment load and transport rate in the ice covered rivers.

Lower shear stress and water velocity during the stable ice cover period reduce the sediment initiation into the flow and the sediment transport rate. We observed lower suspended sediment load during the stable ice cover period compared to the open water condition which is consistent with developed theories and previous studies. However, during the break-up period, acoustic backscatter intensity increased, presumably due to increased suspended sediment concentration. This is mainly due to the significantly higher water velocity and shear stress during the break-up period. The same effect on bed load is also expected for ice cover period. Since the shear power of flow is applied on two surfaces on the top and the bottom, the shear stress on the bed is expected to decrease during the stable ice cover period. It is notable that no direct measurement is performed on bed load in this study. Sediment load measurements were only restricted to the acoustic backscatter analysis therefore only represents the suspended load.

6.7 Numerical simulation of ice cover formation and removal

We improved an existing river ice simulation model in this research. The dynamic river ice simulation model, ICESIM, developed by Hatch was the main subject of this improvement. The ICESIM model is a steady state, one dimensional model originally developed and compiled in Fortarn. We changed the programming language of the model to Matlab in order to provide more flexible programming platform for future developments. Model conversion and calibration performed as the initial steps of numerical simulation of the river ice processes in Nelson River.

As the second major improvement to the model, we introduced new subroutines to the model in order to simulate the river ice cover during the break-up period majorly for the simulation of ice cover thermal decay and mechanical break-up. It is notable that very dynamic stage of ice jam formation and removal is not included in the model at the current stage. Instead, the model accounts for the cover retreat and removal in the form of thermal decay and equilibrium mechanical cover thickness. It is notable that though simulation of ice cover retreat is considerable improvement to the model, it is yet far from the non-equilibrium state of ice jams formation during the break-up period.

The third important improvement of the model was the addition of the capability of sediment transport simulation to the model. The newly added sediment transport subroutine accounts for suspended and bed load simulation though the non-cohesive model of vanRijn for suspended load and series of bed load simulation models comprehensively described in section 3.4.4.

As a final improvement, a graphical user interface was designed and developed for the model in order to provide a graphical interaction for the model. The designed GUI makes the simulation and post processing more interactive and convenient.

6.8 Future perspectives

In terms of future perspectives for this study, multiple objectives can be defined in several aspects. The primary objective for future works is to expand the spatial extents of the study to several locations in the river. Such an effort improves our understanding of river ice dynamics in Lower Nelson River. Furthermore, due to the high correlation between the stream geometry and ice cover condition, different processes of ice cover formation and the effect of flow geometry on them can be studied.

Meanwhile, we are interested to further investigate the application of the bi-frequency technique to study the ice cover physical characteristics during the cover progression, namely the cover density. The same technique looks to be applicable for the study of the nature of the slush ice and its hydraulic characteristics. Flow hydraulics during the slush ice period is also a potential field of further investigations. Slush ice movement also can be studied theoretically and be validated based on findings of the field investigations. Application of sheet flow concept seems to be promising in slush ice flow under the existing ice cover.

Secondly, this work can be extended in terms of numerical simulation of fluid dynamics in presence of ice cover. For this purpose, river ice processes, in micro scale, can be simulated using available computational fluid dynamic models. In this field, simulation of frazil ice and its evolution into the ice pans, as well as the movement of the ice pans and ice floes are the considerable subjects for further investigations. Numerical simulation software such as OpenFOAM and Smooth Particle Hydrodynamic (SPH) software such as SPHyics are potentially applicable for this task.

Another notable perspective of this work is the investigation of climate change influence on ice regimes in northern rivers. The combination of approaches for climate change investigations and numerical modeling of river ice is likely to reveal interesting aspects of river ice effects on winter flow regime in rivers. The immediate effect of climate change on river ice can be expected to be the appearance of frequent, premature break-up events during early winter time which can lead to freeze-up ice jam formations and releases.The process potentially can cause several floods during the early winters with a flood severity to be determined.

The last immediate perspective of this study is the further improvement of the developed model i.e. ICESIMAT to increase the applicability and flexibility of the model. In this perspectives, the subjects can be defined as performance improvements and enhancement of model conceptual capabilities.

The performance improvements of the model can be addressed as further improvements of ICESIMAT graphical user interface to incorporate the input data in a more efficient manner which facilitates the model application for consecutive simulations.

The other important improvement in the performance area is the addition of the auto-calibration capability to the model. We would like to add extra algorithms to the model to enable the model to modify the calculation parameters and calibrate itself. Such a process increases the model accuracy and decreases the computational cost of the numerical simulation.

In terms of conceptual improvements, the main subject is to add the ice jam simulation capability to the model. This improvement, not only increases the model flexibility for simulation of different ice stages, but is expected to increase the model simulation accuracy during the pre break-up stages significantly. Similarly, more precise simulations of flow hydraulics result in higher accuracy level in sediment transport simulations.

This study highlights the capabilities of acoustic techniques in river and ice investigations in remote study sites. Acoustic instruments, operating in different frequencies can provide considerable range of information enabling us to further increase our understanding of river ice influences on several aspects of river hydraulics and river morphology. Findings of this study emphasizes the significant influence of river ice cover formation and presence on river hydraulics and sediment transport and accentuates the special attention to the phenomenon in theoretical and practical studies related to river hydraulics and sediment transport.

Appendices

Appendix A

Energy Equations (*Bernoulli* Principal)

A.1 Backwater profile determination Using Standard Step Method

ICESIMAT applies Standard Step Method for back water profile determination at unknown cross sections using the hydraulic information at adjacent cross section. Energy equation in two hypothetical cross section can be presented as:

$$z_2 + y_2 + \alpha_2 \frac{V_2^2}{2g} = z_1 + y_1 + \alpha_1 \frac{V_1^2}{2g} + h_f + h_e \tag{A.1}$$

in which $z_i$is the bottom elevation, y_i is the flow depth at the cross section, α_i is the Coriolis coefficient, V_i is the water velocity at the cross section, h_f is the energy loss due to friction, $h_e$is the energy loss due to eddies and g is the gravity acceleration.

Energy loss due to friction can be written as the function of average slope of energy grade line and distance between tow cross sections:

$$h_f = \bar{S}_f \Delta x = 1/2\ (S_{f_1} + S_{f_2})\Delta x \tag{A.2}$$

Energy grade line slope can be expressed as:

$$S_f = \frac{n^2 Q^2}{A^2 R^{(4/3)}} \tag{A.3}$$

In this equation, n is the Manning roughness coefficient, Q is the flow discharge, A is the cross section area and R is the hydraulic radius.

Energy loss due to flow eddies can be calculated as:

$$h_e = C_e \left| \frac{\alpha_1 V_1^2 - \alpha_2 V_2^2}{2g} \right| \tag{A.4}$$

in which the C_e is the transition coefficient.

Assuming the h=y+z and H=h+$\alpha\frac{V^2}{2g}$, equation A.1 can be presented as:

$$H_2 = H_1 + h_f + h_e \tag{A.5}$$

Equation A.5 can be solved using trial and error process.

Henderson (1989) suggested following method to adjust H_2 value for i+1^{th} iteration based on the i^{th} iteration:

$$H_E = [H_2 - (H_1 + h_f + h_e)] \tag{A.6}$$

The H_E value can be minimized by changing the y_2 value:

$$\frac{dH_E}{dy_2} = \frac{d\ [y_2 + z_2 + \alpha_2\frac{v_2^2}{2g} - y_1 - z_1 + \alpha_1\frac{v_1^2}{2g} - 1/2\Delta x(S_{f_1} + S_{f_2}) - C_e\left|\frac{\alpha_1 V_1^2 - \alpha_2 V_2^2}{2g}\right|]}{dy_2} \tag{A.7}$$

In the equation above, y_1,z_1,z_2 and v_1 are constant values, so equation A.7 can be shown as:

$$\frac{dH_E}{dy_2} = \frac{d\ [y_2 + (1 + C_e)\alpha_2\frac{v_2^2}{2g} - 1/2\Delta x(S_{f_1} + S_{f_2})]}{dy_2} = \frac{d}{y_2}\ y_2\ + \frac{d}{y_2}\ ((1 + C_e)\alpha_2\frac{v_2^2}{2g}) \tag{A.8}$$

$$-\frac{d}{y_2}\ (1/2\Delta x(S_{f_1} + S_{f_2})) = 1 - 1/2\Delta x\frac{dS_{f_2}}{dy_2} + (0(\alpha_2\frac{v_2^2}{2g}) - \frac{\alpha_2}{2g}(\frac{d}{dy_2}((\frac{Q^2}{A_2^2})(1 + C_e)) =$$

$$1 - 1/2\Delta x\frac{dS_{f_2}}{dy_2} - (1 + C_e)\frac{Q^2\frac{dA_2}{dy_2}}{gA_2^3}$$

Assuming $\frac{dA_2}{dy_2} = T_2$, it is possible to re write equation A.8 as:

$$\frac{dH_E}{dy_2} = 1 - 1/2\Delta x\frac{dS_{f_2}}{dy_2} - (1 + C_e)\frac{Q^2 T_2}{gA_2^3} \tag{A.9}$$

for a rectangular channel : $\frac{dS_{f_2}}{dy_2} = -\frac{3.33\ S_{f_2}}{R_2}$

Appendix B

ICESIMAT Subroutines

The ICESIMAT river ice engineering simulation model is composed of a GUI file (ICESIMAT) which loads input file, runs the main file of ICESIMAIN and presents and save the results of the simulation. ICEMAN utilizes subroutines to perform individual simulation tasks.

The subroutines which perform a given function are grouped into modules which are as follows:

- **INOUT**

  reads in data , echoes pertinent data and generates processed cross section file.

- **INCONV**

  contains subroutine INOUT and subroutine CONV which adjusts conveyance for variable n values when dummy values (n=1.0) are used in cross section data set.

- **BKW**

  contains the subroutine for computing the backwater profile of the channel under open water and/or ice cover conditions using standard step method. In addition, the subroutine estimates the extent of border ice cover and remaining open water area available for ice generation.

- **COEFF**

  contains subroutines to calculate conveyance curves (top width, area, wetted perimeter, critical depth, etc.) from cross section data file.

- **CURVES**

  collection of interpolation functions.

- **DPOSIT**

  simulates the deposition of a volume of ice under an existing cover.

- **ERODE**

  simulates the erosion of the underside of the ice cover.

- **ICEGEN**

  calculates the rate of ice production (volume) using mean daily air temperatures and open water area.

- **PACK**

  subroutine which computes ice thickness for ice cover progression by packing.

- **PROGRS**

  contains subroutine which determines if ice front can progress to the next cross section upstream by the juxtaposition process based on hydraulic pararmeters.

- **RESULT**

  output subroutine which summarizes the simulation results at specific intervals based on time or ice from location.

- **SHOVE**

  contains subroutine which determines ice cover internal strength and simulates a shove if total forces exerted on ice cover exceed the covers maximum internal resistance.

- **TIMEDAY**

  determines the cumulative Degree Days of freezing.

- **VOLUME**

  subroutine which computes volume of ice cover between cross sections.

Appendix C

ADCP and SWIPS Setting

ADCP

Instrument S/N: 13264

Frequency: 1228800 HZ

Configuration: 4 BEAM, JANUS

Match Layer: 10

Beam Angle: 20 DEGREES

Beam Pattern: CONVEX

Orientation: UP

Sensor(s): HEADING TILT 1 TILT 2 DEPTH TEMPERATURE PRESSURE

Parameters (2012)

CF11101	Flow control (default)
EA0	Heading alignment (Default)
EB0	Heading bias (default)
ED0	Transducer depth
ES0	Salinity
EX11111	Coordinate transform (Default)
EZ1111101	Sensor sources (Default)
WD111100000	Data Out (Default)
WF44	Blank Distance
WN79	Number of depth cells
WP50	Pings per ensemble
WS25	Depth cell size

WV175	Ambiguity velocity (cm/s)
TE00:07:30.00 (hh:mm:ss.ff)	Time per ensemble
TP00:09.00 (mm:ss.ff)	Time between pings

Parameters (2013 and after)

CF11101	Flow control (default)
EA0	Heading alignment (Default)
EB0	Heading bias (default)
ED0	Transducer depth
ES0	Salinity
EX11111	Coordinate transform (Default)
EZ1111101	Sensor sources (Default)
WD111100000	Data Out (Default)
WF25	Blank Distance
WN59	Number of depth cells
WP2	Pings per ensemble
WS25	Depth cell size
WV175	Ambiguity velocity (cm/s)
TB00:30:00.00	Time per burst
TC165	Ensemble per burst
TE00:00:01.00 (hh:mm:ss.ff)	Time per ensemble
TP00:00.50 (mm:ss.ff)	Time between pings

SWIPS

	Phase One	**Phase Two**	**Phase Three**	**Phase Four**
Acquisition Period	03/17- 04/11	04/11-05/11	05/11-06/10	06/10-cont.
Duration	25 days	30 days	30 days	30 days
Phase Type	Normal	Normal	Normal	Normal
Ping Period	30 seconds	3 seconds	2 seconds	1 seconds
Pings Per Profile	5 pings	10 pings	15 pings	15 pings
Collection time	150 sec.	30 sec.	30 sec.	15 sec.
Profile Interval	600 sec.	300 sec.	180 sec.	180 sec.
Frequency	546 kHz	546 kHz	546 kHz	546 kHz
Digitization rate	64 kHz	64 kHz	64 kHz	64 kHz
Gain	1	1	2	3
Pulse Length	$150\mu.s$	$150\mu.s$	$150\mu.s$	$150\mu.s$
Range	24.98 meters	24.75 meters	24.98 meters	24.75 meters
Lock Out	0	0	0	0
Range Averaging	0.01 meters	0.01 meters	0.01 meters	0.01 meters

Appendix D

ICESIM Cross section Geometry Information(XSECDATA.PRO)

Cross Section Name **500**	Elevation	Area	Conveyance	Top Width	Critical Discharge	Ice Conveyance
	0	0	0	518	0	0
	1.0526	910.4049	755.6664	1203.769	2478.526	467.8875
	2.1053	2545.648	2885.918	2108.506	8756.348	1803.627
	3.1579	4818.048	8200.003	2169.255	22478.35	5130.733
	4.2105	7104.857	15633.27	2175.682	40192.81	9803.958
	5.2632	9398.431	24868.4	2182.109	61060.15	15614.13
	6.3158	11698.77	35745.69	2188.537	84673.3	22460.44
	7.3684	14005.88	48151.61	2194.964	110755.4	30271.33
	8.4211	16319.75	61999.64	2201.391	139102.4	38992.3
	9.4737	18640.38	77220.77	2207.818	169556.2	48579.91
	10.5263	20967.79	93758.13	2214.246	201989.6	58998.41
	11.5789	23301.95	111563.8	2220.673	236297.6	70217.65
	12.6316	25642.89	130596.5	2227.1	272391.5	82211.74
	13.6842	27990.59	150820.4	2233.528	310195.4	94958.12
	14.7368	30345.05	172203.7	2239.955	349643.3	108436.9
	15.7895	32706.28	194777	2246.382	390759	122664.9
	16.8421	35074.28	218544.5	2252.81	433541	137645
	17.8947	37449.04	243462.6	2259.237	477919.3	153349
	18.9474	39830.56	269716.1	2265.664	524164.9	169894.7
	20	42218.86	297047.2	2272.091	571903.7	187120.1

Appendix E

ICESIMAT Input Variables

Card No.	Variable Name	Description	Variable Type
1	TITLE	Title of job.	Char
2	NSEC	Number of cross sections in run.	I
	CHAIN1	Actual chainage at downstream section (km).	R
	NFLWS	Number of values in inflow hydrograph (maximum of 20 can be specified).	I
	NTWLS	Number of values in tailwater hydrograph (maximum of 20 can be specified).	I
2a	DDQ(I)	Time entry for flow in hydrograph (days)	R
	QDAY(I)	Associated flow (m^3/s).	R
2b	DDTW(I)	Time entry for tailwater hydrograph (days)	R
	TWL(I)	Associated tailwater level (m).	R

Note: This option can be used to simulate the changes in river flow throughout the course of the winter.

Note: Repeat Card 2A NFLWS times and card 2B NTWLS times.

3	IPRINT	Output trigger whenever number of sections ice cover advance $\geq$IPRINT.	I

	DPRINT	Output trigger whenever distance ice cover advances ≥DPRINT (m).	R
	TPRINT	Output trigger whenever change in time between output ≥JPRINT (day).	R
	IDEB	DEBUG trigger 0 for no echo 1 for echo (appears in output file) gives a record of all subroutines called.	I
	IDEB	Debug code (0-off, 1 or 2).	I
	DEBT1	Time 1 for debug.	R
	DEBT2	Time 2 for debug.	R
	IDEBS1	Section 1 for debug.	I
	IDEBS2	Section 2 for debug.	I
4	DAYST	Starting day.	R
	DAYEND	Ending day.	R
5	VMAX	Maximum allowable velocity at which ice is deposited under an ice cover (m/s).	R
	VERODE	Erosion velocity (m/s).	R
	SMX	Maximum slope (warning if BKW gradient is >SMX).	R
	VGRAD	Maximum volume of ice deposited in on call to DPOSIT (m^3).	R
	VRED	Option to modify VMAX for all cross sections upstream of ISECT	R
	ISECT	Cross section upstream of which VRED will be adopted for maximum deposition velocity	I
6	NAO	Number of values in upstream open water variable relationship (Maximum of 20)	I

	NAODAY (I)	Day for open water area "hydrograph"	I
	AOWUS (I)	Open water area upstream of upstream boundary section on day NAODAY (m^2).	R
	Note:	Repeat Card 6 NAO times.	
7	COHSN	Cohesion of ice to riverbank (Pa).	R
	COHSNTH	Cohesion of thermal ice to riverbank (Pa).	R
	COHSNPK	Cohesion of packed ice to riverbank (Pa).	R
	TCZERO	Time in days for ice to reach full cohesion (CONSN) after forming a leading edge.	R
8	NSTH	Thermal ice section number (Upstream Limit).	I
	TLAKE	Thermal ice thickness (m).	R
	ENLAKE	Manning's 'n' roughness of thermal ice.	R
	RAISE	Nominal increases in downstream water level when ice is passed beyond boundary (m).	R
9	NPKSTRT	Section number at downstream extent of packing.	I
	NPKSTP	Section number at upstream extent of packing.	I
	ENPACK	Manning's 'n' roughness of pack ice.	R
10	NREAL	Code which determines roughness value 0 - dummy n-1.0 values used to process data (prefered) 1 - actual n value used to process data.	I
	IWINTER	Code which indicates daily time series 0 - daily air temperatures 1 - daily volume of ice	I
	NCALOW	Open water or ice run (0 - open water, 1-ice).	I

	ACCUR	Tolerance of backwater convergence (m).	R
11	FRCRIT	Critical Froude number.	R
	KBANK	$K_1 \tan \Phi$.	R
	KICE	Coefficient analogous to Rankine's passive soil coefficient, K_2.	R
	FUNIT	Wind drag force (Pa).	R
	DICE	Average content of ice in ice cover (kg/m^3).	R
11AA	NFR	Number of sections with a variable critical Froude number.	I
11AB	NNFR	Section number.	I
	FRNEW	New critical Froude number.	R
	Note:	Repeat Card 11AB NFR times.	
12	NSILT	Number of sections having a shift in cross section invert.	I
Note:	Data for Card 13 required only if NSILT >0. Repeat Card 13 NSILT times.		
13	NSIL	Cross section number.	I
	SIL	Datum shift amount.	R
14	ISTOBORD	Code which indicates method of border Ice Generation. (0) Uses coefficient MCOEF in border ice equation. (Initial border ice determined by degree day of freezing relationship). (1) Uses border ice factor which is a relationship between degree days of freezing and fraction of border ice area and is common for all sections. (2) Same as (1), but each section is identified with its own relationship. (3) Uses an initial input fraction of border ice, with additional growth generated by border ice equation.	I

Note: Data for 14A required only if Istbord = 0 or 3.

14A	MCOEF	Coefficient in border ice equation.	R

Note: Data for 14B required only if Istbord = 3.

14B	XSECB	Cross section number.	I
	BORDINT	Fraction of border ice area.	R

Card 14B repeated NSEC times.

Note: Data for Cards 15 and 16 required only if ISTBORD = 1 or 2.

15	NPBI	Number of points in degree-days/fraction of open water area relationship.	I
16	DD	Degree Days.	R
	PBIA	Fraction of open water area.	R

Note: Cards 15 and 16 are repeated NSEC times and Card 16 repeated NPBI times (after each Card 15) except when ISTBORD = 1, then Cards 15 and 16 are done once with Card 16 repeated NPBI times.

17	NUMSW	Number of section with varying open water or ice roughness.	I
	VNCHAN	Manning's 'n' roughness of channel at downstream section.	R
	VNICE(1)	Manning's 'n' roughness of ice at downstream section for 5 m ice thickness.	R
	VNN2(1)	Manning's 'n' roughness of ice at downstream section for 0.1 m ice thickness.	R
	VKRN	Ice roughness reduction factor varies between 0.005-0.050.	R

Note: Data for Card 18 required only if NUMSW >0. Card 18 repeated NUMSW times.

18	NSWITCH	Cross section number.	I
	VNCHAN	Manning's 'n' roughness of channel at section NSWITCH.	R
	VNICE	Manning's 'n' roughness at section NSWITCH for 5 m ice thickness.	R
	VNN2	Manning's 'n' ice roughness at section NSWITCH for 0.1 m ice thickness.	R

Note: The roughness characteristics will remain as that specified in Card 18 for all sections upstream of NSWITCH, until adjusted by a new set of roughness characteristics for sections specified further upstream.

18A	NSHRGH	Code which indicates if ice roughness will be reset to initial roughness if a shove occurs at a section 0 - Reset ice roughness 1 - Not reset ice roughness.	I
	NDPRGH	Code which indicates if ice roughness will be reset to initial roughness if deposition occurs at a section 0 - Reset ice roughness 1 - Not reset ice roughness.	I
19	NOBSTER	Number of obstructions.	

Note: Data for Card 20 required only if NOBSTER >0. Card 20 is repeated NOBSTR times.

20	NA	Cross section number.	I
	DISTADD	Additional shoreline distance (due to island etc.) (m).	R
	BFACTOR	Reduction in ice forces to account for grounding of ice etc.	R

Note: Data for Cards 21, 22 and 23 required only if NCALOW-1.

Note: Data for Card 21 and 22 is required only if IWINTER = 0 or 2. Card 21 and 22 is repeated from day DAYST to day DAYEND, maximum 10 values per line.

20A	TEMPEND	Day to which temperature and volume data are entered.	I
21	TEMP	Daily air temperature (°C).	R

Note: Data for Card 21, temperature data for days prior to DAYST may be input, which will allow cumulative degree days of freezing to be calculated for initial starting conditions. If this is not required, then temperature data should start with DAYST.

22	TAILTMP	Daily upstream water temperature (0°C).	R

Note: Upstream water temperature is used to simulate starting upstream inflow which is slightly above 0°C. This will reduce the effective open water area which is capable of generating ice. If these conditions are not present, enter an initial upstream water temperature of 0°C. TAILTMP $\geq$ 0°C.

23	VOLADD	Daily ice inflow volume to study area (m^3).	R

Appendix F

Lower Nelson River Flow Data

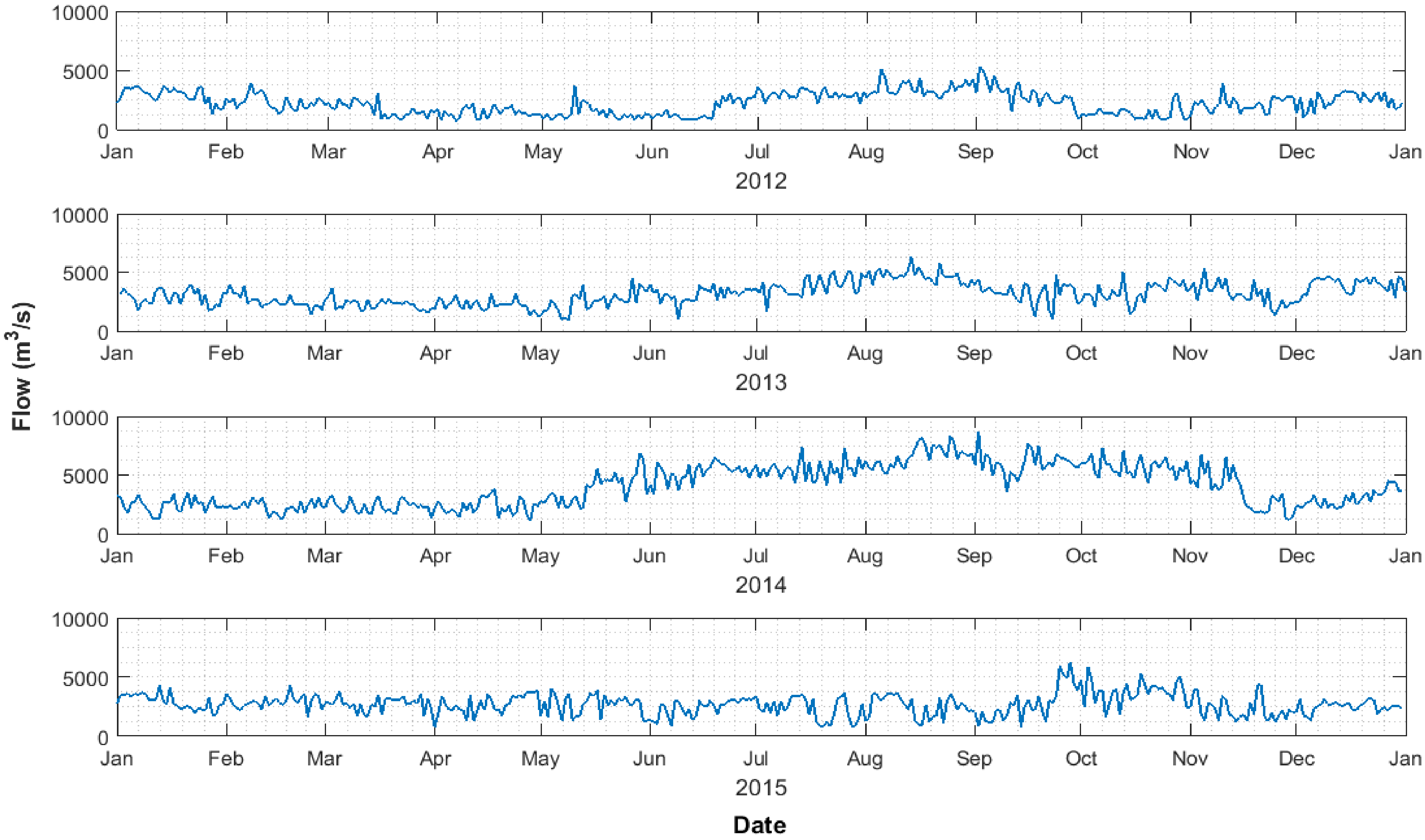

Lower Nelson River flow discharge data (daily averaged), 2012-2015 based on values recorded at Limestone Generating Station

References

Peter Ackers and William R White. Sediment transport: new approach and analysis. *Journal of the Hydraulics Division*, 99(hy11), 1973.

Hossein Afzalimehr and Colin D Rennie. Determination of bed shear stress in gravel-bed rivers using boundary-layer parameters. *Hydrological sciences journal*, 54(1):147–159, 2009.

Monty E Alford, Eddy Clark Carmack, et al. *Observations on ice cover and streamflow in the Yukon River near Whitehorse during 1984/85*, volume 155. IWD, 1987.

WJ Altberg. Twenty years of work in the domain of underwater ice formation (1915–1935). *International Association of Scientific Hydrology*, 6:373–407, 1936.

David D Andres and PG Van der Vinne. Calibration of ice growth models for bare and snow covered conditions: a summary of experimental data from a small prairie pond. In *11th workshop on river ice: River ice processes within a changing environment. CGU HS Committe on River Ice Proccesses and the Environment (CRIPE)*, 2001.

DD Andres and G Van der Vinne. Effects of climate change on the freeze-up regime of the peace river. In *Ice in surface waters. Proceedings of 14th International Symposium on Ice*, pages 27–31, 1998.

ED Andrews and Gary Parker. Formation of a coarse surface layer as the response to gravel mobility. *Sediment Transfer in Gravel-Bed Rivers. John Wiley & Sons New York. 1987. p 269-300, 13 fig, 37 ref. U. S. E. P. A. Grant*, 1987.

R Andrishak and F Hicks. Simulating the effects of climate change on the ice regime of the peace river. *Canadian Journal of Civil Engineering*, 35(5):461–472, 2008.

L. Anselin. Local indicators of spatial association-lisa. *Geographical Analysis*, 272:93–115, 1975.

RS Arden and TE Wigle. Dynamics of ice formation in the upper niagara river. In *International Symposium on the Role of Snow and Ice in Hydrology, Banff, Alberta: UNESCO-WMO-IHAS*, volume 2, pages p1296–1313, 1972.

George D Ashton. *River & Lake Ice Engineering.* Water Resources Publication, 1986.

RP Asvall. Frazil formation causing flooding. In *Ice in surface waters: proceedings of the 14th International Symposium on Ice*, pages 27–31, 1998.

RA Bagnold. An approach to the sediment transport problem. *General Physics Geological Survey, Prof. paper*, 1966.

RA Bagnold. An empirical correlation of bedload transport rates in flumes and natural rivers. In *Proceedings of the Royal Society of London A: Mathematical, Physical and Engineering Sciences*, volume 372, pages 453–473. The Royal Society, 1980.

Harry Hawthorne Barnes. *Roughness characteristics of natural channels.* US Government Printing Office Washington, DC, 1967.

Howard Turner Barnes. *Ice engineering.* Renouf Publishing Company, 1928.

Jane Bauer and Seelye Martin. A model of grease ice growth in small leads. *Journal of Geophysical Research: Oceans (1978–2012)*, 88(C5):2917–2925, 1983.

S Beltaos. A conceptual model of river ice breakup. *Canadian Journal of Civil Engineering*, 11(3):516–529, 1984.

S Beltaos. Ice jam processes, 1995a.

S Beltaos. Onset of river ice breakup. *Cold Regions Science and Technology*, 25(3):183–196, 1997.

S. Beltaos. *River ice break-up.* Water Resources Publications, Highlands Ranch, CO, 2008a.

S. Beltaos. Extreme sediment pulses during ice breakup, saint john river, canada. *Cold Regions Science and Technology*, 128:38–46, 2016.

S Beltaos, Arnold M Dean, and HARZA-EBASCO Susitna Joint Venture. *Field investigations of a hanging ice dam.* 1981.

S Beltaos, DJ Calkins, LW Gatto, TD Prowse, S Reedyk, GJ Scrimgeour, and SP Wilkins. Physical effects of river ice. *Environmental impacts of river ice. National Hydrology Research Institute, Saskatoon, Saskatchewan, Canada*, pages 12–15, 1993.

S Beltaos, BC Burrell, and S Ismail. Ice and sedimentation processes in the saint john river, canada. In *Proc., 12th Int. Association for Hydraulic Research Symposium on Ice. Norwegian Institute of Technology, Trondheim, Norway*, pages 11–21, 1994.

Spyridon Beltaos. River ice jams: Theory, case studies, and applications. *Journal of Hydraulic Engineering*, 109(10):1338–1359, 1983.

Spyros Beltaos. *River ice jams.* Water Resources Publication, 1995b.

Spyros Beltaos. Advances in river ice hydrology. *Hydrological processes*, 14(9):1613–1625, 2000.

Spyros Beltaos. Hydraulic roughness of breakup ice jams. *Journal of Hydraulic Engineering*, 127(8):650–656, 2001.

Spyros Beltaos. Collapse of floating ice covers under vertical loads: test data vs. theory. *Cold Regions Science and Technology*, 34(3):191–207, 2002a.

Spyros Beltaos. Effects of climate on mid-winter ice jams. *Hydrological Processes*, 16(4): 789–804, 2002b.

Spyros Beltaos. Numerical modelling of ice-jam flooding on the peace–athabasca delta. *Hydrological Processes*, 17(18):3685–3702, 2003.

Spyros Beltaos. River ice breakup processes: recent advances and future directions. *Canadian Journal of Civil Engineering*, 34(6):703–716, 2007.

Spyros Beltaos. Progress in the study and management of river ice jams. *Cold Regions Science and Technology*, 51(1):2–19, 2008b.

Spyros Beltaos. River flow abstraction due to hydraulic storage at freezeup. *Canadian Journal of Civil Engineering*, 36(3):519–523, 2009.

Spyros Beltaos. Developing winter flow rating relationships using slope-area hydraulics. *River Research and Applications*, 27(9):1076–1089, 2011.

Spyros Beltaos. Mackenzie delta flow during spring breakup: uncertainties and potential improvements. *Canadian Journal of Civil Engineering*, 39(5):579–588, 2012.

Spyros Beltaos and Brian C Burrell. Climatic change and river ice breakup. *Canadian Journal of Civil Engineering*, 30(1):145–155, 2003.

Spyros Beltaos and Brian C Burrell. Water temperature decay under breakup ice jams. *Cold regions science and technology*, 45(3):123–136, 2006.

Spyros Beltaos and Brian C Burrell. Ice-jam model testing: Matapedia river case studies, 1994 and 1995. *Cold Regions Science and Technology*, 60(1):29–39, 2010.

Spyros Beltaos and Tom Carter. Field studies of ice breakup and jamming in lower peace river, canada. *Cold Regions Science and Technology*, 56(2):102–114, 2009.

Spyros Beltaos and Terry D Prowse. Climate impacts on extreme ice-jam events in canadian rivers. *Hydrological Sciences Journal*, 46(1):157–181, 2001.

Spyros Beltaos and R Roswell. Field study of pre-breakup river waves. In *Proc. 11th Workshop on River Ice, Ottawa*, pages 4–17, 2001.

Spyros Beltaos and Patrick Tang. Applying hec-ras to simulate river ice jams: snags and practical hints.

Spyros Beltaos and Jonathan Wong. Downstream transition of river ice jams. *Journal of Hydraulic Engineering*, 112(2):91–110, 1986.

Spyros Beltaos, Brian C Burrell, and Lindon Miller. A study of the interaction of ice and bridges: Southwest miramichi river, new brunswick. In *Proceedings, 15th Canadian Hydrotechnical Conference*, 2001.

Spyros Beltaos, Brian C Burrell, Lindon Miller, and David Sullivan. Hydraulic interaction between ice and bridges. In *Proc., 12th Workshop on the Hydraulics of Ice Covered Rivers*. CGU-HS Committee on River Ice Processes and the Environment Edmonton, Canada, 2003a.

Spyros Beltaos, Sayed Ismail, and Brian C Burrell. Midwinter breakup and jamming on the upper saint john river: a case study. *Canadian Journal of Civil Engineering*, 30(1): 77–88, 2003b.

Spyros Beltaos, Patrick Tang, and Robert Rowsell. Ice jam modelling and field data collection for flood forecasting in the saint john river, canada. *Hydrological Processes*, 26(17):2535–2545, 2012.

Arthur C Benke and Colbert E Cushing. *Rivers of North America*. Academic Press, 2011.

Sylvain Biancamaria, Paul D Bates, Aaron Boone, and Nelly M Mognard. Large-scale coupled hydrologic and hydraulic modelling of the ob river in siberia. *Journal of Hydrology*, 379(1):136–150, 2009.

Peter A Bieniek, Uma S Bhatt, Larry A Rundquist, Scott D Lindsey, Xiangdong Zhang, and Richard L Thoman. Large-scale climate controls of interior alaska river ice breakup. *Journal of Climate*, 24(1):286–297, 2011.

Milan Bijeljanin. Application of crissp-2d finite element modelling in predicting ice formation processes upstream of the jenpeg generating station. 2013.

Michael A Bilello. Maximum thickness and subsequent decay of lake, river and fast sea ice in canada and alaska. Technical report, DTIC Document, 1980.

Lennart Billfalk. Breakup of solid ice covers due to rapid water level variations. Technical report, DTIC Document, 1982.

JB Bird. Geomorphic processes in the arctic. *Arctic and alpine environments*, pages 703–20, 1974.

J.B. Bird. The geomorphic role of river, sea and lake ice. Technical report, John Hopkins Press, Baltimor,MD., 1976.

Jean-François Bisaillon and Normand E Bergeron. Modeling anchor ice presence–absence in gravel bed rivers. *Cold Regions Science and Technology*, 55(2):195–201, 2009.

A Breland and R.W Carson. Studies and field tests of ice cover effectson the yokun river. In *Canadian Electrical Association*, 1995.

Carl B Brown. Sediment transportation, 1950.

Laura C Brown and Claude R Duguay. The response and role of ice cover in lake-climate interactions. *Progress in physical geography*, 34(5):671–704, 2010.

Richard S Brown, Wayne A Hubert, and Steven F Daly. A primer on winter, ice, and fish: what fisheries biologists should know about winter ice processes and stream-dwelling fish. *Fisheries*, 36(1):8–26, 2011.

RS Brown, G Power, S Beltaos, and TA Beddow. Effects of hanging ice dams on winter movements and swimming activity of fish. *Journal of Fish Biology*, 57(5):1150–1159, 2000.

Blair H Brumley, Ramon G Cabrera, Kent L Deines, Eugene Terray, et al. Performance of a broad-band acoustic doppler current profiler. *Oceanic Engineering, IEEE Journal of*, 16(4):402–407, 1991.

J Buermans, D Fissel, J Marko, and M Jasek. Progress in shallow water ice profiling sonar (swips) for river and lake ice monitoring. In *Proceedings of 20th International Symposium on Ice, Lahti, Finland*, 2010.

Kristin Bunte and Steven R Abt. Sampling surface and subsurface particle-size distributions in wadable gravel-and cobble-bed streams for analyses in sediment transport, hydraulics, and streambed monitoring. 2001.

Darryl J Calkins. Ice jams in shallow rivers with floodplain flow. *Canadian Journal of Civil Engineering*, 10(3):538–548, 1983.

Darryl J Calkins. Ice cover melting in a shallow river. *Canadian Journal of Civil Engineering*, 11(2):255–265, 1984.

Darryl J Calkins, David S Deck, and Carl R Martinson. Resistance coefficients from velocity profiles in ice-covered shallow streams. *Canadian Journal of Civil Engineering*, 9(2):236–247, 1982.

Mines Canada. Department of Energy and Resources. Surveys Branch. *The National Atlas of Canada: L'Atlas National Du Canada*. Department of Energy, Mines and Resources, 1978.

AH Cardoso, Walter Hans Graf, and Giselher Gust. Uniform flow in a smooth open channel. *Journal of Hydraulic Research*, 27(5):603–616, 1989.

KEVIN L Carey. Observed configuration and computed roughness of the underside of river ice, st. croix river, wisconsin. *US Geological Survey Professional Paper*, pages B192–B198, 1966.

R.W Carson. Experience with river ice at the limeston site. In *Workshop on Hydraulic Resistance of River Ice*, 1982.

RW Carson and JL Groeneveld. Evolution of the icesim model. In *Proceedings of the 9"Workshop on River Ice. Fredericton, New Brunswick, Canada*, 1997.

R.W Carson and L.P Jonassen. River diversion during construction of limestone generating station. Fourth National CSCE hydrotechnical Conference, 1979.

RW Carson, S Beltaos, D Healy, and J Groeneveld. Tests of river ice jam modelsphase 2. In *Proceedings of the 12th Workshop on the Hydraulics of Ice Covered Rivers, Edmonton, Alta*, pages 19–20, 2003.

Torkild Carstens. *Experiments with supercooling and ice formation in flowing water*. Univ.-Forl., 1966.

EF Chacho, DE Lawson, and BE Brockett. Frazil ice pebbles: frazil ice aggregates in the tanana river near fairbanks, alaska. In *Proc. IAHR Symp. on Ice, Iowa City, Iowa*, volume 1, pages 465–474, 1986.

SP Chee and MRI Haggag. Flow resistance of ice-covered streams. *Canadian Journal of Civil Engineering*, 11(4):815–823, 1984.

Ven T Chow. Open-channel hydraulics. In *Open-channel hydraulics*. McGraw-Hill, 1959.

Michael Church. River studies in northern canada: reading the record from river morphology. *Geoscience Canada*, 4(1), 1977.

S Clark and JC Doering. Laboratory observations of frazil ice. In *Proc., 16th Int. Symp. on Ice*, pages 127–133. IAHR, 2002.

Clarence Samuel Clay and Herman Medwin. *Acoustical oceanography: principles and applications*, volume 15. John Wiley & Sons, 1977.

JA Code. *The stability of natural slopes in the Mackenzie Valley*. Task Force on Northern Oil Development, Environmental-Social Committee, Northern Pipelines, 1973.

Bruce Ronald Colby and Cloyd H Scott. *Effects of water temperature on the discharge of bed material*. US Government Printing Office Washington, DC, 1965.

John D Collinson. Some effects of ice on a river bed. *Journal of Sedimentary Research*, 41 (2), 1971.

Mary J. Crance and Kelly M. Frothingham. The impact of ice cover roughness on stream hydrology. 65 Eastern Snow Conference, Fairlee, Vermont, USA, 2008.

Steven F Daly. Frazil ice dynamics. Technical report, DTIC Document, 1984.

Steven F Daly. Data assimilation in river ice forecasting. In *Proceedings of the 16th international symposium on ice œ Ice in the environment. Dunedin, New Zealand*, pages 2–6, 2002.

Steven F Daly and Carrie M Vuyovich. Modeling river ice with hec-ras. In *Proceedings of the 12th CGU-HS CRIPE Workshop on River Ice, Edmonton, Alta*, 2003.

ID Danilov. Ice as a factor of relief formation and sedimentation. *Problemy Krioliltogii*, 2: 137–143, 1972.

Kersi S Davar, Spyros Beltaos, and Bruce Pratte. A primer on hydraulics of ice covered rivers. *Journal of Cold Regions Engineering*, page 165, 1998.

Sylvio Demers, Thomas Buffin-Bélanger, and André G Roy. Macroturbulent coherent structures in an ice-covered river flow using a pulse-coherent acoustic doppler profiler. *Earth Surface Processes and Landforms*, 38(9):937–946, 2013.

C Derksen, SL Smith, M Sharp, L Brown, S Howell, L Copland, DR Mueller, Y Gauthier, CG Fletcher, A Tivy, et al. Variability and change in the canadian cryosphere. *Climatic Change*, 115(1):59–88, 2012.

Con Desplanque and Dale I Bray. Winter ice regime in the tidal estuaries of the northeastern portion of the bay of fundy, new brunswick. *Canadian Journal of Civil Engineering*, 13(2):130–139, 1986.

William E Dietrich and Peter Whiting. Boundary shear stress and sediment transport in river meanders of sand and gravel. *Water Resources Monograph*, 12:1–50, 1989.

J-C Dionne et al. How drift ice shapes the st. lawrence. 1974.

JC Doering, LE Bekeris, MP Morris, KE Dow, and WC Girling. Laboratory study of anchor ice growth. *Journal of cold regions engineering*, 15(1):60–66, 2001.

John C Doering and Michael P Morris. River ice engineering/ingénierie des glaces fluviales a digital image processing system to characterize frazil ice. *Canadian Journal of Civil Engineering*, 30(1):1–10, 2003.

John C Doering, Michael P Morris, William C Girling, and Karen Dow. Laboratory studies of anchor ice growth using a digital image processing system. In *10th Workshop on River Ice. River Ice Management with a Changing Climate: Dealing with Extreme Events*, pages 377–388. Winnipeg, MB, 1999.

RV Donchenko. Peculiarities of ice cover formation on reservoirs. In *Proc. of the Banff Symposium on the Role of Snow and Ice in Hydrology*, pages 564–574, 1972.

N Ernest Dorsey. Properties of ordinary water-substance. 1940.

PF Doyle. Damage resulting from a sudden river ice breakup. *Canadian Journal of Civil Engineering*, 15(4):609–615, 1988.

Robert Drucker, Seelye Martin, and Richard Moritz. Observations of ice thickness and frazil ice in the st. lawrence island polynya from satellite imagery, upward looking sonar, and salinity/temperature moorings. *Journal of Geophysical Research: Oceans (1978–2012)*, 108(C5), 2003.

Jérôme Dubé, Thomas Buffin-Bélanger, and N Bergeron. Interannual field observations and analysis of river ice dynamics at a fluvial transition on the rimouski river, quebec. In *Proceedings of the 15th Workshop on River Ice. St. John's: NL, Canada*, 2009.

W Dupre and R Thompson. The yukon delta: Amodel for deltaic sedimentation in an ice-dominated environment. In *Offshore Technology Conference*, 1979.

Armand John Eardley. Yukon channel shifting. *Geological Society of America Bulletin*, 49 (3):343–357, 1938.

Hans Albert Einstein. *The bed-load function for sediment transportation in open channel flows*. Number 1026. US Department of Agriculture, 1950.

Josée Emond, Brian Morse, Martin Richard, Edward Stander, and AA Viau. Surface ice observations on the st. lawrence river using infrared thermography. *River Research and Applications*, 27(9):1090–1105, 2011.

Johanna Engström, Roland Jansson, Christer Nilsson, and Christine Weber. Effects of river ice on riparian vegetation. *Freshwater biology*, 56(6):1095–1105, 2011.

Robert Ettema. Loose-bed issues in river-ice hydraulics. In *Cold Regions Engineering@ sPutting Research into Practice*, pages 588–599. ASCE, 1999a.

Robert Ettema. Review of river-ice impacts on alluvial-channel stability. In *Workshop on River Ice, 10th*, pages 8–11, 1999b.

Robert Ettema. Review of alluvial-channel responses to river ice. *Journal of Cold Regions Engineering*, 16(4):191–217, 2002.

Robert Ettema. Ice effects on sediment transport in rivers. *Sedimentation engineering*, pages 613–648, 2008.

Robert Ettema and Steven F Daly. Sediment transport under ice. Technical report, DTIC Document, 2004.

Robert Ettema and Edward W Kempema. River-ice effects on gravel-bed channels. *Gravel-Bed Rivers: Processes, Tools, Environments*, pages 523–540, 2012.

Robert Ettema and Leonard Zabilansky. Ice influences on channel stability: insights from missouri's fort peck reach. *Journal of Hydraulic Engineering*, 130(4):279–292, 2004.

ROBERT Ettema, MARIAN Muste, and STEPHEN Coleman. Flume notes on sediment transport and boil formation in ice-covered channels. In *Proceedings of the IIHR XXVIII Biennial Congress [CD-ROM] Iowa Inst. of Hydraul. Res. Iowa City*, 1999a.

Robert Ettema, Marian Muste, and Anton Kruger. Ice jams in river confluences. Technical report, DTIC Document, 1999b.

Robert Ettema, F Braileanu, and Marian Muste. Method for estimating sediment transport in ice-covered channels. *Journal of cold regions engineering*, 14(3):130–144, 2000.

Robert Ettema, Zhiming Chen, and Yong Lai. Frazil-ice ingestion by a submerged water intake: numerical-model and ice-tank findings. In *Proceedings of the 16th international symposium on ice–Ice in the environment*, pages 14–21, 2002.

Vito Ferro and Giorgio Baiamonte. Flow velocity profiles in gravel-bed rivers. *Journal of Hydraulic Engineering*, 120(1):60–80, 1994.

FH Fisher and VP Simmons. Sound absorption in sea water. *The Journal of the Acoustical Society of America*, 62(3):558–564, 1977.

Bergeron N. G. Allard, Buffin-Belanger T. Frazil ice as a geomorphic agent. 2009.

Lawrence W Gatto. Soil freeze-thaw effects on bank erodibility and stability. Technical report, DTIC Document, 1995.

Roberto Gaudio, Antonio Miglio, and Subhasish Dey. Non-universality of von kármán's κ in fluvial streams. *Journal of Hydraulic Research*, 48(5):658–663, 2010.

F Gauthier, M Allard, and B Hétu. Ice wall growth and decay: Meteorological analysis and modelling. *Permafrost and Periglacial Processes*, 26(1):84–102, 2015.

Y Gauthier, TBMJ Ouarda, M Bernier, and A El Battay. Monitoring the ice cover of a medium size river from radarsat-1: preliminary results. In *Proceedings 11th Workshop on River Ice. River ice processes within a changing environment. Canada Committee on River Ice Processes and the Environment. CGU-HS. Ottawa, Canada*, 2001.

J.F. Kennedy G.D. Ashton. Ripples on underside of river ice covers. *Journal of Hydraullic Div.*, (98), 1972.

Solomon Gebre, Knut Alfredsen, Leif Lia, Morten Stickler, and Einar Tesaker. Review of ice effects on hydropower systems. *Journal of Cold Regions Engineering*, 27(4):196–222, 2013.

A.D Gerrard and R.W Carson. Control of river ice during construction of limestone generating station. 1987.

Soheil Ghareh Aghaji Zare, Stephanie A. Moore, Colin D. Rennie, Ousmane Seidou, and Habib Ahmari. Estimating the influence of river ice break-up on suspended sediment transport using acoustic techniques. In *Proceedings of Canadian hydrotechnical conference*, 2013.

Soheil Ghareh Aghaji Zare, Stephanie A. Moore, Colin D. Rennie, Ousmane Seidou, and Habib Ahmari. Influence of river ice break-up on stream hydraulics and sediment. Proceedings of IAHR International Conference on Fluvial Hydraulics, 2014.

Soheil Ghareh Aghaji Zare, Stephanie A. Moore, Colin D. Rennie, Ousmane Seidou, and Habib Ahmari. Boundary shear stress in an ice covered river during break-up. *Journal of Hydraulic Engineering, ASCE*, 2015. In press.

Tadros R Ghobrial, Mark R Loewen, and Faye Hicks. Laboratory calibration of upward looking sonars for measuring suspended frazil ice concentration. *Cold Regions Science and Technology*, 70:19–31, 2012.

Tadros R Ghobrial, Mark R Loewen, and Faye E Hicks. Continuous monitoring of river surface ice during freeze-up using upward looking sonar. *Cold Regions Science and Technology*, 86:69–85, 2013.

Tadros Riad Ghobrial, MR Loewen, and Faye Hicks. Frazil ice measurements using the shallow water ice profiling sonar. In *Proceedings of 15th Workshop on River Ice, St. John's, Newfoundland and Labrador*, pages 14–26, 2009.

TR Ghobrial, M Loewen, F Hicks, and J Maxwell. Monitoring frazil ice evolution during freeze-up using the shallow water ice profiling sonar. In *Proceedings of the 20th IAHR International Symposium on Ice, Lahti, Finland, June*, volume 14, 2010.

WC Girling and J Groeneveld. Anchor ice formation below limestone generating station. In *10th Workshop on River Ice. River Ice Management with a Changing Climate: Dealing with Extreme Events*, pages 160–173. Winnipeg, MB, 1999.

JP Gosink and TE Osterkamp. *Measurements and analyses of velocity profiles and frazil ice-crystal rise velocities during periods of frazil-ice formation in rivers*. Defense Technical Information Center, 1983.

Holly L Goulding, Terry D Prowse, and Barrie Bonsal. Hydroclimatic controls on the occurrence of break-up and ice-jam flooding in the mackenzie delta, nwt, canada. *Journal of hydrology*, 379(3):251–267, 2009.

Gordon M Greene and Samuel I Outcalt. A simulation model of river ice cover thermodynamics. *Cold Regions Science and Technology*, 10(3):251–262, 1985.

P Grover, C Vrkljan, S Beltaos, and D Andres. Prediction of ice jam water levels in a multi-channel river: Fort albany, ontario. In *Proceedings of the 10th Workshop on River Ice, Winnipeg, Man*, pages 8–11, 1999.

Laodong Guo, Yihua Cai, Claude Belzile, and Robie W Macdonald. Sources and export fluxes of inorganic and organic carbon and nutrient species from the seasonally ice-covered yukon river. *Biogeochemistry*, 107(1-3):187–206, 2012.

Qizhong Guo. Applicability of criterion for onset of river ice breakup. *Journal of Hydraulic Engineering*, 128(11):1023–1026, 2002.

Decker Hains and Leonard Zabilansky. Laboratory test of scour under ice: Data and preliminary results. Technical report, DTIC Document, 2004.

LE Hamelin. The bechevnik: a river bank feature from siberia. *The Musk Ox*, 25:70–72, 1979.

L Hammar, HT Shen, KU Evers, T Kolerski, Y Yuan, and L Sobczak. A laboratory study of freeze-up ice runs in river channels. In *16th IAHR International Symp. on Ice*, 2002.

S Hancu. Modelarea hidraulica in curenti de aer sub presiune. *Editura Academici Republic Socialiste Romania,(text in Romanian)*, 1967.

Melissa Aynslie Marie Haresign. *Modelling river ice freeze-up on the Red River near Netley Cut*. PhD thesis, University of Manitoba, 2012.

D Healy and F Hicks. Estimating streamflow during spring breakup. In *Mackenzie GEWEX Study (MAGS) Phase 1, Proceedings, 6th Scientific Workshop*, pages 15–17, 2000.

Dan Healy, Faye Hicks, and Mark Loewen. Unsteady velocity profiles under a floating cover. In *Ice in the Environment: Proceedings of the 16th IAHR International Symposium on Ice, Dunedin, New Zealand*, pages 2–6, 2002.

RE Hecky and SJ Guildford. Primary productivity of southern indian lake before, during, and after impoundment and churchill river diversion. *Canadian Journal of Fisheries and Aquatic Sciences*, 41(4):591–604, 1984.

Francis Martin Henderson. *Open channel flow*. Macmillan, 1989.

Richard D Hey and Colin R Thorne. Stable channels with mobile gravel beds. *Journal of Hydraulic Engineering*, 112(8):671–689, 1986.

Faye E Hicks. Ice as the geomorphologic agent in an anastomosing river system. In *Proceedings of the Workshop on Environmental Aspects of River Ice*, number 12, pages 3–20. National Hydrology Research Institute, Saskatoon, Saskatchewan, NHRI Symposion Series, 1993.

Faye Ellen Hicks. Finite element modeling of open channel flow. *Dissertation Abstracts International Part B: Science and Engineering*, 51(11), 1991.

FE Hicks and PM Steffler. Characteristic dissipative galerkin scheme for open-channel flow. *Journal of Hydraulic Engineering*, 1992.

K Hirayama, K Terada, M Sato, K Hirayama, M Sasamoto, and M Yamazaki. Field measurements of anchor and frazil ice. 1997.

P.Y. Ho. Dependence of bedload movement on grain shape and water temperature. 1939.

Karen L Hodel. The sagavanirktok river, north slope alaska; characterization of an arctic stream. Technical report, US Geological Survey,, 1986.

Rou-Jai Hong, MF Karim, and John F Kennedy. Low-temperature effects on flow in sand-bed streams. *Journal of Hydraulic Engineering*, 110(2):109–125, 1984.

Mikko Huokuna, Juha Aaltonen, and Noora Veijalainen. Frazil ice problems in changing climate conditions. In *Proceedings of the 15th workshop on River Ice, St Johns, Newfoundland, Canada*, pages 14–17, 2009.

T Kowalczyk Hutchison and FE Hicks. Observations of ice jam release waves on the athabasca river near fort mcmurray, alberta. *Canadian Journal of Civil Engineering*, 34 (4):473–484, 2007.

RD Instruments. Adcp coordinate transformation- formulas and calculations. *RD Instruments, San Diego*, 2010.

River Direct Instruments. Acoustic doppler current profilers principles of operation: A practical primer. *RD Instruments, San Diego*, 36, 1996.

E. Ismail and K. S. Davar. Resistance to channel flow under a very rough top boundary-analogous to broken ice cover. pages pp. 443–448. International Association for Hydraulic Research Symposium on Ice Problems. Lulea, Swcden, 1976.

J Janowicz. Observed trends in the river ice regimes of northwest canada. 2010.

M Jasek, J Marko, and D Fissel. Acoustic detection of ice and water velocities on the peace river during the 2008–2009 winter. In *Proceedings of 20th International Symposium on Ice, Lahti, Finland*, 2010.

M Jasek, JR Marko, and DR Topham. Analyses of 2011-2012 four-frequency peace river azfp data. 2013.

Martin Jasek. Analysis of ice jam surge and ice velocity data. In *Proceedings of the 10th Workshop on the Hydraulics of Ice covered Rivers*, pages 174–184, 1999.

Martin Jasek. Ice jam release surges, ice runs, and breaking fronts: field measurements, physical descriptions, and research needs. *Canadian Journal of Civil Engineering*, 30(1): 113–127, 2003.

Martin Jasek and John Marko. Instrument for detecting suspended and surface ice runs in rivers. In *Proc. 14th Workshop on River Ice. CGU-HS CRIPE, Quebec*, 2007.

Martin Jasek, John Marko, David Fissel, Murray Clarke, Jan Buermans, and Kerry Paslawski. Instrument for detecting freeze-up, mid-winter and break-up ice processes in rivers. In *Proc. 13th Workshop on River Ice. CGU-HS CRIPE, Hanover*, pages 151–183, 2005.

Martin Jasek, T Ghobrial, M Loewen, and F Hicks. Comparison of crissp modeled and swips measured ice concentrations on the peace river. In *Proc. 16th CGU-HS CRIPE Workshop on River Ice, Winnipeg, MB*, pages 249–273, 2011.

Krupnik I. Aporta C. Gearheard S. Laidler G. Johns, A. and L. Kielsen Holm. Inuit sea ice terminology in nunavut and nunatsiavut (2009 draft), in siku: Knowing our ice. *Springer*, pages 401–412, 2009.

Gregory C Johnson, Rolf G Lueck, and Thomas B Sanford. Stress on the mediterranean outflow plume: Part ii. turbulent dissipation and shear measurements. *Journal of Physical Oceanography*, 24(10):2084–2092, 1994.

DG Judge, ST Lavender, RW Carson, and S Ismail. Headpond ice jams- where will they occur? In *Proceedings of the 9. workshop on river ice*, 1997.

Robert K and Gary N Sykes. *Nature's Lifeline: Prairie and Northern Waters: a Technical Report.* Calgary: Canada West Foundation, 1982. Canada West Foundation and Devonian Group of Charitable Foundations and Lane,.

Andreas Kääb, Maxim Lamare, and Michael Abrams. River ice flux and water velocities along a 600 km-long reach of lena river, siberia, from satellite stereo. *Hydrology and Earth System Sciences*, 17(11):4671–4683, 2013.

Sujuan Ke, Guangqi Lu, and Zhiyuan Ren. Study on mechanism of ice jam formation in bayangaole section of yellow river. *Shuili Xuebao/Journal of Hydraulic Engineering*, 7: 66–69, 2000.

Rolf Kellerhals and Michael Church. Comment on effects of channel enlargement by river ice processes on bankfull discharge in alberta, canadaby dg smith. *Water Resources Research*, 16(6):1131–1134, 1980.

Ed Kempema, Erk Reimnitz, and Ralph Eugene Hunter. *Flume studies and field observations of the interaction of frazil ice and anchor ice with sediments.* US Department of the Interior, Geological Survey, 1986.

Edward W Kempema and Robert Ettema. Anchor ice rafting: observations from the laramie river. *River research and applications*, 27(9):1126–1135, 2011.

EW Kempema, Erk Reimnitz, JR Clayton, and JR Payne. Interactions of frazil and anchor ice with sedimentary particles in a flume. *Cold Regions Science and Technology*, 21(2): 137–149, 1993.

David J Kerr, Hung Tao Shen, and Steven F Daly. Anchor ice formation and growth on gravel channel bed. In *Proceedings, 9th Workshop on River Ice*, pages 24–26, 1997.

David J Kerr, Hung Tao Shen, and Steven F Daly. Evolution and hydraulic resistance of anchor ice on gravel bed. *Cold Regions Science and Technology*, 35(2):101–114, 2002.

Garbis Hovannes Keulegan. *Laws of turbulent flow in open channels*, volume 21. National Bureau of Standards US, 1938.

Abdul Aziz Khan, Peter M Steffler, and Robert Gerard. Dam-break surges with floating debris. *Journal of Hydraulic Engineering*, 126(5):375–379, 2000.

WA King and IP Martini. Morphology and recent sediments of the lower anastomosing reaches of the attawapiskat river. *Sedimentary Geology*, 37(4):295–320, 1984.

BA Kironoto, Walter Hans Graf, et al. Turbulence characteristics in rough non-uniform open-channel flow. *Proceedings of the ICE-Water Maritime and Energy*, 112(4):336–348, 1995.

HR Kivisild. River and lake ice terminology. 1970.

J. Komura and Sumbal. Head losses in channels with ice covers. pages pp. 25.1–25.5. lnternational Association for Hydraulic Research Symposium on Ice Problems. Colorado State University, Fort Collins, CO, 1967.

Lambert H Koopmans. *The spectral analysis of time series*. Academic press, 1995.

B.W Korbaylo and R.W Carson. River ice management during construction of lower nelson hydroelectric stations. In *11th International Ice Symposium*, 1992.

Ray Kostaschuk, Jim Best, Paul Villard, Jeff Peakall, and Mark Franklin. Measuring flow velocity and sediment transport with an acoustic doppler current profiler. *Geomorphology*, 68(1):25–37, 2005.

Twyla Kowalczyk and Faye Hicks. Observations of dynamic ice jam release on the athabasca river at fort mcmurray, ab. In *Proc. 12th Workshop on River Ice, Edmonton, June19-20*, 2003.

Don Kuryk. Winter roads in manitoba. In *CGU HS Committee on River Ice Processes and the Environment. 12th Workshop on the Hydraulics of Ice Covered Rivers*, 2003.

AM Wasantha Lal and Hung Tao Shen. Mathematical model for river ice processes. *Journal of hydraulic engineering*, 117(7):851–867, 1991.

Emory Wilson Lane. *A study of the shape of channels formed by natural streams flowing in erodible material*. US Army Engineer Division, Missouri River, 1957.

EW Lane, EJ Carlson, and OS Hanson. Low temperature increases sediment transport in colorado river. *Civil engineering*, pages 45–46, 1949.

P Larsen and L Billfalk. Ice problems in swedish hydro power operation. In *Proceedings of the IAHR Symposium on Ice Problems, Delft, The Netherlands*, 1978.

Peter Larsen. Hydraulic roughness of ice covers. *Journal of the Hydraulics Division*, 99 (Pap n 9498), 1973.

Peter A Larsen. Head losses caused by an ice cover on open channels. *Journal of Boston Society of Civil Engineering, Vol 56, No 1, P 45-67, Jan 1969. 23 P, 20 Fig, 4 Ref.*, 1969.

Y Lam Lau and Bommanna G Krishnappan. Sediment transport under ice cover. *Journal of Hydraulic Engineering*, 111(6):934–950, 1985.

YL Lau. Velocity distributions under floating covers. *Canadian Journal of Civil Engineering*, 9(1):76–83, 1982.

I. I. Levi. *Dynamics of open channle flows*. 1948. text in Russian.

Karl-Erich Lindenschmidt, Joost van der Sanden, Allyson Demski, Hugo Drouin, and Torsten Geldsetzer. Characterising river ice along the lower red river using radarsat-2 imagery. In *CGU HS Committee on River Ice Processes and the Environment (CRIPE), 16th Workshop on River Ice, Winnipeg*, pages 18–22, 2011.

Karl-Erich Lindenschmidt, Maurice Sydor, and Richard W Carson. Modelling ice cover formation of a lake–river system with exceptionally high flows (lake st. martin and dauphin river, manitoba). *Cold Regions Science and Technology*, 82:36–48, 2012.

Lianwu Liu, Hai Li, and Hung Tao Shen. A two-dimensional comprehensive river ice model. In *Proceedings of the 18th IAHR Symposium on River Ice, Sapporo, Japan*, 2006.

Atle Lohrmann, Bruce Hackett, and Lars Petter Røed. High resolution measurements of turbulence, velocity and stress using a pulse-to-pulse coherent sonar. *Journal of Atmospheric and Oceanic Technology*, 7(1):19–37, 1990.

Shunan Lu, Hung Tao Shen, and Randy D Crissman. Numerical study of ice jam dynamics in upper niagara river. *Journal of cold regions engineering*, 13(2):78–102, 1999.

Youyu Lu and Rolf G Lueck. Using a broadband adcp in a tidal channel. part ii: Turbulence. *Journal of Atmospheric and Oceanic Technology*, 16(11):1568–1579, 1999.

Youyu Lu, Rolf G Lueck, and Daiyan Huang. Turbulence characteristics in a tidal channel. *Journal of Physical Oceanography*, 30(5):855–867, 2000.

DK Mackay, DA Sherstone, and KC Arnold. Channel ice effects and surface water velocities from aerial photography of mackenzie river break-up. *Hydrological aspects of northern pipeline development. Task Force on Northern Oil Development, Environmental–Social Program, Northern Pipelines, Report*, pages 74–12, 1974.

J Ross Mackay and DK Mackay. The stability of ice-push features, mackenzie river, canada. *Canadian Journal of Earth Sciences*, 14(10):2213–2225, 1977.

Sarah M Mager, Inga J Smith, Edward W Kempema, Benjamin J Thomson, and Gregory H Leonard. Anchor ice in polar oceans. *Progress in Physical Geography*, page 0309133313479815, 2013.

J Malenchak, J Doering, and HT Shen. Modeling of anchor ice and aufeis formation at sundance rapids. cgu hs committee on river ice processes and the environment. In *16th Workshop on River Ice, Winnipeg, MB*, 2011.

Jarrod Malenchak, Michael Morris, Hung Tao Shen, and Jay Doering. Modeling anchor ice growth at sundance rapids. In *Proceedings of the 18th IAHR Symposium on River Ice, Sapporo, Japan*, 2006.

N Marcotte. Anchor ice in lachine rapids, results of observations and analysis. In *Proceedings of the IAHR International Symposium on Ice*, volume 1, pages 151–159, 1984.

N Marcotte and Sf Robert. Elementary mathematical modeling of anchor ice. In *Proceedings of the IAHR 8th International Symposium on Ice, Iowa City, Iowa*, pages 18–22, 1986.

JR Marko and DB Fissel. Realtime monitoring of ice thickness and growth from seafloor-mounted upward-looking sonar instrumentation. 2005.

JR Marko and M Jasek. Frazil monitoring by multi-frequency shallow water ice profiling sonar (swips): present status. In *Proceedings of the 20th IAHR International Symposium on Ice, Lahti, Finland, June*, volume 14, 2010a.

JR Marko and M Jasek. Sonar detection and measurements of ice in a freezing river i: Methods and data characteristics. *Cold Regions Science and Technology*, 63(3):121–134, 2010b.

JR Marko and Martin Jasek. Estimation of frazil particle size and concentration from swips measurements in the peace river: an assessment of options and prospects. In *15th CRIPE workshop on River Ice, St. Johbs. Nfld*, 2009.

JR Marko, DB Fissel, and M Jasek. Recent developments in ice and water column profiling technology. In *Proceedings of the 18th IAHR International Symposium on Ice, Sapporo, Japan*, pages 37–44, 2006.

JR Marko, M Jasek, and DR Topham. Multifrequency analyses of 2011–2012 peace river swips frazil backscattering data. *Cold Regions Science and Technology*, 110:102–119, 2015.

James H Marsh. *The Canadian Encyclopedia.* The Canadian Encyclopedia, 1999.

Seelye Martin. Frazil ice in rivers and oceans. *Annual Review of Fluid Mechanics*, 13(1): 379–397, 1981.

Ya I Marusenko. The action of ice on river banks. *Priroda*, 45(12):91–93, 1956.

Darrell D Massie, Kathleen D White, Steven F Daly, and Regan McDonald. Predicting ice jams with neural networks. In *ASME 2002 21st International Conference on Offshore Mechanics and Arctic Engineering*, pages 669–673. American Society of Mechanical Engineers, 2002.

V Matousek. Regularity of the freezing up of the water surface and heat exchange between water body and water surface. In *Actes du Symposium de lAIRH sur la glace, Hamburg*, 1984a.

V Matousek. Types of ice run and conditions for their formation. In *IAHR International Symposium on Ice, Hamburg, Germany*, 1984b.

J Maxwell, F Hicks, and M Loewen. Study of freeze-up ice characteristics on the north saskatchewan river.

R McDonald, Kathleen D White, S Daly, and Darrell D Massie. Implementation of an ice jam predictor with user interface. In *Proceedings of the 16th international symposium on ice œ Ice in the environment. Dunedin, New Zealand*, pages 2–6, 2002.

Norm A McFarlane, GJ Boer, JP Blanchet, and M Lazare. The canadian climate centre second-generation general circulation model and its equilibrium climate. *Journal of Climate*, 5(10):1013–1044, 1992.

Paul McKay, Cheryl Ann Blain, Daniela Di Iorio, and Heath Hansell. Mixing and turbulence in a flooding coastal river. *Journal of Hydraulic Engineering*, 139(12):1213–1222, 2013.

Humfrey Melling, Paul H Johnston, and David A Riedel. Measurements of the underside topography of sea ice by moored subsea sonar. *Journal of Atmospheric and Oceanic Technology*, 12(3):589–602, 1995.

Malcolm Mellor. Engineering properties of snow. *Journal of Glaciology*, 19:15–66, 1978.

AG Mercer and RH Cooper. River bed scour related to the growth of a major ice jam. In *Proceedings of the 3rd Canadian Hydrotechnical Conference, Que*, pages 30–31, 1977.

JH Mercer. The physiography of arctic canada; with special reference to the area south of parry channel j. brian bird. *The Journal of Geology*, 76(6), 1968.

Eugen Meyer-Peter and R Müller. Formulas for bed-load transport. IAHR, 1948.

B Michel and M Drouin. Backwater curves under ice covers on la-grande river. *Canadian Journal of Civil Engineering*, 8(3):351–363, 1981.

B Michel and RO Ramseier. Classification of river and lake ice. *Canadian Geotechnical Journal*, 8(1):36–45, 1971.

Bernard Michel. Winter regime of rivers and lakes. 1971.

Bernard Michel. Ice mechanics. 1978.

D Milburn and BG Krishnappan. Modelling under-ice movement of cohesive sediments: Hay river, northwest territories, canada. In *Ice in the Environment: Proceedings of the 16th IAHR International Symposium on Ice, Dunedin, New Zealand*, pages 2–6, 2002.

D Milburn and TD Prowse. Open-water versus under-ice rating curves for suspended sediment: an example from a large northern river. In *Proceedings of the 13th IAHR Ice Symposium*, pages 27–31, 1996.

D Milburn and TD Prowse. The role of an ice cover on sediment transport and deposition in a northern delta. In *Proc., IAHR Ice Symp*, 1998.

D Milburn and TD Prowse. Under-ice movement of cohesive sediments before river-ice breakup. *Hydrological Processes*, 16(4):823–834, 2002.

Clark B Millikan. A critical discussion of turbulent flows in channels and circular tubes. In *Proc. 5th Int. Congr. Appl. Mech*, volume 386, 1938.

JN Moore and EM Landrigan. Mobilization of metal-contaminated sediment by ice-jam floods. *Environmental Geology*, 37(1-2):96–101, 1999.

SA Moore. Monitoring flow and fluxes of suspended sediment in rivers using side-looking acoustic doppler current profilers. *University of Grenoble, Grenoble*, 2012.

Stephanie A. Moore, Soheil Ghareh Aghaji Zare, Colin D. Rennie, Ousmane Seidou, and Habib Ahmari. Monitoring suspended sediment under ice using acoustic instruments: presentation of measurements made under break-up. Committee on River Processes and the Environment, 2013. Proceedings of 17 th Workshop on river ice.

Stephanie A. Moore, Soheil Ghareh Aghaji Zare, Colin D. Rennie, Habib Ahmari, Ousmane Seidou, and Jarrod Malenchak. Dual frequency acoustic monitoring of sediment transport in an ice covered river. Elsevier, 2014.

Brian Morse. Dynamics of ice forces on booms. *Cold regions science and technology*, 33 (1):29–43, 2001.

Brian Morse and Faye Hicks. Advances in river ice hydrology 1999–2003. *Hydrological processes*, 19(1):247–263, 2005.

Brian Morse and Tung-Thanh Quach. Preventing frazil ice accumulations at hydroelectric facilities. In *Proceedings of the 16th international symposium on ice–Ice in the environment*, pages 99–107, 2002.

Brian Morse and Martin Richard. A field study of suspended frazil ice particles. *Cold Regions Science and Technology*, 55(1):86–102, 2009.

Brian Morse, Jean Francoeur, Hugues Delcourt, and Michel Leclerc. Ice control structures using steel nets. In *CGU HS Committee on River Ice Processes and the Environment. 12th Workshop on the Hydraulics of Ice Covered Rivers*, 2003.

CR Neill. Scour holes in a wandering gravel river. In *Symposium on Inland Waterways for Navigation, Flood Control and Water Diversions: 3rd Annual Symposium of the Waterways, Harbors and Coastal Engineering Division*, pages 1301–1317, 1976.

Robert Newburry and Marc Gaboury. Exploration and rehabilitation of hydraulic habitats in streams using principles of fluvial behaviour. *Freshwater Biology*, 29(2):195–210, 1993.

R Newbury and G Malaher. *The destruction of Manitoba's last great river.* Canadian Nature Federation, 1973.

R. W. Newbury. *The Nelson river In The geology of North America*, volume Vol. 0-1, Surface water hydrology. Geological Society of America, Boulder, Colorado., 1990.

RW Newbury. *The Nelson Rivera study of subarctic processes.* PhD thesis, Ph. D. thesis, The Johns Hopkins University, Baltimore, Md, 1968.

RW Newbury, GK McCullough, and RE Hecky. The southern indian lake impoundment and churchill river diversion. *Canadian Journal of Fisheries and Aquatic Sciences*, 41 (4):548–557, 1984.

RA Nezhikhovskiy. Coefficients of roughness of bottom surface of slush-ice cover. *Soviet hydrology*, (2):127–150, 1964.

Iehisa Nezu and Hiroji Nakagawa. Turbulence in open-channel flow. iahr monograph. *Balkema Pub*, 1993.

Iehisa Nezu and Wolfgang Rodi. Open-channel flow measurements with a laser doppler anemometer. *Journal of Hydraulic Engineering*, 112(5):335–355, 1986.

Vladimir Nikora, Stephen McLean, Stephen Coleman, Dubravka Pokrajac, Ian McEwan, Lorna Campbell, Jochen Aberle, Dougal Clunie, and Katinka Koll. Double-averaging concept for rough-bed open-channel and overland flows: Applications. *Journal of hydraulic Engineering*, 133(8):884–895, 2007.

J NIKURADSE Nikuradse. Jstromungsgesetze in rauhen rohren. *VDI-Forschungsheft*, 361, 1933.

NorthSouthConsultants. Substrate distribution of the nelson river downstream of limestone gs., 2010. provided by: Manitoba Hydro.

Arthur RM Nowell and Michael Church. Turbulent flow in a depth-limited boundary layer. *Journal of Geophysical Research: Oceans (1978–2012)*, 84(C8):4816–4824, 1979.

Elizabeth A Nystrom, Chris R Rehmann, and Kevin A Oberg. Evaluation of mean velocity and turbulence measurements with adcps. *Journal of hydraulic engineering*, 133(12): 1310–1318, 2007.

K Ohashi and T Hamada. Flow measurements of ice-covered rivers in hokkaido. 1970.

Alan V Oppenheim, Ronald W Schafer, John R Buck, et al. *Discrete-time signal processing*, volume 2. Prentice-hall Englewood Cliffs, 1989.

TE Osterkamp and JP Gosink. Frazil ice formation and ice cover development in interior alaska streams. *Cold Regions Science and Technology*, 8(1):43–56, 1983.

E Pariset and R Hauser. Formation and evolution of ice covers on rivers. 1961.

E Pariset, R Hausser, and A Gagnon. Formation of ice covers and ice jams in rivers. *Journal of the Hydraulics Division*, 92(6):1–24, 1966.

Gary Parker. Surface-based bedload transport relation for gravel rivers. *Journal of hydraulic research*, 28(4):417–436, 1990.

Gary Parker, Sundararajan Dhamotharan, and Heinz Stefan. Model experiments on mobile, paved gravel bed streams. *Water Resources Research*, 18(5):1395–1408, 1982.

Claire L Parkinson, Josefino C Comiso, H Jay Zwally, Donald J Cavalieri, Per Gloersen, and William J Campbell. Arctic sea ice, 1973-1976: Satellite passive-microwave observations. 1987.

FE Parkinson. Water temperature observations during breakup on the liard-mackenzie river system. In *Proceedings of the Workshop on Hydraulics of Ice-Covered Rivers*, pages 1–2, 1982.

VC Patel and MR Head. Some observations on skin friction and velocity profiles in fully developed pipe and channel flows. *Journal of Fluid Mechanics*, 38(01):181–201, 1969.

S Petryk, U Panu, and F Clement. Recent improvements in numerical modeling of river ice. In *Proceedings of Workshop on Hydraulic Resistance of Ice, Canadian Center for Inland Waters, Burlington, Ontario. Leading*, 1980.

VV Piotrovich. *Formation of depth-ice*. Directorate of Scientific Information Service, DRB Canada, 1956.

Anatoliĭ Aleksandrovich Pivovarov. *Thermal conditions in freezing lakes and rivers*. John Wiley & Sons, 1973.

Stephen B. Pope. *Turbulent flows*. Cambridge University Press, 2000.

L Prandtl. Report on investigation of developed turbulence. *NACA Report TM-1231*, 1925.

BD Pratte. Review of flow resistance of consolidated smooth and rough ice covers. In *Proc., Canadian Hydrology Symposium: 79 held at Vancouver*, pages 52–92. Associate Committee on Hydrology, National Research Council of Canada Ottawa, 1979.

T Prowse and Kirsten Brown. Hydro-ecological effects of changing arctic river and lake ice covers: a review. 2010.

TD Prowse. Suspended sediment concentration during river ice breakup. *Canadian Journal of Civil Engineering*, 20(5):872–875, 1993.

TD Prowse and T Carter. Significance of ice-induced storage to spring runoff: a case study of the mackenzie river. *Hydrological Processes*, 16(4):779–788, 2002.

TD Prowse and MN Demuth. Strength variability of major river-ice types. *Hydrology Research*, 24(2-3):169–182, 1993.

TD Prowse and MG Ferrick. Preface-hydrology of ice-covered rivers and lakes: scoping the subject. *Hydrological processes*, 16(4):759–762, 2002.

TD Prowse and P Marsh. Thermal budget of river ice covers during breakup. *Canadian Journal of Civil Engineering*, 16(1):62–71, 1989.

Terry D Prowse. River-ice ecology. i: Hydrologic, geomorphic, and water-quality aspects. *Journal of Cold Regions Engineering*, 15(1):1–16, 2001.

Terry D Prowse and Spyros Beltaos. Climatic control of river-ice hydrology: a review. *Hydrological Processes*, 16(4):805–822, 2002.

Terry D Prowse and Joseph M Culp. Ice breakup: a neglected factor in river ecology. *Canadian Journal of Civil Engineering*, 30(1):128–144, 2003.

Terry D Prowse, Barrie R Bonsal, Martin P Lacroix, and S Beltaos. Trends in river-ice breakup and related temperature controls. In *Ice in the environment. 16th IAHR international symposium on ice*, volume 3, pages 64–71, 2002.

YX Qu and J Doering. Laboratory study of anchor ice evolution around rocks and on gravel beds. *Canadian Journal of Civil Engineering*, 34(1):46–55, 2007.

Maria Rădoane, Valerian Ciaglic, and Nicolae Rădoane. Hydropower impact on the ice jam formation on the upper bistrita river, romania. *Cold Regions Science and Technology*, 60(3):193–204, 2010.

AJ Raudkivi and DL Hutchison. Erosion of kaolinite clay by flowing water. *Proceedings of the Royal Society of London. A. Mathematical and Physical Sciences*, 337(1611):537–554, 1974.

Arved J Raudkivi. *Loose boundary hydraulics.* CRC Press, 1998.

MR Raupach, RA Antonia, and S Rajagopalan. Rough-wall turbulent boundary layers. *Applied Mechanics Reviews*, 44(1):1–25, 1991.

E Reimnitz, EW Kempema, WS Weber, JR Clayton, and JR Payne. Suspended-matter scavenging by rising frazil ice. *CRREL Monogr*, 90(1):97–100, 1990.

Colin Rennie. Sediment transport (cvg5160), 2012. University of Ottawa-Department of Civil Engineering.

Colin Rennie and Rajib Ahsan. Conawapa physical environment-existing sedimentation environment. Technical report, Manitoba Hydro, Hatch corporation Canada, 2010.

Colin D Rennie and Alex Hay. Reynolds stress estimates in a tidal channel from phase-wrapped adv data. *Journal of Coastal Research*, pages 157–166, 2010.

André Robert and Thang Tran. Mean and turbulent flow fields in a simulated ice-covered channel with a gravel bed: some laboratory observations. *Earth surface processes and landforms*, 37(9):951–956, 2012.

J Urick Robert. Principles of underwater sound. *New York: McGraw-Hill Book Company*, 1983.

C Robichaud and FE Hicks. A remote water level network for break-up monitoring and flood forecasting. In *Proceedings of the 11th Workshop on River Ice*, 2001.

Wolfgang Rodi. *Turbulence models and their application in Hydraulics, Astate-of-the-art review.* A.A.Balkema, 1993.

William W Sayre and GB Song. Effects of ice covers on alluvial channel flow and sediment transport processes. Technical report, DTIC Document, 1979.

Mehmet Secil Uzuner. The composite roughness of ice covered streams. *Journal of Hydraulic Research*, 13(1):79–102, 1975.

Yuntong She, Faye Hicks, Peter Steffler, and Dan Healy. Constitutive model for internal resistance of moving ice accumulations and eulerian implementation for river ice jam formation. *Cold Regions Science and Technology*, 55(3):286–294, 2009.

HT Shen and DS Wang. Simulation and analysis of upper niagara river ice conditions. *Rep. No. 93*, 10, 1993.

Hung T Shen, Goranka Bjedov, Steven F Daly, and AM Wasantha Lal. Numerical model for forecasting ice conditions on the ohio river. Technical report, DTIC Document, 1991.

Hung Tao Shen. Development of a comprehensive river ice simulation system. In *Proceedings of the 16th international symposium on ice–Ice in the environment*, pages 142–148, 2002.

Hung Tao Shen. River ice researchprogress and missing links. In *Proc. 12th Workshop on the Hydraulics of Ice Covered Rivers. CGU-HS CRIPE, Edmonton, AB*, pages 1–9, 2003.

Hung Tao Shen. Mathematical modeling of river ice processes. *Cold Regions Science and Technology*, 62(1):3–13, 2010.

Hung Tao Shen and Li-Ann Chiang. Simulation of growth and decay of river ice cover. *Journal of Hydraulic Engineering*, 110(7):958–971, 1984.

Hung Tao Shen and Terrence O Harden. The effect of ice cover on vertical transfer in stream channels1. *JAWRA Journal of the American Water Resources Association*, 14 (6):1429–1439, 1978.

Hung Tao Shen and Lianwu Liu. Shokotsu river ice jam formation. *Cold Regions Science and Technology*, 37(1):35–49, 2003.

Hung Tao Shen and De Sheng Wang. Under cover transport and accumulation of frazil granules. *Journal of hydraulic engineering*, 121(2):184–195, 1995.

Hung Tao Shen and Poojitha D Yapa. A unified degree-day method for river ice cover thickness simulation. *Canadian Journal of Civil Engineering*, 12(1):54–62, 1985.

Jinyu Sheng and Alex E Hay. An examination of the spherical scatterer approximation in aqueous suspensions of sand. *The Journal of the Acoustical Society of America*, 83(2): 598–610, 1988.

Albert Shields. Application of similarity principles and turbulence research to bed-load movement. Technical report, Soil Conservation Service, 1936.

AI Shiklomanov and RB Lammers. River ice responses to a warming arcticrecent evidence from russian rivers. *Environmental Research Letters*, 9(3):035008, 2014.

Daryl B Simons and Fuat Şentürk. *Sediment transport technology: water and sediment dynamics*. Water Resources Publication, 1992.

Michael R Simpson. *Discharge measurements using a broad-band acoustic Doppler current profiler*. US Department of the Interior, US Geological Survey,Open File Report 01-1, 2001.

Graeme M Smart. Turbulent velocity profiles and boundary shear in gravel bed rivers. *Journal of Hydraulic Engineering*, 125(2):106–116, 1999.

Graeme M Smart, Maurice J Duncan, and Jeremy M Walsh. Relatively rough flow resistance equations. *Journal of Hydraulic Engineering*, 128(6):568–578, 2002.

Lars H Smedsrud. Estimating aggregation between suspended sediments and frazil ice. *Geophysical Research Letters*, 25(20):3875–3878, 1998.

Lars H Smedsrud and Adrian Jenkins. Frazil ice formation in an ice shelf water plume. *Journal of Geophysical Research: Oceans (1978–2012)*, 109(C3), 2004.

Brennan T Smith and Robert Ettema. Flow resistance in ice-covered alluvial channels. *Journal of hydraulic engineering*, 123(7):592–599, 1997.

Brennan Thomas Smith and Robert Ettema. *Ice-cover influence on flow and bedload transport in dune-bed channels*. PhD thesis, University of Iowa., 1995.

Derald G Smith and Cheryl M Pearce. River ice and its role in limiting woodland development on a sandy braid-plain, milk river, montana. *Wetlands*, 20(2):232–250, 2000.

Derald G Smith and Cheryl M Pearce. Ice jam-caused fluvial gullies and scour holes on northern river flood plains. *Geomorphology*, 42(1):85–95, 2002.

DG Smith. Effects of channel enlargement by river ice processes on bankfull discharge in alberta, canada. *Water Resources Research*, 15(2):469–475, 1979.

T Song, WH Graf, and U Lemmin. Uniform flow in open channels with movable gravel bed. *Journal of Hydraulic Research*, 32(6):861–876, 1994.

Mark T Stacey, Stephen G Monismith, and Jon R Burau. Measurements of reynolds stress profiles in unstratified tidal flow. *Journal of Geophysical Research*, 104:10935–10949, 1999.

Ödön Starosolszky. *Ice in hydraulic engineering*. Division of Hydraulic Engineering, Norwegian Institute of Technology, University of Trondeim, 1970.

TN Stevenson. A modified velocity defect law for turbulent boundary layers with injection. Technical report, College of Aeronautics Cranfield, 1963.

Morten Stickler and Knut T Alfredsen. Anchor ice formation in streams: a field study. *Hydrological processes*, 23(16):2307–2315, 2009.

Morten Stickler, Knut T Alfredsen, Tommi Linnansaari, and Hans-Petter Fjeldstad. The influence of dynamic ice formation on hydraulic heterogeneity in steep streams. *River research and applications*, 26(9):1187–1197, 2010.

Lorenz George Straub. *Effect of water temperature on suspended sediment load in an alluvial river*. University of Minnesota, St. Anthony Falls Hydraulic Laboratory, 1955.

Jueyi Sui, Desheng Wang, and Bryan W Karney. Suspended sediment concentration and deformation of riverbed in a frazil jammed reach. *Canadian Journal of Civil Engineering*, 27(6):1120–1129, 2000.

Jueyi Sui, Faye E Hicks, and Brian Menounos. Observations of riverbed scour under a developing hanging ice dam. *Canadian Journal of Civil Engineering*, 33(2):214–218, 2006.

Jueyi Sui, Jun Wang, Ram Balachandar, Zhaochu Sun, and Desheng Wang. Accumulation of frazil ice along a river bend. *Canadian Journal of Civil Engineering*, 35(2):158–169, 2008.

Jueyi Sui, Jun Wang, Yun He, and Faye Krol. Velocity profiles and incipient motion of frazil particles under ice cover. *International Journal of Sediment Research*, 25(1):39–51, 2010.

Alexander Sukhodolov, Michael Thiele, Heinz Bungartz, and Christof Engelhardt. Turbulence structure in an ice-covered, sand-bed river. *Water resources research*, 35(3): 889–894, 1999.

U Svensson, L Billfalk, and L Hammar. A mathematical model of border-ice formation in rivers. *Cold regions science and technology*, 16(2):179–189, 1989.

V. I. Synotin. Velocity structure of flow under ice cover. volume Vol. V, pp. 43537, 1965.

Tom Cheung Chiu Tang and Kersi S Davar. *Resistance to flow in partially-covered channels*. University of New Brunswick, 1985.

Wang Tao, Yang Kailin, and Guo Yongxin. Application of artificial neural networks to forecasting ice conditions of the yellow river in the inner mongolia reach. *Journal of Hydrologic Engineering*, 13(9):811–816, 2008.

Jean-Claude Tatinclaux and Mustafa Gogus. Asymmetric plane flow with application to ice jams. *Journal of Hydraulic Engineering*, 109(11):1540–1554, 1983.

Brent D Taylor and Vito A Vanoni. Temperature effects in low-transport, flat-bed flows. *Journal of the Hydraulics Division*, 98(8):1427–1445, 1972.

E. Tesaker. Measurements of ice cover roughness and the effect of ice cover on water levels in three norwegian rivers. International Association for Hydraulic Research Symposium on Ice, Reykjavik., 1970.

E Tesaker. Interaction between ice and water flow in rapids. In *Proceedings of the 13th International IAHR Ice Symposium*, 1996.

Isabelle Thériault, Jean-Philippe Saucet, and Wael Taha. Validation of the mike-ice model simulating river flows in presence of ice and forecast of changes to the ice regime of the romaine river due to hydroelectric project. In *20th IAHR International Symposium on Ice, Lahti, Finland*, pages 14–18, 2010.

K Theriault. Incoherent multibeam doppler current profiler performance: Part i–estimate variance. *Oceanic Engineering, IEEE Journal of*, 11(1):7–15, 1986.

Peter D Thorne and Ramazan Meral. Formulations for the scattering properties of suspended sandy sediments for use in the application of acoustics to sediment transport processes. *Continental Shelf Research*, 28(2):309–317, 2008.

W Tietze. Über die erosion von unter eis fließendem wasser. *Mainzer Geogr. Studien*, 1: 125–142, 1961.

M Tilston, C Rennie, RWC Arnott, and G Post. On the nature of coherent turbulent structures in channel bends: burst-sweep orientations in three-dimensional flow fields. In *33rd IAHR Congress: Water Engineering for a Sustainable Environment, ISBN*, pages 978–94, 2009.

GW Timco and AM Cornett. The influence of variable-thickness ice on the loads exerted on sloping structures. *Cold regions science and technology*, 26(1):39–53, 1997.

J.C Anderson T.J. Day. Observations on river ice, thomsen river, banks island, district of franklin. Technical Report 76-1B, Geological Survey of Canada, 1976.

Brian T Tracy and Steven F Daly. River ice delineation with radarsat sar. In *Proceedings CGU HS Committee on River Ice Processes and the Environment, Workshop on the Hydraulics of Ice Covered Rivers*, volume 12, 2003.

C Tropea. A note concerning the use of a one-component lda to measure shear stress terms. *Experiments in fluids*, 1(4):209–200, 1983.

Gee Tsang. *Frazil and anchor ice: a monograph.* Published under the auspices of NRC Subcommittee on Hydraulics of Ice Covered Rivers, 1982.

Benoit Turcotte and Brian Morse. Ice processes in a steep river basin. *Cold Regions Science and Technology*, 67(3):146–156, 2011.

Benoit Turcotte, Brian Morse, Normand E Bergeron, and André G Roy. Sediment transport in ice-affected rivers. *Journal of Hydrology*, 409(1):561–577, 2011.

AM Tuthill, CM Vuyovich, and KD White. Ice-affected stage-frequency development along the connecticut river. In *Proceedings, 12th Workshop on the Hydraulics of Ice Covered Rivers*, pages 19–20, 2003.

RJ Urick. The absorption of sound in suspensions of irregular particles. *The Journal of the acoustical society of America*, 20(3):283–289, 1948.

Robert J Urick. *Principles of underwater sound for engineers*. Tata McGraw-Hill Education, 1967.

Alaska U.S. Army Engineer District. Galena streambank protection. galena, alaska section 14 reconnaissance rep., alaska district, anchorage, alaska. Technical report, 1983.

USACE. Method to evaluate potential for ice impacts on sediment stability in ice engineering. Technical report, US Army Engineer Reaserach and Development Center, Hannover, Nh, 2005.

Lars S Uunila. Effects of river ice on bank morphology and riparian vegetation along peace river, clayhurst to fort vermilion. In *Proceedings of the 9th Workshop on River Ice*, pages 24–26, 1997.

Mehmet S Uzuner and John F Kennedy. Theoretical model of river ice jams. *Journal of the Hydraulics Division*, 102(9):1365–1383, 1976.

JJ Van Der Sanden and H Drouin. Polarimetric radarsat-2 for river freeze-up monitoring; preliminary results. In *Proceedings of the 5th International Workshop on Science and Applications of SAR Polarimetry and Polarimetric Interferometry (SP-695)*, 2011.

Leo C van Rijn. Equivalent roughness of alluvial bed. *Journal of Hydraulic Engineering*, 108(10):1215–1218, 1982.

Leo C Van Rijn. Sediment transport, part i: bed load transport. *Journal of hydraulic engineering*, 110(10):1431–1456, 1984.

Leo C vanRijn. Sediment transport, part ii: suspended load transport. *Journal of hydraulic engineering*, 110(11):1613–1641, 1984.

D Vischer. The strickler formula, a swiss contribution to hydraulics. *Wasser, Energie, Luft*, 79(7):8, 1987.

Th Von Kármán. Mechanische änlichkeit und turbulenz. *Nachrichten von der Gesellschaft der Wissenschaften zu Göttingen, Mathematisch-Physikalische Klasse*, 1930:58–76, 1930.

HJ Walker. *Some aspects of erosion and sedimentation in an arctic delta during breakup*. Coastal Studies Institute, Louisiana State University, 1970.

DS Wang, HT Shen, Q Zhu, S Hou, Z Li, and Z Wang. Simulation and analysis of ice conditions in the lower yellow river. In *Proceedings, 13th IAHR Symposium on Ice*, volume 2, pages 721–728, 1996.

Shuang Ming Wang and JC Doering. Numerical simulation of supercooling process and frazil ice evolution. *Journal of Hydraulic Engineering*, 131(10):889–897, 2005.

Frank Weber, Dan Nixon, and Jeff Hurley. Semi-automated classification of river ice types on the peace river using radarsat-1 synthetic aperture radar (sar) imagery. *Canadian Journal of Civil Engineering*, 30(1):11–27, 2003.

Peter D Welch. The use of fast fourier transform for the estimation of power spectra: A method based on time averaging over short, modified periodograms. *IEEE Transactions on audio and electroacoustics*, 15(2):70–73, 1967.

CHESTER K Wentworth. The geologic work of ice jams in sub–arctic river. *Contributions in Geology and Geography*, pages 49–82, 1932.

Gesa A Weyhenmeyer, David M Livingstone, Markus Meili, Olaf Jensen, Barbara Benson, and John J Magnuson. Large geographical differences in the sensitivity of ice-covered lakes and rivers in the northern hemisphere to temperature changes. *Global Change Biology*, 17(1):268–275, 2011.

Kathleen D White. Review of prediction methods for breakup ice jams. *Canadian Journal of Civil Engineering*, 30(1):89–100, 2003.

Kathleen D White and Jeffrey P Laible. Small temporal scale winter dissolved oxygen processes. In *16th International Symposium on IceIce in the Environment*, pages 289–303, 2002.

WR White and TJ Day. *Transport of graded gravel bed material*, volume 181. Wiley, New York, 1982.

Peter J Whiting and William E Dietrich. Boundary shear stress and roughness over mobile alluvial beds. *Journal of Hydraulic Engineering*, 116(12):1495–1511, 1990.

TE Wigle. Investigations into frazil, bottom ice and surface ice formation in the niagara river. 1970.

Peter R Wilcock and Joanna C Crowe. Surface-based transport model for mixed-size sediment. *Journal of Hydraulic Engineering*, 129(2):120–128, 2003.

Garnett P Williams. *Flume width and water depth effects in sediment-transport experiments*. Citeseer, 1970.

Agata Wojtowicz, Faye Hicks, Robyn Andrishak, Michael Brayall, Julia Blackburn, and Joshua Maxwell. 2-d modeling of ice cover formation processes on the athabasca river, ab. 2009.

Agata Maria Wojtowicz. Two-dimensional modeling of freeze-up processes on the athabasca river downstream of fort mcmurray, alberta. In *Masters Abstracts International*, volume 48, 2010.

J Wong, S Beltaos, and BG Krishnappan. Seepage flow through simulated grounded ice jam. *Canadian Journal of Civil Engineering*, 12(4):926–929, 1985.

JL Wuebben. A laboratory study of flow in an ice-covered sand bed channel. In *Proceedings of the 8th International Symposium on Ice, International Association for Hydraulic Research*, 1986.

JL Wuebben. Effects of an ice cover on flow in a movable bed channel. In *Proc., IAHR Symp. on Ice*, pages 136–147, 1988a.

JL Wuebben. A preliminary study of scour under an ice jam. In *Proceedings of the 5th Workshop on Hydraulics of River Ice–Ice Jams, Manitoba Water Resources Branch, Winnipeg, Man*, pages 21–24, 1988b.

JL Wuebben. Ice effects on riprap, 1995.

M Selim Yalin. Mechanics of sediment transport. 1963.

Mehmet Selim Yalin and Mehmet Selim. *River mechanics.* Pergamon Press Oxford, 1992.

M Yamazaki, K Hirayama, S Sakai, M Sasmoto, M Kiyohara, and H Takiguichi. Formation of frazil and anchor ice. In *Proceedings of the IAHR Ice Symposium*, pages 488–496, 1996.

Chih Ted Yang. Sediment transport: theory and practice. *MCGRAW-HILL BOOK CO,(USA). 1996.*, 1996.

S Ye and JC Doering. A model for the vertical distribution of frazil ice. In *Proceedings of the 12th Workshop on River Ice, Edmonton, AB*, pages 19–20, 2003.

JY Yoon, VC Patel, and R Ettema. Numerical model of flow in ice-covered channel. *Journal of Hydraulic Engineering*, 122(1):19–26, 1996.

Leonard J Zabilansky. Ice cover effects on bed scour: Case studies. In *Cold Regions Engineering@ sCold Regions Impacts on Transportation and Infrastructure*, pages 795–803. ASCE, 2002.

Leonard J Zabilansky, Robert Ettema, James Wuebben, and Norbert Yankielun. Survey of river ice influences on channel bathymetry along the fort peck reach of the missouri river, winter 1998-1999. Technical report, DTIC Document, 2002.

I Zaier, C Shu, TBMJ Ouarda, O Seidou, and F Chebana. Estimation of ice thickness on lakes using artificial neural network ensembles. *Journal of hydrology*, 383(3):330–340, 2010.

Jon E Zufelt. Flooding analysis using hec-ras. In *Impacts of Global Climate Change*, pages 1–6. ASCE, 2005.

Jon E Zufelt and Robert Ettema. Fully coupled model of ice-jam dynamics. *Journal of Cold Regions Engineering*, 14(1):24–41, 2000.